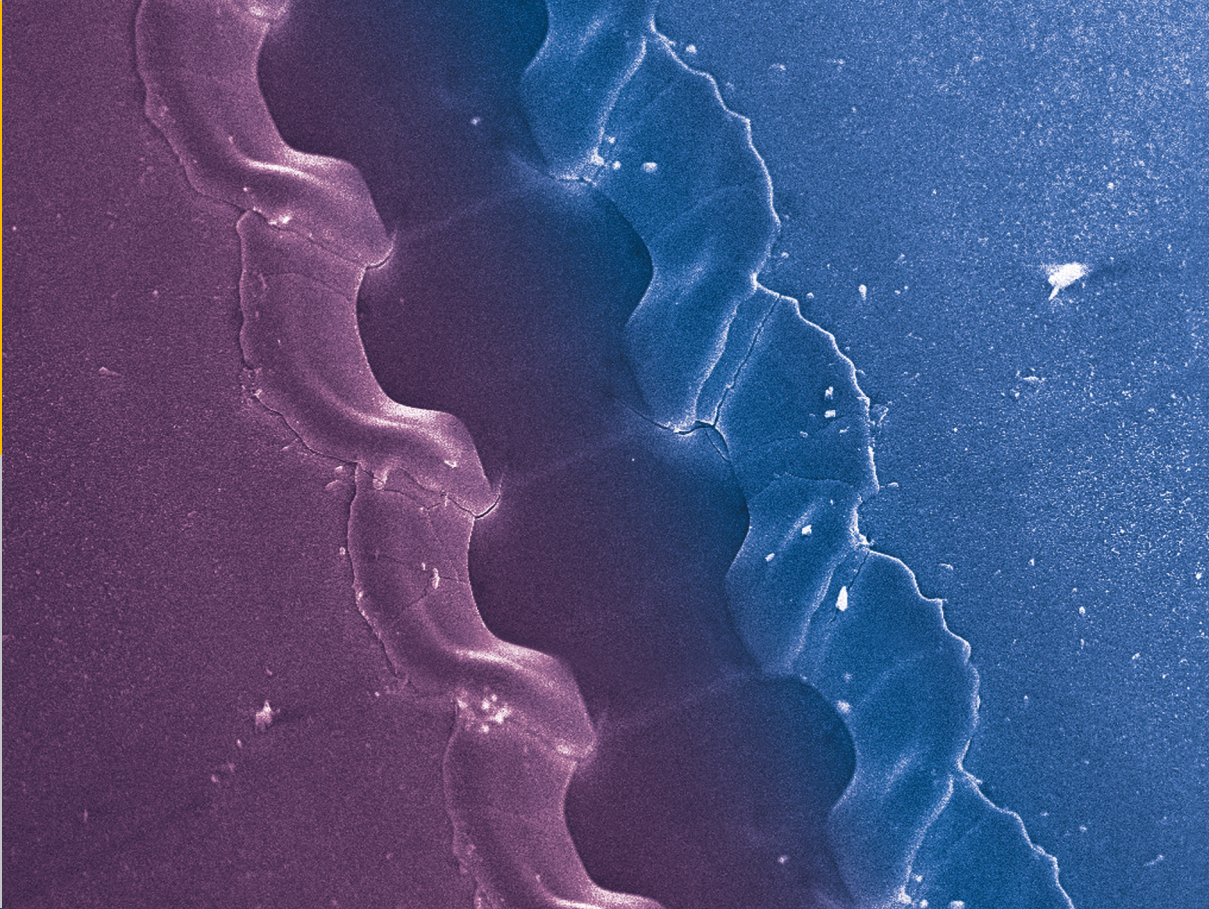


Laser processing for the integrated series connection of thin-film silicon solar cells

Bugra Turan



Member of the Helmholtz Association

**Energie & Umwelt /
Energy & Environment
Band / Volume 306
ISBN 978-3-95806-119-4**

 **JÜLICH**
FORSCHUNGSZENTRUM

Forschungszentrum Jülich GmbH
Institute of Energy and Climate Research (IEK)
Photovoltaics (IEK-5)

Laser processing for the integrated series connection of thin-film silicon solar cells

Bugra Turan

Schriften des Forschungszentrums Jülich
Reihe Energie & Umwelt / Energy & Environment

Band / Volume 306

ISSN 1866-1793

ISBN 978-3-95806-119-4

Bibliographic information published by the Deutsche Nationalbibliothek.
The Deutsche Nationalbibliothek lists this publication in the Deutsche
Nationalbibliografie; detailed bibliographic data are available in the
Internet at <http://dnb.d-nb.de>.

Publisher and
Distributor: Forschungszentrum Jülich GmbH
Zentralbibliothek
52425 Jülich
Tel: +49 2461 61-5368
Fax: +49 2461 61-6103
Email: zb-publikation@fz-juelich.de
www.fz-juelich.de/zb

Cover Design: Grafische Medien, Forschungszentrum Jülich GmbH

Printer: Grafische Medien, Forschungszentrum Jülich GmbH

Copyright: Forschungszentrum Jülich 2016

Schriften des Forschungszentrums Jülich
Reihe Energie & Umwelt / Energy & Environment, Band / Volume 306

D 82 (Diss. RWTH Aachen University, 2016)

ISSN 1866-1793
ISBN 978-3-95806-119-4

The complete volume is freely available on the Internet on the Jülicher Open Access Server (JuSER)
at www.fz-juelich.de/zb/openaccess.

Neither this book nor any part of it may be reproduced or transmitted in any form or by any
means, electronic or mechanical, including photocopying, microfilming, and recording, or by any
information storage and retrieval system, without permission in writing from the publisher.

Abstract

The integrated series connection of solar cells is an essential aspect for thin-film photovoltaic technology. With a series connection a high output voltage of the module is achieved while the output current is kept low. Thus, Ohmic losses in the contact materials are kept low as well.

In thin-film silicon solar technology the steps to create the interconnection are commonly done by laser ablation integrated in-between the depositions of the solar cell layer materials. In three steps laser scribing is used to selectively remove layers locally in the form of lines across the module substrate. In a first step the front-contact is removed for electrical insulation and cell stripe definition. Afterwards, the absorber is removed locally exposing the front-contact beneath. Finally, the interconnection is formed when the back-contact is removed locally as well.

The area that is needed for the interconnection of two neighboring cells is no longer active for current generation. Depending on the technology 5–10% of active area is lost. The reduction of this area holds an attractive potential for an increase of the module efficiency. The topic of this thesis is the investigation of the lower geometrical limits for the dead area reduction for substrate side laser processing of thin-film silicon solar cells. It is well-known that the interconnection and the laser processes can have an impact on the performance of the solar module. Therefore, the characterization of the impact on the performance is of special importance when laser processes are used that are capable of generating a reduced interconnection width.

P1: for the front-contact insulation process it was found out that the scribe quality strongly depends on the used laser wavelength. Ablation mechanisms that are driven by material phase changes (scribing with 532 nm or 1064 nm) can lead to smoother scribe edges compared to mechanisms dominated by stress-induced removal (355 nm) where non-uniform rip-off at the edges occurs.

However, in certain processing regimes, strong ablation debris redeposition in direct vicinity of the P1 scribe is observed when small beam spot radii ($<10\ \mu\text{m}$) are used. Such redeposition has a severe impact on the solar cell performance in this region. With proper wet-chemical cleaning the amount of redeposited debris on the front-contact and the negative impact on the solar module can be minimized.

Parasitic shunting of two neighboring cell stripes by deposition of absorber material into the P1 scribe increases when the scribe width is reduced. Measurements show that the overall magnitude of the shunt is in a value range that impact on the solar module is negligible for commonly used cell topologies.

P2: the width reduction approach was extended for the absorber removal process (P2). To ensure the selectivity of silicon removal without damaging of the front-contact beneath, only 532 nm was used for scribing. For this wavelength ablation is strongly assisted by mechanical stresses generated by hydrogen diffusion from the absorber layer and/or thermal expansion of the absorber layer.

Mechanical constraints limiting the lower scribe width are found that depend on the absorber thickness and the laser beam spot size. Such behavior can be explained directly from linear elastic fracture mechanics where removal of the layer is determined by the relation between delamination at the interface and fracture of the absorber along the circumference of the spot. It can be concluded that for substrate side laser-induced ablation thin scribe lines are only possible for thin layers.

The parasitic series resistance formed by P2 also increases as the scribe width is decreased. However, for processing of amorphous silicon absorbers, with a beam radius 10 μm , the minimal achievable resistance value is strongly increased. In fact, much more than what would be expected just by the geometrical contact area reduction. This is most likely owed to changes of the specific contact resistance due to increased debris redeposition within the P2 scribe prior to back-contact deposition. In contrast, such effects are not observed for processing of tandem absorber where debris redeposition is less pronounced. Here, low series resistances, with only minor impact on the module performance, are achieved for all investigated beam spot sizes.

P3: the back-contact insulation process (P3) is similar to P2 since the back-contact is removed indirectly by removal of the absorber beneath. Shunting between front- and back-contact can occur at the direct P3 scribe edges. These shunts are possibly formed due to heat generated by sub-threshold energy intake of excess energy from the shoulders of Gaussian distribution of the laser.

The mechanical constraints on the minimal achievable scribe widths are even stronger than what was observed for the optimization of the P2 process. This is owed to the additional overall thickness of the layer-stack due to the back-contact. Furthermore, for tandem solar cell processing the scribe edges are strongly distorted by delaminated material while clean edges are obtained for a-Si:H solar cells.

The parasitic shunting by P3 scribing increases by many orders of magnitude when a processing beam radius of 10 μm is used. However, just like it was observed from P2, an overall weaker deterioration is obtained for scribing of tandem solar cells than for amorphous silicon cells. It is possible that material modifications are more localized in the a-Si:H top-cell. Together with the higher thickness of the tandem cells (300 nm vs. 1.4 μm) the impact on the whole device is not as pronounced.

Kurzfassung

Die integrierte Serienverschaltung zur Herstellung von Solarmodulen ist ein essentieller Aspekt von Dünnschicht-Solarmodulen. Mithilfe einer Serienverschaltung können hohe Ausgangsspannungen erzeugt werden, gleichzeitig wird der Ausgangsstrom niedrig gehalten. Dadurch wird eine signifikante Senkung Ohm'scher Verluste in den Kontaktschichten erzielt.

In der Silizium-Dünnschichttechnologie wird die Serienverschaltung mittels Laserablation realisiert. Die einzelnen Schritte werden dabei in die Herstellungsprozesse der Solarzelle integriert. In drei Ablationsschritten wird Material selektiv in Form von Gräben vom Substrat entfernt ohne die darunterliegende Schicht zu beschädigen.

Zunächst wird der Frontkontakt strukturiert um eine elektrische Isolation zwischen den einzelnen Zellstreifen zu erreichen. Anschließend wird der Absorber lokal entfernt und der darunter liegende Frontkontakt wieder freigelegt. Im dritten und letzten Schritt wird auch der Rückkontakt selektiv entfernt und die Serienverbindung schließlich hergestellt.

Die Fläche welche benötigt wird um zwei benachbarte Zellen miteinander zu verbinden trägt nicht mehr zur Stromgenerierung bei. Abhängig von der Dünnschichttechnologie können diese Flächenverluste 5–10% der Modulfläche ausmachen. Die Verringerung dieser toten Fläche birgt Potential zur Steigerung der Moduleffizienz. Die Reduktion und etwaige geometrische untere Grenzen der toten Fläche mittels optimierter Laserprozesse für die Bearbeitung von Silizium-Dünnschicht-Solarmodulen von der Substratseite ist das Thema dieser Arbeit. Der negative Einfluss der Serienverbindung selbst und der Laserprozesse auf das Solarmodul ist bekannt. Daher ist die Charakterisierung möglicher Beeinflussungen der Performance insbesondere wichtig für Laserprozesse die es ermöglichen verkleinerte Verschaltungslinien zu erzeugen.

P1: Bei der Strukturierung des Frontkontakts (P1) zeigen sich Unterschiede bei der Qualität des Grabens abhängig von der zur Bearbeitung verwendeten Wellenlänge. Ablationsmechanismen die getrieben sind durch Phasenübergänge (Prozessierung mit 532 nm und 1064 nm) können weichere Grabenkanten erzeugen im Gegensatz zu Mechanismen die vorwiegend getragen werden durch mechanische Spannungen (Bearbeitung mit 355 nm). Hierbei kann das Abrissverhalten der Schicht zu undefinierten Grabenkanten führen.

Für bestimmte Prozessparameter, im Zusammenhang mit Laser-Spotradien unter 10 μm , wird eine verstärkte Beeinflussung des verbliebenen Frontkontakts in direkter Umgebung des Grabens beobachtet. Diese Beeinflussung kann zurückgeführt werden auf massive Redeposition von Ablationsresten. Diese haben dann einen negativen Einfluss auf die Solarzelle in direkter Umgebung des Grabens. Jedoch ist es möglich mit einer entsprechenden nasschemischen Nachbehandlung den Einfluss zu minimieren.

Die Stärke des parasitären Parallelwiderstands, welcher sich nach der Absorberdeposition im P1 Graben zwischen zwei benachbarten Zellstreifen ausbildet, nimmt mit Verkleinerung des Grabens zu. Jedoch ist die spezifische Höhe des Widerstands so hoch, dass der Einfluss für üblicherweise eingesetzte Zelltopologien zu vernachlässigen ist.

P2: Die Reduktion der Verschaltungsbreite wurde auf den zweiten Prozess zur Strukturierung des Absorbers (P2) ausgeweitet. Hierbei gilt es eine Beschädigung des freigelegten Frontkontakts möglichst zu vermeiden. Daher ist es von Vorteil einen Laser mit der Wellenlänge von 532 nm einzusetzen. Mit 532 nm ist die Ablation dominiert von einer mechanisch induzierten Entfernung des Absorbermaterials. Die Kräfte können dabei entweder durch thermische Expansion des Absorbers entsteht und/oder durch Gasdruck einer Blase die durch Diffusion von Wasserstoff an der Grenzfläche Frontkontakt/Absorber entsteht.

Es wurden untere Grenzen für die minimale Grabenbreite gefunden. Sie hängen stark vom Laser-Spotradius und Schichtdicke des Absorbers ab. Eine solche Abhängigkeit zwischen Ablationsverhalten und Geometrie lässt sich direkt aus der Bruchmechanik zwischen Delamination und Bruch entlang des Umfangs des Absorbers beschreiben. Zusammenfassend lässt sich sagen, dass für die P2 Bearbeitung durch die Substratseite sehr dünne Gräben nur möglich sind für dünne Absorberschichten.

Der parasitäre Serienwiderstand, welcher sich durch P2 nach der Rückkontaktdeposition ausbildet, steigt an für verkleinerte Grabenbreiten. Jedoch zeigt sich bei der Bearbeitung von amorphem Silizium mit einem Laser-Spotradius von 10 μm , dass der Widerstand weitaus höher ansteigt als von rein geometrischen Überlegungen angenommen. Dies lässt sich zurückführen auf eine erhöhte Redeposition von Ablationsresten auf den freigelegten Frontkontakt. Es ist bekannt, dass Redeposition der Hauptgrund für die Ausbildung eines parasitären Kontaktwiderstands ist. Solche Effekte werden für die Bearbeitung von Tandemabsorbern nicht beobachtet wo die Redeposition weniger stark ausgeprägt ist. Hierbei werden niedrige Kontaktwiderstände mit einer vernachlässigbaren Beeinflussung der Moduleigenschaften für alle untersuchten Laser-Spotradien erreicht.

P3: Der Strukturierungsprozess P3 ist sehr ähnlich zum Prozess P2 da der Rückkontakt bei P3 indirekt durch Ablation des Absorbers entfernt wird. Ein parasitärer Parallelwiderstand zwischen Front- und Rückkontakt am Rand des Ablationsgrabens kann durch zusätzliche Wärmeeinwirkung aufgrund der Gauß-Verteilung des Lasers entstehen.

Wie vermutet ergeben sich noch stärkere Einschränkungen bei der minimalen Grabenbreite durch die erhöhte Gesamtschichtdicke des Systems aus Absorber und Rückkontakt. Des Weiteren, ergeben bei der Bearbeitung von Tandemsolarzellen starke Unregelmäßigkeiten am Grabenrand. Im Gegenteil dazu werden bei der Bearbeitung von Solarzellen aus amorphem Silizium saubere Grabenkanten beobachtet ohne besondere Flitterbildung.

Der eingangs erwähnte negative Einfluss auf die elektrischen Eigenschaften ist erhöht für verringerte Laser-Spotradien. Jedoch, wie schon bei P2 beobachtet, ist die Beschädigung bei der Bearbeitung von Tandemsolarzellen weitaus geringer als für Zellen aus amorphem Silizium. Der parasitäre Parallelwiderstand kann sich um mehrere Größenordnungen verringern wenn ein Laser-Spotradius von 10 μm verwendet wird. Es ist möglich, dass bei Tandemsolarzellen die Schädigung lokalisiert ist auf die Top-Zelle aus amorphem Silizium da hier ein Großteil der

Laserenergie absorbiert wird. Zusammen mit der höheren Absorberdicke (300 nm vs. 1.4 μm) folgt ein geringerer Einfluss auf die elektrischen Eigenschaften des Gesamtdevices.



Contents

Abstract	v
Kurzfassung	vii
1 Introduction	1
2 Fundamentals	5
2.1 Solar cells	5
2.1.1 The electrical solar cell properties	8
2.2 The monolithic series connection	14
2.2.1 Realization of the interconnection	15
2.2.2 Modeling of interconnection losses	17
3 Laser material processing	23
3.1 Laser sources	23
3.2 Optic basics	26
3.3 Laser structuring system	30
3.3.1 Laser processing parameters	31
3.3.2 Material laser ablation properties	33
3.3.3 Determination of the processing beam spot size	35
4 Characterization methods	39
4.1 Ablation mechanisms	39
4.2 Conductivity Atomic Force Microscopy	41
4.3 Laser Beam Induced Current	44
5 Front-contact structuring process P1	47
5.1 Material ablation behavior	47
5.2 Mechanisms driving laser ablation processes	50
5.3 Geometrical scribe width optimization	58
5.4 Near scribe edge material modifications	62
5.4.1 Post-scribe cleaning	73
5.5 Impact on electrical properties	78
5.6 Process implementation in solar mini modules	84
	xi

Contents

6 Absorber removal process P2	87
6.1 Material ablation behavior	87
6.1.1 Visually optimized scribe lines	91
6.2 Absorber ablation mechanisms	93
6.3 Modeling of removal mechanisms	96
6.3.1 Temporal and spatial temperature distribution	96
6.3.2 Vapor-Stress induced ablation mechanisms	109
6.3.3 Thermal-Stress induced ablation	115
6.4 Impact on electrical properties	117
6.4.1 Ablation debris redeposition	122
6.4.2 Atmospheric conditions	125
6.4.3 Series resistance solar module losses	127
6.5 Process implementation in mini solar modules	130
7 Back-contact insulation process P3	135
7.1 Material ablation behavior	135
7.1.1 Geometrical scribe width minimization	139
7.2 Impact on electrical properties	140
7.2.1 Sub-threshold energy intake for Gaussian laser beams	142
7.2.2 Shunting behavior of P3 processed solar cells	146
7.3 Near scribe edge material modifications	156
7.4 Process implementation in mini solar modules	162
8 Conclusion	165
Bibliography	171
Publications	185
Acknowledgements	187

1 Introduction

Climate change, rising costs of fossil energy, and safety concerns for nuclear energy lead to a significant expansion of renewable energy sources. The share of renewable energies on the overall electrical power generation in Germany massively increased in the last decade. In recent years, governmental incentives boosted the installation of photovoltaic power generation with solar cells. This increased demand led to a significant solar module cost reduction and cell efficiency increase.

Today, bulk silicon wafer solar cells account for a vast majority of the world's photovoltaic cell production with record cell efficiencies up to 25% [1]. Although struggling with lower cell efficiencies, thin-film solar technology constitutes an attractive alternative to wafer-based solar cells. Due to production processes that allow depositions on substrates with areas of up to 5.7 m² [2] lower \$/W values compared to wafer solar cells can be achieved.

One important difference of thin-film solar cells to wafer cells is how the solar module is formed. Within one module, for bulk silicon solar cells each individual wafer is usually connected in series by metal strings connecting the cathode of one cell with the anode of the next cell. In contrast to this, for most thin-film solar cell technologies the series connection of the individual cells is integrated monolithically within the deposition process.

Laser ablation is dominantly used for the realization of the solar cell series connection in most thin-film technologies. Due to the thin contact layer materials (thickness nm– μ m) the series connection is from utter importance to reduce Ohmic losses.

Three patterning or scribing steps are required for the formation of the interconnection. The processes are integrated in-between the deposition steps of the solar cell. After the first contact layer (front-contact) is deposited laser scribing is used to selectively remove the contact layer for the definition of individual cell stripes (P1). Subsequently, after deposition of the solar cell absorber a second scribe line next to the first P1 scribe removes the absorber exposing the underlying contact layer (P2). In a last step, after deposition of the second contact layer (back-contact) a third scribe line is placed next to the P2 scribe removing the second contact layer selectively without damaging of the first contact layer beneath (P3).

Introduction

However, the area needed for the interconnection processes P1–P3 with the margin in-between the scribes is no longer active for current generation. This loss factor can be significant with 5–10% area lost depending on the thin-film solar technology. Yet, in literature not much research is found on the reduction of this lost area.

The main purpose of P1 laser scribing of the first contact layer (or front-contact) is the electrical insulation and definition of the solar cell stripes. The material is removed down to the substrate. After absorber deposition a parasitic conductivity is formed between two neighboring front-contact stripes within the P1 scribe. This parasitic conductivity is influenced by the dimensions of the P1 scribe line. Especially with respect to the reduction of lost area impact on the solar modules performance is possible when the scribe width is reduced.

In Chapter 5 the front-contact removal process P1 will be investigated with regards to the electrical and morphological properties of the scribes. It was found out that significant ablation debris redeposition on the remaining front-contact in vicinity of P1 scribe edge can occur with negative impact on the solar cell in this region. However, processing impact can be minimized when proper wet-chemical cleaning after processing is carried out.

For the absorber removal process P2 the selective ablation without damaging of the front-contact material beneath is required. The P2 scribe exposes the front-contact so that after back-contact deposition the interconnection between two neighboring cells is formed. The whole solar module current needs to flow from the back-contact of one cell, through this P2 scribe, to the front-contact of the next cell. Due to non-ideal laser processes a barrier layer can be formed leading to a parasitic series resistance. Again, with respect to the width reduction of this scribe, the series resistance is influenced by the contact area as well.

Chapter 6 is dedicated to the investigation of the P2 process. It will be shown that severe constraints on the lower scribe width limit are found. Due to the dominant ablation mechanisms driving this process thin scribe lines are only possible for thin absorber layers. For processing of certain absorber materials, impact of the laser beam spot size on the contact resistance can be found as well.

The back-contact insulation process P3 is required for the final definition of the individual cell stripes of the solar module. The process is similar to P2 since the back-contact is removed indirectly by removal of the absorber below. However, damaging of the front-contact should be avoided because the whole cell current needs to flow through the exposed front-contact TCO. The main challenge for P3 processing is the minimization of the impact on active solar cell material in direct vicinity to the scribe edges. Electrical shunting between front- and back-contact can occur due to excess heat generated by the laser beam in the scribe edges leading to module deterioration.

In Chapter 7 the back-contact insulation process P3 will be characterized with laser beams of different spot sizes. For structuring, similar constraints on the minimal achievable scribe widths as for absorber removal P2 are expected. Beside the constraints on the minimal

achievable P3 scribe width impact of processing with decreasing laser beam spot sizes on the degree of shunting is of interest.

Due to the additional back-contact large differences of the scribe edge quality between a-Si:H and tandem solar cell processing were found, especially for scribing with a laser spot size of 10 μm . A clean edge without flaking is achieved for a-Si:H while a significant amount of delaminated material is observed for tandem solar cells.

The degree of shunting increases drastically for a-Si:H solar cells when the laser spot size is decreased. In contrast, for tandem solar cells only minor changes of shunting are observed as a function of the beam spot size.

2 Fundamentals

The first chapter gives a basic introduction into the solar cell material systems and different device topologies that were in focus of this work. The main solar cell parameters that are determining the performance will be briefly defined. Subsequently, the need for an integrated series connection of solar cells will be motivated and its realization will be introduced. For the integrated series connection possible loss mechanisms will be identified and their impact on the solar module will be calculated. A potential way for the optimization of the integrated series connection will be presented at the end of this chapter.

2.1 Solar cells

Thin-film silicon solar cells often have a drift-dominated transport of the generated carriers. This is different for crystalline solar cells which have a current flow dominated by carrier diffusion. Differences in the carrier collection gives rise to very different requirements on cell dimensions, optical and electrical layer properties. Some of these differences can be seen in Figure 2.1 showing a schematic sketch of a crystalline silicon wafer solar cell and a thin-film silicon solar cell. The most obvious difference between both technologies is the much lower thickness of the thin-film device in Figure 2.1 (b). Therefore, the glass substrate constitutes the main mechanical support of the thin-film cell. The second difference can be seen from the current flow path. The doped layers in the case of the thin-film solar cell only have a very low in-plane conductivity. This is the reason why besides the metal back-contact an additional window layer, usually a transparent conductive oxide (TCO), is required for the current transport on the front side.

A detailed sketch of thin-film silicon solar cells can be seen in Figure 2.2. In general, solar cells in thin-film technology can be realized in two different layer-stack topologies. One is called substrate configuration while the other is called superstrate configuration (Figure 2.2) with distinct differences [3]. The major difference is the direction of incidence of sun light whether it is irradiating through the substrate or not. In superstrate configuration the substrate needs to be transparent while in substrate configuration it can be opaque (for example steel or plastic foils [4]). Besides these optical requirements on the substrate there are also demands on the

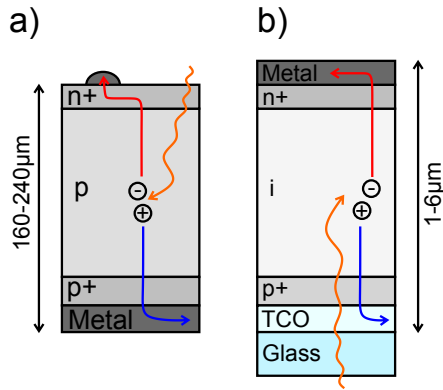


Figure 2.1: Schematic sketch of the cell topologies of two different solar cell technologies with carrier generation and transport. Each sketch shows: a) A crystalline bulk silicon cell. b) A thin-film cell in superstrate configuration. Dimensions are not to scale.

mechanical properties. The main purpose of the substrate is the mechanical support of the thin functional solar cell layers with thicknesses in the micrometer scale. The nomenclature of p-i-n and n-i-p solar cell originates from the order of layer deposition of the solar cell [5].

Most of the discussed fundamentals also apply for bulk silicon solar cells or other thin-film technologies. Nevertheless, the main focus lies on thin-film silicon solar cells since this technology will be investigated in the present work.

From here on p-i-n thin-film silicon solar cells in superstrate topology will be set as the standard topology for all investigations (Figure 2.2(b)). Please note that, although superstrate topology was set as standard, the superstrate will be referred to as the substrate of the solar cell. Onto the substrate different layers are deposited successively and in the following the function of each layer will be presented.

The front-contact: the first layer deposited onto the substrate is usually a transparent conductive oxide (TCO). The front-contact TCO layer has to be electrically conductive since it is in contact with the absorber where the carriers are generated. At the same time it has to be transparent because the sun light passes through this layer into the absorber. Commonly used materials are metal oxides like tin dioxide (SnO_2) doped with indium or fluorine and zinc oxide (ZnO) doped with aluminum, gallium or boron. A nice overview of the broad spectrum of different TCOs and their applicability in solar cells is given in a review by Gordon [6].

The front-contact needs to exhibit a rough surface texture because, besides of being transparent, there are additional optical requirements. Due to the rather thin absorber layers it is necessary to create a texture with different feature sizes. A surface texture enhances the light in-coupling into the absorber as well as elongates the light path in the absorber. This is equivalent with an increase of the effective optical absorber thickness [7]. These textures are either created intrinsically by the deposition process (for example $\text{SnO}_2:\text{F}$ by CVD [8]

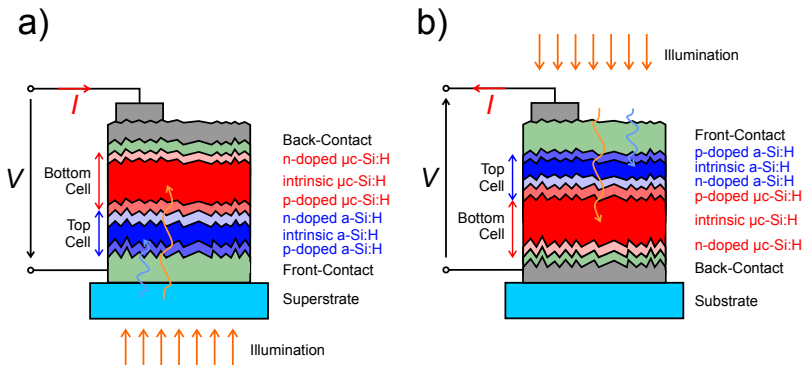


Figure 2.2: Schematic sketch of the layer-stacks of two a-Si:H/ μ c-Si:H thin-film silicon tandem solar cell in: a) Superstrate configuration. b) Substrate configuration. Dimensions are not to scale.

and ZnO:B by low pressure CVD [9]) or by wet-chemical etching after deposition (sputtered ZnO:Al [10]). The thickness of the front-contact can vary depending on the required optical and electrical properties. For fluorine-doped tin dioxide and sputtered ZnO:Al (before etching) thicknesses are commonly 700–800 nm. For ZnO:B thicknesses between 1.5–2 μ m are typical.

The absorber: in the subsequently deposited layer-stack the charge carriers are generated from sunlight. The absorber is deposited upon the textured front-contact. The absorber stack consists of a p-doped silicon layer followed by an intrinsic silicon layer and finally an n-doped silicon layer. These layers are typically deposited by Plasma Enhanced Chemical Vapor Deposition (PECVD) [11, 12]. It is also common to stack two p-i-n junctions on top of each other and have them connected in series. Thus, it is possible to absorb light with two absorbers that exhibit different optical band gaps [13, 14]. For single junction cells hydrogenated amorphous silicon (a-Si:H) is an allotropic form of silicon and commonly used as an absorber material [15].

In the so-called tandem or micromorph solar cells, on top of the amorphous silicon solar cell an absorber with a smaller band gap like microcrystalline silicon (μ c-Si:H) is deposited [16]. In this way an a-Si:H/ μ c-Si:H double-junction solar cell (see Figure 2.2) is created. A tandem of these two absorbers is advantageous since it reduced thermalization and transmission losses compared to a single junction device. The band gap of the a-Si:H cell is around $E_g=1.75$ eV whereas μ c-Si:H has a band gap of $E_g=1.1$ eV. Since these two cells are connected in series, the same current density will flow through both of them. The intrinsic layer thicknesses are adjusted accordingly to achieve same photo current generation in both cells [17]. The a-Si:H intrinsic layer thickness is in the range of 150–250 nm whereas the layer thickness for μ c-Si:H is typically 1–3 μ m. There are concepts with more than two junctions but current matching between all absorbers increases the deposition complexity significantly [18].

The thin heavily doped layers need to be as thin as possible due to the high parasitic light absorption by additional defects in the material introduced by the dopant [19]. The function

of the doped layers is to establish an electric field across the intrinsic layer where the light is absorbed and charge carriers are created (p-i-n solar cell [20]). The carriers are then separated by the electric field and drift towards the contacts with the average drift length $L_{\text{drift}} = \mu\tau E$. The parameters μ and τ are the carrier mobility and lifetime, respectively. This is necessary due to the low diffusion length in thin-film silicon solar cells. If transport would only be based on diffusion high recombination losses would prevail (for reasonable absorber thicknesses). There are additional constraints limiting the absorber thicknesses since a-Si:H solar cells suffer from light-induced degradation. For details refer to the Staebler-Wronski-Effect (SWE) [21]. For $\mu\text{c-Si:H}$ solar cells economical factors like the deposition time and material consumption are further limiting the absorber thickness which limits the maximal reasonable thickness.

The back-contact: the last layer-stack that is deposited on top of the absorber layers consists of a TCO and/or metal layer. The functional purpose of the back-contact is the electrical connection of the absorber. Since the sun light is irradiating from the substrate side (thus through the front-contact) there is no need for this layer to be transparent. In fact, the back-contact should be highly reflective elongating the path of sunlight that was not absorbed by the absorber. Silver and aluminum are commonly used metal back-contact layers due to their good electrical conductivity and optical reflectivity [22]. Due to parasitic absorption by surface plasmon excitation in the metal, an additional thin TCO layer in front of the metal can help to lower these losses [23, 24]. Another approach is the use of a highly conductive TCO at the back-contact together with a dielectric mirror. In the simplest case this could be white paint (TiO_2 particles) [25]. The overall thickness for the back-contact is in the range of 300–400 nm for metal-based topologies and 1.5–2 μm for a back-contact based on TCO and dielectrics.

For a more thorough introduction into the thin-film silicon solar cell technology please refer to the literature in [26, 27, 28].

2.1.1 The electrical solar cell properties

A thin-film silicon solar cell can be modeled by an electrical equivalent circuit with lumped components. Figure 2.3 shows a commonly used one-diode equivalent circuit of a solar cell [29]. There are more sophisticated models with multiple diodes and/or additional current sources [30]. However, for the proper representation of the basic electrical behavior of the solar cell such models are not necessary. If not specifically defined differently, all area dependent values are referred to 1 cm^2 cell area. The series resistance R_s represents the Ohmic losses in the contact materials as well as contact resistances and series resistances of the absorber layer. The values for R_s are usually below 10 Ω .

Another path of possible power losses is represented by the parallel resistance R_p . In general, this resistance represents losses by shunting of the solar cell. The value for R_p is in the range of 10^3 – $10^6 \Omega$.

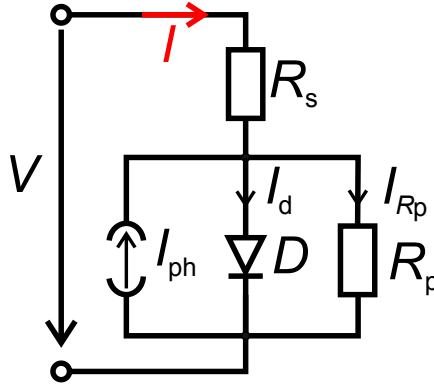


Figure 2.3: One diode equivalent circuit of a thin-film silicon solar cell with lumped elements. The resistances R_s and R_p represent the series and parallel resistance, respectively. An ideal current source represents the generated photo current I_{ph} under illumination. An ideal diode is used to model the exponential p-i-n behavior of the solar cell with the corresponding current I_d .

The diode in Figure 2.3 reassembles the behavior p-i-n diode of the solar cell. The current-voltage relation is given in Equation 2.1.

$$I_d(V_d) = I_0 \left[\exp\left(\frac{V_d}{nV_T}\right) - 1 \right] \quad (2.1)$$

When $n=1$ the equation equals the Shockley ideal diode equation with I_0 as the reverse bias saturation current, V_d as the voltage across the diode, ideality factor n , and the thermal voltage $V_T = kT/q$. For amorphous silicon solar cells I_0 is in the range of 10^{-13} – 10^{-11} A. The ideality factor is determined by the relative contributions of surface recombination at the contacts ($n \rightarrow 1$) and recombination in the intrinsic absorber ($n \rightarrow 2$).

The ideal current source with the current I_{ph} is proportional to the incident light intensity and represents the photo current of the solar cell. There is a voltage dependence of I_{ph} as well [31] but it is not of importance for the description of the solar cell behavior at this point.

The overall current-voltage characteristics of the equivalent circuit can be found with the Kirchoff point and loop rules (Equation 2.2).

$$I + I_{ph} = I_d + I_{Rp} \quad \text{and} \quad V = V_{R_s} + V_d \quad (2.2)$$

With these equations the current-voltage function can be written as,

$$I(V) = I_0 \left[\exp\left(\frac{V - R_s I(V)}{nV_T}\right) - 1 \right] + \frac{V - R_s I(V)}{R_p} - I_{ph}. \quad (2.3)$$

Equation 2.3 is transcendental since there is no algebraic function to describe the current I .

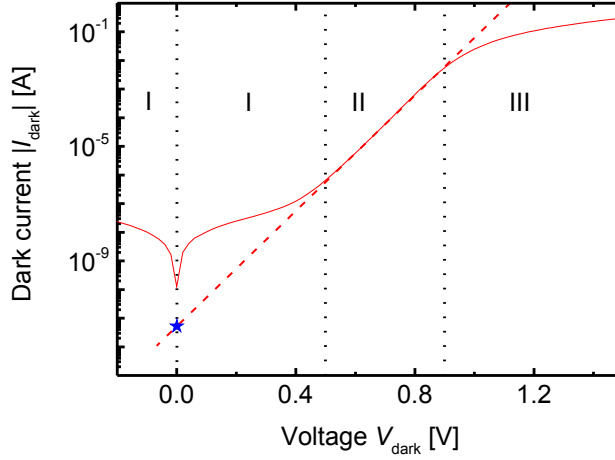


Figure 2.4: Measured dark $I - V$ curve of an amorphous silicon solar cell (a-Si:H) with different regimes I to III of Ohmic and exponential behavior. Dashed line represents a linear regression of the diode behavior in regime II.

Under dark conditions: the $I - V$ characteristics exhibits different regimes where behavior of certain elements from the equivalent circuit can be separated. Under dark conditions the photo current source I_{ph} from the lumped elements model is set to zero. Figure 2.4 shows the $I - V$ curve of an amorphous silicon solar cell measured under dark conditions. The absolute value of the current flow is plotted in a logarithmic scale. This is helpful to identify different regimes with exponential or Ohmic behavior. Regime I shows Ohmic behavior for both positive and negative voltages. For this case the equivalent circuit can be simplified by removing the diode. The remaining Ohmic elements lead to the following $I - V$ characteristics,

$$I_{\text{dark}}(V_{\text{dark}}) \approx \frac{V_{\text{dark}}}{R_s + R_p}. \quad (2.4)$$

Generally, series resistance values of R_s are many orders of magnitude lower than the parallel resistance R_p . Equation 2.4 can therefore be simplified even further to,

$$I_{\text{dark}}(V_{\text{dark}}) \approx \frac{V_{\text{dark}}}{R_p}. \quad (2.5)$$

Hence, it is possible to determine shunting behavior of R_p from $I - V$ characteristics under dark conditions in regime I.

In regime II a linear behavior is obtained which corresponds to an exponential $I - V$ characteristic since the current is plotted logarithmically. The diode is biased in forward direction in this voltage regime. The overall current flow is determined by the diode characteristics. This is

owed to the much higher conductance of the diode in comparison to the parallel resistance R_p . Equation 2.3 can be simplified to,

$$I_{\text{dark}}(V_{\text{dark}}) \approx I_0 \exp\left(\frac{V_{\text{dark}}}{nV_T}\right). \quad (2.6)$$

If Equation 2.6 is plotted logarithmically, like shown in Figure 2.4, the ideality factor n can be derived from the slope of a linear regression in this regime. The intercept with the y -axis will yield the saturation current coefficient I_0 .

In regime III there is a deviation from the linear behavior observed. The conductance of the diode is very high and the $I - V$ characteristics are influenced by the series resistance R_s . In this regime Equation 2.3 can be simplified to,

$$I_{\text{dark}}(V_{\text{dark}}) \approx I_0 \exp\left(\frac{V_{\text{dark}} - R_s I_{\text{dark}}(V)}{nV_T}\right). \quad (2.7)$$

The slope of the approximate function in Equation 2.7 is proportional to the inverse of the series resistance R_s . The derivative of Equation 2.7 is defined as,

$$\frac{dI_{\text{dark}}(V_{\text{dark}})}{dV_{\text{dark}}} \approx \frac{1}{R_s + \frac{nV_T}{I_{\text{dark}}(V)}} \approx \frac{1}{R_s} \quad \left(\text{for } R_s \gg \frac{nV_T}{I_{\text{dark}}(V)}\right). \quad (2.8)$$

Equation 2.8 is proportional to the inverse of the series resistance R_s .

Under illumination: the previous assumption of $I_{\text{ph}}=0$ is no longer valid under illumination since charge carriers are generated and contribute to the current source in Figure 2.3. For this case Figure 2.5 shows the $I - V$ characteristics of the solar cell under AM1.5 illumination. This is equivalent with the typical sun light spectrum and intensity when passing 1.5 times the air mass of the atmosphere ($=48^\circ$ angle of incidence). The plot in Figure 2.5 has certain points that are specifically named and give information on the solar cell performance that are helpful for evaluation.

Under short-circuit conditions the voltage across the solar cell is zero ($V_{\text{suns}}=0$). The majority of the generated photo current will flow through the series resistance R_s . There is almost no current flow through the diode since biasing by R_s is small for typical series resistance/photo current values. Furthermore, current flow through the parallel resistance will be low as well due the large differences of the resistances (parallel circuitry at the current divider). R_p is many orders of magnitude larger than R_s . Therefore, the current flow under short-circuit conditions is almost equal to I_{ph} and is usually called I_{sc} .

The other important value is the voltage under open-circuit conditions. Under these conditions no current is flowing out of the solar cell ($I_{\text{suns}}=0$). There is no voltage drop across the series resistance R_s and it can be neglected. The generated photo current is split by the diode and the parallel resistance ($I_{\text{ph}}=I_{\text{diode}} + I_{R_p}$). The open-circuit voltage V_{oc} is primarily correlated with the band gap of the solar cell (more specifically the built in voltage V_{bi}) [32].

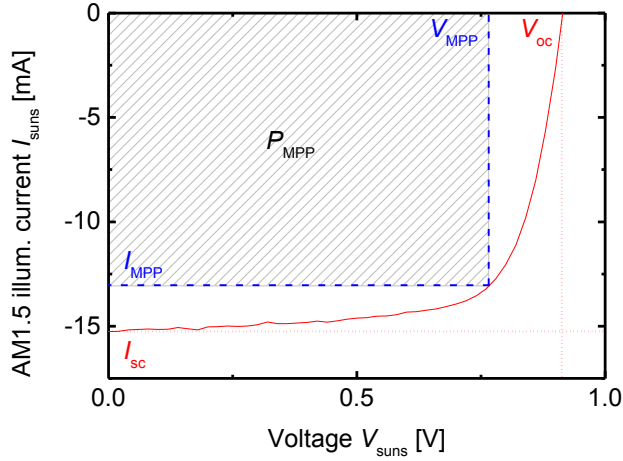


Figure 2.5: Measured $I - V$ curve under AM1.5 illumination of an amorphous silicon solar cell (a-Si:H). Shaded area corresponds to the generated power of the solar cell in the maximum power point (MPP).

At both points I_{sc} and V_{oc} the respective voltage or current is zero leading to no power output of the solar cell ($P = VI$). The operating point where the voltage/current product is maximized is called the maximum power point (MPP) with the respective voltage V_{MPP} and current I_{MPP} .

The efficiency η of the solar cell is then defined as,

$$\eta = \frac{I_{MPP} V_{MPP}}{P_{AM1.5}}. \quad (2.9)$$

The value of $P_{AM1.5}$ in Equation 2.9 is the incident power. A useful measure for the parasitic losses of the solar cell is the fill-factor. It is defined as followed,

$$FF = \frac{I_{MPP} V_{MPP}}{I_{sc} V_{oc}}. \quad (2.10)$$

The fill-factor is usually between 60–80% and very important for the identification of shunting problems as well as high series resistances of the solar cell.

Figure 2.6 shows two parametric plots of a solar cell modeled in SPICE [33] according to the equivalent circuit from Figure 2.3. When the series resistance is varied (Figure 2.6(a)) the graphs show that the resistance has a big influence on the maximum power point (MPP) as well as on the fill-factor (FF). However, the value of V_{oc} is not affected since there is no voltage drop across R_s under open circuit conditions. For very high series resistances I_{sc} can be affected because of increasing current flow through diode that is biased by the voltage drop across R_s .

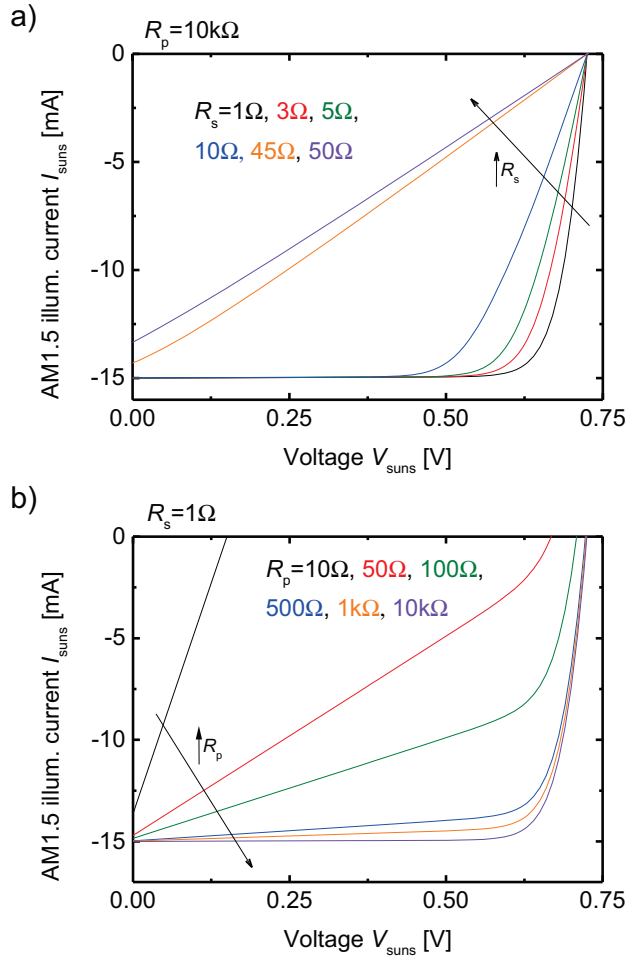


Figure 2.6: Parametric plots of calculated $I - V$ curves under illumination ($I_{\text{ph}}=15\text{ mA}$) and ideal diode ($V_j=0.75\text{ V}$, $n=1$). Plots show: a) Sweep of different series resistance values for R_s and fixed value of $R_p=10\text{ k}\Omega$. b) Sweep of different parallel resistance values for R_p and fixed value of $R_s=1\Omega$.

In contrast to this, when R_p is varied (Figure 2.6(b)) not only the MPP, FF, and I_{sc} are affected, but the open circuit voltage V_{oc} is highly influenced as well.

If the parallel resistance R_p is very large it can be neglected in the equivalent circuit. Thus, it is possible to correlate the differential resistance from the inverse slope of the $I - V$ curve under open circuit conditions to the series resistance R_s ,

$$\left. \frac{dI}{dV} \right|_{V=V_{oc}} = R_{oc}^{-1} \approx R_s^{-1}. \quad (2.11)$$

$$(2.12)$$

The same is valid for the shunting resistance R_p if the series resistance can be neglected. The inverse slope of the $I - V$ curve under short-circuit conditions is correlated to the parallel resistance R_p ,

$$\left. \frac{dI}{dV} \right|_{V=0} = R_{sc}^{-1} \approx R_p^{-1}. \quad (2.13)$$

$$(2.14)$$

Both values R_{oc} and R_{sc} can be related to the series and parallel resistances from the dark $I - V$ curve but are not the same [34]. Furthermore, for thin-film silicon solar cell the value of the parallel resistance depends on the illumination level [35].

2.2 The monolithic series connection

In the previous section it was shown that the series resistance of the solar cell can have a detrimental impact on the cells performance. These series resistance losses are partly owed to Ohmic losses in the contact materials. There is always a trade-off between transparency and electrical conductivity in the front-contact material for the commonly used TCO materials. For reasonable high optical transparency typical sheet resistances are in the range of 5–10 Ω [6].

One advantage of thin-film solar technology over wafer-based solar cells is the possibility to deposit the cells onto large substrates of up to 5.7 m² [2]. The generated current scales proportional with the aperture area of the cell. Typical current values in the MPP are approx. 10–15 mA for 1 cm² cell areas. Scaling of such currents to large substrate areas would result in a very large current flow in the contact materials. Especially in the front-contact this would result in high Ohmic losses since the sheet resistance of this layer is rather high. The losses would make the solar cell unusable for power generation.

The solution to this problem is the series connection of solar cells to increase the overall output voltage while maintaining a low current. When the current is kept low Ohmic losses will be low as well. For crystalline silicon all solar cells on one module substrate are connected in series and/or parallel with additional process steps by soldering the contact grids accordingly [36].

As mentioned above in all thin-film solar technologies the cell is deposited onto the whole substrate in one cycle. Therefore, a solar cell series connection that is made monolithically on the same substrate integrated in the module production process is favorable [37]. This way, a great degree of freedom for the output voltage/current parameters of the module is achieved while at the same time power losses are kept low.

In the following the realization of the integrated series connection for thin-film silicon solar modules will be introduced. Each interconnection process will be reviewed with estimations of further implications on the solar modules performance.

2.2.1 Realization of the interconnection

Figure 2.7 shows a sketch of an interconnected thin-film silicon solar module in superstrate configuration. A typical wafer silicon solar module is given for comparison as well. Although the dimensions from the sketches are not to scale, it is a fact that the minimal distances between two neighboring silicon wafers are limited by the metal grids connecting the cathode from one cell with the anode of the next cell (cf. Figure 2.7(b)). The series connection is usually done manually by soldering the interconnection strings to the cell grids. In contrast, for thin-film silicon solar modules the interconnection is integrated into the deposition process.

In thin-film technology the overall cell area is divided into many smaller cells which are connected in series by the interconnection labeled as the dead area width w_d in Figure 2.7(a). The output voltage is multiplied by the number of cells connected in series. The overall current is defined by the area of one cell since they are connected all in series. The series connection is realized by connecting the front-contact of one cell with the back-contact of the neighboring cell. For better visualization the interconnection is shown in Figure 2.8 in more detail. Figure 2.8 shows that three process steps, with removal of individual functional layers, are required for the interconnection of neighboring solar cell stripes. The layer removal is done in the manner of scribe lines across the whole module area perpendicular to the series connection. For thin-film silicon modules this is commonly done precisely by laser ablation [37, 38]. However, for certain technologies like CIGS or sometimes CdTe mechanical scribing with needles is used as well [39, 40]. But recently, laser scribing with ultra short pulsed lasers shows promising results for all-laser interconnected CIGS modules [41, 42].

In the literature and industry the processes are called P1–P3 and their electrical functions can be described as followed.

The interconnection processes: the process P1 is required for the division of the front-contact layer to create individual cell stripes of front-contact material which are all electrically insulated from each other. A high insulation resistance is required between two neighboring separated front-contact stripes.

Next to the P1 scribe another scribing process P2 is required for the interconnection of the back-contact from one cell with the front-contact of the next cell. After back-contact deposi-

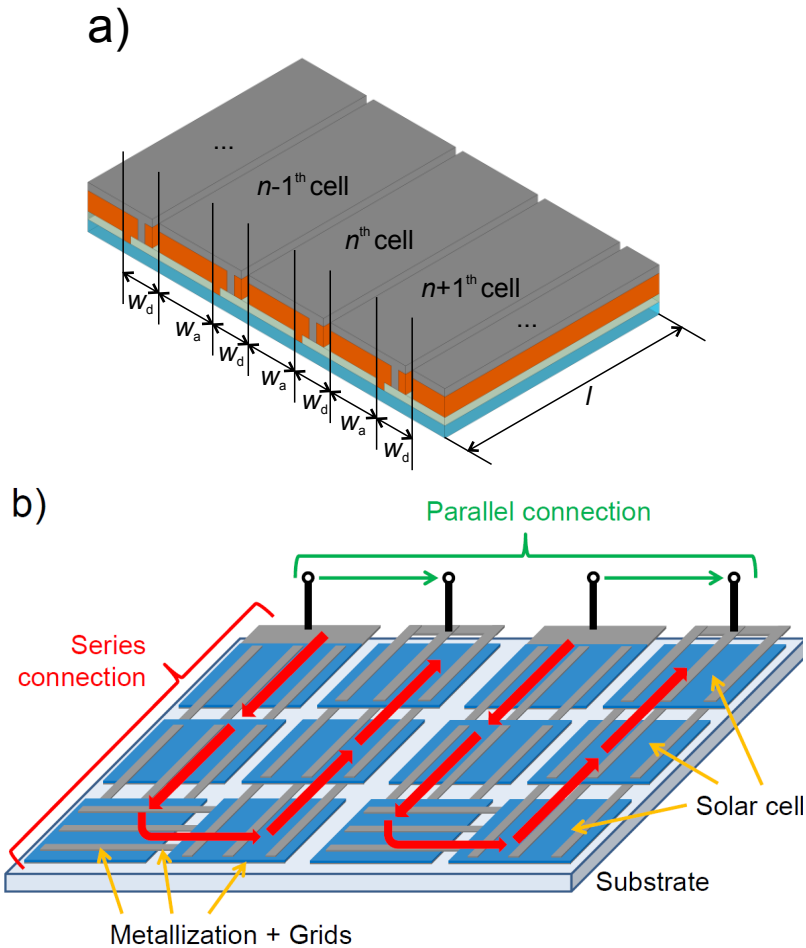


Figure 2.7: Comparison of schematic sketches for the realization of solar modules with two different approaches. Sketches show: a) Typical thin-film silicon solar module in superstrate configuration with interconnections for the integrated series connections of the individual cell stripes. The area required for each interconnection is labeled as the dead area width w_d whereas the active cell area is illustrated by w_a . b) Exemplary configuration of a crystalline silicon wafer solar module with series and parallel connections of wafers by metal grids/strings.

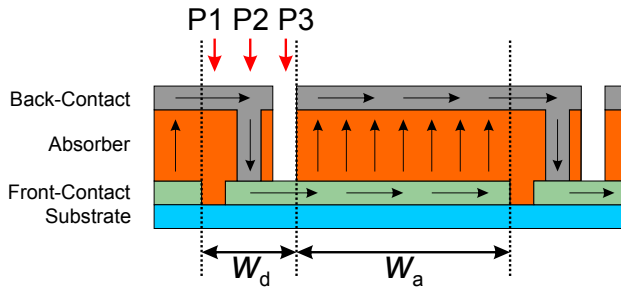


Figure 2.8: Magnified sketch of a thin-film silicon solar module in superstrate configuration with interconnections for the integrated series connections of the individual cells. The individual processes for the interconnection are labeled with P1–P3. The area required for each interconnection is labeled as the dead area width w_d whereas the active cell area is illustrated by w_a . The current flow through the cell stripes is depicted by the black arrows.

tion the actual interconnection is formed. A low series resistance of the contact between the two adjacent cells is desired.

Lastly, a third scribing process called P3 is required for the electrical insulation of the back-contact just like for the front-contact process P1. With this step each solar cell stripe is defined and the series connection is formed.

A closer look to Figure 2.8 shows that the laser scribing processes are done at different steps of the module deposition process. This is necessary for the proper electrical insulation and interconnection between the layers.

Figure 2.9 illustrates how the series connection is integrated in-between the layer deposition steps. In this example all laser processing is done through the transparent substrate side. Processing from the substrate side has major advantages but also certain disadvantages over processing from the film side which will be discussed in detail later on. For thin-film silicon solar modules in superstrate configuration processing is generally done from the substrate side and all processing in this thesis is done from this side.

Figure 2.9 shows how each laser scribing process is integrated in the solar cell deposition process. The use of an appropriate laser processing wavelength for every individual scribing step ensures a selective layer removal. The layer is removed without damaging the layer underneath. The integration in-between the deposition steps is necessary to assure the electrical insulation (steps b) and c) in Figure 2.9) and layer opening (step d) in Figure 2.9).

2.2.2 Modeling of interconnection losses

The selection of the optimal geometries for the interconnection depends on the electrical properties of the solar cell along with the contact material properties. A simple model introduced by Gupta et al. [43] can be used to calculate the optimal active cell stripe width

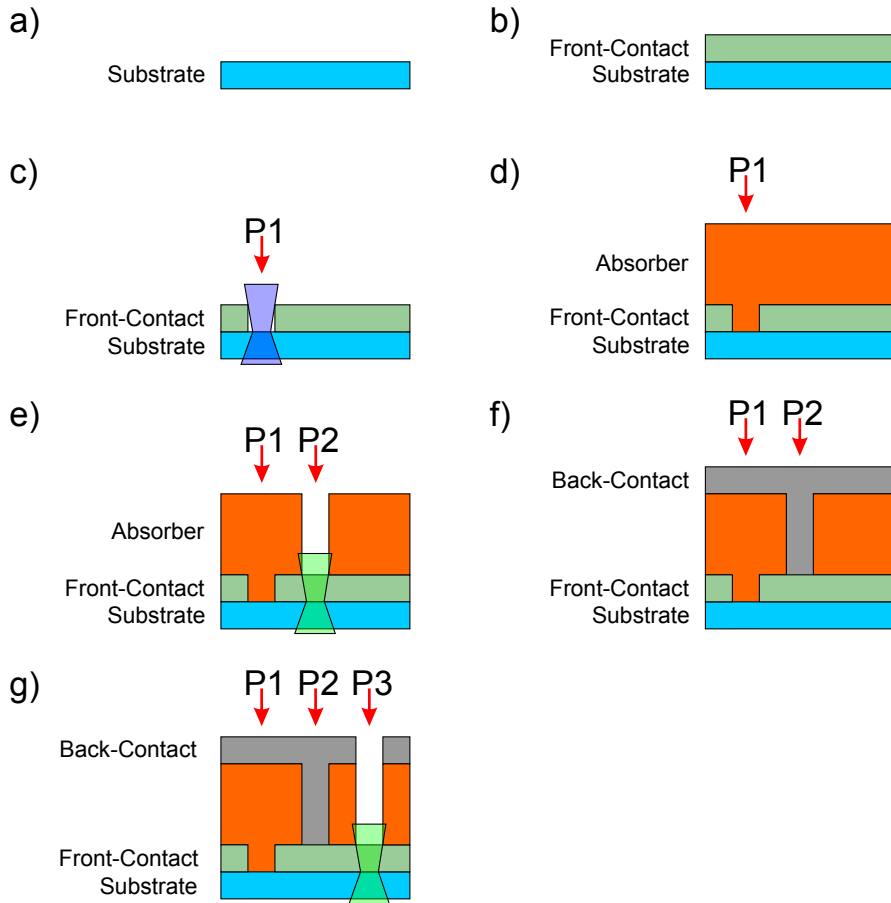


Figure 2.9: Sketch of the monolithic series connection process chain for thin-film silicon solar module in superstrate configuration integrated in-between the solar module layer deposition steps. Laser scribing is done through the substrate side with 355 nm processing wavelength for P1 (step (c)) and 532 nm for P2 and P3 (steps (e) and (g)).

w_a depending on the cell parameters. Thus, modules with minimal additional losses due to the interconnection are achieved. Additional losses means in this context difference in performance of the single solar cell and the interconnected solar module. For this, the single solar cell is scaled to the module area but without any Ohmic losses in the contact materials. These module loss mechanisms need to be introduced in the following before the calculations for optimal module geometries can be made.

Loss of active area: the most obvious losses are created by the reduction of active area due to the the interconnection of the neighboring cells. The required region is often called dead area, depicted by the dead area width w_d in Figure 2.8, since it is no longer contributing to the power generation of the solar module. Each different loss mechanism can be accounted for by fractional functions. These are setting the output power lost due to the specific loss mechanism in relation with the power which would be created without losses. For the area losses f_d the following equation can be defined,

$$f_d = \frac{P_d}{P_{\max}}. \quad (2.15)$$

This equation sets the power lost P_d in relation with the ideal power generated P_{\max} . Both can be written out as,

$$P_d = V_{\text{MPP}} J_{\text{MPP}} w_d l \quad \text{and} \quad P_{\max} = V_{\text{MPP}} J_{\text{MPP}} (w_d + w_a) l \quad (2.16)$$

with the solar cells voltage V_{MPP} and current density J_{MPP} in the MPP, the dead area width w_d , and active cell width w_a . The value of l is the length of the module perpendicular to the series connection. Substitution into the definition of f_d eventually results in the following equation,

$$f_d = \frac{V_{\text{MPP}} J_{\text{MPP}} w_d l}{V_{\text{MPP}} J_{\text{MPP}} (w_d + w_a) l} = \frac{w_d}{w_d + w_a} \quad (2.17)$$

which is simply the dead area fraction of the module.

Ohmic losses in the front-contact: the second important loss factor that accounts for the resistive losses in the front-contact can be defined by the following equation,

$$f_{\text{FC}} = \frac{P_{\text{FC}}}{P_{\max}}. \quad (2.18)$$

Like before, the power lost in the front-contact P_{FC} and the maximum power P_{\max} are set in relation. The Ohmic losses in the front-contact depend on the current in the front-contact, which is not constant along the cell stripe. The current at any given distance x off the cell stripes edge can be expressed by,

$$I_{\text{FC}} = J_{\text{MPP}} A = J_{\text{MPP}} l x. \quad (2.19)$$

The current density J_{MPP} is multiplied with the area A spanned by the distance x and the cell stripe length l . The front-contact resistance R_{FC} can be expressed for an infinitesimal width increase dx ,

$$r_{FC} = R_{SH} \frac{dx}{l} \quad (2.20)$$

with the front-contact sheet resistance $R_{SH} = \rho_{FC} / t$ (layer thickness t). Both expressions are combined to calculate the front-contact losses P_{FC} ,

$$P_{FC} = I_{FC}^2 R_{FC} = \int_0^{w_a} \left[(J_{MPP} x l)^2 \frac{R_{SH}}{l} \right] dx = \frac{R_{SH}}{3} J_{MPP}^2 w_a^3 l. \quad (2.21)$$

Together with the maximal power P_{max} the front-contact loss fraction f_{FC} is obtained,

$$f_{FC} = \frac{R_{SH} J_{MPP}}{3 V_{MPP}} \frac{w_a^3}{w_a + w_d}. \quad (2.22)$$

The front-contact losses strongly increase when the active cell stripe width w_a is increased whereas the dead area fraction f_d decreases when the cell stripe width is increased.

For the sake of completeness it shall be mentioned here that, of course, similar Ohmic losses are present in the back-contact as well. But due to the high conductivity of the back-contact material the losses are negligible (for the typical cell stripe widths) and module geometries are dominated by the front-contact properties.

The overall loss fraction is derived by the sum of both loss fractions. In Figure 2.10 graphs are shown with each loss fraction and the sum. The fractional losses are plotted as a function of the active cell stripe width w_a . For the dead area width a commonly used value of $w_d = 300 \mu\text{m}$ was assumed [44]. The opposing behavior of the dead area losses f_d and front-contact losses f_{FC} will lead to a certain optimal cell stripe width $w_{a,opt}$. At the optimum the rel. module losses are minimized (minimum of sum $f = f_d + f_{FC}$). However, even at the optimum, with the given interconnection/solar cell parameters, the output power of the module will decrease. Approx. rel. 5% compared to the theoretical maximum power is lost.

Reduction of module losses: one approach to lower the module losses at the optimum cell stripe width $w_{a,opt}$ is the reduction of the dead area loss fraction f_d . In the sample calculations a typical interconnection width of $w_d = 300 \mu\text{m}$ was used. Figure 2.11 shows the overall module losses parameterized for different w_d between the standard $300 \mu\text{m}$ down to $50 \mu\text{m}$. A reduction of the overall module losses from rel. 5% down to less than 2% is predicted when w_d is decreased from $300 \mu\text{m}$ down to $50 \mu\text{m}$. This attractive potential of possible loss reductions gives the motivation for this work.

These inherent losses due to the interconnection do not incorporate any impact of the laser processing on the active solar cell. However, each laser process that is required for the realization of the interconnection can have an impact on the solar modules electrical and optical properties. Deterioration the module efficiency due to non-optimized laser scribing was

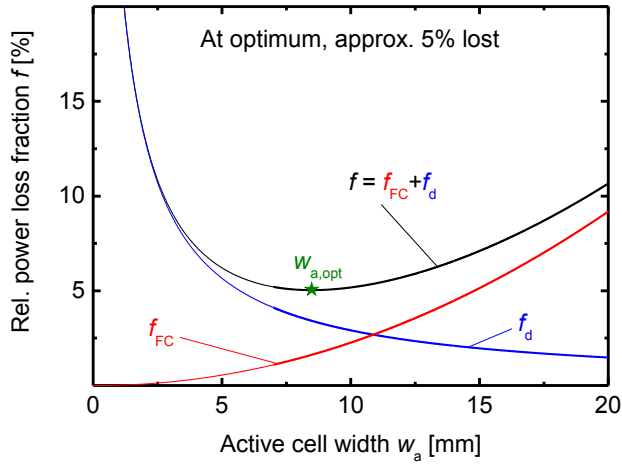


Figure 2.10: Calculated tandem solar module loss fractions due to the integrated series connection plotted vs. the active cell stripe width w_a . The star marks the optimal cell stripe width $w_{a,opt}$ where the overall loss fraction f is minimized. Tandem solar cell input parameters are: $J_{MPP}=9.7$ mA/cm², $V_{MPP}=1.11$ V, $R_{SH}=8$ Ω , and $w_d=300$ μ m.

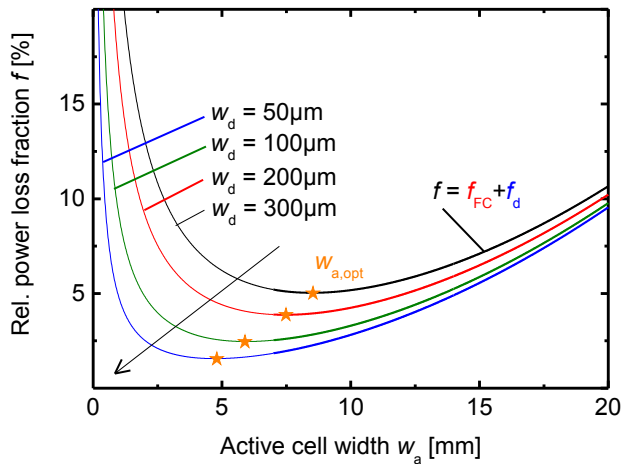


Figure 2.11: Calculated tandem solar module overall loss fraction due to the integrated series connection plotted vs. the active cell stripe width w_a parameterized for different interconnection widths w_d . The stars mark the optimal cell stripe width $w_{a,opt}$ where the overall loss fraction f is minimized. Tandem solar cell input parameters are: $J_{MPP}=9.7$ mA/cm², $V_{MPP}=1.11$ V, and $R_{SH}=8$ Ω .

Chapter 2. Fundamentals

already shown by Haas [45, 46]. These additional loss mechanisms are also dependent on the geometrical scribe width and will be investigated in the main part of the thesis.

In the following, a small introduction into the topic of laser material processing will be given. Laser sources, optics, and the scribing system can have a big influence on the resulting laser processing properties and certain limiting constraints.

3 Laser material processing

In the previous section it was pointed out that the integrated series connection of thin-film silicon solar modules is realized by selective laser ablation of the individual solar cell layers. This chapter gives a broad introduction into the laser material processing of thin-films. Especially the mechanisms and systems that are relevant for the laser ablation of solar cell layer materials will be discussed. The laser sources used for this work will be introduced. Basic properties of the optical systems, together with the structuring system, will define first constraints on the possible processing dimensions.

3.1 Laser sources

For laser material processing, sources with very different laser pulse durations are used depending on the specific process. Besides continuous-wave (CW) mode operation, sources with almost every time scale are commercially available. The time scales span from the nanosecond regime to picosecond lasers down to femtosecond sources which are already adopted in certain industrial environments with 24/7 operations [47, 48]. The pulse duration can have an influence on the ablation properties [49, 50] for almost every type of material. Generally, it can be said that shorter pulse durations tend to have lower damaging influence on the processed material [51].

It is not surprising that ultra-short pulsed (USP) lasers are much more cost intensive than for example laser sources in the nanosecond regime. Complex architectures are required to generate pulses below 100 ps. All laser processing in this work was done with nanosecond laser sources which are the industry standard due to their good cost/process efficiency ratio. All relevant laser parameters of the three laser sources used for this thesis are given in Table 3.1. The base architecture of all three laser sources is the same. They are all nanosecond Q-switched lasers with diode-pumped Nd:YVO₄ crystals. The base output wavelength of this type of laser is 1064 nm (NIR). With subsequent second and third harmonic generation (SHG and THG) the wavelengths of 532 nm (VIS) and 355 nm (UV) are generated.

Chapter 3. Laser material processing

Table 3.1: Overview of the laser properties of the laser sources used for material processing.
*Maximum values for the relevant operation region used for this work.

Model/Name	ROFIN Powerline RSM 10 E	ROFIN Powerline RSY 20 E / SHG II	ROFIN Powerline RSY 20 E / THG
Wavelength λ	1064 nm	532 nm	355 nm
Average power P_{avg}	6 W at 20 kHz	1.3 W at 20 kHz	0.8 W at 15 kHz
Laser crystal	Nd:YVO ₄	Nd:YVO ₄	Nd:YVO ₄
Pump source	diode-pumped	diode-pumped	diode-pumped
Beam mode	TEM ₀₀	TEM ₀₀	TEM ₀₀
Beam quality M^2	< 1.3	< 1.5	< 1.5
Pulse duration τ_p	10 ns at 20 kHz	10 ns at 20 kHz	6 ns at 15 kHz
Frequency f_{PRF}	0 - 200 kHz	15 - 200 kHz	15 - 100 kHz
*Peak power P_p	75 kW at 5 kHz	7.2 kW at 10 kHz	8.8 kW at 15 kHz
*Pulse energy E_p	400 μ J at 10 kHz	75 μ J at 10 kHz	53 μ J at 15 kHz

Since no cavity dumping [52] is used for these lasers a proper characterization of the whole operating area is required. Without this feature multiple parameters of the laser are affected by the pump diode current and frequency which are the main adjustment parameters of the laser. These parameters are the pulse duration, pulse energy, pulse-to-pulse stability, and even the temporal pulse shape.

The laser output power: the relation between diode pump current I_d and average power P_{avg} is important for laser processing since I_d is the main control parameter. A thermopile sensor is used for the measurement of the output power. These sensors measure the average power by the temperature increase of the absorber which is measured by the Seebeck-Effect. It is therefore important that the reference temperature of the sensor is fixed and no heat accumulation occurs that would disturb the measurement. One approach to ensure this is to make short duration measurements for instance 10 s beam illumination followed by a waiting period until the reference point is reached again. The definition of 10 s illumination time was made because transient behavior of the measured power showed linear behavior up until this point. For longer periods an exponential rise is observed. The sensor is capable of measuring an output power of up to 30 W. When a low power regime is measured substantial noise can be present. Therefore, the deviation of the measured values are estimated by $\pm 10\%$ especially in the low power regime.

Figure 3.1 shows selected pump current vs. average power curves for the 1064 nm and 532 nm laser sources. There is a fairly linear behavior between current and output power for both lasers. However, for the laser with 532 nm (Figure 3.1(b)) above a certain pump diode current the power is rapidly decreasing. This regime is outside the safe operating area (SOA) of the laser and the identification of this transition point is important since it depends on the used pulse repetition frequency. Furthermore, the frequency has an impact on the slope of the relation as well as on the maximal values. The average output power increases with increasing frequencies. This behavior is typical for diode-pumped Q-switch lasers [53]. For higher frequencies the effect saturates.

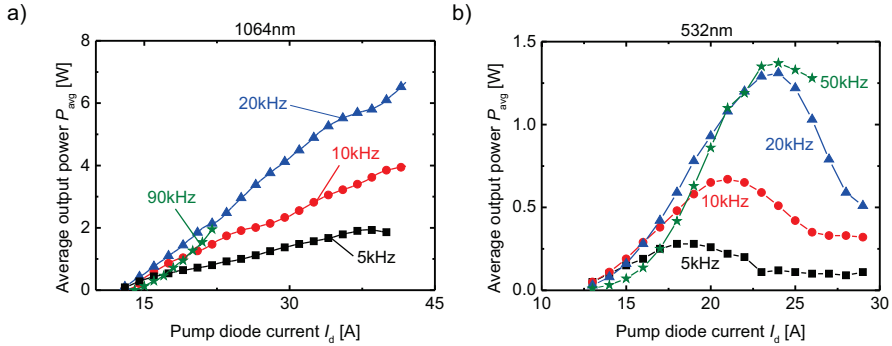


Figure 3.1: Average output power of the laser sources plotted vs. the pump diode current for different pulse repetition frequencies. Plots show: a) 1064 nm. b) 532 nm. A thermopile sensor was used and each point was measured with a 10 s beam illumination time with subsequent relaxation period to avoid heat accumulation.

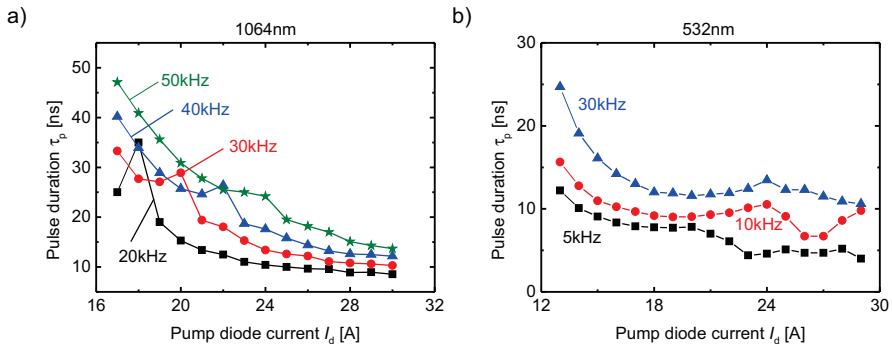


Figure 3.2: Parameterized pulse duration of the laser sources plotted vs. the pump diode current for different pulse repetition frequencies. Plots show: a) 1064 nm. b) 532 nm. The pulse width is defined by the FWHM averaged over 2000 measurements.

The laser pulse duration: the temporal shape of nanosecond laser pulses can be measured with a fast photo diode and a high bandwidth oscilloscope. The typical pulse duration was measured across the whole operating area of the lasers. For the 1064 nm and 532 nm lasers the pulse durations tend to increase for low pump diode currents. Figure 3.2 shows exemplary the results of the pulse duration measurements as a function of the pump diode current parameterized for different frequencies. There is a strong pump current dependency of the pulse duration for the 1064 nm laser source (Figure 3.2(a)). The duration varies between 50 ns and 10 ns in the minimum. There is also a generally higher pulse duration observed when the frequency is increased. These large differences of the duration can have an impact on the ablation behavior of the material [54] and need to be considered when the processing operating point is selected.

In contrast, variation of the duration for the 532 nm laser (Figure 3.2(b)) is not as pronounced as for the 1064 nm laser. However, the same behavior of a general increase of the duration as a function of frequency is found here as well. It is possible that for this laser the operating point can have an impact on the ablation behavior as well.

The dependencies of the output power and pulse duration on the input parameters pump diode current and pulse repetition frequency was only shown for the 1064 nm and 532 nm. The 355 nm laser is operating at a fixed frequency and current value because the stable operation area of this laser is rather small. However, the desired pulse energy can be set by a motorized beam attenuator which consists of a rotating polarizer and a Glan-Taylor prism. The rotation of the polarizer angle leads to a sinusoidal output power dependence. This setup is convenient since with this approach it is possible to adjust the pulse energy independent of all other parameters. On the downside additional space is required and extra costs hinders the use of this setup for all three laser sources. Due to the fixed operation point (15 kHz and 29 A) of the 355 nm laser the output power can be varied from about 20 mW to 800 mW with a fixed pulse duration of 6 ns.

The relevant optical laser parameters will be briefly introduced in the following.

3.2 Optic basics

All three laser sources exhibit a Gaussian intensity distribution at the output. The raw beam radius of Gaussian laser beams is commonly defined by the radius where the beam intensity is lowered by 86% of the maximal intensity at the center of the beam ($1/e^2$). Other definitions include FWHM, 2nd Moment, and Knife-Edge methods [55].

Different optical elements within the laser beam path can be used to adjust the beam diameter and beam divergence. The beam diameter can easily be measured by a CCD camera with a sufficiently large aperture. But focusing of the laser beam is required to reach the intensities necessary for the laser ablation of the material. It is therefore reasonable to measure the laser beam directly in the focal plane of the objective. The characterization of the lasers and the different optical systems was done with a MicroSpot Monitor from PRIMESTM.

Figure 3.3 shows a compilation of the beam intensity distribution in the focal plane of all three lasers with the different lens systems used in this work. Focusing is possible without any large distortion of the Gaussian shape of the laser beam. However, for both lens systems of the laser with a wavelength of 355 nm (Figure 3.3(a) and (b)) there are some deviations of the background at the outer rim of the spot. It is possible that the beam attenuation setup is responsible for this behavior. There are also more severe distortions at the outer rim of the beam for the 1064 nm laser (Figure 3.3(f) and (g)). In general, ellipticity of the laser spots is low, especially for the 532 nm laser with all three different optics (Figure 3.3(c) to (e)). It was also found out that the beam shape and spot size rarely depend on the operating point of the laser. Additional beam profile measurements spanning over the relevant parameter spectrum lead to deviations of the spot size that are between 4% and 15%.

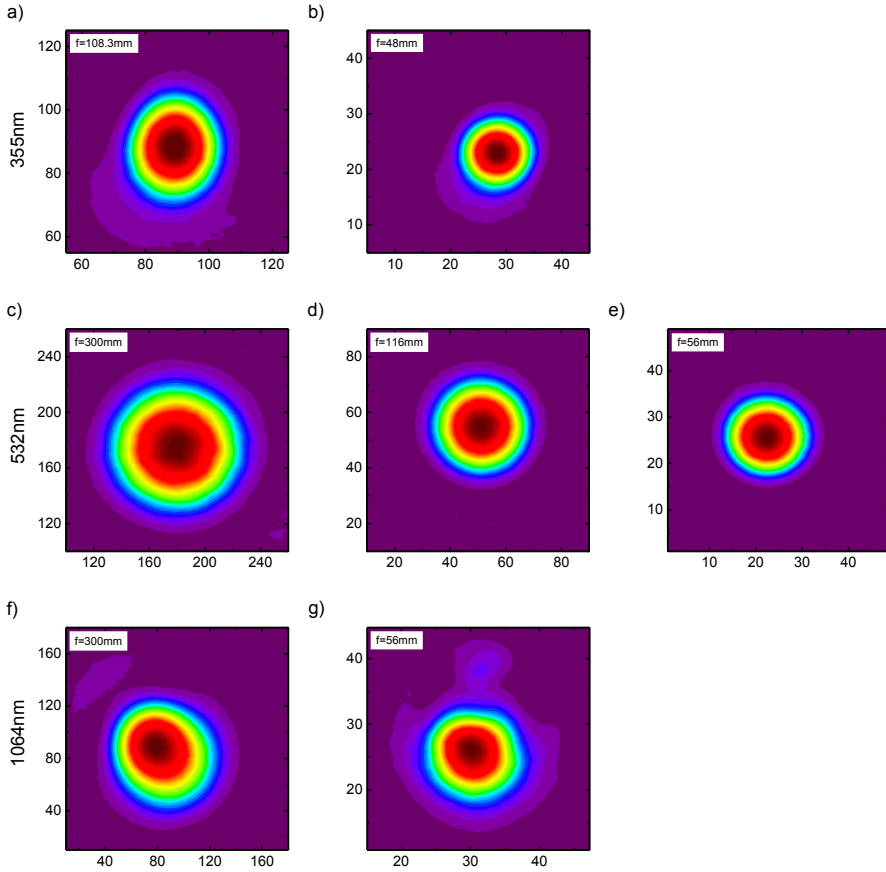


Figure 3.3: Laser beam intensity distribution in the focal plane measured with a beam profiler for different wavelengths and optical lens systems. Upper row: a) and b) belong to the 355 nm laser. Middle row: c) and e) shows the results of three different focusing optics for the 532 nm laser. Lower row: f) and g) shows the 1064 nm laser. Absolute dimension in microns.

The focusing optics with a focal length of $f=108.3$ mm and 300 mm serve as the reference optics for standard processing. With these focusing optics scribing behavior is well-known and a broad spectrum of solar cell materials can be processed. The choice of the particular focal lengths of the higher focusing optics ($f=48$ mm and 56 mm) was made due to additional optical constraints.

Depth of focus: in general, much smaller spot sizes are possible with further higher focusing optics. Under the assumption of an ideal laser beam an approximate relation between focal length and spot size in focus can be found from Gaussian beam optics [56] with the following equation,

$$2\omega_0 = \frac{4\lambda f}{\pi D}. \quad (3.1)$$

Here, λ is the wavelength of the laser, f is the focal length of the objective, and D is beam diameter at the input aperture of the objective. It is possible to change the focal length and/or raw beam diameter to create smaller spot sizes. Unfortunately, as the fraction of f/D is decreased the depth-of-focus (DOF) is decreased as well. The Gaussian beam radius changes (converges and diverges) along the beam propagation axis. The DOF is defined as the depth along this axis where the beam radius decreases/increases above/below a certain value, for instance $\sqrt{2}$ times the minimal spot radius ω_0 . For this example the DOF is defined as,

$$\text{DOF} = \frac{8\lambda}{\pi} \left(\frac{f}{D} \right)^2. \quad (3.2)$$

The equation is fairly similar to the previous equation with the definition of the spot size. However, the f/D fraction is squared leading to a much more severe influence on the DOF when the fraction is decreased.

The example definition of the DOF is commonly used for the description of the beam spreading along the beam axis. Generally, the beam spot size along this axis is defined as [56],

$$2\omega(z) = 2\omega_0 \sqrt{1 + \left(\frac{\lambda z}{\pi\omega_0^2} \right)^2} = 2\omega_0 \sqrt{1 + \left(\frac{z}{z_R} \right)^2} \quad \text{with,} \quad z_R = \frac{\pi\omega_0^2}{\lambda}. \quad (3.3)$$

The parameter z_R is called the Rayleigh length and describes the direct relation between the spot radius and depth-of-focus (DOF) which is commonly used in literature [56]. As in the example definition before, z_R describes the depth along the propagation axis z where the beam radius is $\sqrt{2}$ times larger than the radius at the focus ω_0 .

Laser beam caustic: the laser beam propagation properties are important to characterize the specific optical/laser system. The used beam profiler is also capable of measuring the caustic and calculate the Rayleigh length z_R . Figure 3.4 shows a plot with the propagation curves of the laser/optics setups from Figure 3.3. As expected, a dramatic decrease of the DOF is observed even for this intermediate degree of focusing. Table 3.2 shows all important optical beam parameters extracted from the caustic measurements. The decrease of the Rayleigh length

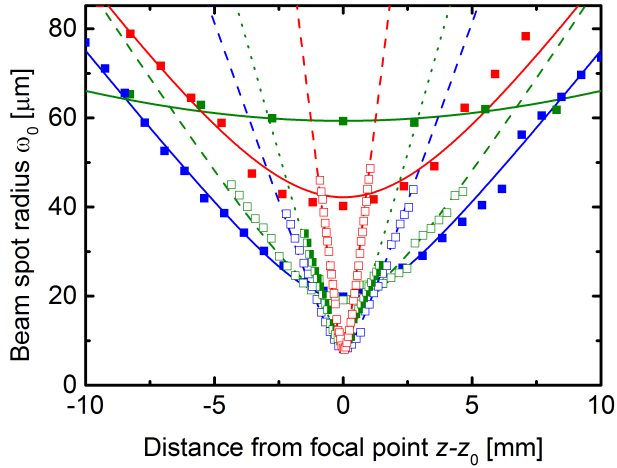


Figure 3.4: Evolution of laser beam radius ω_0 (decay to $1/e^2$ of the peak intensity) measured vs. the distance from the focal point along the propagation axis z . The plots show: In blue 355 nm with $f=108.3$ mm (filled squares) and $f=48$ mm (empty squares). In green 532 nm with $f=300$ mm (filled circles), $f=116$ mm (empty circles), and $f=56$ mm (half-empty circles). In red 1064 nm with $f=300$ mm (filled triangles) and $f=56$ mm (empty triangles). The solid, dashed and dotted lines are non-linear curve fits of Equation 3.3.

Table 3.2: Overview of the laser parameters extracted from the caustic measurements of all laser/optics setups from Figure 3.3 and Figure 3.4.

Wavelength λ , focal length f	Radius in focus ω_0	Rayleigh length z_R	Raw beam diameter D	Beam quality M^2	Divergence angle θ
355 nm, 108.3 mm	$19.3 \mu\text{m}$	2.3 mm	1.4 mm	1.4	16.8 mrad
355 nm, 48 mm	$8.0 \mu\text{m}$	0.4 mm	1.4 mm	1.3	37.5 mrad
532 nm, 300 mm	$58.7 \mu\text{m}$	14.7 mm	1.9 mm	1.4	7.9 mrad
532 nm, 116 mm	$20.1 \mu\text{m}$	1.9 mm	1.9 mm	1.2	20.8 mrad
532 nm, 56 mm	$10.5 \mu\text{m}$	0.5 mm	1.9 mm	1.4	45.3 mrad
1064 nm, 300 mm	$48.0 \mu\text{m}$	5.3 mm	6.3 mm	1.3	18.1 mrad
1064 nm, 56 mm	$8.1 \mu\text{m}$	0.2 mm	6.3 mm	1.2	103.7 mrad

can be quite dramatic for the higher focusing optics. All developed optimized processes in this work have the attempt to be industrially relevant with existing systems and materials. It would not be reasonable to use even higher focusing/beam diameter with a z_R below 0.2 mm. Substrate thickness tolerances and roughness of the machine axes could distort the effective substrate/optics distance and therefore change the laser spot size. Please note that from here on for simplicity reasons the radii of 58.7 μm , 20.1 μm , and 10.5 μm will be referred to as 60 μm , 20 μm , and 10 μm .

Circumvention of DOF limitations: new approaches that can possibly increase the DOF for highly focused laser beams can be found in literature. One interesting approach is the use of non-diffracting beams like Gauss-Bessel beams [57] generated by self-interference created by an axicon. With this type of laser beam it is possible to generate beam spot sizes (the main lobe of the beam or airy disk) comparable with the corresponding normal focusing lens systems. The main difference is a DOF which is ten to twenty times higher [58, 59, 60].

Top-Hat laser beams: a short description of laser beams with a flat plateau intensity distribution and their propagation properties will be given. Different approaches are used to generate a circular or rectangular laser beam intensity distribution with a flat plateau [61]. However, the laser beam spot size is always 1.5-2x larger than the diffraction-limited Gaussian laser beam [62]. Furthermore, changes of the beam shape along the propagation axis occur as well (shown for super Gaussian beams by Parent et al. [63]).

In the next section a description of the structuring system where the laser sources and optics are integrated will be given.

3.3 Laser structuring system

All laser sources are integrated into a commercial laser patterning system with fast linear translational stages ($X - Y$ direction) providing velocities up to 1000 mm/s. The holder can take substrates with sizes of up to 40 cm by 40 cm. The laser beam is directed on the substrate via flying optics and focusing is done with the lens systems attached to a motorized axis (Z direction). The Z -axis also holds a camera system for mark recognition of patterns on the sample. The patterns are used for detection of angular and spatial misalignment of the sample. The substrate holder is placed on a fourth rotational axis that is used for angular compensation of the sample.

As indicated earlier, high focusing with a Rayleigh length larger than 0.2 mm was chosen as a lower limit due to possible distortions of the lens/sample distance. Such distortions can originate from substrate thickness tolerances, warp, waviness or bending depending on where the substrate is clamped. An additional source of distortion is the roughness of the axes. Displacement measurements of the Y -axis (portal axis) of the structuring systems revealed a maximal deviation $<60 \mu\text{m}$ along the travel length and should not add too much additional distortion to the optics/sample distance.

In conclusion, the decision for a certain spot size for optimized processing of narrow scribes is not only constrained by the optical systems. It is rather influenced by the whole setup of laser, optics, substrate, material and scribing machine [64].

Substrate side vs. film side: in this work all laser processing was done through the substrate side. It is also possible to process the sample from the film side just by turning the substrate upside down. A particle suction system will remove coarse debris from both sides of the sample. There are many reasons for and against the processing from the substrate side as well as for and against scribing from the film side [65]. However, most industrial scribing systems for the series connection of thin-film silicon solar modules in superstrate configuration do the scribing from the substrate side.

Advantages are: higher energy efficiency of the ablation process, no laser/plasma interaction or shadowing [66, 67], much lower degree of particle redeposition on the sample or the optics (depending on the optical setup). Furthermore, a high selectivity of the layer removal is given for large differences of the layers absorption coefficients.

However, the biggest down side for this processing setup is the high dependency on absolute clearness of the substrate. Even small scratches or glass corrosion can deflect the laser beam which would result in discontinuous lines. Of course, opaque and flexible substrates with low transmission cannot be processed from the substrate side [68].

3.3.1 Laser processing parameters

As described earlier, power measurements as well as precise knowledge of the laser spot size in focus are important process parameters. Both values are used to calculate the so-called peak fluence F_p . It is commonly used to describe the laser intensity for pulsed laser (in contrast to this for CW lasers the power density or intensity is commonly used). The temporal and spatial laser intensity is defined as [69],

$$I(r, z = 0, t) = I_0 \exp\left(\frac{-2r^2}{\omega_0^2}\right) \exp\left(-4\ln(2)\frac{t^2}{\tau_p^2}\right). \quad (3.4)$$

Here, I_0 is the peak intensity of the laser beam, ω_0 and τ_p are the beam radius in focus and laser pulse duration, respectively. The spatial beam radius ω_0 is commonly defined at $1/e^2$ of the maximal intensity. In contrast, the temporal pulse duration is usually given by the FWHM, hence the conversion factor of $4\ln(2)$. The spatial pulse fluence distribution is derived from the temporal integral of Equation 3.4,

$$F(r, z = 0) = \int_{-\infty}^{\infty} I(r, z = 0, t) dt = F_p \exp\left(\frac{-2r^2}{\omega_0^2}\right). \quad (3.5)$$

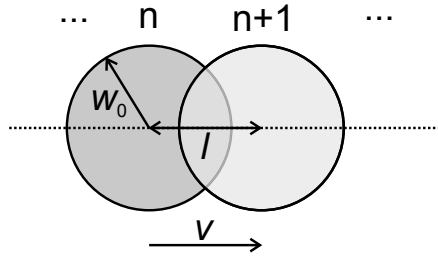


Figure 3.5: Parameter definition for the calculation of the laser pulse overlap. Shown is the n -th and $n+1$ -th pulse with beam radius ω_0 and velocity v . The distance between two spots is depicted by the length l .

The value F_p is defined as the peak fluence and is related with the pulse energy as followed,

$$E_p = \int_0^{2\pi} \int_0^{\infty} F(r) d\phi r dr \quad (3.6)$$

$$= \int_0^{\infty} F(r) 2\pi r dr \quad (3.7)$$

$$= \int_0^{\infty} F_p \exp\left(\frac{-2r^2}{\omega_0^2}\right) 2\pi r dr \quad (3.8)$$

$$= \frac{\pi \omega_0^2 F_p}{2}. \quad (3.9)$$

Equation 3.9 can be also written as,

$$F_p = \frac{2E_p}{\pi \omega_0^2}. \quad (3.10)$$

The factor two is often forgotten in literature but is important for Gaussian shaped laser beams. For Top-Hat shaped and super Gaussian beams the peak fluence is derived differently.

The pulse overlap: when scribe lines or area processes are specified, the pulse overlap characterizes, together with the peak fluence, the effective laser illumination of the material. Figure 3.5 illustrates the parameters necessary for the definition of the pulse overlap. The distance l between two consecutive laser spots is defined as $l = v / f_{PRF}$ with v as the laser feed velocity and f_{PRF} as the pulse repetition frequency. The overlap ov is defined as,

$$ov = 1 - \frac{l}{2\omega_0} = 1 - \frac{v}{2\omega_0 f_{PRF}}. \quad (3.11)$$

In most cases, the three process parameters of pulse duration, peak fluence, and pulse overlap are sufficient to describe a specific laser scribing process. However, in reality additional effects like thermal diffusion or a spot size dependence of the ablation behavior can have an impact on the laser process [70].

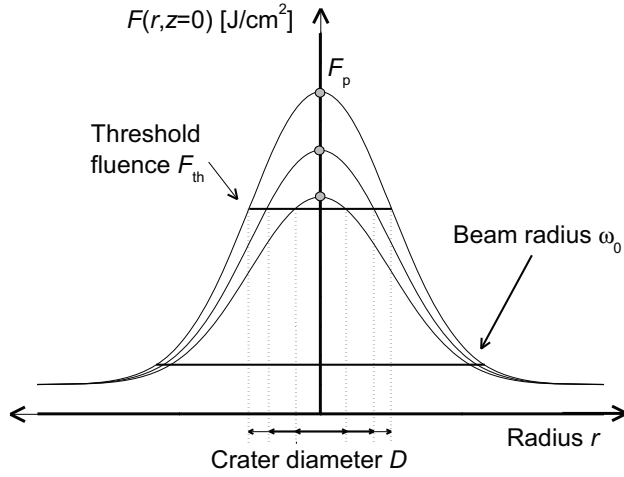


Figure 3.6: Schematic sketch of the spatial pulse fluence distribution plotted with different peak fluences F_p . The threshold fluence F_{th} denotes the minimal fluence necessary for processing of the material. The diameter D is the resulting ablation crater (or processing diameter) for the specific peak fluence.

3.3.2 Material laser ablation properties

In the previous section the important laser processing parameters were defined. It would be helpful to characterize the ablation behavior in the same manner with one value that describes how the material behaves for a certain peak fluence. A commonly used procedure in the literature was first proposed by Liu [69]. Originally the method was used to determine the threshold of amorphization for laser processing of crystalline silicon wafers. Figure 3.6 shows a schematic plot of the spatial pulse fluence distribution from Equation 3.5. To describe the relation between the ablation crater diameter D and the used peak fluence F_p Equation 3.5 can be rewritten to,

$$D^2 = 2\omega_0^2 \ln\left(\frac{F_p}{F_{th}}\right) \quad \text{or} \quad (3.12)$$

$$= 2\omega_0^2 \left[\ln\left(\frac{2E_p}{\pi\omega_0^2}\right) - \ln(F_{th}) \right] \quad (3.13)$$

$$= 2\omega_0^2 [\ln(E_p) - \ln(E_{th})]. \quad (3.14)$$

Equation 3.14 shows that due to the Gaussian shape of the laser beam it is possible to reproduce the Gaussian fluence distribution. A requirement is a processing behavior of the material with a constant threshold fluence $F_{th}=2E_{th}/\pi\omega_0^2$ (with E_{th} as the threshold energy). When the squared ablation crater diameter D^2 is plotted as a function of the natural logarithm of the peak fluence $F_p=2E_p/\pi\omega_0^2$ (or E_p) a linear behavior is expected.

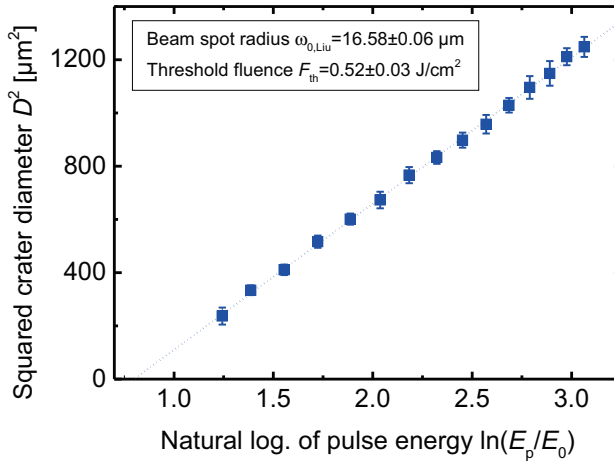


Figure 3.7: Example of a Liu-Plot for substrate side processing of $\text{SnO}_2:\text{F}$ with a wavelength of 355 nm and a beam spot radius of $\omega_0=19.3 \mu\text{m}$. A linear regression is inserted with a dotted line. Extracted parameters are: $\omega_{0,\text{Liu}}=16.6\pm 0.06 \mu\text{m}$ and $F_{\text{th}}=0.52\pm 0.03 \text{Jcm}^{-2}$. Processing was done through the substrate side. Normalization factor E_0 is 1 J.

An example of such evaluation according to the method proposed by Liu is shown in Figure 3.7. The graph shows the squared single spot crater diameter plotted against the natural logarithm of the laser pulse energy. Front-contact TCO material ($\text{SnO}_2:\text{F}$) was used for processing from the substrate side with a laser wavelength of 355 nm. The slope of the linear regression equals $2\omega_0^2$ and gives a good estimate of the actual laser beam spot size on the sample. For the example given in Figure 3.7 the laser beam spot radius ω_0 measured with a beam profiler was $19.3 \mu\text{m}$ whereas the extracted value is $\omega_{0,\text{Liu}}=16.6 \mu\text{m}$. In the original reference a maximal deviation in the range of 20% is stated for processing from the film side. Therefore, good agreement between both values leads to conclude that processing of material is done approximately in focus.

The second parameter, for characterization of the material properties, is the value extracted from the extrapolation of the linear regression with the x -axis (extrapolation to $D^2 \rightarrow 0$). This value is a measure for the amount of laser pulse energy that is required for the ablation of a given crater diameter and is called threshold energy E_{th} [69]. An increase of this material/process parameter would lead to a shift along the x -axis, ergo an increased energy is required to achieve a similar crater diameter. From the example a value of $F_{\text{th}}=0.52\pm 0.03 \text{Jcm}^{-2}$ is extracted which is in good agreement with values from literature for a similar setup [71, 72].

Changes of the slope that are observed in the Liu-Plot can indicate a change of ablation behavior. A change of behavior can be caused by, for example, nonlinear effects like multi-photon absorption at high peak intensities [73, 74]. However, distortions of laser beam shape at a high power operating regime can be a reason as well [75].

For substrate side processing a certain behavior is observed in the Liu-Plot. In reality, an arbitrary downscaling of the ablation diameter to the threshold fluence is not possible. A certain minimal necessary fluence is required for full ablation of the material. Below this so-called onset fluence or energy only bulging and blistering of the layer is observed. It is always higher than the threshold fluence and further details on this behavior will be given later on.

3.3.3 Determination of the processing beam spot size

Careful determination whether processing is done in focus or not is an additional application of the Liu method. Especially when higher focusing optics are used, with a rather small Rayleigh length, processing is sensitive on the z value of the axis. If the slope, derived from the linear regression of the Liu-Plot, is plotted as a function of optics/sample distance z a relation corresponding to the caustic of the beam is observed.

Figure 3.8 show the results for the determination of the focal point, exemplary for the higher focusing optics of the 532 nm laser (see 3.2). It can be seen that the DOF is in good correlation with the measurements from the beam profiler in Figure 3.4. Unfortunately, even though many measurement points are taken, large deviations can be seen for certain optics/sample distances. This is partly owed to the characterization method that is used for the determination of the ablation crater diameter.

In Figure 3.9 the evaluation procedure is shown and the difficulties involved with this approach that are also relevant for the accuracy of the extracted threshold energies/fluences. An open source software called ImageJ was used for image processing of the optical microscopy picture of the laser ablation craters [76].

First a batch of microscope images is loaded into the software. In a next step the images are converted into 8 Bit grayscale images. Then a grayscale color threshold is adjusted for proper detection of the crater diameters. The threshold images are used for edge detection of the individual craters. The edge is finally fitted to ellipses and the major diameter is used for the evaluation. Each measurement set usually consists of 5–10 craters per processing parameter.

One important detail can be seen in Figure 3.9 when looking at the threshold step. The area that determines the ablation crater is highly dependent on the set contrast threshold. Although, batch processing will use the same threshold for the whole series of images, an offset created by this threshold directly translates into the threshold fluence F_{th} which is a possible error source. The slope extracted from the Liu-Plot is not affected by this evaluation procedure as long as the threshold is constant throughout the whole set of images.

Another possible error source is observed for certain material/laser combinations when changes of the ablation behavior occur. Changes of the crater edge morphology translate into jumps and offsets of the detected diameter. It is necessary to adjust the image processing threshold in these regimes or measure every crater manually. An example of such changes of

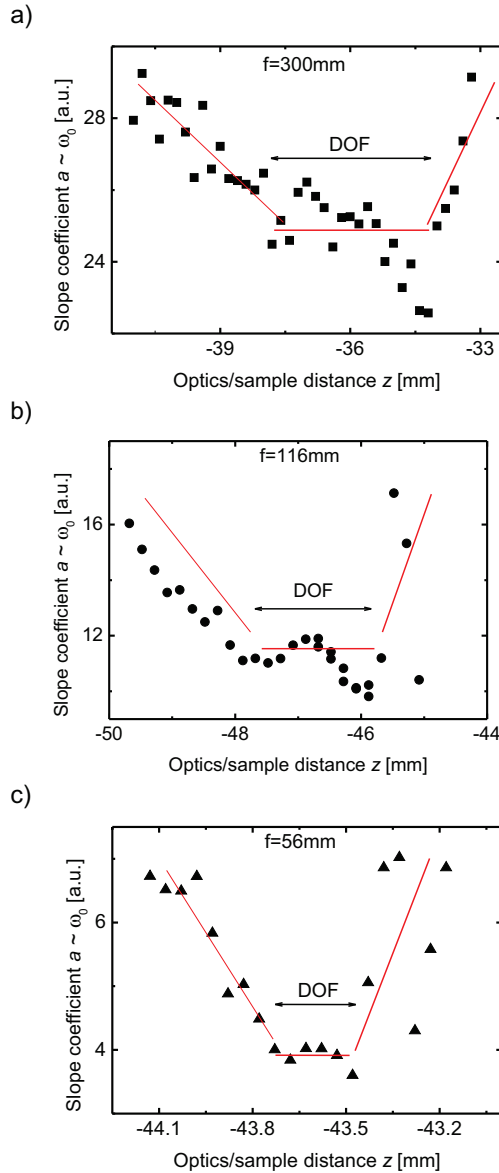


Figure 3.8: Results of focus sweep via Liu-Plot processing of amorphous silicon (a-Si:H) material for different focusing optics of the 532 nm laser. Focal lengths are: a) $f=300$ mm. b) $f=116$ mm. c) $f=56$ mm. Each point the graph corresponds to the slope of the linear regression of a Liu-Plot at the specific optics/sample distance. Each Liu-Plot made for six different pulse energies and each squared crater diameter determined by the average major axis diameter of three different laser spots via an elliptical curve fit (one point for $f=300$ mm).

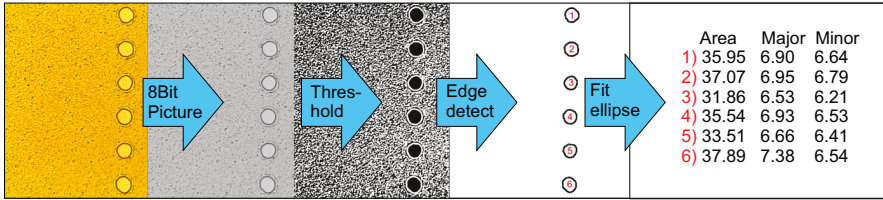


Figure 3.9: Image processing approach for ablation crater diameter determination shown exemplary for processing of $\text{SnO}_2\text{:F}$ TCO material with 532 nm, $E_p=5.7 \mu\text{J}$, and a focal length of $f=56 \text{ mm}$. Fit parameters are the crater area in μm^2 and diameter of the major axis of the fit ellipse in μm .

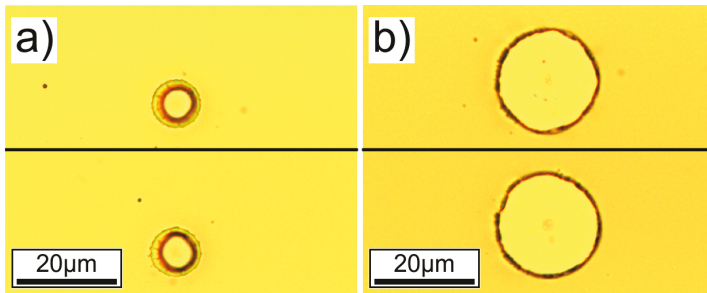


Figure 3.10: Optical microscopy images for single crater ablation of ZnO:Al TCO material processed with 532 nm. Parameters are: a) Low peak fluence regime. b) High fluence regime. Distinct differences of the crater edge morphology between both regimes are observed.

the crater edge morphology is shown in Figure 3.10. A change of ablation behavior between a low and high peak fluence regime for processing of ZnO:Al TCO material with 532 nm lead to differences of the crater edge morphology. The crooked edge for the low peak fluence regime (cf. Figure 3.10(a)) will yield a different crater diameter than the sharp crater edge in Figure 3.10(b).

4 Characterization methods

This chapter is dedicated to the characterization of the laser processed materials and/or the solar cells properties affected by the nearby laser scribes. Various spatially resolved methods and setups were used in this thesis. Alongside with these methods, special test-structures are introduced, that offer simplified evaluation of the macroscopic electrical properties of the laser scribes. Therefore, deterioration of performance by the laser processes can be identified without the implementation into fully processed solar modules. Thus, allowing a separation of interfering effects.

But first, for the investigation of the laser ablation mechanisms a simple procedure for the qualitative evaluation will be introduced in the next section. This method can be applied for each scribing process P1 to P3 (and therefore processing of the different materials).

4.1 Ablation mechanisms

To understand the driving mechanisms behind laser ablation it is important to get insight into the laser ablation behavior. The behavior can be strongly affected by the material and laser wavelength combinations used for the processes P1 to P3. A qualitative approach to get an idea of the maximal temperatures or material phase changes is the evaluation of the ablated material.

A simple setup is shown in Figure 4.1 that is used for the collection of the ablated material. Two spacers are placed on the film side of the sample with a thickness of 2–3 mm. On these spacers a transparent adhesive tape is used for capturing the laser ablation debris that was accelerated from the laser scribe. After processing, the debris captured with the tape can be evaluated with an optical microscope. It is possible to conduct this experiment for each process P1 to P3 since the contrast between debris and the tape is high under the optical microscope.

It is further possible to remove the tape and attach it upside down to a glass slide for the evaluation with a scanning electron microscope (SEM). Unfortunately, for this case it is necessary to use a vacuum compatible tape (for instance Kapton tape from DuPont). However, it is

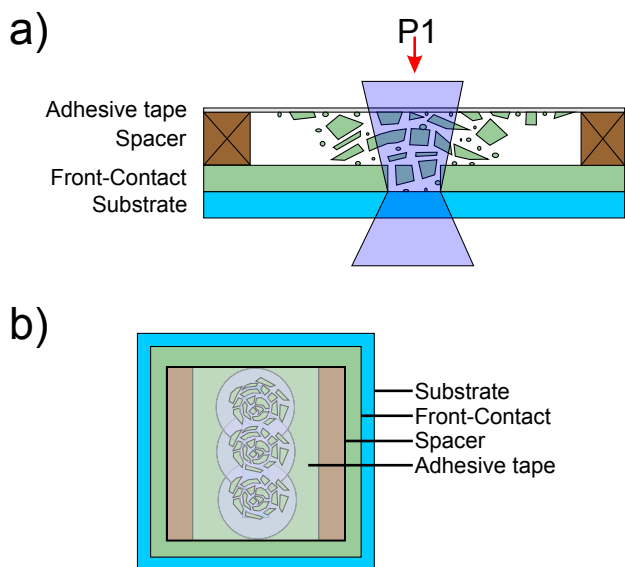


Figure 4.1: Schematic sketch of the sample setup used for the collection of ablated material debris. The number of deposited layers corresponds to the specific process under investigation (only glass and front-contact for P1, additional absorber for P2, and whole layer-stack for P3). Sketches show: a) Side view with illumination direction through the substrate. b) Top view with scribing direction for single spot ablation.

not transparent enough for pre-evaluation with the optical microscope. To avoid electrical charging of the polyimide tape in the SEM a thin 1–2 nm thick iridium layer is sputtered onto the tape.

From the size, shape, and number of the debris particles it is then possible to differentiate between different ablation driving processes and regimes. From the contrast of the particles it is also possible to relate each particle to the different layer materials.

This method is more suitable for higher focused beams. The divergence of the laser beam needs to be sufficiently large so that no heating/damaging of the tape by the laser beam occurs.

4.2 Conductivity Atomic Force Microscopy

The first spatially resolved measurement technique that is primarily used for the electrical characterization of the front-contact material is the conductivity Atomic Force Microscopy (c-AFM) [77]. Figure 4.2 shows the setup of the c-AFM measurement system. The front view in Figure 4.2(a) shows the AFM cantilever and tip hinged at a piezo scanner in Z direction for control of the cantilever deflection/contact force. The deflection is measured by laser interference on the highly reflective back side of the cantilever. The impinging laser beam is reflected and interferes destructively or constructively depending on the deflection of the cantilever. This leads to an intensity modulation of the reflected laser beam. The top view in Figure 4.2(b) shows the scanning routine of the AFM measurement. Each line is scanned in forward and backward direction. Thus, two separate topography scans are obtained which should show no differences if the control parameters are set properly (PI coefficients).

In contrast to pure topography scanning, an electrically conductive AFM tip is used which is in mechanical contact with the sample surface [78]. The sample is contacted with a conductive silver tape and biased with a DC voltage between -10 V and 10 V. The AFM tip is electrically grounded acting as the back electrode for the current flow. The overall current flow is dominated by the conductivity of the material at the direct tip/surface contact. This is owed to the small current flow through the sample and current constriction near the direct tip/sample surface. Hence, different distances to the ground electrode through the front-contact material do not distort the measurement.

A logarithmic current/voltage amplifier is used for current detection because of their large measurement range [79]. The minimal detectable current flow is approx. 1 nA. This lower limit is perfectly sufficient for the AFM tip and front-contact material combinations that were under investigation. There are further approaches that make use of Lock-In amplification to improve the signal to noise ratio [80].

There is a large variety of conductive AFM tips and cantilever geometries available on the market. But only a few of them are suitable for contact mode measurements that require long cantilever lengths. A long cantilever is equivalent with a low spring constant (0.01–2 N/m) for gentle scanning of the surface with a small contact force in the range of 1–2 nN. Sometimes

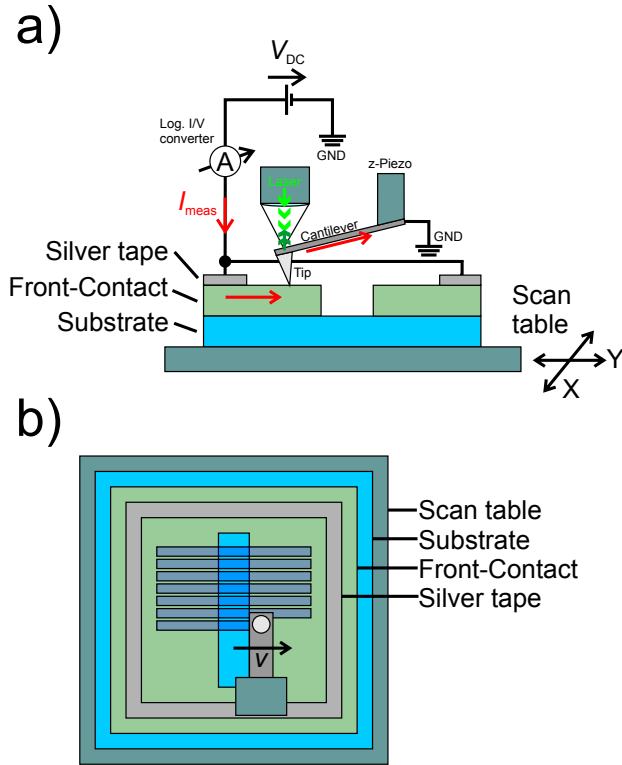


Figure 4.2: Sample setup for the c-AFM measurement system that is used for the electrical characterization of the front-contact material after P1 processing near the laser scribe edge. View are: a) The distance measurement of the cantilever with the help of the interference of a laser beam with the back surface of the tip and current measurement circuitry with voltage source V_{DC} . b) The geometry of grounding via silver tape and the scan direction of the cantilever. Each line is scanned in forward and backward direction.

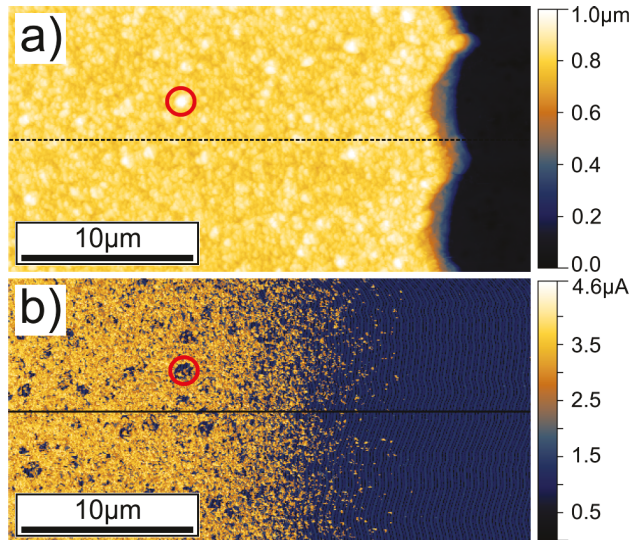


Figure 4.3: Typical c-AFM measurement at the laser scribe edge (P1) of $\text{SnO}_2\text{:F}$ front-contact material processed a 355 nm laser. Plots show: a) Topography. b) Current flow map. The red circle marks the spots top compare geometrical effects of the topography with the corresponding current flow at the same spot.

higher forces (μN) are also applied, for instance, when the sample surface is covered with a non-conducting oxide layer [81].

The conductive AFM tip often consists of structured crystalline silicon, that defines the tip shape. Subsequently the bare tip is coated with conductive material like Gold, Silver, Platinum, or Chromium [82]. There are also tips that are coated by metal alloys like Platinum with Iridium (PtIr5, for example PPP-ContPt from Nanosensors). Furthermore, diamond-coated tips that are doped with boron (CDT-CONTR from Nanosensors) are also commonly used [83].

It is understandable that the coated conductive AFM tip radius is always higher than the radius of the bare silicon tip. The bare tip radius is typically in the range of 10–30 nm. When a conductive coating is deposited a radius of 30 nm is the lower limit of commercially available AFM tips. However, tips coated with the boron-doped diamond exhibit a much larger tip radius between 100 nm and 200 nm.

For the measurements done for this work all experiments were conducted with boron-doped diamond coated AFM tips. A sub-100 nm resolution is not absolutely necessary and the higher mechanical durability compared to AFM tips coated with PtIr5 is much more advantageous.

Figure 4.3 shows a typical c-AFM measurement of $\text{SnO}_2\text{:F}$ front-contact TCO material near the scribe edge created with 355 nm. There are distinct differences of the topography and the current flow, particularly in the direct vicinity of the scribe. More importantly, geometrical effects can have a huge impact on the specific current flow that is measured. Generally, the

measured c-AFM current flow is dominated by the resistivity of the material that is scanned. However, it also depends on the contact force of the tip and the effective contact area between AFM tip and sample surface [84, 85]. Quantitative conclusions of the resistivity are only reasonable for very smooth surfaces so that there are no changes of the contact force and area during scanning.

For the region marked with the red circle in Figure 4.3 it can be seen that the corresponding current flow in this region is below the detection limit of the current amplifier. Differences of the conductivity at these points (more of these artifacts can be found in the measurement) are unlikely. It is possible that this drop in current flow is due to a decreased tip/sample contact area. Another explanation for the artifacts could be deviations of the contact force by the control loop caused by steep slope changes of the topography.

In literature the influence of the sample geometry on the measurement is well known for potential or capacitance measuring non-contact methods. These methods usually also require very smooth surfaces. Cross-talk from deviations of the interaction area by a rough topography can be quite high [86]. There are approaches for signal correction [87] that can maybe also applied for c-AFM by modeling of the tip/sample contact [88]. But these were not applied in the scope of this thesis.

4.3 Laser Beam Induced Current

For the determination of possible impact from laser processes on the actual solar cell performance Laser Beam Induced Current (LBIC) measurements on fully processed cells were carried out [89]. Figure 4.4 shows simplified front and top view sketches of the measurement setup that was used. The measurement laser beam is directed through a focusing microscope onto the sample surface from the substrate side. The sample movement is controlled by a $X - Y$ translational stage. The excitation is done with a Helium-Neon (HeNe) cw laser source with a wavelength of 633 nm exhibiting a TEM_{00} mode output. The average power of the laser is adjusted with neutral density filter. Focusing is done with a 20x/0.4NA microscope objective leading to a spot diameter of approx. $3 \mu\text{m}$ on the sample. However, due to illumination through the substrate side and light scattering at the roughed front-contact material the effective spot size is slightly larger. The average power is adjusted to 60 nW and an intensity of 8.45 kW/m^2 is estimated. With this intensity a good signal-to-noise ratio is ensured with low distortion by the temperature increase during the measurement for all investigated types of solar cells.

The reference back-contact systems consisting of ZnO:Al/Ag/ZnO:Al is used. Hence, illumination of the sample is done through the substrate side.

For the current measurement the laser beam is first modulated with a chopper with a rotation frequency of 214 Hz to create the signal for the Lock-In amplifier [84]. The solar cell is contacted electrically with adhesive silver tape at the front- and back-contact. The current measurement

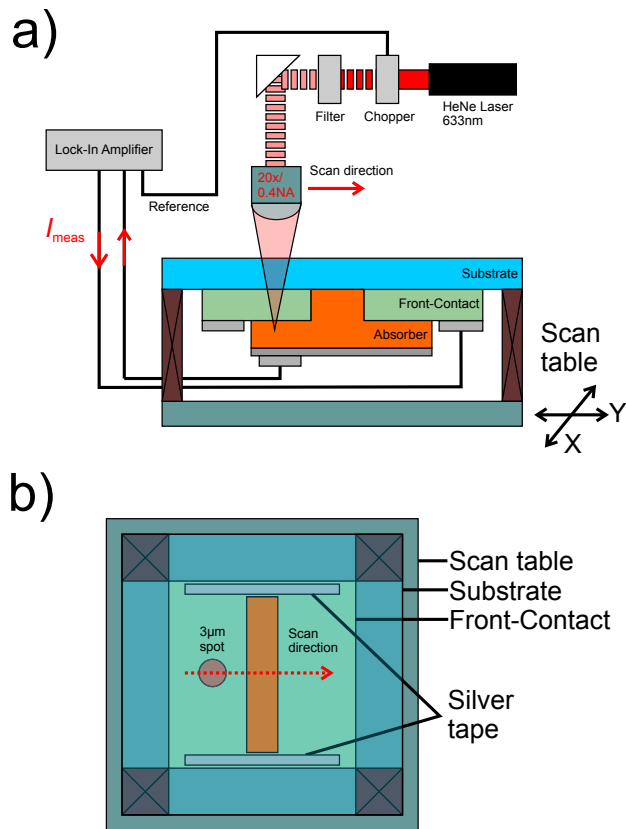


Figure 4.4: Laser Beam Induced Current (LBIC) measurement setup sketch. The laser beam of a 633 nm HeNe laser source is focused and illuminates the sample from the substrate side with an average intensity of 8.45 kW/m^2 . The views show: a) The solar cell is contacted at the front- and back-contact and the generated photo current is measured with a Lock-In Amplifier under short-circuit conditions. b) Top view shows the scan direction of a single line scan across the P1 scribe processed within the solar cell. A laser beam spot size of approx. $3 \mu\text{m}$ is used for the measurement.

Chapter 4. Characterization methods

under short-circuit conditions is done directly with the Lock-In amplifier (type SR830 from Stanford Instruments).

Scanning of the sample is done with a step size of 500 nm and two seconds relaxation time for the mechanical system before the next point is measured (see Figure 4.4(b)). Due to the long measurement times with such high resolution only single line scans are reasonable without mechanical drift. Each line is scanned across the laser scribe under test with a pre-evaluation of the scribe edge positions with the optical microscope.

5 Front-contact structuring process P1

The first step to realize the series connection of thin-film solar modules, in p-i-n superstrate configuration, is the front-contact removal process (P1) for individual cell stripe definition (cf. Figure 2.9). The P1 process and the geometrical scribe width minimization is the matter of investigation of this chapter.

To allow for geometrical scribe width minimization first, the material ablation behavior of two commonly used transparent conductive oxide materials (TCO) was characterized for different laser processing wavelengths. These two TCOs were sputtered aluminum-doped zinc oxide (ZnO:Al) and fluorine-doped tin dioxide (SnO₂:F) (deposited by CVD).

In the second part, possible driving mechanisms behind laser ablation in dependence of the wavelength are introduced and discussed. Afterwards, extent and origin of visual changes of the front-contact material in direct adjacency to the scribe lines were characterized. The visual changes lead to a negative impact on the solar cell properties. Additionally, characterization was done with and without wet-chemical post-treatment (etching or cleaning of the TCO layer). Finally, impact on electrical properties from width-reduced scribes was calculated and results of process implementation in a-Si:H/ μ c-Si:H tandem solar modules will be shown.

5.1 Material ablation behavior

The first section presents the results of the front-contact laser structuring behavior of ZnO:Al and SnO₂:F TCO material. Processing was done by laser sources with the wavelengths of 355 nm, 532 nm, and 1064 nm. Single spot ablation from the substrate side was used for the determination of the relationship between crater dimensions and illuminating laser pulse energy.

The Liu method was used to characterize material properties, processing windows, and laser beam parameters. This was possible since all laser sources exhibit a spatial Gaussian intensity distribution (cf. Section 3.3) [69]. Please refer to Section 3.3.2 where the evaluation of the experimental data is described.

The Liu-Plots for processing of both TCO materials with three different laser wavelengths are shown in Figure 5.1. A comparison of the intercept with the x -axis shows the thresholds for processing of both TCO materials. When 355 nm is used the thresholds are at least one order of magnitude lower than for processing with 532 nm and 1064 nm. For a better overview, all extracted values are listed in Table 5.1. A comparison of measured beam spot radii from the

Table 5.1: Overview of extracted values from Liu-Plots in Figure 5.1 for processing of ZnO:Al and SnO₂:F TCO material with laser wavelengths of 355 nm, 532 nm, and 1064 nm.

Material	Wavelength λ	Beam profiler spot radius ω_0	Extracted spot radius $\omega_{0,\text{Liu}}$	Threshold fluence F_{th}
SnO ₂ :F	355 nm	8.0 μm	11.2 \pm 0.3 μm	0.38 \pm 0.12 Jcm ⁻²
SnO ₂ :F	532 nm	10.5 μm	7.1 \pm 0.3 μm	3.63 \pm 0.33 Jcm ⁻²
SnO ₂ :F	1064 nm	8.1 μm	6.6 \pm 0.4 μm	3.60 \pm 0.51 Jcm ⁻²
ZnO:Al	355 nm	8.0 μm	9.2 \pm 0.3 μm	0.25 \pm 0.05 Jcm ⁻²
ZnO:Al	532 nm	10.5 μm	14.3–17.7 μm	4.08–6.11 Jcm ⁻²
ZnO:Al	1064 nm	8.1 μm	8.4 \pm 0.3 μm	3.67 \pm 0.41 Jcm ⁻²

beam profiler with extracted values from the Liu-Plots shows some differences. It should be noted that the thickness of the substrate for the SnO₂:F TCO material and ZnO:Al TCO material were different (3 mm and 1.1 mm) and irradiation was done through the substrate. Even though the distance between optical system and sample were adjusted accordingly, differences of the beam spot radius on the material surface are possible. All extracted laser beam radii are more or less within the 20% accuracy margin proposed in the original reference [69].

One exception is observed for ZnO:Al processing with 532 nm where the extracted value of $\omega_{0,\text{Liu}}$ =14.3–17.7 μm is significantly higher than what was measured by the beam profiler. The difference between both radii can be accounted to changes of the crater morphology as a function of the laser pulse energy. There is a jump between a low pulse energy regime and a high pulse energy regime with a similar slope within each regime (compare linear regressions in Figure 5.1(b)).

The observed jump is mainly attributed to the method of crater evaluation. The evaluation depends on the color threshold that is set for the crater edge detection. Refer to Section 3.3.2 for a detailed description of the evaluation process. If the ablation behavior changes the threshold changes as well leading to an offset of the crater diameter between different regimes.

The uncertainty of crater evaluation is also the reason why there are gaps in the Liu-Plot for ZnO:Al processing with 355 nm (compare value range of $\ln(E_p/E_0)$ between 0.6 and 1 in Figure 5.1(a)). A clear diameter could not be defined due to non-circular ablation craters in certain pulse energy regimes.

Non-uniformity and low control of the crater edge morphology is unfavorable for a clean scribe line definition. It is a first sign that 355 nm, in combination with small beam spot sizes, is not ideal for front-contact structuring. Especially for TCO material that shows a highly brittle fracture behavior (critical strain <1% [90]).

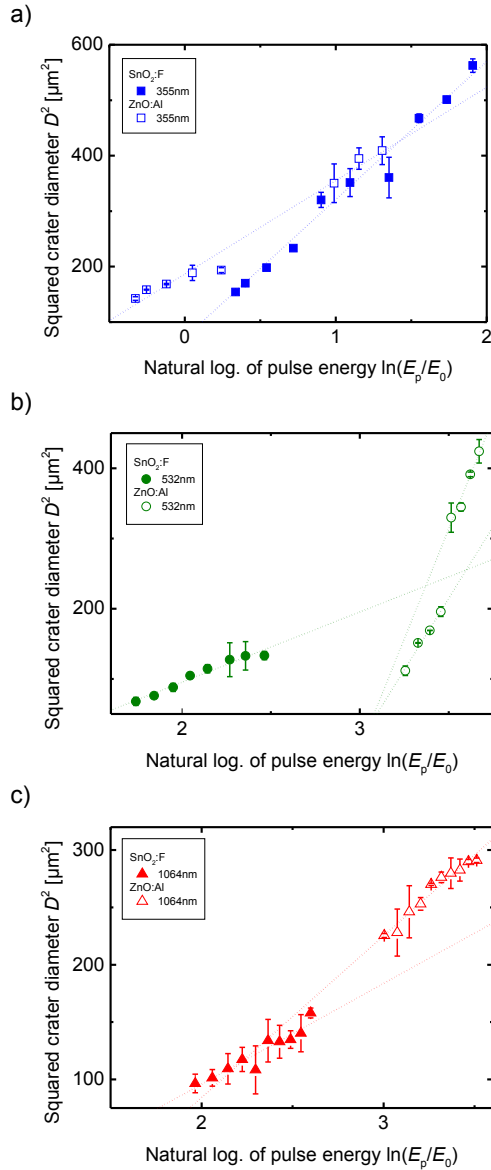


Figure 5.1: Squared single spot crater diameter vs. natural log. of laser pulse energy for processing of SnO₂:F (filled symbols) and ZnO:Al (empty symbols) front-contact material. Processing parameters are: a) 355 nm and $\omega_0=8.0 \mu\text{m}$. b) 532 nm and $10.5 \mu\text{m}$. c) 1064 nm and $8.1 \mu\text{m}$. Dotted lines represent linear regressions for each measurement set. Substrate thickness for SnO₂:F is approx. 3 mm and 1.1 mm for ZnO:Al. Processing was done through the substrate side.

Large differences of the threshold fluences between 355 nm and 532 nm/1064 nm are found for both TCO material systems. A much lower peak fluence is required when processing is done with 355 nm. Furthermore, for processing of SnO₂:F there are no big differences in the threshold fluences between processing with 532 nm and 1064 nm. However, when comparing those two wavelengths for processing on ZnO:Al the threshold for 532 nm is higher. In the literature some similar measurements were found for processing 532 nm and 1064 nm. In general, the values for F_{th} differ quite substantially to the present results [91, 92].

Just by considering the extracted threshold fluences it follows that ablation efficiency is the highest for processing with 355 nm. It is important to know where differences of the threshold fluence originate from. It seems that especially the processing wavelength has a high influence on the ablation efficiency as well as the process quality. In the next section the mechanisms behind laser ablation of TCO material were investigated.

5.2 Mechanisms driving laser ablation processes

Investigations of the material ablation behavior showed that there are distinct differences of the threshold fluences depending on which processing wavelength is used. Insight into the driving ablation mechanisms is required.

In general, pulsed laser ablation with pulse durations in the nanosecond regime can have different physical mechanisms dominating material removal [93]. In the following, the different mechanisms will be briefly introduced and their applicability to interpret the results for TCO ablation will be compared.

Vapor-Stress Induced Laser Ablation: mechanical forces generated by the gas pressure of evaporated material can be a significant driving mechanism behind laser ablation [94, 95, 96, 97].

In the simplest case, the material which is ought to be ablated is deposited onto a substrate which is highly transparent for the used laser wavelength. In contrast, the layer itself is highly absorbing. Thus, when illumination with the laser is done through the substrate the highest absorption of the laser pulse energy is at the substrate/layer interface region. The material is heated, melted, and finally evaporated in a rather small volume at the interface. Mechanical work is done by the expansion of the gas bubble or blister. This leads to high mechanical stresses in the remaining, mostly solid, layer material. Above a certain yield or critical stress in the layer the gas bubble breaks and the layer material above is accelerated and removed. The ablation energy efficiency can be quite high for vapor-stress induced ablation since a phase change takes only place for a small fraction of material.

Thermal-Stress Induced Laser Ablation: another possible mechanically-assisted ablation mechanism is supported by stresses generated from thermal expansion. Many different modes of stresses and strains are potential mechanisms of removal depending on the thermal material properties and layer-stack topology. These are:

5.2. Mechanisms driving laser ablation processes

- High differences of the thermal expansion coefficient (CTE) between different layers that are in contact. Large mechanical stresses can form upon uniform temperature increase [98].
- Large temperature gradients within individual layers can create high mechanical stresses as well. A strong spatial gradient in temperature is possible when laser heating of the material is non-uniform due to, for example, a high optical absorption coefficient [99].
- Since optical absorption between substrate and the layers on top can be very different large temperature differences between the layers can occur. Consequently, depending on the thermal expansion coefficients of the involved material, large thermal stresses can build up.

Just like ablation assisted by gas pressure, mechanisms dominated by thermal-stress can be very energy efficient since no material is objected to any phase transitions [100].

Classical laser ablation: thermal heating, melting, and evaporation is the most common type of laser ablation. The optical energy is absorbed and transferred into thermal heating with subsequent melting and finally evaporation of the layer material. Compared to the two prior described mechanisms, ablation efficiency is the lowest when classical ablation behavior is dominating. This is owed to the absence of any mechanically-assisted force removing the layer material. The layer is removed by a complete phase change into the vapor phase [101].

The ablation behavior of many material systems which are all irradiated from the film side can be described by classical ablation mechanisms. Good agreement between experiment and model simulations can be found [102, 103]. However, there was no extensive research found for laser ablation from the substrate side.

Correlation to the present results: a comparison of the different domination ablation mechanisms with the experimental findings can be done. For this, the optical absorption of the laser pulse energy according to the Lambert-Beer law is assumed. Furthermore, for laser processing with pulse durations in the nanosecond regime, it is reasonable to assume a direct correlation between optical absorption and thermal heating of the TCO material. The absorption coefficient detected with low intensity illumination was evaluated for the laser processing wavelengths 355 nm, 532 nm, and 1064 nm.

Figure 5.2 shows transmission and reflectance measurements of both TCO materials for all laser processing wavelengths. In Figure 5.2 as-sputtered flat ZnO:Al exhibits significant fringes due to the interferences at the interfaces [104]. For SnO₂:F these interferences are almost leveled out due to the rough surface texture. Table 5.2 shows a summary of the calculated absorption coefficients from the spectra in Figure 5.2 for the processing wavelengths. The highest absorption coefficients are observed for 355 nm on both material systems. Direct absorption is dominant in the wavelength regime close to the optical band gap. For a wavelength of 532 nm the absorption is decreased more for ZnO:Al than for SnO₂:F. Both materials are highly transparent in the visible wavelength region (VIS) and only defect absorption is

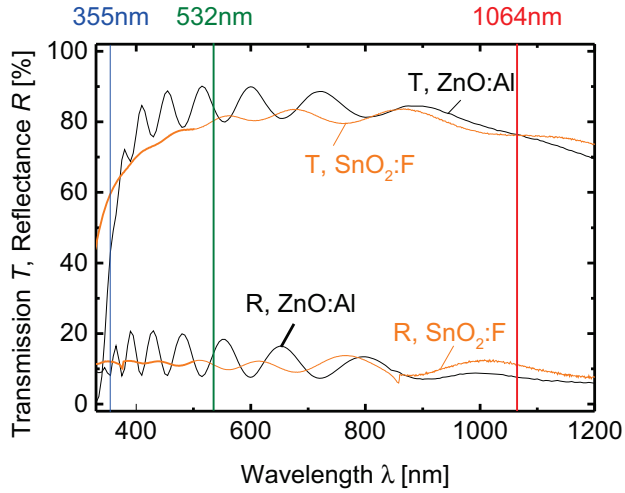


Figure 5.2: Transmission and reflectance spectra for both, as-sputtered flat ZnO:Al, and SnO₂:F TCO material. The inset lines mark the corresponding values at the three relevant laser processing wavelengths. The thickness of both front-contact materials was measured to be approx. 800 nm.

Table 5.2: Overview of calculated absorptions coefficients from the spectra in Figure 5.2 for wavelengths of 355 nm, 532 nm, and 1064 nm.

Material	Evaluation wavelength λ	Absorption coefficient α	Optical penetration depth δ
SnO ₂ :F	355 nm	4886 cm ⁻¹	2.1 μ m
SnO ₂ :F	532 nm	1266 cm ⁻¹	7.9 μ m
SnO ₂ :F	1064 nm	1926 cm ⁻¹	5.2 μ m
ZnO:Al	355 nm	9442 cm ⁻¹	1.1 μ m
ZnO:Al	532 nm	220 cm ⁻¹	45.5 μ m
ZnO:Al	1064 nm	2366 cm ⁻¹	4.2 μ m

5.2. Mechanisms driving laser ablation processes

present [105]. In the near infrared region (NIR) at 1064 nm absorption is increased due to the free carrier absorption [106].

For both materials the absorption coefficient for 355 nm is much higher than for 532 nm or 1064 nm. A higher fraction of the incoming laser pulse energy is absorbed throughout the TCO layer. Large differences of the absorption coefficient could explain the differences of the threshold fluences that were observed from the Liu-Plots (cf. Table 5.1).

However, there are discrepancies between the threshold fluence F_{th} and the optical absorption coefficient α observed for processing of ZnO:Al. On the one hand, processing with 532 nm ($4.08\text{--}6.11\text{ Jcm}^{-2}$) and 1064 nm ($3.67\pm 0.41\text{ Jcm}^{-2}$) leads to small differences of F_{th} . On the other hand, the difference of α between 532 nm and 1064 nm (220 cm^{-1} vs. 2366 cm^{-1}) is significant.

Thermal laser annealing of ZnO:Al is known to have an impact on the free carrier absorption [107, 108] decreasing the absorption coefficient for 1064 nm. For processing with 1064 nm on ZnO:Al a transient annealing could be one reason for the discrepancy between processing behavior and optical measurements.

Quite different values of the optical penetration depths δ are obtained between the processing wavelengths and TCO materials. Yet, the lowest value of $1.1\ \mu\text{m}$ is the only value comparable with the layer thickness of 800 nm. The high optical penetration lengths would mean that heating of the layer is almost homogeneous throughout the thickness layer.

In general, the changes in ablation behavior cannot be completely explained by the different optical properties of the TCOs for most material/wavelength combinations. To investigate whether this can be explained by different ablation mechanisms further experiments were carried out.

Ablation debris recollection: during laser processing of $\text{SnO}_2\text{:F}$, ablation material was collected as described in Section 4.1. The ablation debris particle number, size, and especially the shape can give information on the ablation mechanisms. Figure 5.3 shows optical microscopy images of ablation debris collected from processing. The particle size drastically decreases when the processing wavelength of 355 nm in Figure 5.3(a) is changed to 532 nm (Figure 5.3(b)) and 1064 nm (Figure 5.3(c)). Besides the change of particle size between different processing parameters there is also a change in shape observed.

When processing is done with 355 nm most particles exhibit an angular shape as well as sharp, pointed edges. Debris collected from processing with 532 nm show sharp, pointed edges as well, but with a smaller average particle size compared to 355 nm. Processing with 1064 nm leads to more spherically shaped particles. However, a small fraction of particles with sharp edges and angular shape can be found here as well.

For a better visualization of the different particle shapes, both processes from Figure 5.3(a) and Figure 5.3(c) are shown with higher magnification in Figure 5.4. The clearly spherically shaped particles for processing with 1064 nm (red circles in Figure 5.4(b)) indicate that debris from

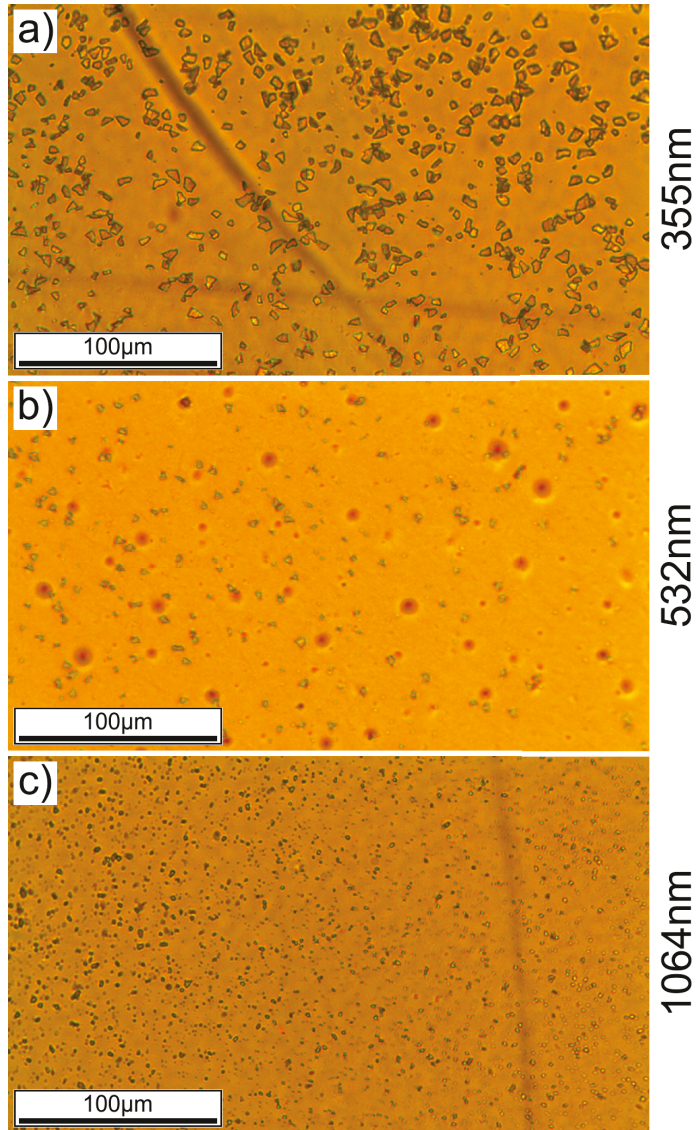


Figure 5.3: Optical microscopy images of ablation debris captured from SnO₂:F front-contact material processing. The used parameters are: a) $\lambda=355$ nm and $F_p=1.74$ Jcm⁻². b) $\lambda=532$ nm and $F_p=2.43$ Jcm⁻². c) $\lambda=1064$ nm and $F_p=4.50$ J/cm². The distance between adhesive tape and TCO layer is approx. 2–3 mm.

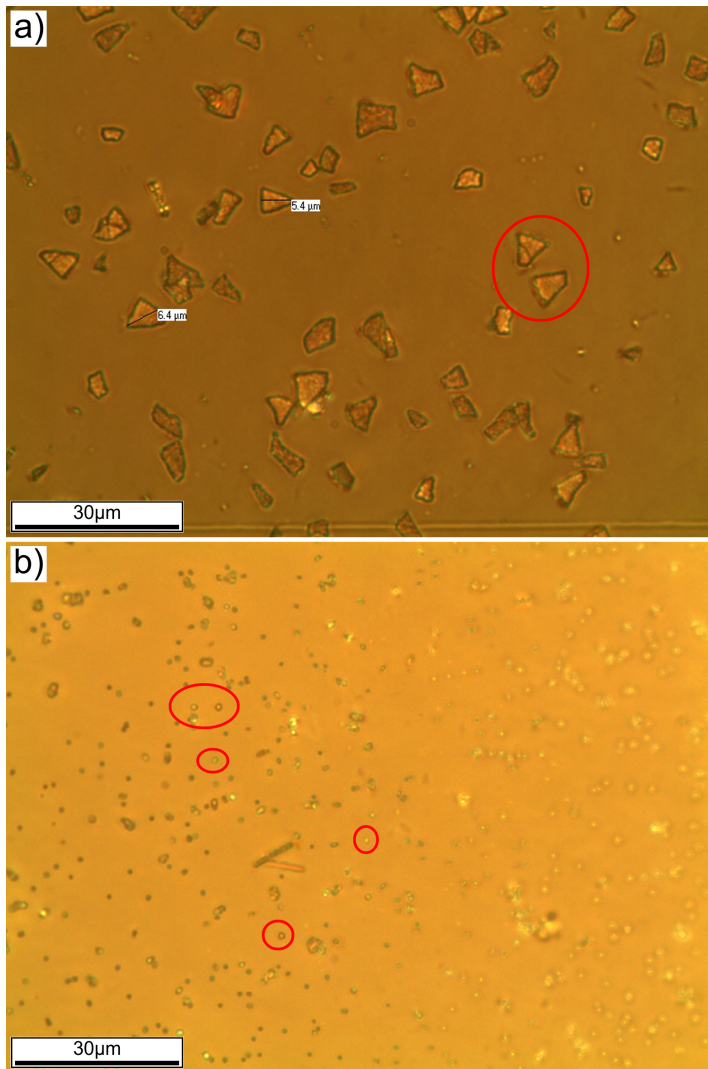


Figure 5.4: Magnified view of optical microscopy images of ablation debris captured from SnO₂:F front-contact material processing. Parameters: a) $\lambda=355$ nm and $F_p=1.74$ Jcm⁻². b) $\lambda=1064$ nm and $F_p=4.50$ Jcm⁻².

ablation is in fact resolidified molten material. In the contrary, no signs of molten material can be found in for processing with 355 nm in Figure 5.4(a).

These results were confirmed as well for processing of ZnO:Al. It shows that there can be fundamental differences between the dominating ablation mechanisms depending on the used laser wavelength and/or parameters.

Ablation with 355 nm is highly assisted by mechanical forces while it is less pronounced for 532 nm. For processing with 1064 nm a transition to a predominantly classic thermal ablation regime is observed. The remaining question is whether classical, vapor-stress or thermal-stress induced ablation is the driving mechanism behind ablation with 355 nm.

Thermal heating behavior: in a first step simple calculations were made to estimate if evaporation of the whole TCO layer occurs during processing with a wavelength of 355 nm. Experimental data of the ablated volume and used laser pulse energy was required and extracted from the corresponding Liu-Plot. Together with thermal properties of the processed TCO a calculation of the required energy for evaporation of said volume was carried out.

The optical properties are not considered and absorption of the complete pulse energy is assumed. Thus, the energy is used for heating of the material volume. The Equation 5.1 describes the required phase change energy (compare [94]),

$$E_{sv} = \frac{\pi}{4} D^2 t \rho [c_p (T_v - T_{amb}) + \Delta_f H^0 + \Delta_{fus} H]. \quad (5.1)$$

Where E_{sv} is the required energy for a phase transition from solid to vapor, D^2 is the squared crater diameter, t the layer thickness, ρ the density, and c_p the heat capacity at constant pressure. Furthermore, boiling and ambient temperatures are given by T_v and T_{amb} . Since both materials sublime above their melting temperature only the enthalpy of formation $\Delta_f H^0$ and enthalpy of fusion $\Delta_{fus} H$ are required. Table 5.3 lists an overview of the material properties for bulk ZnO and SnO₂ from literature used for these calculations. For the calculation, the

Table 5.3: Overview of material properties used for calculations according to Equation 5.1 of full phase transitions of ZnO and SnO₂.

Material	Property	Value	Original Ref.
ZnO	Density ρ	5704 kg/m ³	[109]
ZnO	Heat capacity c_p	505 J/K kg	[110]
ZnO	Boiling temperature T_v	2223 K	[111]
ZnO	Enthalpy of fusion $\Delta_{fus} H$	860 kJ/kg	[112]
ZnO	Enthalpy of formation $\Delta_f H^0$	4305 kJ/kg	[112]
SnO ₂	Density ρ	7020 kg/m ³	[113]
SnO ₂	Heat capacity c_p	354 J/K kg	[113]
SnO ₂	Boiling temperature T_v	2203 K	[113]
SnO ₂	Enthalpy of fusion $\Delta_{fus} H$	155 kJ/kg	[112]
SnO ₂	Enthalpy of formation $\Delta_f H^0$	3833 kJ/kg	[112]

5.2. Mechanisms driving laser ablation processes

experimental crater diameter and corresponding pulse energy close to experimental values where debris experiments indicate clear mechanical behavior (cf. Figure 5.4(a)) are used. The theoretical energy required for a complete phase change is derived for a volume calculated from the crater diameter and layer thickness. A comparison between the calculated and experimental energies is listed in Table 5.4. The calculated values from Table 5.4 indicate

Table 5.4: Comparison between experimental and calculated energies required for removal of material volume of ZnO and SnO₂. *Calculations were made with material parameters of undoped crystalline ZnO and SnO₂.

Material	Wavelength λ	Experimental pulse energy E_p	Crater diameter D	*Calculated energy E_{sv}
ZnO:Al	355 nm	0.70 μ J	11.0 μ m	2.74 μ J
SnO ₂ :F	355 nm	1.40 μ J	12.4 μ m	3.10 μ J

that for processing with 355 nm the required energy E_{sv} is significantly higher than the raw experimental pulse energy value. Even with the rough assumption of complete absorption by neglecting the optical properties the energy is not sufficient for classical ablation.

In a second step, vapor-stress induced ablation by a differential phase transition is considered as a possible reason for ablation. The prior calculated values of E_{sv} are compared with the required energy density for a differential phase transition at the TCO/substrate interface considering decaying absorption. The absorption coefficient for 355 nm is used for the calculations. The amount of energy absorbed in the depth z can be defined by the following equation,

$$E(z) = E_p [1 - \exp(-\alpha z)]. \quad (5.2)$$

Here, E_p is the pulse energy and α as the absorption coefficient. Furthermore, the derivative of Equation 5.2 can be calculated to obtain the pulse energy density in z direction,

$$\frac{dE(z)}{dz} = E_p \alpha \exp(-\alpha z). \quad (5.3)$$

The maximum of Equation 5.3 can be found for $z=0$ which is simply $E_p \alpha$. Furthermore, the energy density calculated divided by the layer thickness E_{sv}/t can be evaluated as well. Table 5.5 shows a comparison of both values. The comparison of the maximal apparent

Table 5.5: Comparison between experimental and calculated energy density for the values derived from Table 5.4.

Material	Wavelength λ	Required energy density E_{sv}/t	Maximal energy density $E_p \alpha$
ZnO:Al	355 nm	3.43 J/m	0.66 J/m
SnO ₂ :F	355 nm	3.88 J/m	0.68 J/m

($E_p \alpha$) with the calculated required energy density (E_{sv}/t) shows significant differences. This leads to conclude that in fact vapor-stress induced ablation is not the driving mechanism

behind ablation with 355 nm. Under the assumption of a constant absorption coefficient thermal-stress is most probably the dominating ablation mechanism.

Please note that absorption coefficients detected under low light intensity illumination were used for these calculations. Further phase transition calculations showed that for processing with 532 nm and 1064 nm the required energy densities cannot be reached as well. Therefore it is possible that optical properties are not transferable to describe the transient properties during nanosecond laser ablation. It is possible that the absorption coefficient is influenced by the temperature [114, 115] and/or illumination intensity due to multi-photon absorption [116].

In a next step, results from single spot ablation behavior were used for the realization of optimized P1 scribe line processes with a reduced scribe width. Origins for limitations were identified and will be discussed. It will be shown that a scribe width well-below 10 μm is achievable for every processing setup.

5.3 Geometrical scribe width optimization

From the Liu-Plots of each TCO material and processing wavelength combination it could already be seen that crater diameters well-below the optical laser beam spot size are achievable. A crater diameter below the beam spot size is only possible due to the Gaussian intensity distribution of the laser beam. Figure 5.5 shows the different approaches that were used to find the optimal front-contact structuring parameters for processing of $\text{SnO}_2\text{:F}$ and ZnO:Al TCO material.

Approaches for scribe width reduction: in principle there are two main ways to reduce the width of laser scribed lines when using laser beams with a spatial Gaussian intensity distribution. Figure 5.5 shows schematically the pulse fluence distribution $F(r, z)$ of the focused laser beam on the sample surface. The peak fluence F_p is defined as, $F_p = 2E_p / \pi\omega_0^2$ with E_p as the laser pulse energy and ω_0 as the laser beam radius in focus. The width w_{p1} of the laser scribe is defined where the pulse fluence is above the ablation threshold fluence F_{th} (see Figure 5.5(a)). Ablation only occurs where $F(r, z)$ is higher than F_{th} .

One path to decrease the scribe width w_{p1} is to adjust the laser pulse energy so that the peak of the fluence distribution is closer to F_{th} (Figure 5.5(b) curve 2). A scribe width well-below the beam spot diameter $2\omega_0$ can be achieved.

However, this simple method is limited by the fact that with peak fluences close to F_{th} small material inhomogeneity across the sample can lead to variations of the effective threshold fluence. This can be represented simplified by dF_{th} in Figure 5.5(b). Furthermore, pulse-to-pulse deviations of E_p can have an influence on the effective pulse fluence on the sample surface causing processing instabilities.

The second way is to use stronger focusing optics and change the fluence distribution to obtain a steeper slope and a smaller beam spot radius ω_0 (curve (3) in Figure 5.5). Again, with

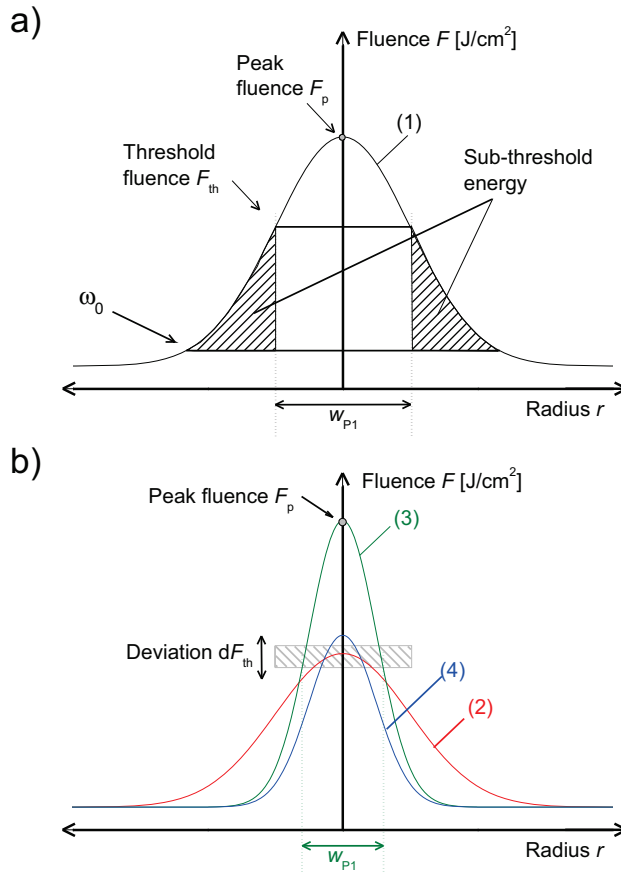


Figure 5.5: Schematic plot of the pulse fluence distribution of a laser beam in focus with a Gaussian intensity distribution. Plots show: a) The shaded area marks the sub-threshold laser energy. Above the threshold fluence F_{th} ablation occurs and the scribe width is defined by the width w_{p1} . b) Influence of stronger focused beams and deviations of the threshold fluence F_{th} over the sample area (dF_{th} and shaded box). The curves (1)–(4) represent different laser beam radii ω_0 and peak fluences F_p in accordance with the two different width reduction approaches.

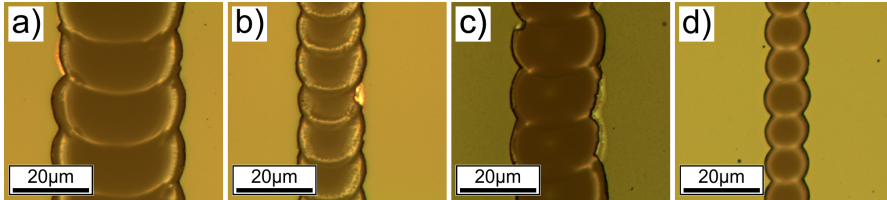


Figure 5.6: Optical microscope images of width reduction process for substrate side scribing of ZnO:Al TCO material with 355 nm. Parameters are: a) Standard process $F_p=1.72 \text{ Jcm}^{-2}$ and $\omega_0=19.3 \mu\text{m}$. b) Lower pulse energy $F_p=0.68 \text{ Jcm}^{-2}$ and $\omega_0=19.3 \mu\text{m}$. c) Stronger focusing $F_p=8.26 \text{ Jcm}^{-2}$ and $\omega_0=8.0 \mu\text{m}$. d) Stronger focusing and optimized pulse energy $F_p=0.68 \text{ Jcm}^{-2}$ and $\omega_0=8.0 \mu\text{m}$.

an adjustment of the peak fluence close to F_{th} reduced scribe widths w_{p1} can be achieved (curve (4) in Figure 5.5).

Indeed, the use of stronger focusing optics has certain drawbacks as well. Due to the decrease of depth-of-focus (DOF) the process is sensitive against variations of the distance between focusing optics and sample surface.

Both paths have advantages and disadvantages. The optimal trade-off is depending on the whole system setup consisting of the material, optics, and mechanical machine properties.

In this work a combination of both approaches was chosen and the beam spot radius ω_0 was lowered from $19.3 \mu\text{m}$ to $8.0 \mu\text{m}$ for 355 nm, from $58.7 \mu\text{m}$ to $10.5 \mu\text{m}$ for 532 nm and from $48.0 \mu\text{m}$ to $8.1 \mu\text{m}$ for 1064 nm. A measure of the process stability needs to account for every deviation of the scribing machine in the Z -plane like flatness of the axes or substrate waviness [64]. A Z -axis sweep can be used to evaluate the optical process depth (cf. Section 3.3.3). For all three wavelengths with stronger focusing the processing depth was measured to be at least $\pm 0.2 \text{ mm}$ allowing a stable operation with the scribing tool.

The results of both approaches are shown in Figure 5.6 for substrate side processing of ZnO:Al TCO material with a wavelength of 355 nm. The achieved scribe widths w_{p1} are in good correlation to the behavior of the schematic examples from Figure 5.5. With optimized laser parameters and a beam spot radius of $8.0 \mu\text{m}$ a width reduction of w_{p1} from $35 \mu\text{m}$ down to $12 \mu\text{m}$ can be realized. A high electrical insulation between two adjacent cell stripes is obtained as well. Optimized laser parameters mean not only a minimized geometrical scribe width but also a clean edge definition without flakes evaluated visually by optical microscopy. The width reduction process was done for both TCO material systems ZnO:Al and SnO₂:F with the three laser wavelengths 355 nm, 532 nm, and 1064 nm.

Optimized scribe lines: a display of the achieved minimal scribe widths w_{p1} is shown in Figure 5.7. All lines were processed without subsequent substrate cleaning for SnO₂:F TCO material or wet-chemical etching of the ZnO:Al samples. The minimal achievable scribe widths w_{p1} are all in a similar range and well-below $10 \mu\text{m}$. The colored circle above each scribe is an illustration of the theoretical laser beam spot size for the individual process. Except for

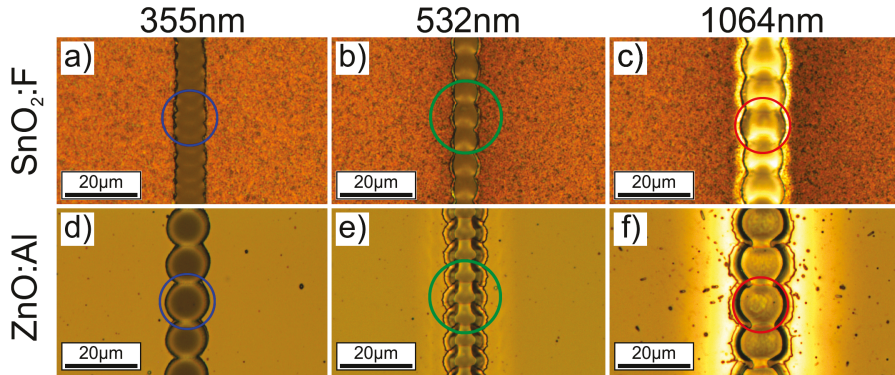


Figure 5.7: Optical microscope images of achieved minimal P1 scribe widths for substrate side scribing of ZnO:Al and SnO₂:F TCO material without etching or cleaning. Parameters are: a) $F_p=0.70 \text{ Jcm}^{-2}$. b) $F_p=2.44 \text{ Jcm}^{-2}$. c) $F_p=10.20 \text{ Jcm}^{-2}$. d) $F_p=0.64 \text{ Jcm}^{-2}$. e) $F_p=8.0 \text{ Jcm}^{-2}$. f) $F_p=11.6 \text{ Jcm}^{-2}$. The circle inset in each image represents the beam spot size in focus.

processing with 1064 nm the realized width is only slightly below the spot size. Surprisingly the lowest stable scribe widths are achieved for processing with the largest spot radius of $10.5 \mu\text{m}$ with 532 nm (Figure 5.7(b) and Figure 5.7(e)). However, the scribe edges are not as well-defined as for processing with 355 nm.

A comparison between the optimized processing parameters between the different wavelengths is difficult. Multiple factors like process stability, overlap, and focal length are all important for determining the optimized process parameters. For example, due to the used wavelength, raw beam diameter, and focal length rather large differences of the depth-of-focus (DOF) can occur. It is possible that due to a limited DOF an increased peak fluences is required to obtain a stable scribe line (cf. Section 3.2).

In terms of ablation and energy efficiency 355 nm might be suited best for processing due to the significantly lower threshold fluence (cf. Table 5.1). However, if thin scribe lines are required it could be more reasonable to use 532 nm for processing. For this wavelength ablation is driven by thermal evaporation (classic behavior) instead of stress-induced ablation. Mechanically-assisted removal can exhibit a non-uniform scribe edge morphology (cf. missing data points in Figure 5.1).

However, the results from Figure 5.7 also show that for processing with 355 nm scribe lines with a clean scribe edge were achieved for SnO₂:F as well as for ZnO:Al.

Nonetheless, for certain TCO materials a much higher dependence of the materials fracture behavior on the used processing wavelength was observed. A different type of SnO₂:F TCO material was processed with 355 nm as well as with 532 nm to compare the distinct differences in ablation behavior. Figure 5.8 shows optical microscopy images of optimized scribes for both wavelengths. For processing with 355 nm (Figure 5.8(a)) it is not possible to create thin scribes well-below the spot size without a highly non-uniform edge and flake formation. In

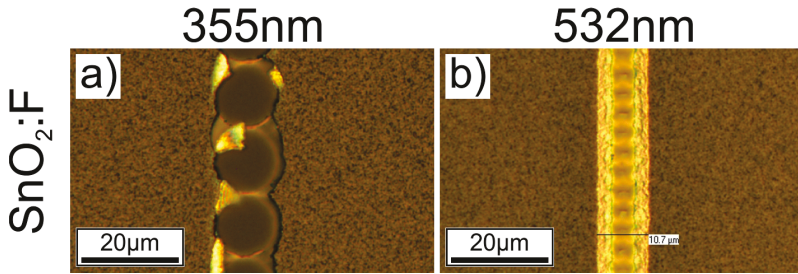


Figure 5.8: Optical microscope images of achieved minimal P1 scribe widths for substrate side scribing of $\text{SnO}_2:\text{F}$ TCO material from the Asahi Glass Company (type VU). Parameters: a) 355 nm and $\omega_0=8.0 \mu\text{m}$. b) 532 nm and $\omega_0=10.5 \mu\text{m}$.

contrast, processing with 532 nm creates a smooth scribe edge and very narrow scribe lines. One process is driven by mechanically-assisted ablation, where rip-off behavior at the edge is determined by the materials fracture behavior [117]. The other process is dominated by phase changes and is easily controllable by the laser pulse energy.

These differences of lower scribe width limitations were found for other types of TCO material as well (not shown here, $\text{ZnO}:\text{B}$ TCO material with $1.5 \mu\text{m}$ layer thickness). In conclusion, knowledge of the possible mechanisms that are driving ablation, for a given material/processing wavelength combination is crucial for evaluation and optimization of the scribing process.

Another look on Figure 5.7 shows that, except for processing with 355 nm, the front-contact material close to the scribe edge shows color changes. There are brighter or darker regions, as well as splatters from the ablation for processing of $\text{ZnO}:\text{Al}$ with 1064 nm. In the following these changes and their impact will be discussed in detail.

5.4 Near scribe edge material modifications

Laser processing for both TCO materials lead to visible material changes in the direct vicinity of the scribe edge. In literature, these effects are often referred to as heat-affected zones (HAZ). A HAZ can originate from the sub-threshold energy intake into the non-ablated material (for example shown in Figure 5.5(a)). The fraction of the pulse energy that is absorbed below the threshold dissipates thermally and can change the films electrical and/or optical properties [118]. Recent works from Canteli et al. showed changes of the TCO microstructure by Raman spectroscopy near the scribe edge which can originate from heat-affected zone formation [119, 72]. It is important to know whether these optical changes have an impact on the electrical and/or optical properties. It would be counterproductive if the geometrical scribe width is optimized to narrow lines but the remaining material aside is highly deteriorated leading to an effective increase of the dead area losses.

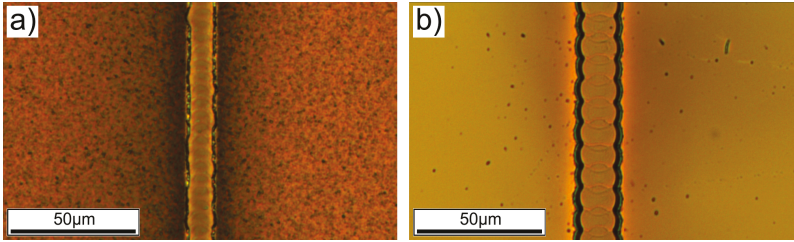


Figure 5.9: Optical microscope images for processing parameters with a high degree of visual changes of the TCO material near the scribe edge. Parameters: a) $\text{SnO}_2:\text{F}$ processed with 532 nm and $F_p=3.1 \text{ Jcm}^{-2}$. b) $\text{ZnO}:\text{Al}$ processed with 1064 nm and $F_p=10.7 \text{ Jcm}^{-2}$.

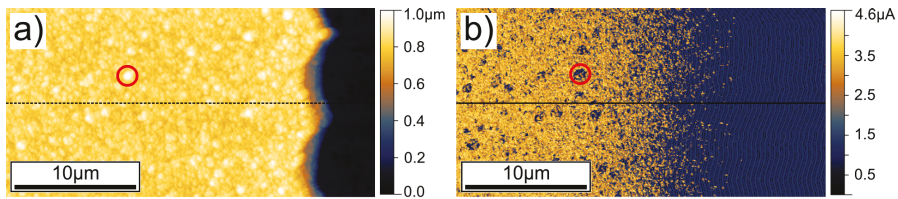


Figure 5.10: Conductive Atomic Force Microscopy measurement of $\text{SnO}_2:\text{F}$ TCO material processed with 532 nm and optimized laser parameters. Plots shown in: a) Topography. b) Current map. The dashed and solid lines mark the position where averaged line scans were further evaluated.

Figure 5.9 shows exemplary optical microscope images of two scribes on $\text{SnO}_2:\text{F}$ and $\text{ZnO}:\text{Al}$ TCO material. Both parameters were chosen so that the scribe edge material exhibits a high amount of visible changes. An extent of up to $50 \mu\text{m}$ into the adjacent TCO material is observed. The optical microscopy image in Figure 5.9(a) shows a darkened region in vicinity of the scribe line while a brighter region is observed for processing of $\text{ZnO}:\text{Al}$ in Figure 5.9(b). The extent of visual changes are approx. $20\text{--}30 \mu\text{m}$ into the remaining material aside the scribe.

Electrical properties: to determine the influence of these modifications on the electrical properties c-AFM measurements were carried out close at the scribe edge, with the setup described in Section 4.2. The tip was biased with a DC voltage of $+2 \text{ V}$ and a contact force of 2 nN was applied. Two parameter sets were compared for each TCO material system and each processing wavelength. One parameter set was chosen to show minimal scribe widths and minimal visible changes (optimized parameters equal to the parameters from Figure 5.7). The second parameter set was chosen to create scribe lines with a high amount of visible changes (referred to as non-ideal or non-optimized).

Topography and current map from c-AFM measurements of a scribe line processed with 532 nm and optimized parameters on $\text{SnO}_2:\text{F}$ are shown in Figure 5.10. Here, no visible changes were observed with the optical microscope. Nonetheless, when comparing the position of the scribe edge in the topography with the current map a region near the edge with a strongly decreased current flow is observed. At a distance of about $15 \mu\text{m}$ off the edge the

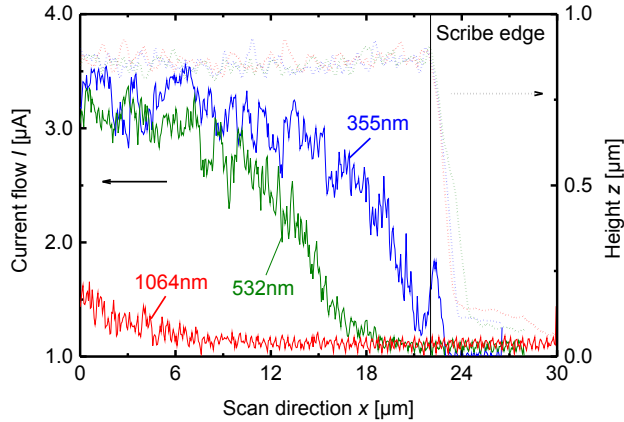


Figure 5.11: Conductive Atomic Force Microscopy line scans of $\text{SnO}_2\text{:F}$ processed with optimized parameters and different wavelengths (see Figure 5.10). Solid lines represent current flow for 355 nm (blue), 532 nm (green), and 1064 nm (red). Dashed lines correspond to the topography profile. The current line scans are averaged across $\pm 3 \mu\text{m}$ along the scribe for better visualization.

current flow recovers to the reference value of the sample. A lowered current flow is observed homogeneously along the scribe line. Both measurements in forward and backward direction showed no differences. Therefore, current flow changes due to a non-ideal force/distance control loop at the scribe edge (steep height change) can be ruled out. One remark is important to mention for these measurements. The current flow reduction at certain points (see red circle in Figure 5.10) is most likely due to a topography effect (see Section 4.2). The current flow is sensitive to the contact area variations between sample surface and tip. Slight changes of the tip-surface contact area can result in huge differences of the local contact resistance and therefore current flow.

To compare the influence of the processing wavelengths line scans perpendicular to the laser scribe were evaluated (see solid and dashed line in Figure 5.10). Figure 5.11 shows a plot of several line scans of the current flow as well as topography profiles for processing of $\text{SnO}_2\text{:F}$ with the different wavelengths and optimized laser parameters. The smallest lateral extent of the region with lowered current flow is observed for processing with 355 nm. For 532 nm the extent is almost twice as wide. The highest influence on the current flow can be seen for scribing with 1064 nm. At a distance of more than $25 \mu\text{m}$ from the edge a measurable current increase is first observed. A larger scan field revealed the same gradual increase in current flow with increasing distance similar to both other processing wavelengths. A gradual increase or recovering of the current flow can be described by thermally induced changes of the front-contact material originating from sub-threshold energy intake.

The second parameter set (non-ideal) for processing of $\text{SnO}_2\text{:F}$ material with a high amount of visible changes near the scribe edge, was measured with c-AFM as well. Here, for all processed samples no current flow above the noise level of the measurement setup was detected. No

5.4. Near scribe edge material modifications

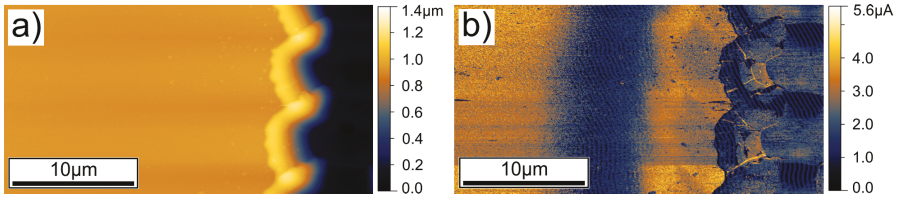


Figure 5.12: Conductive Atomic Force Microscopy measurement of ZnO:Al TCO material, before post-treatment, processed with 532 nm and optimized parameters. Plots shown in: a) Topography. b) Current map.

current flow was observed within a $50 \times 50 \mu\text{m}^2$ scan field for any processing wavelength. It is possible that there is a larger extent of electrically impaired material present for these processing parameters.

Measurements with c-AFM for experiments on ZnO:Al TCO material with 532 nm and the optimized parameter set showed a slightly different behavior. The current flow shown in Figure 5.12 for processing with 532 nm reveals a different shape and distribution compared to processing of SnO₂:F material with 532 nm. In direct vicinity of the scribe edge no reduction of the current flow is detected. Just at about $5 \mu\text{m}$ off the edge a lowered current flow is observed. The observed behavior seems to be in contradiction with thermal deterioration of the edge-adjacent material due to heat-affected zone formation. Due to the Gaussian distribution of the laser beam the effects on the material would most likely be monotonous. An increase of current flow with increasing distance from the scribe edge, similar to processing of SnO₂:F, is expected. Furthermore, there is some residual current flow within the scribe line observed.

Another surprising detail is the highly decreased current flow on top of the melt bulges at the scribe edge. There were only slight differences between forward and backward direction detected. Therefore, attribution of these findings to geometry artifacts is unlikely due to the size and extent of the bulges in comparison to the tip radius of 100 nm–200 nm. Perhaps problems of the control loop for the contact force could describe the observed behavior. If the contact force is decreased the correlated current flow is decreased as well. However, at certain points that seem to be cracks on the bulges, a significant current flow is measured. Either the contact area/force is increased in these cracks or the materials conductivity is only affected on the surface.

Changes of the contact force by the control loop can be also seen in the lower part of the current flow map. A higher overall current flow is observed (stronger signal on the front-contact surface). However, the offset in current flow has no influence on the spatial distribution.

For comparison between the different processing wavelengths for ZnO:Al line scans were evaluated as well. Figure 5.13 shows the current flow and topography plotted as a function of the perpendicular distance to the scribe. The same effect of spatial offset for the region with lowered current flow is observed for processing with 1064 nm as seen in Figure 5.12. Although,

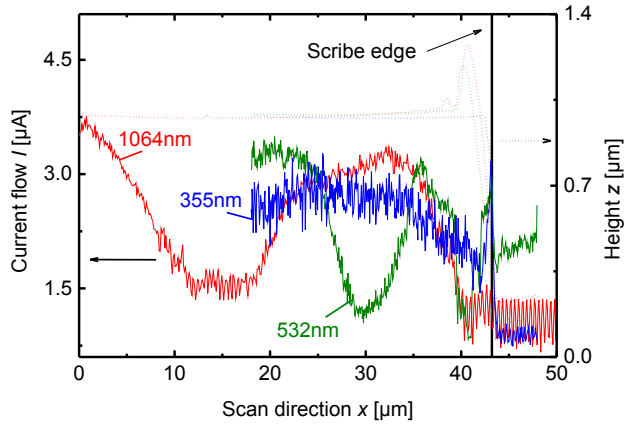


Figure 5.13: Conductive Atomic Force Microscopy line scans of ZnO:Al processed with optimized parameters and different wavelengths. Solid lines represent current flow for 355 nm (blue), 532 nm (green), and 1064 nm (red). Dashed lines correspond to the topography profile. The current line scans are averaged across $\pm 3 \mu\text{m}$ along the scribe for better visualization.

the offset of about $30 \mu\text{m}$ is higher and its extent of $20 \mu\text{m}$ is larger. Only for processing with 355 nm the same gradual increase, as for SnO:F, of the current flow as a function of the distance from the scribe edge is observed. The differences in maximal current flow between the different processing wavelengths could be explained by different effective contact forces or tip wear. This is evident since all three scribe lines were prepared on the same sample in direct vicinity. The topography shows that only for processing with 355 nm no bulging at the scribe edge is observed.

The non-ideal parameter set for processing of ZnO:Al was measured as well. Just as for SnO:F for all scribing wavelengths no current flow could be detected by the c-AFM system. A large extent of the affected area in vicinity of the scribe line could explain the strongly decreased current flow.

The c-AFM measurements were carried out to determine the electrical properties of the non-ablated TCO material near the scribe since it is regarded as active cell area. A spatial extent of deteriorated material in the range of the non-minimized scribe width would contradict with the optimization procedure. But, as seen by comparing c-AFM topography and current maps, these measurements can have artifacts from geometry as well as from a non-ideal control loop for the contact force. Although, quantification of front-contact electrical properties near the scribes is difficult to make from the measured current values, negative impact on the TCO material quality is without any doubt.

Local solar cell properties: Laser Beam Induced Current measurements (LBIC) were conducted to characterize the direct impact on the solar cell level. The setup described in Section 4.3 was used for the measurement of scribe lines prepared on both TCO material systems

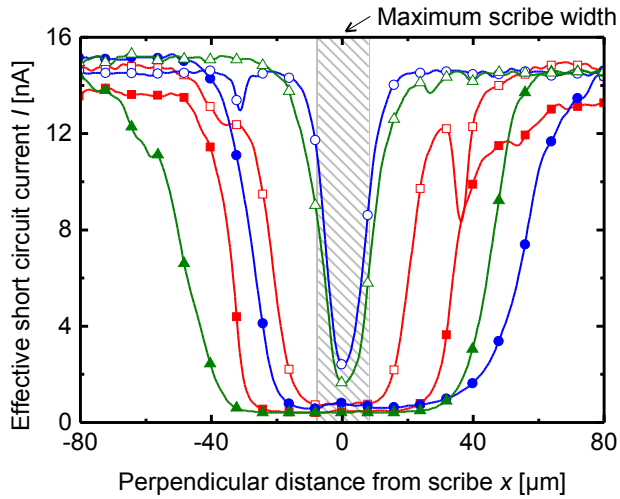


Figure 5.14: Laser Beam Induced Current line scans across the P1 laser scribe of an amorphous silicon (a-Si:H) solar cell on $\text{SnO}_2\text{:F}$ TCO material processed with various laser wavelengths and optimized (empty symbols) or non-ideal (filled symbols) laser parameters. Scan direction is according to sketch from Figure 4.4. Different symbols correspond to processing with 355 nm (circles), 532 nm (triangles), and 1064 nm (squares). The shaded area represents the maximum physical scribe width.

and both laser parameter sets (non-ideal/optimized). For processing on $\text{SnO}_2\text{:F}$ an a-Si:H p-i-n solar cell was deposited whereas a $\mu\text{c-Si:H}$ cell was prepared for processing of ZnO:Al [12].

The current density under short-circuit condition was measured as a function of distance to the scribe line. Figure 5.14 shows the results of line scans across P1 scribe lines prepared with each wavelength/parameter set combination, first for a-Si:H solar cells on $\text{SnO}_2\text{:F}$ TCO. Depending on the used processing wavelength and parameters there is a large region near the P1 scribe line where no current generation is detected at all. In this region the solar cell is strongly deteriorated. Only for processing with optimized parameters and 355 nm or 532 nm a constant current density up to the physical scribe edge, with a steep decrease, is observed. No severe impact on the cell properties is expected for these parameters. The fact that current flow within the scribe does not always reach the same minimal signal value is most likely due to the width of the optimized scribe lines of about $10\ \mu\text{m}$. The diameter of the measuring laser beam is approx. $3\ \mu\text{m}$ and light scattering within the scribe is possible.

The biggest differences between optimized and non-ideal parameters are observed for 355 nm and 532 nm. Whereas, the extent of deterioration is severe for both processing parameters when scribing is done with 1064 nm. The extent into the active solar cell for the optimized parameters is in good agreement with the extent of lowered current observed from the c-AFM measurements. Unfortunately, the current decrease in the affected region cannot be correlated distinctively to an increase of the series resistance in the front-contact. The LBIC

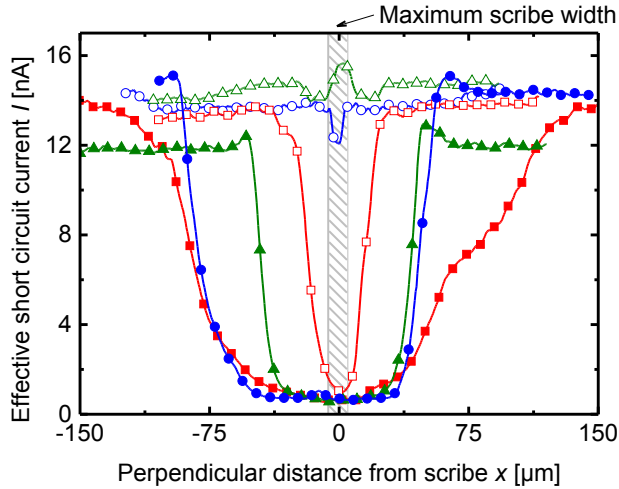


Figure 5.15: Laser Beam Induced Current line scans across the P1 laser scribe of a microcrystalline silicon ($\mu\text{c-Si:H}$) solar cell on ZnO:Al TCO material processed with various laser wavelengths and optimized (empty symbols) or non-ideal (filled symbols) laser parameters. Scan direction is according to sketch from Figure 4.4. Different symbols correspond to processing with 355 nm (circles), 532 nm (triangles), and 1064 nm (squares). The shaded area represents the maximum physical scribe width.

measurements were conducted only under short-circuit conditions (cf. Figure 2.6). Shunting or changes of the optical properties could be an origin for deterioration as well. In any case, high deterioration is apparent leading to increased losses in the nominal active solar cell.

For processing of $\mu\text{c-Si:H}$ on ZnO:Al a similar behavior was observed. Figure 5.15 shows the LBIC line scans for processing of ZnO:Al. For the optimized parameters of processing with 355 nm and 532 nm there is no impact on the current generation in adjacency to the scribe observed. Only for 532 nm directly at the edge a slight dip in current flow is visible that could be assigned to the results from c-AFM. The optimized parameter set of 1064 nm shows a larger extent.

It should be noted that for processing with 355 nm and 532 nm and optimized parameters the current signal did not vanish within the scribe line. Light scattering of the measuring laser beam (spot size $\approx 3 \mu\text{m}$) at the scribe edge in combination with a low scribe width ($\approx 10 \mu\text{m}$) is one possible reason for this behavior.

In general, processing with non-ideal parameters leads to a large region with severe impact on the current generation for all scribing wavelengths. Please note that the reference current value for non-ideal processing with 532 nm is shifted. This shift is owed to the fact that this process parameter was prepared and measured in a separate solar cell.

5.4. Near scribe edge material modifications

A closer look at the shape of the non-ideal/532 nm curve (green filled triangles in Figure 5.15) reveals that recovering of the current generation to the reference value is abrupt with a high slope which also exhibits an overshoot. Again, such behavior is not easily explained by thermal deterioration of the front-contact material and different effects could prevail.

Surface morphology: Scanning Electron Microscopy was carried out near the P1 scribe edge for further investigations of the surface morphology. Figure 5.16 shows exemplary the sample surface of SnO₂:F TCO after processing with 532 nm and optimized parameters at various distances from the scribe edge. Figure 5.16(a) shows that the scribe exhibits a smooth edge due to melting of the TCO material at the scribe edge. There is a massive amount of surface redeposition of ablated material on the front-contact close to the edge observed as well as on the substrate within the scribe. The magnified view in Figure 5.16(b) in direct vicinity of the edge indicates that the front-contact surface coverage by the particles is quite high building an almost continuous layer. The degree of redeposition reduces with increasing distance from the scribe (see Figure 5.16(c)). This is in accordance with c-AFM and LBIC measurements leading to conclude that redeposition plays an important role in the deterioration of front-contact material by laser processing. SEM investigations on SnO₂:F processed with 355 nm and 1064 nm showed a degree of debris redeposition in agreement with the extent determined with c-AFM and LBIC.

SEM images of a scribe line on ZnO:Al TCO processed with 532 nm and optimized parameters can be seen in Figure 5.17. The melt bulges at the scribe edge that were also observed by optical microscopy and from the topography map (c-AFM) are clearly visible. Furthermore, cracks that could be seen by geometry artifacts in the c-AFM current flow map are revealed as well (compare Figure 5.12). The cracks partly extend down to the substrate surface within the scribe which could mean that damaging of the substrate occurs.

A magnified view of the surface in direct proximity to the edge can be seen in Figure 5.17(b). Interestingly the amount of debris redeposition is decreased in this region which is in accordance with the c-AFM measurement in Figure 5.12. One possible explanation for such a particle distribution is shadowing by the melt bulge of the scribe edge screening the surface from debris particles. Debris redeposition on the TCO surface with the offset in accordance with the c-AFM current map can be seen in Figure 5.17(c). Although the coverage is lower than for processing of SnO₂:F in Figure 5.16(b).

The same bulging of the scribe edge can be seen for processing with 1064 nm. Whereas, there is a very steep edge observed for processing with 355 nm (compare topography plotted in Figure 5.13). The absence of any bulging at the edge could explain why there is no spatial offset in current flow measured for processing with 355 nm.

For non-ideal parameters, investigations by SEM of the surface morphology showed an even higher amount of debris redeposition with a spatial extent that was in agreement with the LBIC measurements. The surface coverage was very high and is shown in Figure 5.18 in a magnified view for comparison to the optimized parameters. All images were taken on the TCO surface in the direct vicinity of the P1 scribe. There are no large differences of debris

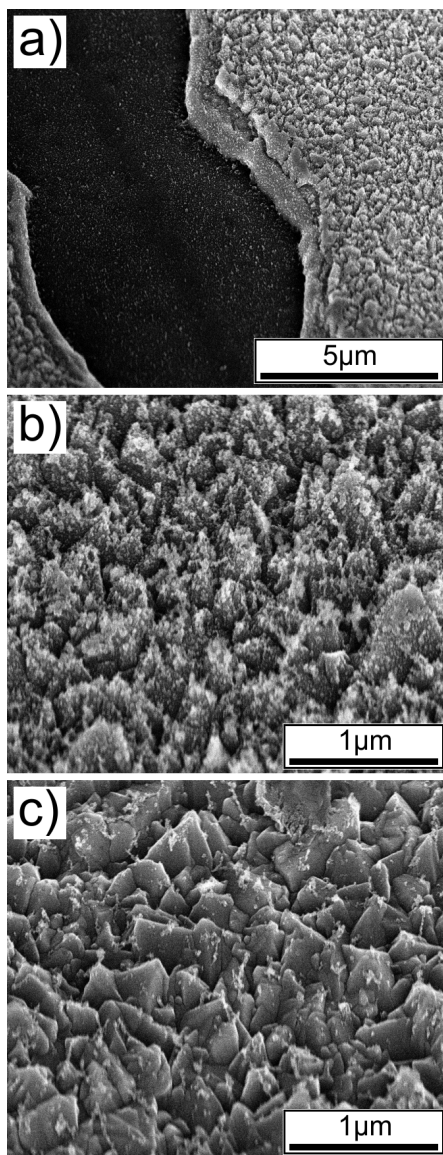


Figure 5.16: Scanning Electron Microscopy images of SnO₂:F TCO processed with 532 nm and optimized parameters at different distances from the scribe edge. Views are: a) Within scribe. b) Surface close to the scribe edge. c) Surface approx. 200 μm off scribe edge.

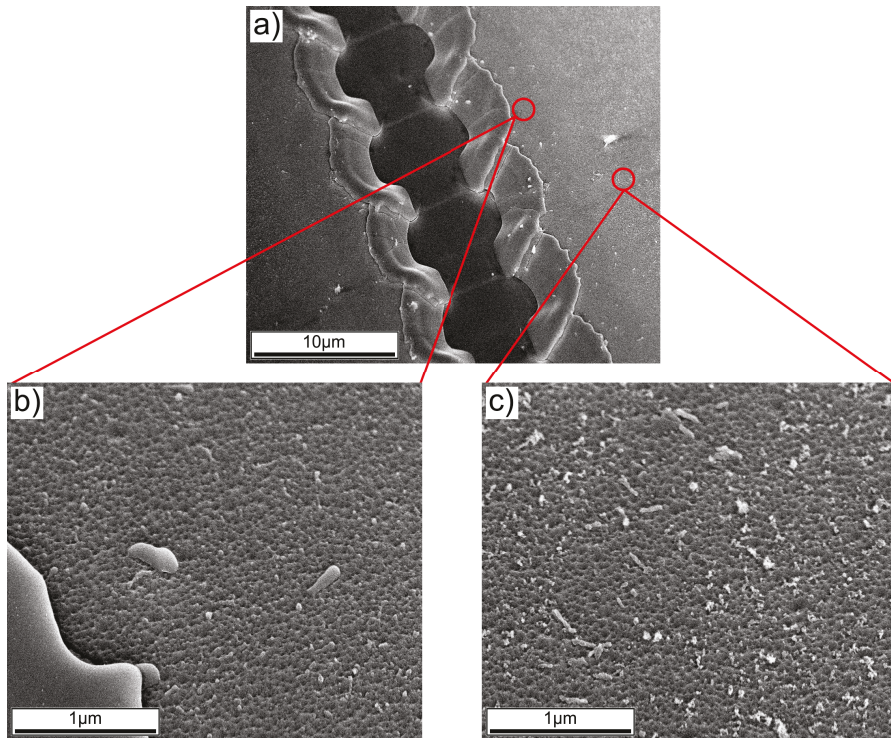


Figure 5.17: Scanning Electron Microscopy images of ZnO:Al TCO processed with 532 nm and optimized parameters at different distances from the scribe edge. Views are: a) Overview of scribe line. b) Surface at the direct scribe edge. c) Surface approx. 10 μm off scribe edge.

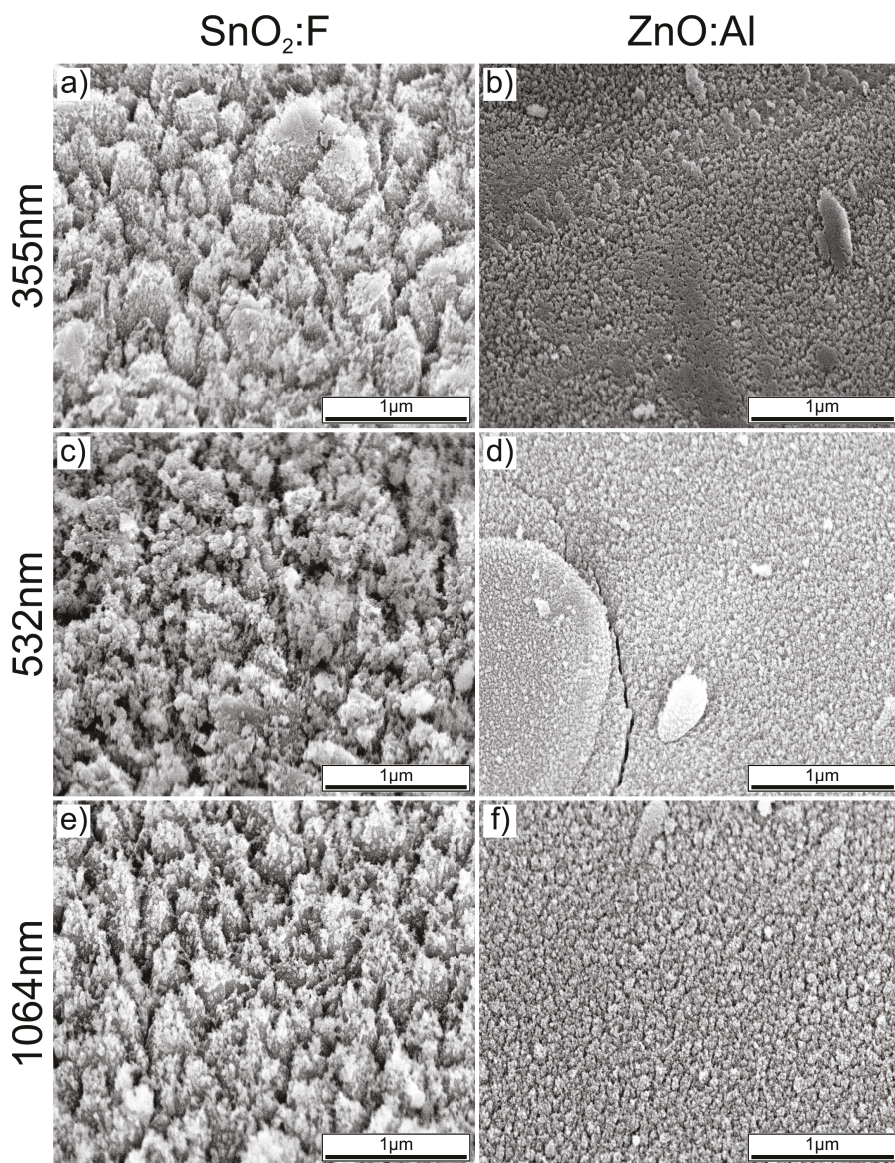


Figure 5.18: SEM images of non-ideal parameter set for $\text{ZnO}:\text{Al}$ and $\text{SnO}_2:\text{F}$ Compilation shows the TCO surface in direct vicinity of the scribe edge. Left column ($\text{SnO}_2:\text{F}$): a) 355 nm. c) 532 nm. e) 1064 nm. Right column ($\text{ZnO}:\text{Al}$): b) 355 nm. d) 532 nm. f) 1064 nm.

coverage or particle size observed between the different processing wavelengths for SnO₂:F material. In general, the redeposition is quite strong. In contrast, due to the flat surface of as-sputtered ZnO:Al the debris particles built an almost continuous layer covering the whole surface (right row in Figure 5.18). Especially for processing with 355 nm in Figure 5.18(b) the sample surface after processing is rather flat (Δ_{RMS} from AFM between 9–18 nm for ZnO:Al and 45–49 nm for SnO₂:F). Therefore, it is possible that absence of current flow (c-AFM) is not owed to geometry effects by debris redeposition. It is more likely that the region near the scribe edge shows an increased series resistance owed to non-conducting debris redeposition, thermal material changes of the whole layer beneath, or both.

To investigate the reasons for deterioration further investigations of all measurements were repeated with a wet-chemical surface treatment after processing. It is important to clarify whether redeposition of debris on the surface or material changes throughout the whole TCO layer are responsible for deterioration measured by c-AFM and LBIC.

5.4.1 Post-scribe cleaning

Both material systems were characterized with and without subsequent wet-chemical cleaning or etching treatment after laser processing. For optimal light in-coupling and light trapping a rather rough surface texture between front-contact and absorber is required. Sputtered ZnO:Al TCO material exhibits a flat surface after deposition. It is usually etched for 30–40 s in 0.5% HCl solution to create the desired texture. Here, to distinguish between surface dominated effects and changes within the whole layer, P1 experiments on ZnO:Al TCO were done with only 10 s etching. Profile measurements of the topography revealed that a 10 s etching step decreases the initial thickness of 800 nm by approx. 100 nm. However, optical properties can already be modified by the developing texture [10]. Fluorine-doped tin dioxide (SnO₂:F) TCO material created by Chemical Vapor Deposition (CVD) exhibits a rough surface texture so that no etching is required. Instead, SnO₂:F was treated with the commercial cleaning agent DeContam™ in solution with deionized water. The substrate was then treated in an ultrasonic bath for 3 hours at 60–70°C before it was dried with nitrogen.

Electrical properties: the c-AFM measurements were repeated on ZnO:Al and SnO₂:F samples with wet-chemical treatment to investigate the influence of the surface residuals. Figure 5.19 shows topography and current maps for both treatment methods exemplary for 532 nm processing and optimized parameters. There is no current flow reduction or gradient apparent perpendicular to the scribe line. Furthermore, for every other parameter set no reduction of the current flow was observed. Even for non-ideal parameters, where no current flow was detected at all before the treatment, no reduction was observed. Some geometry artifacts are still observed especially at the direct scribe edge. High slopes and steep changes of the AFM tip height set point lead to deviations at these points. LBIC measurements were also repeated to see if a recovery of the solar cell properties is observed as well.

Local solar cell properties: LBIC line scans across a P1 scribe of an a-Si:H solar cell on SnO₂:F with wet-chemical treatment prior to cell deposition are shown in Figure 5.20. A

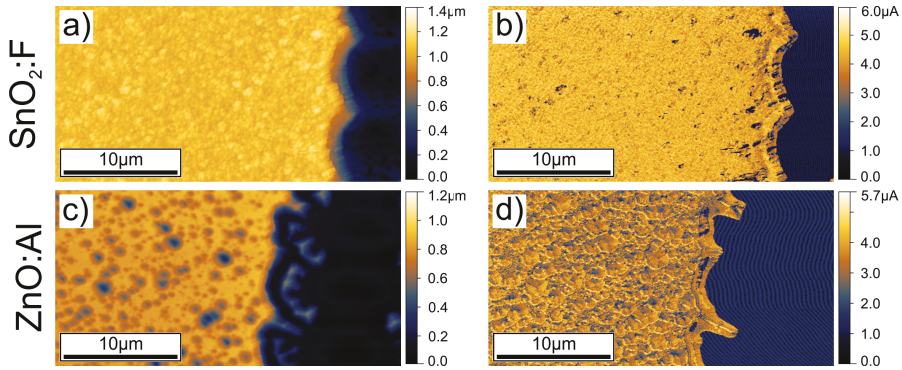


Figure 5.19: Conductive Atomic Force Microscopy measurements of ZnO:Al and SnO₂:F TCO material processed with 532 nm and optimized parameters with a subsequent wet-chemical surface treatment. Plots shown in: a) Topography (SnO₂:F). b) Current map (SnO₂:F). c) Topography (ZnO:Al). d) Current map (ZnO:Al).

steep change of the current generation near the scribe edge lead to conclude that no cell deterioration from the laser processing is present, for all parameters, non-ideal as well as optimized. The only difference of the lateral width where the current begins to decrease is attributed to the different scribe widths. The same results were obtained for the $\mu\text{c-Si:H}$ solar cells on ZnO:Al with the 10 s etching treatment in 0.5% HCl solution before cell deposition. The LBIC measurements for these wavelength/parameters combinations are plotted in Figure 5.21. Just like for processing of SnO₂:F no changes of the current generation is observed up to the scribe edge. Both, optimized and non-ideal parameters show no differences. The measured curves are not as constant or smooth as the curves from Figure 5.20. The developing surface texture by the etching step is responsible for such behavior. The texture feature sizes are in the same range as the measurement laser beam spot size. The current shift of both curves for processing with 355 nm is attributed to the fact that both these parameters had to be measured in another solar cell.

Surface morphology: for both post-treatment processes SEM images indicate the complete removal of the surface residuals. Figure 5.22 shows two images of SnO₂:F processing with 532 nm and wet-chemical post-treatment. The cleaning process is capable of complete removal of redeposited ablation material from the sample surface. Furthermore, in fact there is a region with a heat-affected zone close to the scribe edge. It is indicated by the lack of texture of the material due to melting and resolidification. The c-AFM measurement shows no lowered current flow in the corresponding region (see Figure 5.19). There is no reason to expect strong deterioration of the electrical material properties due to melting. The same results were observed for the melted scribe edge region of SnO₂:F processed with 1064 nm and non-ideal parameters (not shown). At least SnO₂:F TCO material is insensitive against sub-threshold energy intake at the direct scribe edge and strong deterioration of the TCO due to melting is unlikely.

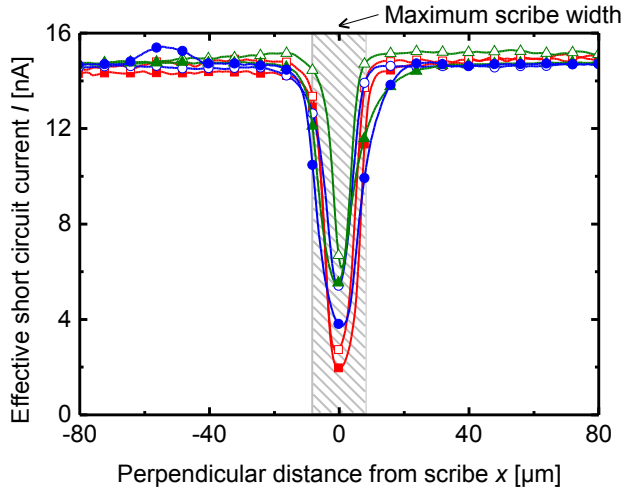


Figure 5.20: Laser Beam Induced Current line scans across the P1 laser scribe of an amorphous silicon (a-Si:H) solar cell on $\text{SnO}_2\text{:F}$ TCO material processed with various laser wavelengths and optimized (empty symbols) and non-ideal (filled symbols) laser parameters with subsequent wet-chemical treatment after laser processing. Different symbols correspond to processing with 355 nm (circles), 532 nm (triangles), and 1064 nm (squares). The shaded area represents the maximum physical scribe width.

The post-treatment indicates that the observed material modifications originate from redeposited ablation debris. There are no signs for changes of the electrical properties throughout the whole layer by the formation of heat-affected zones. The differences of debris redeposition for processing with 532 nm and 1064 nm compared to 355 nm can be explained by the individual dominant ablation mechanism.

As it was found out in Section 5.1 and Section 5.2 for processing with 355 nm, ablation is dominated by stress-induced removal mechanisms. In contrast, there is a transition to classical thermal ablation mechanisms for 532 nm and 1064 nm. In the latter case the TCO material undergoes steps of an almost purely thermally driven process: heating, melting, and evaporation. During plasma plume expansion, ejected material will predominantly be in the liquid and gaseous phase. The processing with 355 nm will lead to ejection of large mostly solid intact clusters of TCO material.

The spatial evolution of laser produced plasma (LPP), particle velocities, size distribution, and the capability of the particle suction system to remove these particles are quite different for both ablation mechanisms. Changes of the spatial particle distribution could explain the differences observed between the different processing wavelengths. For the non-ideal parameter set a shift from mechanically-assisted ablation for 355 nm processing to a dominantly thermal ablation behavior could explain the extent of deterioration. In this regime, deterioration was not very different to 532 nm and 1064 nm processing (cf. Figure 5.14).

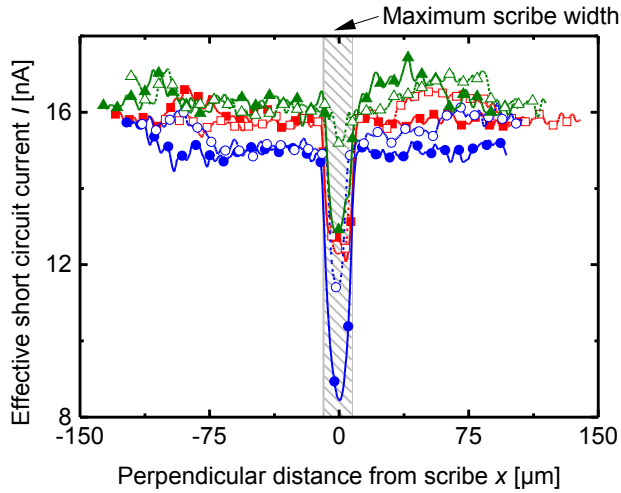


Figure 5.21: Laser Beam Induced Current line scans across the P1 laser scribe of an microcrystalline silicon ($\mu\text{c-Si:H}$) solar cell on ZnO:Al TCO material processed with various laser wavelengths and optimized (empty symbols) and non-ideal (filled symbols) laser parameters with subsequent 10 s etching in 0.5% HCl solution after laser processing. Different symbols correspond to processing with 355 nm (circles), 532 nm (triangles), and 1064 nm (squares). The shaded area represents the maximum physical scribe width.

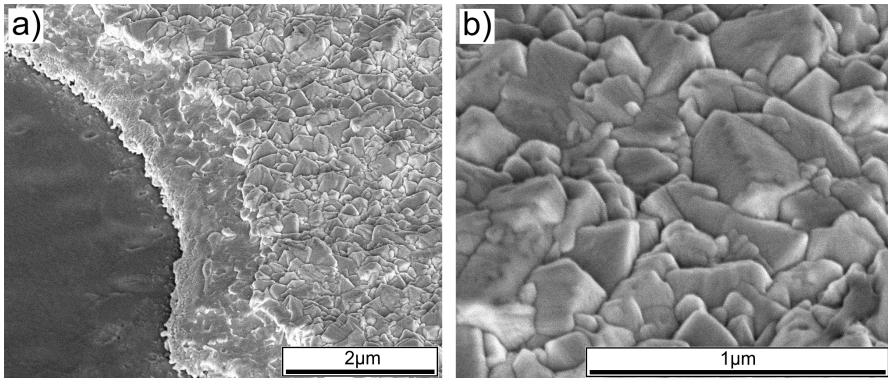


Figure 5.22: Scanning Electron Microscopy images near the scribe edge of $\text{SnO}_2\text{:F}$ TCO processed with 532 nm and optimized parameters after wet-chemical cleaning process. Views are: a) Close to the scribe edge. b) Surface near the scribe edge. The absence of texture at the very edge of the scribe indicates melting and resolidification of the TCO.

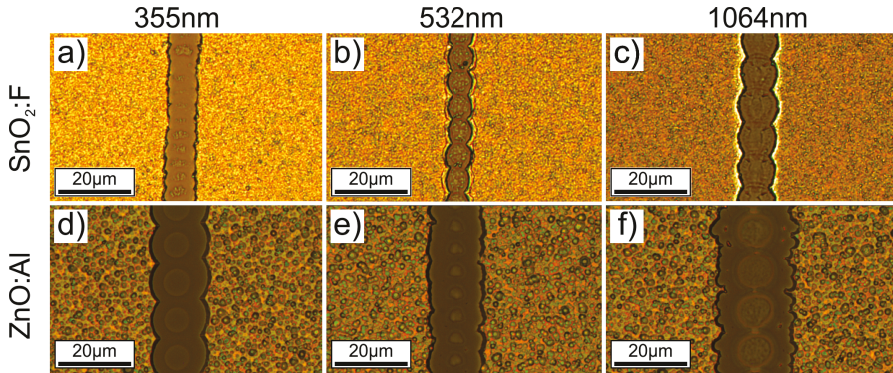


Figure 5.23: Optical microscope images of achieved minimal P1 scribe widths for substrate side scribing of ZnO:Al and SnO₂:F TCO material. Post-treatment parameters: 40 s etching in 0.5% HCl solution for ZnO:Al and wet-chemical cleaning for SnO₂:F. Processing parameters: a) $F_p=0.70 \text{ Jcm}^{-2}$. b) $F_p=2.44 \text{ Jcm}^{-2}$. c) $F_p=10.20 \text{ Jcm}^{-2}$. d) $F_p=0.64 \text{ Jcm}^{-2}$. e) $F_p=8.0 \text{ Jcm}^{-2}$. f) $F_p=11.60 \text{ Jcm}^{-2}$.

Processing with larger beam spot sizes (standard setup) showed that increase of redeposition in vicinity to the scribes is more pronounced for smaller beam spot sizes. It is possible that the shape of the ablation plume distribution is influenced by the laser beam spot size. A change of the plasma plume depending on the beam spot size could explain the increased redeposition in adjacency to the scribe. In literature, modeling of Pulsed Laser Deposition (PLD) indicates that highly focused laser beams exhibit to a strong angular spread of the particle plume [120]. A high angular spread leads to an almost spherical evolution of ablated material [121, 122]. Hence, the trajectories of the ablation debris for processing with 532 nm and 1064 nm can be described by PLD geometry behavior. For processing with 355 nm due to the particles large size, which are mostly in the solid phase, redeposition and the extent of material influence is less pronounced.

Optimized scribes with post-treatment: a compilation of optical microscope images with optimized P1 scribe lines, this time obtained with wet-chemical post-treatment, is shown in Figure 5.23. For processing parameters from Figure 5.7 were used. The post-treatment consisted of 40 s etching for ZnO:Al and wet-chemical cleaning for SnO₂:F. Generally, due to etching, processing of ZnO:Al TCO will produce smooth scribe edges and a clean surface within the scribe. A clean surface is beneficial for the proper electrical separation of neighboring TCO cell stripes. However, etching will increase the scribe width as well. For substrates with SnO₂:F TCO material cleaning is intended instead of etching. After wet-chemical treatment high electrical insulation values (>1 MΩ), between individual stripes of TCO material, are achieved for both materials and all processing wavelengths.

The next section is dedicated to the electrical properties of the optimized scribe lines in terms of insulation capabilities after laser processing and deposition of the solar cell absorber layers.

5.5 Impact on electrical properties

In Section 2.2.2 it was indicated that the dead area and Ohmic front-contact module losses can be extended by losses introduced due to the non-ideal properties of the patterning scribes (shunts for P1/P3, series resistance for P2). Losses due to the front-contact structuring P1 will be defined and impact of scribe width reduction on the solar module performance will be evaluated.

The electrical insulation of two neighboring stripes of front-contact is the main purpose of P1. However, after absorber deposition silicon material is deposited into the scribe line leading to a parasitic conductivity. In a macroscopic view the parasitic conductivity acts as an electrical shunt or parallel resistance to the individual cell stripes. Additional parasitic components lower the overall output power of the module.

Module losses due to P1 processes: Haas [45] showed how the model by Gupta [43] can be extended by an additional loss fraction f_{P1} that describes the shunting losses due to the front-contact insulation process P1. From the work in Ref. [45] the fraction f_{P1} is defined by Equation 5.4 that sets the power lost by shunting P_{P1} in relation with the power generated if no shunting would be present P_{max} .

$$f_{P1} = \frac{P_{P1}}{P_{max}} = \frac{V_{MPP}}{J_{MPP}} \frac{1}{R'_{P1} w_a} \quad (5.4)$$

Here, V_{MPP} and J_{MPP} are voltage and current density in the maximum power point. The specific shunt resistance $R'_{P1} = R_{P1} l$ is defined by the shunt resistance R_{P1} and the length l perpendicular to the interconnection. The shunting losses fraction f_{P1} decreases with increasing active cell stripe width w_a as well as with increasing specific resistance R'_{P1} . Figure 5.24 shows sample calculations of overall module losses plotted as a function of the active cell stripe width. The contribution of shunting to the losses was parameterized over the specific shunting resistance R'_{P1} . For values of R'_{P1} below 50 kΩcm the impact on the overall loss fraction f can increase significantly. The optimal cell stripe width $w_{a,opt}$ (active cell width at minimum of f) shifts towards higher values due to the steep gradient of the f_{P1} loss fraction. The particular evaluation of the losses can be done if the value of R'_{P1} is known for the specific process/topology.

Parasitic shunt resistance: if constant material properties of the deposited absorber are assumed perpendicular to the scribe, a value of R'_{P1} proportional to the scribe width w_{P1} is expected. The following equation can be defined,

$$R'_{P1} = K w_{P1}. \quad (5.5)$$

The specific shunt resistance R'_{P1} can be described by the width w_{P1} and a slope factor K .

The relation defined in Equation 5.5 is disadvantageous for the optimization of P1. A decrease of w_{P1} would result in a decrease of R'_{P1} and therefore increase the shunting loss fraction f_{P1} . It is from utter importance to get insight into the value range of possible shunting to

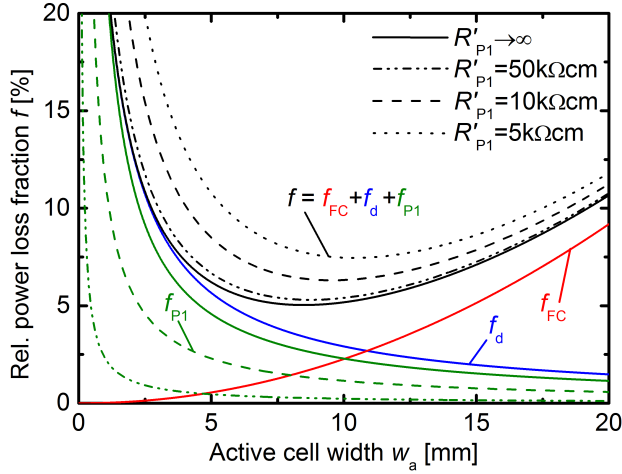


Figure 5.24: Calculated tandem solar module loss fractions due to the integrated series connection plotted against the active cell stripe width w_a and parameterized over different shunting resistances R'_{P1} of 50 k Ω cm, 10 k Ω cm, 5 k Ω cm, and if no shunting is present. Tandem solar cell input parameters are: $J_{MPP}=9.7$ mA/cm², $V_{MPP}=1.11$ V, $R_{SH}=8$ Ω , and $w_d=300$ μ m.

avoid geometrically optimized P1 scribes that cause shunting of the solar module. A contrary behavior between gain of active area vs. stronger shunting is counterproductive for the optimization pursuit.

For the evaluation of the value range of R'_{P1} that can be expected for typical solar cell topologies an experimental series with different layer-stack configurations of amorphous silicon (a-Si:H) deposited on ZnO:Al were characterized.

The topology of a-Si:H on ZnO:Al was chosen as a model system or worst-case scenario in terms of shunting. Worst-case means that a high parasitic conductivity within the P1 scribe is expected for a-Si:H or a-Si:H/ μ c-Si:H tandem solar modules in superstrate configuration on ZnO:Al TCO material. It is a common approach to deposit highly conductive p-doped μ c-Si:H layers as contact layers. This improves the electrical interface properties between the ZnO:Al TCO and the a-Si:H p-layer [123]. It is believed that a highly conductive contact layer at the front-contact interface dominates the parasitic conductivity within the P1 scribe with respect to the other subsequent layers [124].

Shunting behavior: a special test-structure was used to characterize shunting by the absorber deposited within the P1 scribe without complete processing of a solar module. Figure 5.25 shows two sketches of the device setup and the measurement setup used for evaluation. The sample is mounted into a vacuum chamber allowing pressures down to 10^{-6} mbar with the option for annealing (typ. 160 $^{\circ}$ C, 30 min) to remove any residuals from the sample surface. It is possible to illuminate the sample for the evaluation of the photo conductivity. The shunt resistance is then calculated from the $I - V$ characteristics measured from -100 V to 100 V

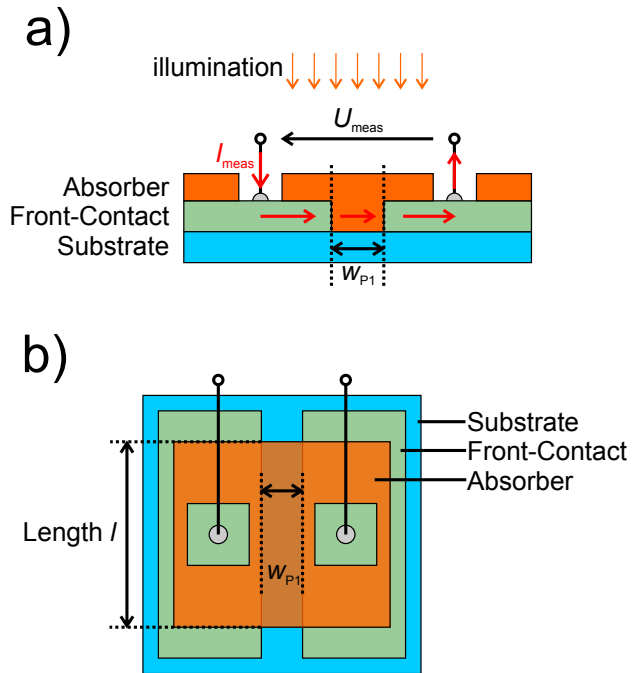


Figure 5.25: Schematic sketch of the test-structure used for the evaluation of the residual conductivity of the P1 scribe after structuring and subsequent absorber deposition. Views show: a) Current flow is measured between the two stripes of front-contact material with the length l . b) Insulation is provided around the structure forcing the current flow through the absorber material within the scribe. A simple two test lead $I - V$ measurement is used.

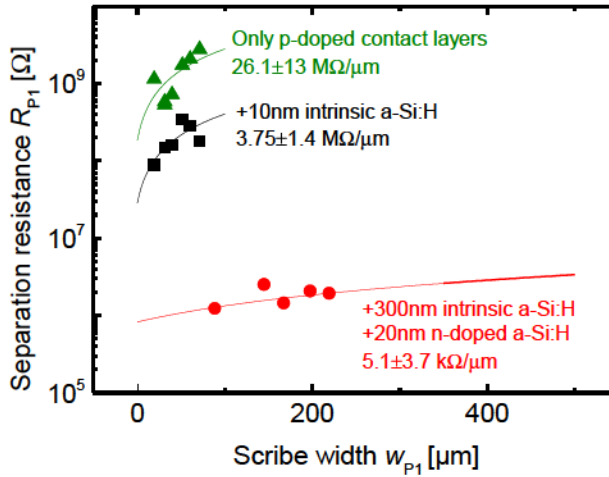


Figure 5.26: Residual P1 scribe resistance plotted against the scribe width w_{p1} for different absorber layer-stack configurations on ZnO:Al TCO material. Green triangles: Only μ c-Si:H contact layer and p-doped layer deposited. Black squares: additionally 10 nm intrinsic a-Si:H deposited. Red circles: full a-Si:H p-i-n solar cell deposition. The test-structure length was 8 mm and the solid lines represent linear regression with the extracted slope parameters.

with a Keithley 617 Electrometer. Due to the high resistivity of the samples a simple two leads measurement setup is used. Contact resistances between lead and front-contact will not create any significant voltage drop in range of the measured current flows.

The experimental series were done for one absorber layer topology measured for different scribe widths w_{p1} . Since for the determination of the slope K in Equation 5.5 it is not necessary to process minimal scribe widths the standard reference P1 process was used. Multiple overlapping scribes were processed to achieve a varying overall width w_{p1} . The single scribe width was approx. 40 μ m and six overlapping lines were processed for the maximal effective scribe width.

Influence of the layer-stack: in a first set of experiments three different layer-stack configurations were evaluated. One layer-stack consisted of p-doped contact layers and a-Si:H p-layer. In the second configuration an additional 10 nm intrinsic a-Si:H layer was deposited. For the third layer-stack the additional intrinsic a-Si:H layer was 300 nm thick. An additional a-Si:H n-layer was deposited as well. The last configuration was equivalent with a standard p-i-n a-Si:H solar cell on ZnO:Al TCO.

Figure 5.26 shows the separation resistance R_{p1} for different layer-stack topologies on etched P1 scribe lines plotted against the scribe width w_{p1} . All samples were measured under vacuum conditions (approx. 10^{-6} mbar), under illumination, and after annealing with 160°C for 30 min. In general, a purely linear Ohmic behavior between voltage and current flow is not observed.

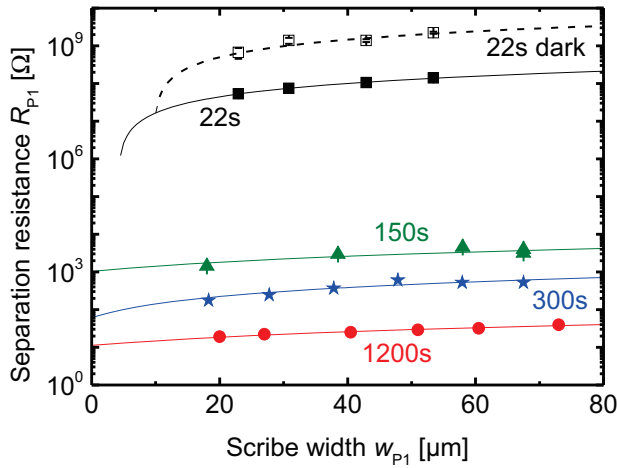


Figure 5.27: Residual P1 scribe resistance plotted against the scribe width w_{P1} for different $\mu\text{-Si:H}$ contact layer thicknesses plus 100 nm intrinsic a-Si:H on ZnO:Al TCO material. Measurement conditions: ambient atmosphere, no thermal annealing, and (no) illumination for 22 s deposition time while ambient illumination for the rest. Four point Kelvin-Probe measurements were used for higher conducting samples. The test-structure length was 8 mm and the solid lines represent linear regressions.

Hence, the separation resistance R_{P1} is not constant and is evaluated by a rough estimation with the average of the whole $I - V$ relation.

The large deviations of R_{P1} are also reflected in the plot as a function of the scribe width w_{P1} . Ideally, a linear relation between R_{P1} and w_{P1} is expected (cf. Equation 5.5) but is not observed.

However, it can also be seen that solely considering the p-doped contact layers as the crucial layers determining the parasitic conductivity is not sufficient. The whole layers stack is of importance for evaluation. The values for the measurement of the p-i-n a-Si:H solar cell layer-stack are almost three orders of magnitude lower than just the contact layers. Especially the intrinsic layer has a huge impact on the conductivity under illumination (compare 10 nm with 300 nm).

Overall, the resistance values are high for all three configurations even considering the large deviations of the slope. The rather small slope for the sample with the whole layer-stack deposited is compensated by an offset of almost $1\text{ M}\Omega$. Offsets were also observed for the other configurations as well. It is not clear where these offsets originate from. In theory, the extrapolation to zero scribe width should yield a low shunting resistance only affected by the contacts resistance.

The p-doped $\mu\text{-Si:H}$ contact layers: in a second set of experiments the contact layer thickness was varied. An intrinsic a-Si:H layer was deposited subsequently with a constant thickness of 100 nm. Figure 5.27 shows these results. Due to the higher conductivity of the samples with

higher contact layer deposition times (150 s, 300 s, and 1200 s) an Electrometer could not be used. A four point Kelvin-Probe measurement with a SourceMeter was done instead under ambient light. For better comparison both illuminated and dark resistance values are plotted for the low conductivity sample characterized with the standard Electrometer measurement setup.

With increasing deposition time the parasitic conductivity within the scribe increases over many orders of magnitude. Due to the non-linear behavior small changes of the layer thickness can lead to strong shunting of the solar module even for standard P1 scribes. These results show how crucial knowledge about the parasitic conductivity is. It is possible that depending on the solar module topology narrower P1 scribe lines could increase shunting significantly. For instance, $\mu\text{c-Si:H}$ single junction solar modules in superstrate configuration or tandem solar modules in substrate configuration both feature highly conductive $\mu\text{c-Si:H}$ layers. These layers also exhibit a higher thickness compared to the contact layers for a-Si:H on ZnO:Al [125]. For other technologies like CIGS, due to the high parasitic conductivities, ideal P1 scribe widths up to 300 μm are calculated [126].

To motivate the approach of scribe width optimization, with regards to shunting losses due to w_{P1} reduction, a worst-case calculation was carried out with the results from Figure 5.26. The slope for the whole p-i-n layer-stack was used without the offset. For consistency the module losses were calculated for the example tandem solar cell parameters (cf. Section 2.2.2).

The value K from Equation 5.5 was replaced with a slope of 5.1 $\text{k}\Omega/\mu\text{m}$ multiplied with the length $l=8$ mm. Finally, Equation 5.4 can be rewritten to,

$$f_{P1} = \frac{V_{MPP}}{J_{MPP}} \frac{1}{K w_{P1} w_a} \quad \text{with,} \quad R'_{P1} = K w_{P1}. \quad (5.6)$$

Furthermore, the constant reference dead area fraction of 300 μm needs to be split into a constant value of $w_{d, \text{const}}=250$ μm (for P2, P3, and the spacing in between) and the parameter of the P1 scribe width w_{P1} . Figure 5.28 shows the results for the calculation of a tandem solar module with the P1 shunting losses parametrized for different scribe widths w_{P1} . The predicted reduction of the overall losses is rather small. This is not surprising since the potential of reduction from a reference value of 50 μm down to 5 μm does not weigh too much into the whole dead area width. The overall width is only reduced from 300 μm to 255 μm . Both subsequent scribe line widths for P2 (90 μm) and P3 (100 μm) have a much higher potential for reduction as it will be shown further on.

A comparison of f_d and f_{P1} shows that in the case of a P1 scribe line with a width of 5 μm (dashed lines in Figure 5.28) the increased shunting outweighs the increase of active area. Actually, the overall losses would be increased. The minimal overall losses are achieved for a P1 scribe width between 10 μm and 20 μm .

Of course these sample calculations serve as an example to show how such an optimization of P1 shunting losses with experimental values could look like. A separate evaluation needs to be done for each individual system. For instance, experimental solar module implementations

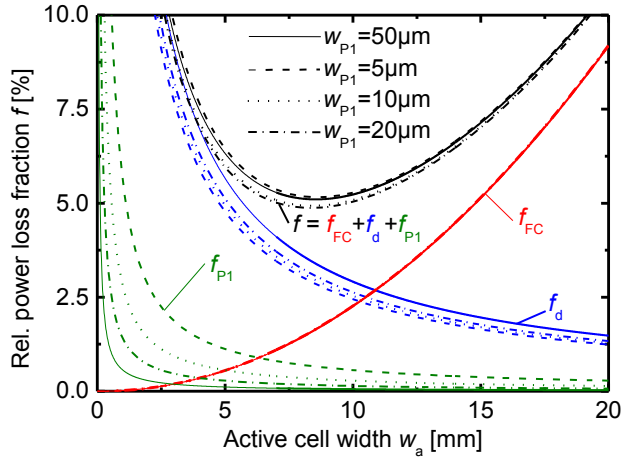


Figure 5.28: Calculated tandem solar module loss fractions due to the integrated series connection plotted against the active cell stripe width w_a and parametrized for different P1 scribe widths w_{p1} of 5 μm , 10 μm , 20 μm , and reference value of 50 μm . The constant part of the interconnection width is set to $w_{d,\text{const}}=250 \mu\text{m}$. Tandem solar cell input parameters are: $J_{\text{MPP}}=9.7 \text{ mA/cm}^2$, $V_{\text{MPP}}=1.11 \text{ V}$, $R_{\text{SH}}=8 \Omega$, and $K=5.1 \text{ k}\Omega/\mu\text{m}$ multiplied by 8 mm.

of optimized P1 scribe lines with a width below 10 μm in tandem solar modules on $\text{SnO}_2:\text{F}$ showed no impact on the shunting or the fill-factor of the module. Most likely due to absence of highly conductive $\mu\text{c-Si:H}$ p-doped contact layers in this topology. In the following the results of these implementations are shown.

5.6 Process implementation in solar mini modules

Solar modules with optimized P1 scribe lines were prepared. Optimized P1 scribes processed with 532 nm and increased focusing were used for evaluation of module performances of a-Si:H/ $\mu\text{c-Si:H}$ modules on $\text{SnO}_2:\text{F}$ front-contact material. Mini modules with an aperture area of $A_{\text{cell}}=8 \text{ cm}^2$, $A_{\text{module}}=64 \text{ cm}^2$ were processed. For P1, scribe lines with the lowest achievable width (see Figure 5.23(b)) alternating with standard scribes ($w_{p1}=40 \mu\text{m}$) were created. Figure 5.29 shows two optical microscope images of the whole interconnection region (Figure 5.29(a)) and magnified P1 scribe line (Figure 5.29(b)). Compared to the scribes from the processes P2 and P3 the width of the front-contact insulation is significantly smaller. Furthermore, spacing between the individual lines was changing due to machine limitations. Therefore, it is not possible to observe any increase of the short-circuit current density for the optimized approach. However, $I-V$ characteristics of the individual cell stripes shown in Table 5.6 exhibit no negative impact by shunting. In median, no differences in the fill-factor (71%–72%) of the individual cell stripes are found between optimized and standard processing parameters. The results encourage the implementation of optimized scribe lines. Not only

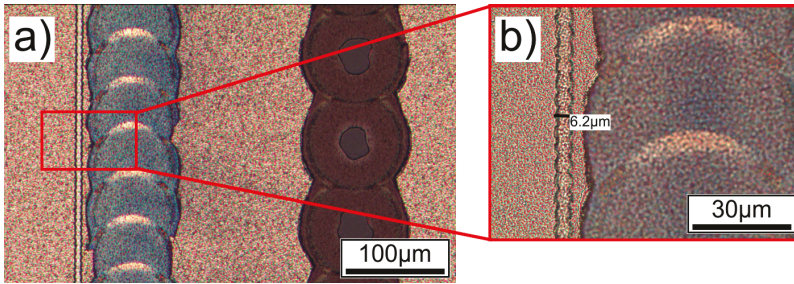


Figure 5.29: Optical microscope images of the interconnection region for an a-Si:H/ μ c-Si:H tandem solar module on SnO₂:F with optimized P1 scribe lines. For P1 processing a wavelength of 532 nm with a laser beam spot radius of 10.5 μ m and a peak fluence of $F_p=2.44$ Jcm⁻² was used. Standard reference parameters were used for P2 and P3 processing.

Table 5.6: AM1.5 $I - V$ characteristics of individual cell stripes of an a-Si:H/ μ c-Si:H tandem solar module on SnO₂:F with optimized P1 scribe lines alternating with standard interconnection processing. For the optimized P1 process a wavelengths of 532 nm with a laser beam spot radius of 10.5 μ m and a peak fluence of $F_p=2.44$ Jcm⁻² was used. For standard processing a wavelength of 355 nm, 19.3 μ m, and $F_p=1.72$ Jcm⁻² was used. In both cases standard interconnection parameters were used for P2 and P3 processing.

Cell stripe number	P1 scribe	Efficiency η	Fill-Factor FF	Open-circuit voltage V_{OC}	Short-circuit current I_{SC}
1	Standard	10.9%	71.1%	1.376 V	88.9 mA
2	Optimized	6.8%	48.1%	1.313 V	86.3 mA
3	Standard	10.9%	71.8%	1.369 V	88.8 mA
4	Optimized	10.7%	71.0%	1.372 V	88.1 mA
5	Standard	11.0%	72.0%	1.373 V	88.6 mA
6	Optimized	10.9%	72.2%	1.374 V	87.5 mA
7	Standard	11.0%	72.6%	1.375 V	87.9 mA
8	Optimized	10.9%	72.7%	1.375 V	87.1 mA

Chapter 5. Front-contact structuring process P1

because of their good electrical properties and potential reduction of the overall module losses, but also because all processing (P1–P3) could be done with 532 nm.

In the upcoming chapter the optimization process is extended for the absorber ablation process P2.

6 Absorber removal process P2

The scribe width optimization for the absorber removal process P2 is the topic of this chapter. Two different absorber materials, 300 nm thick amorphous silicon (a-Si:H) and 1.4 μm thick a-Si:H/ $\mu\text{c-Si:H}$ absorbers were used for processing. Both types were prepared on $\text{SnO}_2\text{:F}$ TCO material and all processing was done with 532 nm. In both cases the laser pulse energy is first absorbed in the a-Si:H (sub-)cell since illumination was done through the substrate side.

The absorber ablation behavior was investigated in the first part by single crater ablation as a function of the laser beam spot size and pulse energy. Subsequently, optimized scribe lines were generated.

The characterization of the driving ablation mechanisms by collection of debris during processing is the topic of the second part. Here also modeling of the laser ablation process was carried out to get insight into the spatial and temporal temperature distribution during processing.

Afterwards, impact on the electrical properties of the solar module was measured. For this, evaluation of the series resistance that is formed at the P2 scribe after back-contact deposition was determined. A special test procedure by the Transmission Line Method (TLM) was used for a precise characterization.

Lastly, an extension of the Gupta model, to account for series resistance losses, was applied to predict possible impact on the module efficiency for optimized P2 scribe lines.

6.1 Material ablation behavior

Before reduction of the scribe width was carried out the single crater ablation of the used material systems for different beam spot radii was evaluated. The influence of the beam spot radius on the ablation of the absorber and undesired ablation of the underlying TCO layer was determined with the previously introduced Liu-Plots (see Section 3.3.2). Knowledge of the single crater ablation properties is helpful to obtain insight on the lower and upper process limits that are relevant for subsequent optimized scribe line processing.

For absorber ablation the silicon material is removed selectively without damaging of the underlying front-contact material. TCO material of $\text{SnO}_2:\text{F}$ exhibits a higher transparency for 532 nm than for 355 nm or 1064 nm. Therefore, a larger process window for absorber removal without TCO damage is expected for this wavelength. Prior experiments with 355 nm and 1064 nm showed that absorber removal of tandem solar cells was not possible without simultaneous TCO ablation/damaging. Especially for processing with small laser beam spot sizes. Hence, process optimization was carried out for scribing with 532 nm due to the large contrast of absorption coefficients between absorber and front-contact [16].

Liu-Plots: single spot ablation of a-Si:H (300 nm) and tandem (1.4 μm) absorber materials on $\text{SnO}_2:\text{F}$ TCO was carried out with different laser beam spot sizes. All ablation was done through the substrate side and the results are shown in Figures 6.1, 6.2, and 6.3. Furthermore, undesired ablation of the underlying TCO layer beneath the tandem absorber is plotted as well. The ablation behavior of the TCO defines a boundary for the laser process where selective ablation of the absorber material is possible. The intercept with the x -axis of each linear

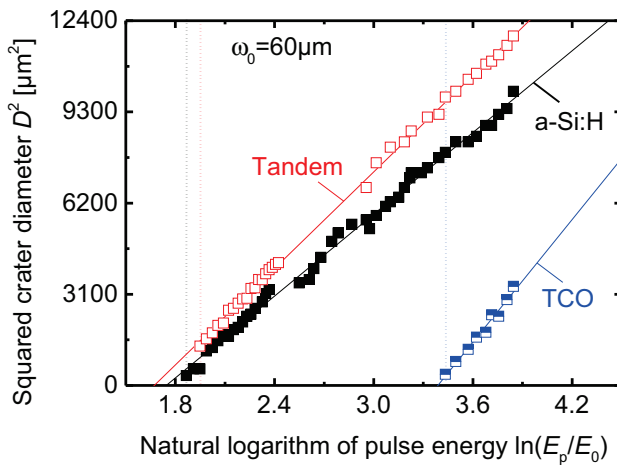


Figure 6.1: Liu-Plot of a-Si:H p-i-n solar cell absorber (filled squares) and tandem material (empty squares) for a laser beam spot radius of 60 μm . Half-filled squares correspond to TCO damage ablation values (for tandem absorber). Dotted lines mark the onset where ablation occurs.

regression will yield the ablation threshold energy E_{th} . For the specific setup this value is a measure for the relation between energy and crater diameter.

However, for absorber processing (from the substrate side) no crater formation is observed near E_{th} and ablation only occurs above a certain threshold which is greater than the extrapolated threshold energy E_{th} . Below this so-called onset pulse energy $E_{\text{p,on}}$ only layer bulging and blistering is observed. The dotted lines in Figures 6.1, 6.2, and 6.3 mark the value of $E_{\text{p,on}}$.

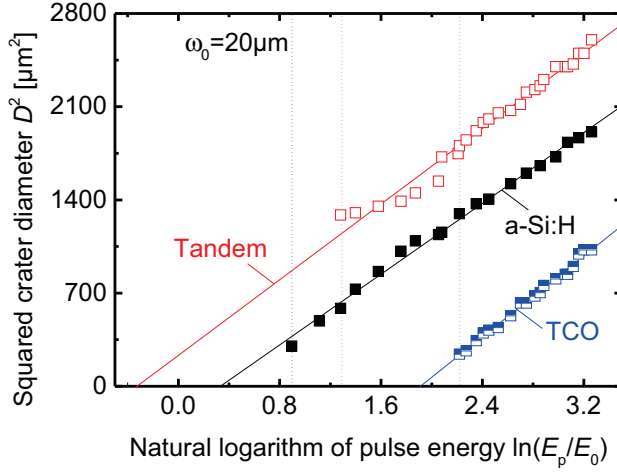


Figure 6.2: Liu-Plot of a-Si:H p-i-n solar cell absorber (filled squares) and tandem material (empty squares) for a laser beam spot radius of $20\ \mu\text{m}$. Half-filled squares correspond to TCO damage ablation values (for tandem absorber). Dotted lines mark the onset where ablation occurs.

Furthermore, the beam spot radius $\omega_{0,\text{Liu}}$ can be evaluated from the line fit slope and can be compared with the measurement from the beam profiler (cf. Section 3.3.2).

Figures 6.1 and 6.2 both show that for all three materials a linear correlation between D^2 and $\ln(E_p/E_0)$ is observed. It is interesting to note that for same pulse energies E_p the squared crater diameter D^2 is always higher for tandem absorber processing than for a-Si:H. One would expect that due to the higher thickness more energy is required to achieve a similar crater diameter.

It is likely that ablation is initiated by delamination at the absorber/TCO interface. Delamination is propagated further in radial direction for the tandem layer than for the thinner a-Si:H absorber due to the higher thickness of the tandem absorber layer. However, the required minimal $E_{p,\text{on}}$ to achieve a proper ablation crater is increased for the higher film thicknesses (see dashed lines in Figures 6.1, 6.2, and 6.3).

Figure 6.3 shows substantial deviations from the linear correlation of $\ln(E_p)$ vs. D^2 observed in both Figures 6.1 and 6.2. For TCO ablation there are two different regimes, due to the change of slope, where the ablation mechanisms probably change [74]. Only tandem absorber processing shows a linear behavior with a slope corresponding to the measured beam spot radius ω_0 .

Onset pulse energy: the interpretation of the onset pulse energy $E_{p,\text{on}}$ gives additional information since no proper ablation can be realized close to E_{th} . To compare the ablation behavior between the three values of ω_0 the onset peak fluence $F_{p,\text{on}}$ was used since it is normalized by

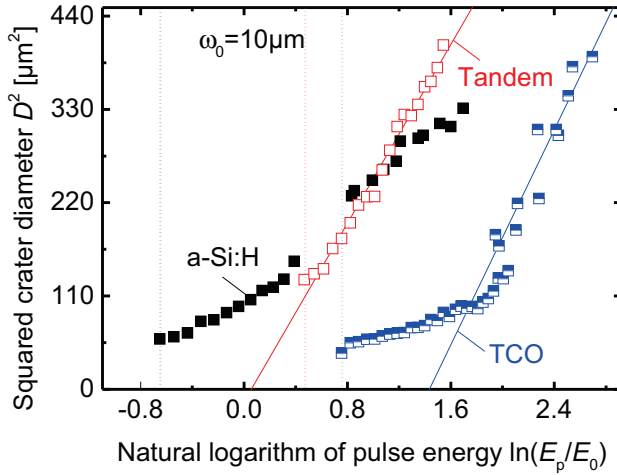


Figure 6.3: Liu-Plot of a-Si:H p-i-n solar cell absorber (filled squares) and tandem material (empty squares) for a laser beam spot radius of $10\ \mu\text{m}$. Half-filled squares correspond to TCO damage ablation values (for tandem absorber). Dotted lines mark the onset where ablation occurs.

the beam spot area ($F_{p,on} = 2E_{p,on}/\pi\omega_0^2$, see Equation 3.10). Table 6.1 shows a comparison of this value. The beam spot radius $\omega_{0,Liu}$ and the threshold fluence F_{th} could not be extracted for every setup due to strong deviations from a linear behavior (cf. Liu-Plot in Figure 6.3). A comparison of the extracted radii shows that most values are below the radii from the beam profile but within the 20% deviation range (cf. Section 3.3.2).

The threshold fluence F_{th} is increased with decreased beam spot radius when a-Si:H is processed. The same behavior is observed for undesired TCO ablation. For tandem absorber processing F_{th} increases strongly when a beam radius of $10\ \mu\text{m}$ is used.

A similar trend is found for the onset pulse fluence $F_{p,on}$ which increases when ω_0 is decreased. However, for amorphous silicon and TCO ablation the values are the highest for processing with $20\ \mu\text{m}$. For the onset fluence of a-Si:H on $\text{SnO}_2:\text{F}$ good agreement was found to values observed by others [72, 99].

A comparison between F_{th} and $F_{p,on}$ is not intended because of the different beam radii that are used for adjustment of the pulse energies. For the onset peak fluence the radius from the beam profiler is used while for F_{th} the extracted radius is chosen. In this way it is possible to evaluate $F_{p,on}$ even when no linear regression of the experimental data from the Liu-Plot is possible.

A possible reason for the decrease of $F_{p,on}$ when $\omega_0=10\ \mu\text{m}$ is used could be the change of ablation behavior (cf. Figure 6.3). The increase of the onset fluence is much more pronounced for tandem layer ablation where $F_{p,on}$ increases from $0.12\ \text{J}/\text{cm}^2$ to $1.02\ \text{J}/\text{cm}^2$.

Table 6.1: Comparison of parameters extracted from Liu-Plots for 300 nm thick a-Si:H absorber layer and 1.4 μm thick tandem absorber on $\text{SnO}_2\text{:F}$ TCO material (refer to Figures 6.1, 6.2, and 6.3). Standard deviation calculated by maximum error estimation by 1st degree Taylor approximation.

Material	Radius ω_0 from profiler	Radius $\omega_{0,\text{Liu}}$ from slope	Threshold fluence F_{th}	Onset peak fluence $F_{\text{p,on}}$
a-Si:H	60 μm	48.2 \pm 0.3 μm	0.16 \pm 0.3 Jcm^{-2}	0.11 Jcm^{-2}
a-Si:H	20 μm	18.2 \pm 0.2 μm	0.27 \pm 0.3 Jcm^{-2}	0.39 Jcm^{-2}
a-Si:H	10 μm	–	–	0.33 Jcm^{-2}
tandem	60 μm	52.3 \pm 0.3 μm	0.12 \pm 0.3 Jcm^{-2}	0.12 Jcm^{-2}
tandem	20 μm	18.8 \pm 0.2 μm	0.13 \pm 0.3 Jcm^{-2}	0.57 Jcm^{-2}
tandem	10 μm	11.5 \pm 0.3 μm	0.51 \pm 0.1 Jcm^{-2}	1.02 Jcm^{-2}
$\text{SnO}_2\text{:F}$	60 μm	58.9 \pm 1.6 μm	0.54 \pm 0.3 Jcm^{-2}	0.55 Jcm^{-2}
$\text{SnO}_2\text{:F}$	20 μm	19.5 \pm 0.2 μm	1.13 \pm 0.3 Jcm^{-2}	1.46 Jcm^{-2}
$\text{SnO}_2\text{:F}$	10 μm	12.6 \pm 0.7 μm	1.69 \pm 0.5 Jcm^{-2}	1.35 Jcm^{-2}

The squared crater diameter that corresponds to processing with the onset peak fluence $F_{\text{p,on}}$ defines an additional constraint on the minimal achievable craters that is different from the limitations of the optical systems. Yet, this lower limit was used as the initial processing parameter for the creation of scribe lines with a reduced width.

6.1.1 Visually optimized scribe lines

Optimized P2 scribe lines were generated using the results from the Liu-Plots. For this, the various onset fluences $F_{\text{p,on}}$ are used as the lower process limit with minimal crater diameter D . For the single spot ablation the maximum feed-rate v of the machine was used to achieve a high separation of the individual ablation craters. Now to create a continuous line v was adjusted accordingly. The pulse energy E_p was then adjusted until a visually optimized scribe line with a minimal scribe width w_{p2} was achieved.

An optimized line is defined by a scribe line created with processing parameters that will lead to minimal signs of bulging at the scribe edges and low TCO damaging inspected by optical microscopy. Figure 6.4 shows optical microscope images of visually optimized scribes for 300 nm a-Si:H absorber processing. A correlation between the used beam spot size $2\omega_0$ (green circles) and the visually optimized scribe width is found. Scribes well-below the laser beam spot sizes are achieved for all three degrees of focusing.

But when comparing the required pulse fluences of $F_p=0.26\text{J/cm}^2$, $F_p=0.62\text{J/cm}^2$, and $F_p=0.48\text{J/cm}^2$ for the spot radii ω_0 of 60 μm , 20 μm , and 10 μm with $F_{\text{p,on}}$ from Table 6.1 they are all shifted towards higher values. This was necessary to stabilize the process against any local change of the material properties and possible pulse-to-pulse variations of the laser source. Clean ablation without bulging at the scribe edge is accomplished for all three values of ω_0 . A scribe width w_{p2} below 10 μm is achieved for scribing with a beam radius $\omega_0=10\mu\text{m}$.

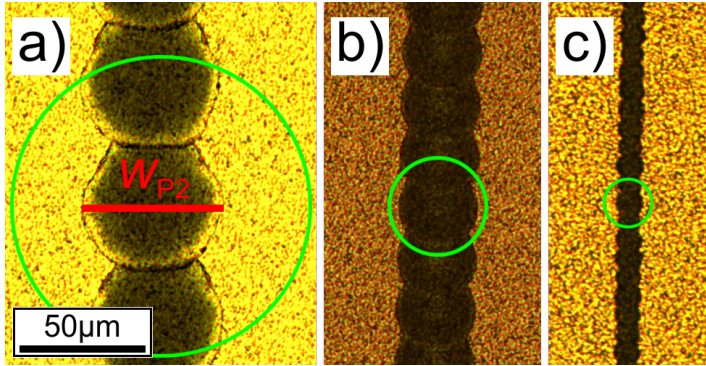


Figure 6.4: Optical microscopy images of P2 scribe width optimization on 300 nm thick a-Si:H p-i-n solar cell material on SnO₂:F TCO. Parameters: a) $\omega_0=60 \mu\text{m}$, $F_p=0.26 \text{Jcm}^{-2}$. b) $\omega_0=20 \mu\text{m}$, $F_p=0.62 \text{Jcm}^{-2}$. c) $\omega_0=10 \mu\text{m}$, $F_p=0.48 \text{Jcm}^{-2}$. An inset of green circles illustrate the laser beam diameter $2\omega_0$ used for processing.

Figure 6.5 shows optical microscope images of the visually optimized processing parameter for scribe width reduction of a 1.4 μm thick tandem absorber. The same processing setup as for a-Si:H ablation was used. These parameter yield a larger scribe width w_{P2} compared to

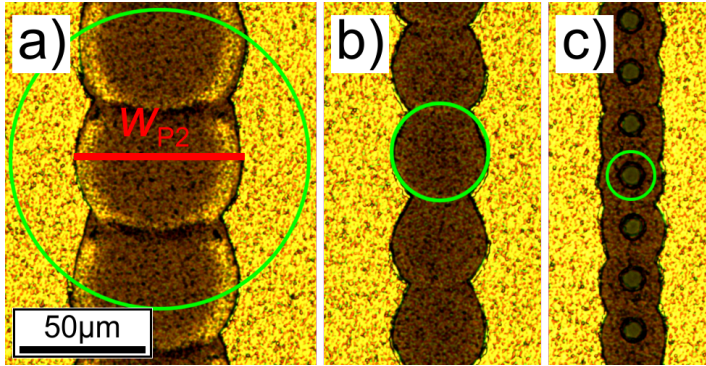


Figure 6.5: Optical microscopy images of P2 scribe width optimization on 1.4 μm thick tandem solar cell material on SnO₂:F TCO. Parameters: a) $\omega_0=60 \mu\text{m}$, $F_p=0.28 \text{Jcm}^{-2}$. b) $\omega_0=20 \mu\text{m}$, $F_p=0.92 \text{Jcm}^{-2}$. c) $\omega_0=10 \mu\text{m}$, $F_p=1.5 \text{Jcm}^{-2}$. An inset of green circles illustrate the laser beam diameter $2\omega_0$ used for processing.

processing of 300 nm a-Si:H material from Figure 6.4. This was already indicated from the ablation behavior characterization (see Figures 6.1, 6.2, and 6.3). There is a deviation between beam diameter reduction and scribe width reduction between b) and c) with no significant additional width reduction. Furthermore, for the smallest beam spot size in c) it is not possible to achieve a proper P2 scribe without partial ablation of the underlying TCO layer. This can be associated with the before mentioned small process window due to the low difference between $F_{p,on}$ for absorber ablation and TCO ablation (see Table 6.1). Due to the pulse overlap it is

possible that this difference is getting even smaller since the TCO layer can be preheated by the previous laser pulses.

Thick tandem absorber: additional experiments on tandem absorber layers with a thickness of $3.5\ \mu\text{m}$ were carried out. This was done to see whether an increase of the lower scribe width limitation is a general behavior depending on the absorber thicknesses. The results confirmed even higher constraints on the minimal achievable scribe width w_{P2} . Just for comparison optical microscope images of optimized scribe lines for the $3.5\ \mu\text{m}$ thick absorber material are shown in Figure 6.6. For this material type, already for processing with $20\ \mu\text{m}$ (Figure 6.6(b)),

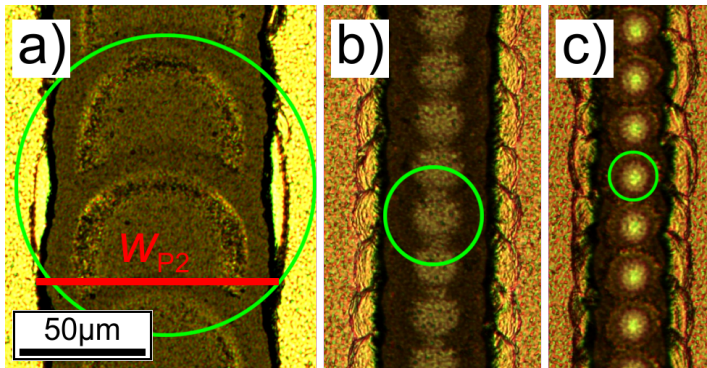


Figure 6.6: Optical microscopy images of P2 scribe width optimization on $3.5\ \mu\text{m}$ thick tandem solar cell material on $\text{SnO}_2:\text{F}$ TCO (type Asahi VU). Parameters: a) $\omega_0=60\ \mu\text{m}$, $F_p=0.46\ \text{Jcm}^{-2}$. b) $\omega_0=20\ \mu\text{m}$, $F_p=1.06\ \text{Jcm}^{-2}$. c) $\omega_0=10\ \mu\text{m}$, $F_p=2.33\ \text{Jcm}^{-2}$. An inset of green circles illustrate the laser beam diameter $2\omega_0$ used for processing.

the scribe width w_{P2} is larger than the beam spot size. Most likely, $F_{p,on}$ is increased for this material type as well. This is in accordance with the other results for processing of $300\ \text{nm}$ and $1.4\ \mu\text{m}$ thick absorber (Figure 6.5(c)). It shows that the thickness of the absorber layer needs to be considered for scribe width reduction with laser-induced substrate side ablation.

The results suggest a strong dependence of ablation behavior and scribe edge quality from the laser scribing geometries (degree of focusing) and absorber layer thickness. This gave motivation for further investigations of the reasons for this behavior. In the next section the ablation mechanisms were investigated by debris recollection.

6.2 Absorber ablation mechanisms

In accordance with Section 5.2 a similar setup as described in Section 4.1 was used to get insight into the driving mechanisms of absorber ablation. Two sets of experiments were carried out for a-Si:H and tandem absorbers each with a beam spot radius of $60\ \mu\text{m}$. Each absorber type was processed with a low and high laser peak fluence.

Figure 6.7 shows two optical microscopy images of ablation debris from processing of a-Si:H and tandem absorber with 60 μm laser beam radius. In general, investigations of absorber

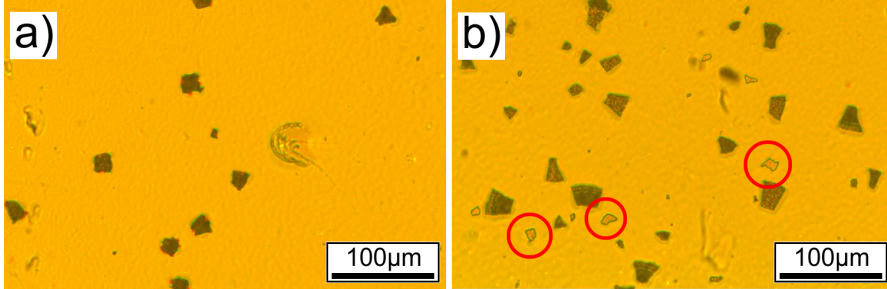


Figure 6.7: Optical microscopy images of ablation debris collected during P2 absorber processing with 532 nm and laser beam spot radius of 60 μm . Parameters are: a) Processing of a-Si:H with a low peak fluence $F_p=0.26\text{Jcm}^{-2}$. b) Processing of tandem absorber with a high peak fluence $F_p=0.83\text{Jcm}^{-2}$. The red circles mark unwanted ablation of the $\text{SnO}_2\text{:F}$ front-contact material.

debris with optical microscope imaging turned out to be not as distinct as compared to ablation debris collected during front-contact processing. Large particles with sharp edges are observed for both a-Si:H and tandem processing. Further experiments with the same beam radius (60 μm) and an increased peak fluence showed a strong decrease of the average particle size for a-Si:H ablation while for tandem processing the particle size and shape remained constant. Not surprisingly, as a function of the beam radius, the average particles size decreased significantly for both a-Si:H and tandem processing. For certain radius/absorber combinations no particles could be observed at all.

Generally, the large size of the particles indicate thermo-mechanical ablation mechanisms as described in Section 5.2. However, transitions to a mostly thermal ablation behavior with a full phase change could not be observed by change of particle shape or size. Rather the absence of any coarser debris indicates this behavior. Due to the small average size, particles could not be seen easily with the optical microscope.

TCO ablation: surprisingly, particles from undesired TCO ablation for tandem absorber processing are observed in the high peak fluence regime (red circles in Figure 6.7(b)). From microscope images of the scribe line it was seen that in the high peak fluence regime it is possible to damage and remove the TCO front-contact layer underneath. However, this happens at a lower peak fluence than what was required for P1 front-contact scribing with 532 nm in the previous Chapter 5.

Experiments from debris recollection show that in fact large intact TCO material clusters are observed (see red circles in Figure 6.7(b)). This is a strong indication for stress-induced ablation mechanism that was dominantly observed for TCO ablation with a wavelengths of

355 nm (compare Figure 5.3). A comparison of the thresholds are significant for processing of SnO₂:F with 532 nm ($F_{th,P2}=0.54\pm0.3\text{ Jcm}^{-2}$ vs. $F_{th,P1}=3.63\pm0.33\text{ Jcm}^{-2}$).

One possible explanation for the driving mechanism of TCO ablation can be found by indirect heating of the SnO₂:F front-contact through the absorber layer. The indirect heating can cause two different scenarios: an increase of the optical absorption for 532 nm leading to stress-induced ablation by gas pressure from evaporation at the TCO/substrate interface. Yet, it is also possible that large thermal-stresses by temperature gradients and/or different coefficients of thermal expansion throughout the layer-stack are decreasing the ablation threshold.

To obtain a magnified view of the fine debris particles that could not be detected with the optical microscope experiments were repeated on a different tape for the characterization with SEM. Figure 6.8 shows a SEM image of debris collected from processing of a-Si:H with a 60 μm laser beam radius. A high degree of melting can be observed on the a-Si:H particle

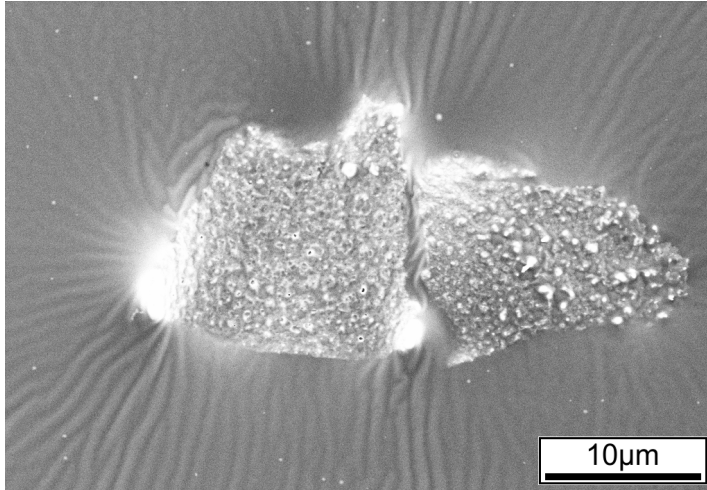


Figure 6.8: SEM images of ablation debris collected during P2 absorber processing of a-Si:H with 532 nm. Parameters are: $\omega_0=60\ \mu\text{m}$ and $F_p=0.26\text{ Jcm}^{-2}$. Spherical particles are observed in the perimeter of the debris particle.

surface. Melting bulges as well as craters can be seen. The indication of melting is supported by the fact that small spherical particles in the perimeter of the ablation debris are observed. These originate from resolidified liquid silicon phases.

In conclusion, unlike front-contact processing, laser ablation properties do not seem to change significantly as a function of focusing degree or laser spot size. The average particle size is decreased for processing with a smaller spot size. However, no change of the shape is observed (not shown) which lead to believe that dominance of the driving mechanism behind ablation does not change significantly.

Additional information was gained from the characterization by SEM where small spherical particles were observed. All processes are mechanically-assisted which is indicated by the occurrence of large debris particles that can show strong signs of melting but remain intact throughout the ablation process.

6.3 Modeling of removal mechanisms

Multiple questions arise from the experimental results of geometrical scribe width reduction in Section 6.1. These can be stated as followed,

- Why does the onset pulse fluence $F_{p,on}$ dramatically increase with decreasing used laser beam spot radius ω_0 for tandem absorber processing (cf. Table 6.1)?
- Why is the squared crater diameter D^2 from the Liu-Plots (for a specific peak fluence) always higher for tandem processing than for a-Si:H layer ablation (above the onset fluence)? In other words, why is the threshold fluence for tandem processing lower than for a-Si:H?
- Why is the onset fluence $F_{p,on}$ lower for a-Si:H processing than for tandem?

In the following, possible answers to these questions were investigated by modeling of the laser ablation process. Modeling with FEA was used for the transient thermal heating of the material stack by a single laser pulse. Subsequently, from the temperature distributions derived from the simulations a simplified model was used to see if the ablation behavior from the experiments could be described by linear fracture mechanics.

Two possible fracture mechanisms were investigated. First, blister formation and rupture by gas pressure due to hydrogen diffusion. Secondly, fracture by thermal stresses along the thickness as well as along the absorber layers radius. For both scenarios the order of magnitude of the occurring mechanical forces was estimated to determine how likely the mechanism was to describe the experimental results. Furthermore, the capabilities to explain the geometrical dependencies of ablation behavior will be discussed as well.

6.3.1 Temporal and spatial temperature distribution

As introduced earlier (Section 5.2), three different ablation mechanisms are often used to describe the majority of laser processes for nanosecond thin-film ablation. These are classical ablation by heating, melting, and evaporation of the material and stress-induced ablation by vapor-pressure or thermal expansion.

The experiments from Section 6.2 showed that for processing of a-Si:H and tandem absorbers with a wavelength of 532 nm ablation behavior is strongly mechanically-assisted. This is not surprising since the absorption coefficient of a-Si:H (first absorbing layer for tandem absorber

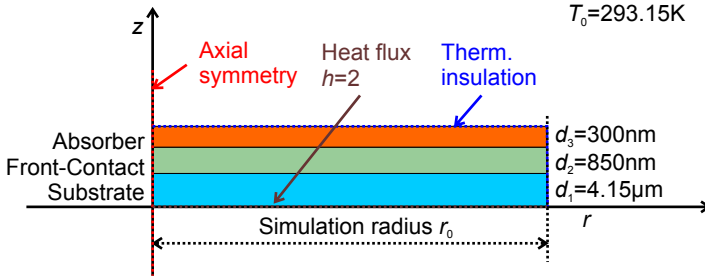


Figure 6.9: Sketch of simulation geometry and boundary conditions for thermal simulation of a-Si:H processing on SnO₂:F TCO with 532 nm. The layer thicknesses are given by d_1 , d_2 , and d_3 . The simulation radius r_0 is varied depending on the used simulation laser beam spot radius between 120 μm , 40 μm , and 20 μm to the corresponding beam radius of 60 μm , 20 μm , and 10 μm , respectively.

as well) is high with $\alpha=1 \cdot 10^5 \text{ cm}^{-1}$. This corresponds to an optical penetration depth of only 100 nm [26] which is lower than the absorber thickness of 300 nm.

Both, thermal-stress and vapor-stress are potential driving mechanisms describing the ablation behavior. However, for processing of hydrogenated amorphous silicon (a-Si:H) one additional process can occur. It is called hydrogen-assisted laser induced forward transfer (HA-LIFT) and needs to be considered as well. Toet et al. accounted the rapid thermal diffusion of the hydrogen bound in the silicon layer as the driving mechanisms for laser ablation of a-Si:H [127]. This process is initiated at much lower temperatures than the melting or vaporization temperature of a-Si:H.

In a first step the temperatures in the layer-stack were estimated with transient thermal simulations. The simulation parameters correspond to the experimental values of pulse energies and radii for both a-Si:H as well as for tandem absorber layers.

Numerical simulations were carried out to determine the maximal temperatures during processing. Therewith, it is possible to discriminate which of the above mentioned driving mechanisms is most likely to be dominant.

The process was modeled with the software COMSOL Multiphysics by a 2D axially symmetric heat conduction partial differential equation. In general, the equation is given as,

$$\rho(T) c_p(T) \frac{\partial T(\vec{r}, t)}{\partial t} - \nabla [\kappa(T) \nabla T(\vec{r}, t)] = Q(\vec{r}, t). \quad (6.1)$$

The individual parameters are $\rho(T)$ as the material density, $c_p(T)$ the heat capacity at constant pressure, $\kappa(T)$ the thermal conductivity, and on the right hand side the volumetric heat source $Q(\vec{x}, t)$. The parameters \vec{r} and t are the spatial coordinates and time, respectively [93].

The geometry of the model is given as a sketch in Figure 6.9 showing the layer-stack as well as the boundary conditions. The thickness of each layer in the stack corresponds to typical

experimental values for the investigated systems. There is one exception for the substrate thickness which is set to 4.15 μm while it is actually 3 mm thick. It is not necessary to choose the real thickness value since the thermal and optical influence is limited to a close region near the substrate/front-contact interface. The simulation radius is chosen to be twice the radius of the simulation laser beam spot radius. This has proven to ensure a negligible temperature increase at the lateral boundary ($-\text{n}\nabla T=0$).

The boundary conditions are chosen to be thermally insulating on top and on the side. No convection on the top nor strong heat conduction in-plane direction is expected for these short time scales under investigation. A heat flux boundary condition with an heat transfer coefficient $h=2\text{ Wm}^{-2}\text{K}^{-1}$ on the air/substrate interface has proven to increase the simulation stability. The value of $2\text{ Wm}^{-2}\text{K}^{-1}$ equals to the free convection of a surface on air without flow of the surrounding medium (air).

For the mesh grid different degrees of element sizes are chosen depending on the expected temperature gradients in the material. In the substrate domain a minimal size of 1 μm and maximum size of 10 μm is chosen. For the front-contact domain 1 μm as max. and 0.1 μm as min. is chosen. The highest resolution can be found for the absorber layer with 40 nm and 10 nm.

In Equation 6.1 the perturbation is given by the heat source term $Q(\vec{x}, t)$ which models the pulse energy intake into the material. The heat source is defined in all three domains exhibiting a spatial and temporal Gaussian distribution. Furthermore, attenuation of the incident power in z direction is accounted for with a Lambert-Beer exponential decay. Equation 6.2 shows the functions used to model thermal heating by the laser pulse.

$$Q(r, z, t) = (1 - R_{d1})(1 - R_{d2})(1 - R_{d3}) I_{\text{peak}} f_{\text{temp}}(t, t_{\text{shift}}, t_p) f_{\text{spat}}(r, \omega_0) f_{\text{abs}}(z) \quad (6.2)$$

In Equation 6.2 R_{d1} to R_{d3} represent the reflection of the laser beam at each interface. It is set to 4% at each interface. I_{peak} is the peak intensity of the laser beam. The functions f_{temp} and f_{spat} are the temporal and spatial distributions of the laser. The attenuation of the laser pulse at the depth z is described by the function f_{abs} . In the following, the functions in Equation 6.2 are further described.

The peak intensity of the laser beam is defined by the following equation,

$$I_{\text{peak}} = \frac{P_{\text{peak}}}{A} = \frac{2\sqrt{\ln(2)}}{\sqrt{\pi}} \frac{E_p}{\pi\omega_0^2\tau_p} \quad [\text{W}/\text{m}^2]. \quad (6.3)$$

where the pulse peak power P_{peak} is divided by the laser beam spot area A [128]. The temporal intensity function in Equation 6.4 is simply defined as,

$$f_{\text{temp}}(t, t_{\text{shift}}, t_p) = \exp\left(-4\ln(2)\left(\frac{t - t_{\text{shift}}}{\tau_p}\right)^2\right) \quad (6.4)$$

which is a Gaussian-shaped pulse with the pulse duration τ_p (FWHM) shifted by t_{shift} . However, it is known that measurements of the temporal shape for nanosecond laser pulses from Q-switched solid-state lasers exhibit a steeper positive slope. It is possible that peak intensities at the rising edge of the pulse could be slightly higher. A Gaussian function was still used mainly to reduce the calculation times. For all calculations t_{shift} was set to 20 ns and τ_p was fixed at 11.3 ns.

The spatial intensity distribution in Equation 6.5 is defined in the same manner as the temporal shape,

$$f_{\text{spat}}(r, \omega_0) = \exp\left(-\frac{2r^2}{\omega_0^2}\right). \quad (6.5)$$

Here, the factor $4\ln(2)$ is not required since the laser beam radius is defined at the $1/e^2$ level instead of the full width at half maximum (FWHM). Measurements of the laser beam with the beam profiler showed that this assumption is likely to be valid except for the slight ellipticity.

Lastly, the attenuation term f_{abs} in the following Equation 6.6 represents the damping of the laser beam by the material in the depth z ,

$$f_{\text{abs}}(z) = \alpha(z) \exp\left(-\int_0^z \alpha(z') dz'\right) \quad [1/\text{m}]. \quad (6.6)$$

Here, the value α is the absorption coefficient for 532 nm for the specific material. A temperature-independent value was assumed. This assumption as well as increased light scattering by the textured front-contact are simplifications which are not accounted for. The individual damping is defined in every domain separately and the coordinates origin in the z -axis is set at the air/substrate interface.

The material properties required for solving the differential equation system in Equation 6.1 are given in Table 6.2. In Table 6.2 not every parameter is listed for every material. For instance, absorption of the laser pulse energy in the substrate is neglected as well as melting and vaporization. Preliminary simulations showed that such high temperatures are not reached within the parameter space that was evaluated. The same is valid for the $\text{SnO}_2\text{:F}$ front-contact material. The absorption coefficient is almost five orders of magnitude lower than for absorption in the amorphous silicon layer. Optical absorption in both, substrate and front-contact material is not modeled.

Phase changes of the amorphous silicon are considered and accounted for by the temperature-dependent behavior of the apparent heat capacity. Enthalpies are commonly represented

Chapter 6. Absorber removal process P2

Table 6.2: Reference material properties used for the thermal heat conduction modeling of Equation 6.1.

Material	Parameter	Value	Ref.	
Substrate	Density ρ [kg/m ³]	2500	[129]	
	Heat capacity c_p [J/kgK]	730	[129]	
	Thermal conductivity κ [W/Km]	1.14	[129]	
SnO ₂ :F	Density ρ [kg/m ³]	6950	[130]	
	Heat capacity c_p [J/kgK]	$511.8 - 604.64 \cdot \exp(-T/209.46)$	[131]	
	Thermal conductivity κ [W/Km]	$7.18 + 73.78 \cdot \exp(-T/351.9)$	[132]	
	Melting temperature $T_{m,TCO}$ [K]	1903	[112]	
	Absorption coefficient α [1/cm]	1266	Table 5.2	
a-Si:H	Density ρ [kg/m ³]	2150	[133]	
	Heat capacity c_p [J/kgK]	$952 + 171 \cdot (T/1685)$ for $T < 1422$, 1000 for $T > 1422$	[134, 135, 136]	
	Thermal conductivity κ [W/Km]	$4.83 \cdot 10^{-9}(T - 900)^3 + 4.83 \cdot 10^{-7}(T - 900)^2 + 3.71 \cdot 10^{-4}(T - 900) + 3.71$ for $T < 1422$, 60 for $T > 1422$	[134, 137]	
	Melting temperature $T_{m,a-Si}$ [K]	1422 ± 9	[138, 136]	
	Vaporization temperature $T_{v,a-Si}$ [K]	2620 ± 15	[93]	
	Latent melt heat ΔH_{al} [J/kg]	$1475 \cdot 10^3$	[138]	
	Latent vap. heat ΔH_{iv} [J/kg]	$16366 \cdot 10^3$	[139]	
	Absorption coefficient α [1/cm]	$1 \cdot 10^5$	[16]	
	c-Si	Density ρ [kg/m ³]	2329	[140]
		Heat capacity c_p [J/kgK]	960 for $T < 1683$, 1000 for $T > 1683$	[135, 136]
Thermal conductivity κ [W/Km]		$1521 \cdot 10^2 T^{-1.226}$ for $300 < T < 1200$, $8.96 \cdot 10^2 T^{-0.502}$ for $1200 < T < 1683$, 60 for $T > 1683$	[135, 137]	
Melting temperature $T_{m,c-Si}$ [K]		1683 ± 10	[136]	
Latent melt heat ΔH_{cl} [J/kg]		$1799 \cdot 10^3$	[136]	
Absorption coefficient α [1/cm]		$1 \cdot 10^4$	[16]	

by modifications of the heat capacity [141]. The following Equation 6.10 shows the modified function of the heat capacity c_p ,

$$c_p(T) = 952 + 171 \left(\frac{T}{1685} \right) + c_{p,\text{melt}}(T) + c_{p,\text{vap}}(T) \left[\frac{\text{J}}{\text{kgK}} \right] \quad \text{with,} \quad (6.7)$$

$$c_{p,\text{melt}}(T) = \Delta H_{\text{al}} \frac{\partial}{\partial T} [\mathcal{H}(T - T_{m,\text{a-Si}}, \Delta T_{m,\text{a-Si}})] \quad \text{and} \quad (6.8)$$

$$c_{p,\text{vap}}(T) = \Delta H_{\text{iv}} \frac{\partial}{\partial T} [\mathcal{H}(T - T_{v,\text{a-Si}}, \Delta T_{v,\text{a-Si}})]. \quad (6.9)$$

$$(6.10)$$

Here, both functions $\mathcal{H}(T - T_{m,\text{a-Si}}, \Delta T_{m,\text{a-Si}})$ and $\mathcal{H}(T - T_{v,\text{a-Si}}, \Delta T_{v,\text{a-Si}})$ are Heaviside functions that are smoothed by the melting and vaporization intervals which increases the stability of the simulation.

Simulation of a-Si:H ablation: a first set of simulations were carried out for a a-Si:H absorber illuminated by three different laser beam radii and pulse energies corresponding the onset pulse energies from the experiments.

Figure 6.10 shows the time-dependent temperature distribution as a function of the depth z at the origin of $r = 0$ for a pulse energy E_p of $7 \mu\text{J}$. This corresponds to the onset pulse energy for processing of a-Si:H with a beam spot radius of $60 \mu\text{m}$ (cf. Table 6.1). It is remarkable to see

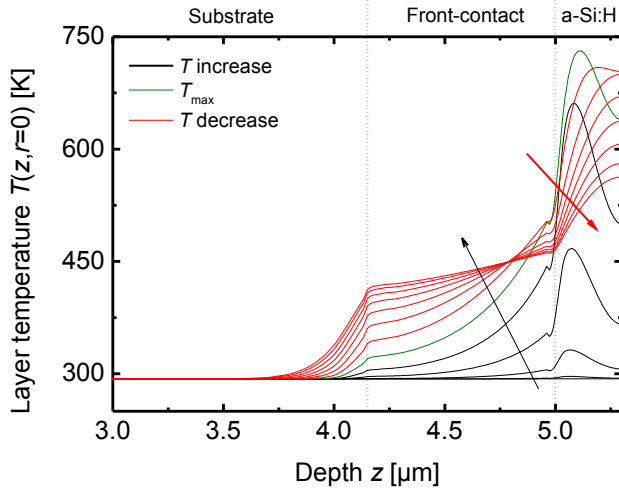


Figure 6.10: Temperature distribution of a-Si:H processing simulation on $\text{SnO}_2\text{:F TCO}$ with 532 nm and a beam radius of $60 \mu\text{m}$ and $7 \mu\text{J}$ pulse energy. The plot shows the temperature evolution in z direction at the origin ($r = 0$) for different times t . Increasing temperatures represented by black lines whereas decreasing temperatures are shown in red. Maximal temperature distribution given in green.

that the maximal temperature from the simulation is approx. 730 K which is significantly lower than the melting temperature of a-Si:H which is 1422 ± 9 K. This is a strong sign supporting the assumption that the ablation process is highly supported by a mechanically-assisted behavior. The process cannot be described by melting alone and especially not by any vaporization of the silicon.

Furthermore, although absorption begins at the TCO/silicon interface, the maximal temperature is observed at a slightly deeper depth approx. 50–80 nm off the interface. This can be explained by a heat flux from the silicon to the front-contact material via heat conduction which decreases the maximal temperature at the immediate interface region.

Figure 6.11 shows the same simulations as in Figure 6.10 but this time for processing with a beam radius of $20 \mu\text{m}$ and $10 \mu\text{m}$. The pulse energies correspond to the onset pulse energies from the experiments. Although, similarities of the temperature distribution to calculations made for a radius of $60 \mu\text{m}$ can be seen, the maximal temperatures are quite different. For both, processing with $20 \mu\text{m}$ as well as for $10 \mu\text{m}$, maximal temperatures close to the melting temperature of amorphous silicon are observed. But still, temperatures in the region of vaporization are not reached.

The differences between the temporal temperature evolution above the maximal temperature T_{max} indicate that for the calculation in Figure 6.11(a) a phase change into the liquid state of a-Si:H is performed. In contrast, Figure 6.11(b) shows that the material is at the lower temperature limit of the amorphous/liquid phase change.

To visualize the lateral temperature distribution results from Figure 6.10 and Figure 6.11 are plotted in Figure 6.12 as a function of the radius for the depth z where the peak temperature was observed.

In general, a Gaussian distribution is obtained which is in accordance with the intensity distribution of the laser beam/heat source. As expected for processing with $20 \mu\text{m}$ as well as for $10 \mu\text{m}$ a phase change boundary is clearly visible with an extent that is marked by $r_{T,\text{max}}$. It is believed that the melted phase at the interface is an determining factor for the resulting crater diameter since the adhesion at this interface area is strongly reduced [101].

Figure 6.13 shows both fictional crater diameter from simulations compared to the experimental crater measurements. The fictional crater diameter is defined by the dimensions (cf. $r_{T,\text{max}}$ in Figure 6.12) of the melt interface region where $T \geq T_{\text{m,a-Si}}$. For a beam radius of $60 \mu\text{m}$ in Figure 6.13(a) a large offset between simulation and experiment is found. However, the simulated onset as well as the trend approaches ($20 \mu\text{m}$) and merges ($10 \mu\text{m}$) the experimental results for processing with smaller beam radii in Figure 6.13(b) and (c). For these two reduced beam radii, good agreement is found between the melt threshold from the simulation (green dotted lines) and the onset pulse energy from the experiment (black dotted lines).

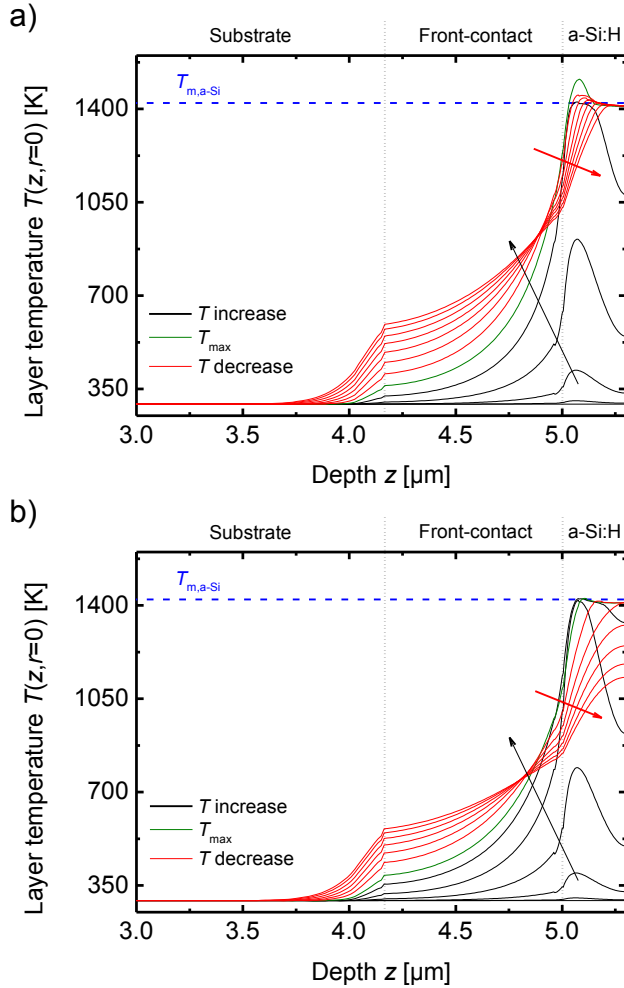


Figure 6.11: Temperature distribution of a-Si:H processing simulation on $\text{SnO}_2\text{:F}$ TCO with 532 nm and a beam radius of: a) Radius of 20 μm and 3 μJ pulse energy. b) 10 μm and 0.6 μJ . The plot shows the temperature evolution in z direction at the origin ($r = 0$) for different times t . Increasing temperatures represented by black lines whereas decreasing temperatures are shown in red. Maximal temperature distribution given in green. Melting temperature $T_{m,a-Si}$ as blue dashed line.

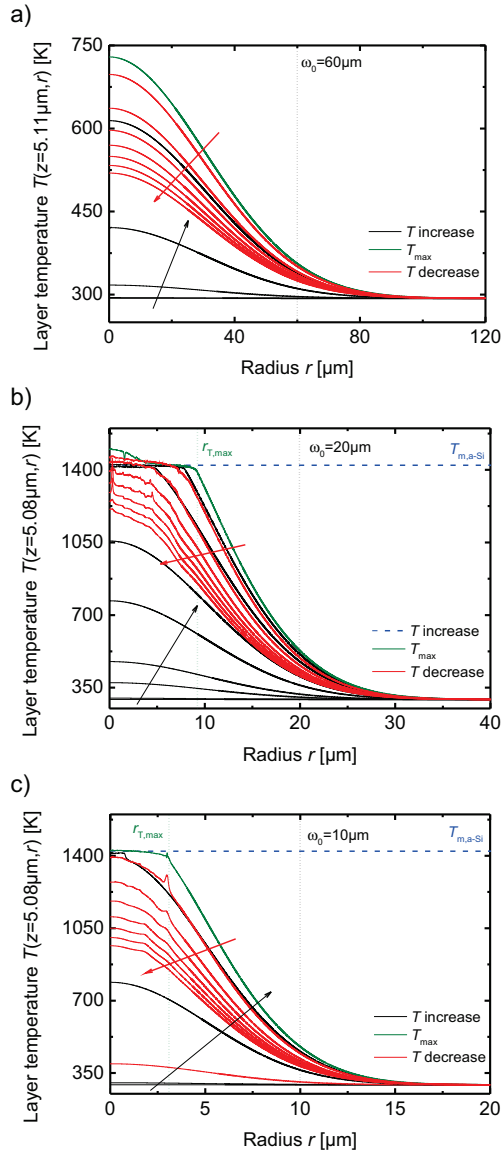


Figure 6.12: Temperature distribution of a-Si:H processing simulation on SnO₂:F TCO with 532 nm and a beam radius of: a) Radius 60 μm and 7 μJ pulse energy b) 20 μm and 3 μJ . c) 10 μm and 0.6 μJ . The plot shows the temperature evolution in r direction at the z -plane with $z=5.11\ \mu\text{m}$ and $z=5.08\ \mu\text{m}$ (processing with 10 μm) for different times t . Increasing temperatures represented by black lines whereas decreasing temperature are shown in red. Maximal temperature distribution T_{max} and radius $r_{T,\text{max}}$ given in green.

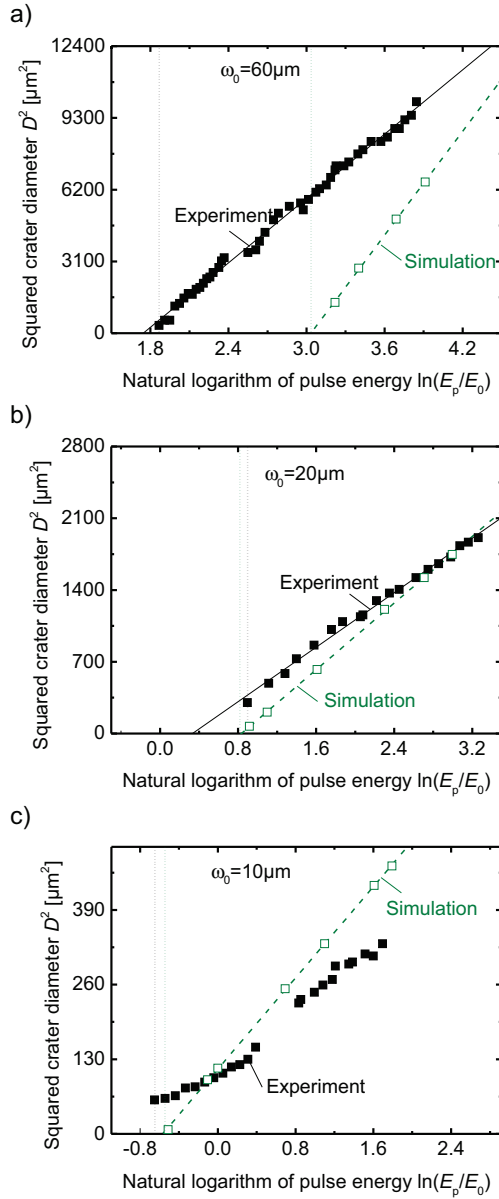


Figure 6.13: Comparison of Liu-Plots for experimental squared crater diameter of a-Si:H processing with simulated melted phase diameter at TCO/absorber interface for different laser beam radii ω_0 . Plots show: a) Processing with $60 \mu\text{m}$. b) $20 \mu\text{m}$. c) $10 \mu\text{m}$. The dotted lines mark the onset and threshold from experiment and simulation, respectively.

The large offset, for processing with 60 μm in Figure 6.13(a), between onset of melting from the simulations and ablation from the experiment is a strong sign that for this setup a reduction of the layers adhesion of the TCO/absorber interface is not a limiting factor.

In contrast, interface adhesion is limiting the ablation process for the higher focused laser beams (cf. Figure 6.13(b) and (c)) so that melting is required. The driving forces are not sufficient to overcome the energy required for the delamination at the interface without a reduction of the adhesive forces by melting. Such behavior would explain the approach and merging between experimental crater diameter and fictional melt diameter from the simulations.

All results indicate that classic ablation by complete phase changes as the driving mechanism behind the ablation process can be ruled out. For pulse energies in the range of the experimental onset pulse energy the calculations predict maximal temperatures significantly lower than the vaporization temperature. In some cases even below the melting temperature.

Simulation of tandem absorber ablation: it was necessary to extend the model for the simulation of tandem layer removal. Since, thermal properties of microcrystalline silicon are only sparsely available in literature, especially not temperature-dependent values. Li et al. showed for thermal conductivity measurements of $\mu\text{c-Si:H}$ that generally higher values were observed than for a-Si:H [142, 143]. A strong dependence on the crystalline volume fraction was found which is reasonable since a higher structural order is expected in the crystalline phase. Although, increasing with temperature, the measurements were only carried out over a small temperature range.

For simplicity reasons the thermal conductivity and heat capacity of $\mu\text{c-Si:H}$ were modeled by a superposition of the properties found for a-Si:H and c-Si. The individual properties were weighted by the crystalline volume fraction. A superposition of both material properties is reasonable since it is known that $\mu\text{c-Si:H}$ exhibits a columnar growth with crystalline grains surrounded by amorphous material. During laser pulse illumination the absorber layer is dominantly heated in the growth direction of the material leading to believe that lateral properties of the $\mu\text{c-Si:H}$ absorber can be neglected.

Both plots in Figure 6.14 show the superposition of a-Si:H and c-Si thermal properties for the simulation of the $\mu\text{c-Si:H}$ bottom cell. The superposition of the individual material parameters of pure a-Si:H and c-Si are weighted by the crystalline volume fraction typical for $\mu\text{c-Si:H}$ with an optimum phase mixture [144]. The plots show that no phase change from the liquid phase into the gas phase is modeled. It was found out by preliminary simulations that the maximal temperatures in the $\mu\text{c-Si:H}$ domain were far lower than the vaporization temperature of silicon.

The thermal conductivity shows differences between a-Si:H and c-Si for lower temperatures but merging occurs for increasing temperatures. The phase change into the liquid state is not easily modeled as seen for the calculated $\mu\text{c-Si:H}$ values in Figure 6.14(a). There is no difference for the thermal conductivity for the temperature region where the amorphous fraction is liquid

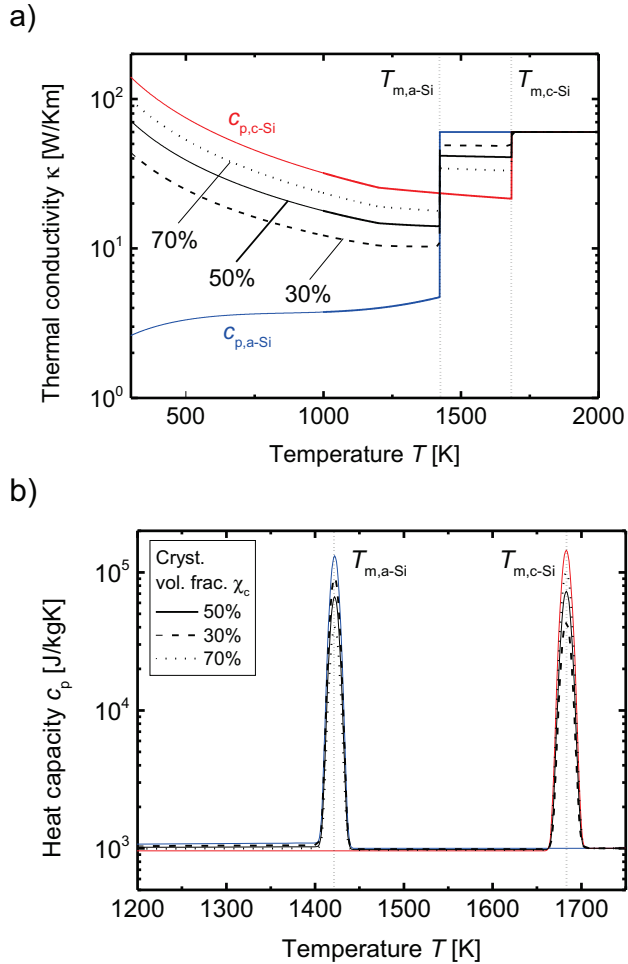


Figure 6.14: Modeling of thermal properties of μc -Si:H by superposition of a-Si:H and c-Si properties weighted by the crystalline volume fraction χ_c . Plots show: a) Thermal conductivity of pure a-Si:H, c-Si, and calculated for μc -Si:H with χ_c of 50%, 30%, and 70%. b) Similar calculations made for the heat capacity.

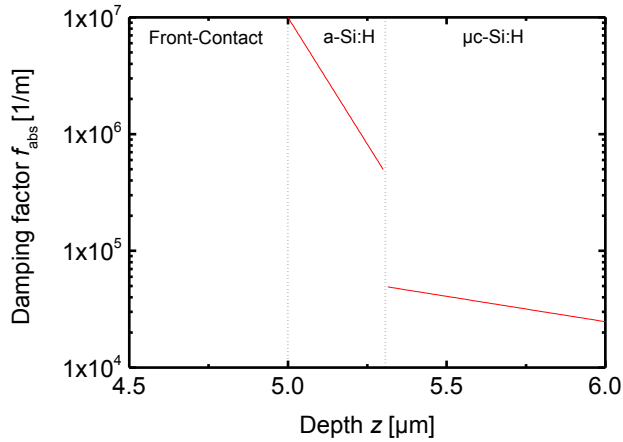


Figure 6.15: Damping factor f_{abs} plotted in z direction at the origin with $r=0$. Absorption coefficient α in a-Si:H domain is $1 \cdot 10^5 \text{ cm}^{-1}$ while in the $\mu\text{c-Si:H}$ bottom cell domain the value for c-Si of $1 \cdot 10^4 \text{ cm}^{-1}$ was considered.

while the crystalline fraction is still solid. This problem is somehow accounted for by the weighted thermal conductivity between $T_{\text{m,a-Si}}$ and $T_{\text{m,c-Si}}$ leading to an effective medium value of the whole layer.

For the heat capacity there is no problem with different phase change temperatures. The latent heat required for melting is weighted with the volume fraction of each material (proportional to the area under each peak in Figure 6.14(b)). Please note that the latent heat in the graph of Figure 6.14(b) is represented by Gaussian peak functions and not by the derivate of a Heaviside function (cf. Equation 6.10) as it is used in the simulation. The smoothed form of the Heaviside function could not be exported from COMSOL.

For all calculations a crystalline volume fraction of 50% was chosen. The calculation were made for laser peak fluences in the same value range as the experiment results from Figure 6.1, 6.2, and 6.3. However, the main focus lies on the temperature distribution close to the onset peak fluence $F_{\text{p,on}}$.

Before the results are shown, the damping function f_{abs} (see Equation 6.6) is plotted in Figure 6.15 to see where the pulse energy is absorbed for the case of tandem absorber ablation. As expected the main part of the incident optical energy is absorbed in the 300 nm thick a-Si:H top-cell while only a small percentage reaches the $\mu\text{c-Si:H}$ bottom-cell. This is of course owed to the fact that the absorption coefficient of a-Si:H for 532 nm of $\alpha=1 \cdot 10^5 \text{ cm}^{-1}$ is rather high. Furthermore, the absorption coefficient in the bottom-cell is one order of magnitude lower. Thus, there will be no significant direct heating of the bottom-cell but rather indirectly by heat conduction from the top-cell.

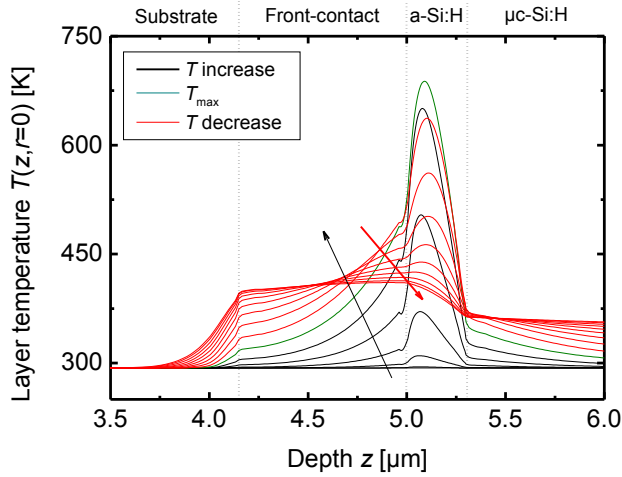


Figure 6.16: Simulated temperature distribution of tandem processing on $\text{SnO}_2\text{:F}$ TCO with 532 nm, a beam radius of $60\ \mu\text{m}$ and a pulse energy of $7\ \mu\text{J}$. The plot shows the temperature evolution in z direction at the origin ($r = 0$) for different times t . Increasing temperatures represented by black lines whereas decreasing temperatures are shown in red. Maximal temperature distribution T_{max} given in green.

Figure 6.16 shows the simulated temperature distribution for tandem absorber processing with a radius of $60\ \mu\text{m}$. For the comparison of the maximal temperatures the pulse energy corresponds to the onset pulse energy for a-Si:H (experiment from Figure 6.1). As expected, the heat flux into the $\mu\text{c-Si:H}$ bottom-cell reduces the maximal temperature in the a-Si:H and therefore the maximal temperature. Furthermore, the maximal temperature in the bottom-cell is significantly lower than in the amorphous silicon reaching values of only up to 375 K.

The reduced temperatures are observed for all laser pulse energies that were simulated. Consistent with the calculations made for a-Si:H processing the melt onset at the TCO/a-Si:H interface is shifted towards higher pulse energies. This behavior originates from pure thermal considerations. It is a partial answer to the prior stated question about why there is a higher onset peak fluence observed for tandem absorber processing compared to a-Si:H P2 structuring.

6.3.2 Vapor-Stress induced ablation mechanisms

Investigations on the ablation mechanisms showed that P2 ablation processes, over a large pulse fluence regime, are strongly mechanically-assisted. Furthermore, at the ablation onset, the temperature distributions from the simulations showed maximal temperatures far below the vaporization temperature of silicon. In some cases the maximal temperature was even below the melt temperature of a-Si:H.

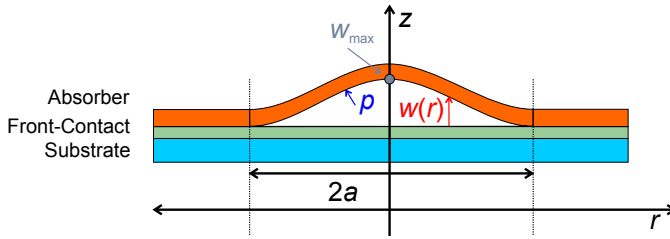


Figure 6.17: Schematic sketch of the deformation of the absorber layer induced by gas pressure. The gas pressure p leads to an uniform load distribution. Deflection is given by $w(r)$ with w_{\max} at the center for $r = 0$. The layer is clamped at $r = \pm a$ so that the deflection $w(r = \pm a) = 0$. Deflection shape is illustrated exemplarily by a Gaussian bell curve.

Both results indicate that vaporization of silicon at the TCO/absorber interface can be ruled out, at least for the lower pulse energy regimes. Hence, gas pressure at the interface by silicon vapor is unlikely. However, vapor-stress induced ablation is still possible by hydrogen diffusion from the heated absorber to the TCO/absorber interface [127]. The dehydrogenation temperature of a-Si:H is 670 K (di-) and 810 K (mono-hydrides) [145]. Such temperatures are in the same region as the temperatures at the onset pulse fluence for processing with $60 \mu\text{m}$ that were extracted from the simulations.

To determine the possibility of hydrogen diffusion as a driving mechanism behind P2 ablation it is necessary to model the mechanical process of laser ablation. This is done by modeling of three different processes of layer blistering, interface delamination, and finally crater formation by layer fracture.

In the following a similar approach as used for the description of blister formation for hydrogen ion-implanted crystalline silicon was modified and extended [146]. Extensive research can be found on the blister formation for wafer splitting (Smart-Cut technology) [147, 148] which is a closely related process.

Deflection: in a first step the layer blistering is modeled by stress induced strain of the absorber layer. The strain can be described simplified by a thin circular plate that is clamped at the edge around its circumference as shown in Figure 6.17. The gas pressure p creates a uniform load distribution on the absorber layer. The deflection of the layer in z direction is described by $w(r)$ with w_{\max} at the center $r = 0$. The circular plate is fixed at $r = \pm a$ so that $w(r = \pm a) = 0$ is forced.

According to Timoshenko et al. [149] the deflection of a circular thin plate clamped at the edges can be derived by,

$$w(r) = \frac{p}{64D} (a^2 - r^2)^2 \quad \text{with,} \quad D = \frac{Eh^3}{12(1 - \nu^2)}. \quad (6.11)$$

In Equation 6.11 p is the pressure that is loading the surfaces uniformly, r is the radius where the buckling is evaluated, a is clamp radius, and D is the flexural rigidity. The value of D is derived by the Young's modulus E , the Poisson's ratio ν , and the thickness of the absorber h .

The volume of the deformed region between TCO and absorber can be evaluated by the volume integral in cylindrical coordinates and the following equation is derived,

$$V = \int_0^{2\pi} \int_0^a w(r) d\phi r dr = \frac{\pi p a^6}{192D}. \quad (6.12)$$

With Equation 6.12 the relation between V , p , and a is obtained. The deflection $w(r)$ can be described as a function of the pressure for a given clamp radius a .

Subsequently, in the next step according to Hong et al. [146] and Yang [150] an evaluation of the mechanical elastic strain energy, that is stored due to the deflection of the layer, can be evaluated. The volumetric strain energy U_{el} is calculated by,

$$U_{el} = \frac{1}{2D} \int_0^{2\pi} \int_0^a \left[\left(\frac{\partial^2 w}{\partial r^2} \right) + \frac{1}{r^2} \left(\frac{\partial w}{\partial r} \right)^2 + \frac{2\nu}{r} \frac{\partial w}{\partial r} \frac{\partial^2 w}{\partial^2 r} \right] d\phi r dr \quad (6.13)$$

$$= \frac{1}{2} p V \quad (6.14)$$

$$= \frac{\pi a^6 p^2}{384D}. \quad (6.15)$$

Equation 6.15 shows that the stored energy is mainly depending on the clamping radius a and pressure p .

Let us assume the pressure in the blister is increasing while the layer is clamped at the radius a . At some point delamination of the layer occurs increasing the clamp radius a . The delamination releases elastic energy from the deflection by the creation of a new free surface at the interface.

Delamination: in the next step delamination is described by the energy that is required to separate both layer materials at the interface. The surface energy of the interface crack is given by,

$$S_{inter} = 2\gamma_{inter}\pi a^2. \quad (6.16)$$

Which is simply two times the surface areas created by the crack multiplied with the interface surface energy γ_{inter} . Hence, the clamp radius a changes due to delamination as long as the strain energy that is released from the deflection is higher than the energy required to create a new surface $A = \pi a^2$.

Fracture: at some point the radial tensile stress at the clamping radius will reach the critical stress of the absorber layer. The maximal stress of the circular clamped plate is given by [149],

$$\sigma_{r,max} = \frac{3}{4} \frac{p a^2}{h^2} \quad (6.17)$$

The equation shows that for a constant pressure p the stress will increase when the radius a increases. Furthermore, $\sigma_{r,\max}$ is reduced when layer thickness h is increased. The Equation 6.17 is solved for the pressure p_{crit} that is required when a blister with the radius a is created where the critical yield or tensile stress σ_{crit} is acting upon the absorber layer at the clamping radius.

$$p_{\text{crit}} = \sigma_{\text{crit}} \frac{4}{3} \frac{h^2}{a^2} \quad (6.18)$$

Furthermore, for the through-thickness fracture of the layer the surface energy S_{abs} is required,

$$S_{\text{abs}} = 2\gamma_{\text{abs}}2\pi ah. \quad (6.19)$$

Which is simply two times the surface energy γ_{abs} of the absorber multiplied with the absorber crack area along the circumference $2\pi a$ and thickness h of the delaminated blister.

Each contribution to the required energy W_{abl} to create an ablation crater with radius a is defined by the sum of all individual energies,

$$W_{\text{abl}} = U_{\text{el}} + S_{\text{inter}} + S_{\text{abs}} \quad (6.20)$$

In Equation 6.20 each contribution to the total energy is: U_{el} as the elastic strain energy that is stored in the deflection of the absorber layer, S_{inter} as the surface energy of delamination of the interface region, and S_{abs} as the fracture energy.

Now that the required energy is derived it is necessary to define the potential energy due to the hydrogen that diffuses into the blister.

Dehydrogenation: the required energy W_{abl} can be extended by the gas potential via the ideal gas law that estimates the amount of hydrogen that would be necessary to diffuse into the blister volume. The gas law is simply given by,

$$W_{\text{gas}} = -pV = -nRT. \quad (6.21)$$

On the left hand side of Equation 6.21 is the pressure p and volume V . On the right hand side n represents the moles of hydrogen molecules in the blister, R as the gas constant, and the gas temperature T . A estimation of n can be obtained by the following equation,

$$n = K_{\text{diff}}(t, T) \frac{X_{\text{H}_2} V_{\text{H}_2}}{m_{\text{Si}}} = K_{\text{diff}}(t, T) \frac{X_{\text{H}_2} \pi a_{\text{H}_2}^2 h_{\text{H}_2}}{m_{\text{Si}}}. \quad (6.22)$$

Here, X_{H_2} is the overall fraction of hydrogen in the absorber layer (typ. 10%), V_{H_2} is the interaction volume from where hydrogen can diffuse into the blister. The value of V_{H_2} is mainly depending on the radius a_{H_2} which is closely related to the final crater radius and the thickness h_{H_2} is the depth into z direction from where hydrogen diffuses to the blister.

The value of a_{H_2} and h_{H_2} are set equal to a and h in a first approximation. For tandem absorber processing the values of h_{H_2} and h would differ significantly since only the a-Si:H top-cell is dominantly heated (cf. Figure 6.16). The interaction volume is divided by the molar volume of silicon m_{Si} to obtain the moles of hydrogen.

Of course the diffusion process is highly depending on the temporal and spatial heating of the material and needs to be simulated by itself. To approximate the fraction of the hydrogen molecules that diffuse to the blister upon heating of the absorber layer the factor $K_{\text{diff}}(t, T)$ is defined that is effectively mainly influenced by the layer temperature T and time t .

In literature Conde et al. showed with ToF-SIMS measurements that SiH concentrations are decreasing upon excimer laser single pulses with peak fluences of 0.1–0.2 Jcm⁻² [145]. This indicates that dehydrogenation of the a-Si:H can occur upon heating/processing by nanosecond laser pulses.

Total energy: now that all contributions are defined the ablation energy W_{abl} and potential energy W_{gas} can be summed and the total energy F_{tot} is derived,

$$F_{\text{tot}} = W_{\text{abl}} + W_{\text{gas}} = U_{\text{el}} + S_{\text{inter}} + S_{\text{abs}} - nRT \quad (6.23)$$

$$F_{\text{tot}} = \frac{\sigma_{\text{r,max}}^2 (1 - \nu^2) h}{18E} \pi a^2 + 2\gamma_{\text{inter}} \pi a^2 + 2\gamma_{\text{abs}} 2\pi a h - K_{\text{diff}}(t, T) \frac{X_{\text{H}_2} \pi a^2 h}{m_{\text{Si}}} RT. \quad (6.24)$$

A close look to Equation 6.24 reveals that all contributions are depending on the radius a^2 except for the fracture energy S_{abs} which depends linearly on the radius a . For better visualization of the different contributions an example is plotted in Figure 6.18. It can be seen from Figure 6.18 that below a certain radius a (marked with a dashed line) the total energy is positive meaning that the potential energy driving the process is not sufficient. Such behavior is mainly owed to the different slopes of the quadratic terms as well as the fact that for small radii the linear term of the fracture energy S_{abs} is dominant. This radius marks an onset where ablation is possible for radii above this value.

For a lower ablation radius the slope of the function W_{gas} needs to be increased. This is equivalent with either a higher temperature T of the hydrogen gas in the blister, a higher temperature of the silicon layer increasing the fraction factor K_{diff} from diffusion out of the absorber layer, or both. In every case a higher energy for heating of the material by the laser pulse is required. This behavior could possibly be an answer to the question: *Why does the onset pulse fluence $F_{p,on}$ dramatically increase with decreasing used laser beam spot radius ω_0 for tandem absorber processing (cf. Table 6.1)?*

Secondly, if the thickness of the absorber layer h is increased the onset where ablation is possible is shifted towards higher radii (cf. dotted lines in Figure 6.18). The shift is attributed to the higher energy that is required for the layer deformation at σ_{crit} as well as the higher area of fracture. Thus, this behavior could be an answer to the remaining questions on the reason why the onset peak fluence is different for processing of both absorber types as well as on why

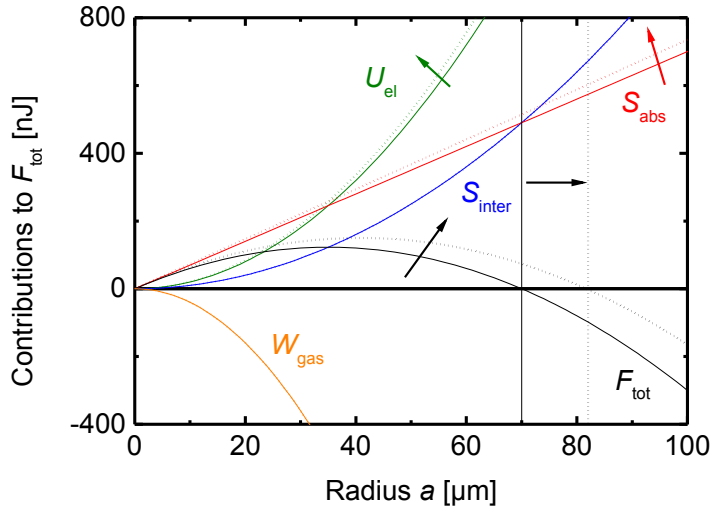


Figure 6.18: Plot of the different contributions to Equation 6.24 calculated with arbitrary material properties to illustrate ablation process behavior in terms of geometrical dependencies of radius a and layer thickness h . Dashed line marks the radius where F_{tot} is negative and is equivalent with an onset for ablation. For radii below this onset a higher potential energy W_{gas} is required. The dotted lines represent the same calculations for a higher absorber thickness $h_2 > h$.

the crater radius is higher for the tandem absorber (for a similar peak fluence) compared to a-Si:H processing.

Applicability: the validity of the proposed model stand and falls with the magnitude of the individual material properties that are used for evaluation. Due to the lack of the properties values, especially the surface energies at the interface and through the layer are unknown, it is only possible to investigate the geometrical trends. Furthermore, for the remaining mechanical properties large deviations of the values are found in literature since, for example, the critical stress is influenced by the specimen size and shape (described by Weibull statistics [151]). Lastly, the intrinsic stress or residual stress of the TCO/absorber layer-stack is highly dominated by the deposition conditions. Thus, for a distinct evaluation all mechanical properties need to be measured for the specific system.

In conclusion it can be said that the ambiguous ablation behavior of the absorber removal process P2 can be possibly described by hydrogen induced gas pressure. The main effect of the increased onset fluence for decreased laser beam radii originates from the fracture relation between delaminated area and cracking along the perimeter.

In the next section similar considerations were done for thermal-stress induced ablation.

6.3.3 Thermal-Stress induced ablation

The following section gives a short evaluation whether thermal-stress assisted ablation is a possible mechanism for the P2 ablation. Bovatsek et al. made thermal 1D simulations of the P2 absorber removal process for a-Si:H [99]. However, their observed maximal temperatures were quite different compared to the findings from this work.

They accounted thermal-stress as the dominant ablation mechanism and compared the occurring elastic stresses in a round plate clamped at the edges. According to Timoshenko [149] the maximal stress along the clamped edge of the plate is given by,

$$\sigma_{\max} = \frac{\alpha \Delta T E}{2(1 - \nu^2)}. \quad (6.25)$$

Surprisingly, no geometrical parameters are required in Equation 6.25 and only the thermal expansion coefficient α , Young's modulus E , and Poisson's ratio ν are used. A linear temperature gradient ΔT along the thickness of the layer is required.

For a temperature gradient of ΔT between 700–1000 K stresses roughly comparable with the tensile strength of amorphous silicon are stated [99]. However, the temperature gradients obtained from this works simulations at the onset fluences were much lower than 700 K. However, in higher pulse energy regimes and especially for tandem absorber processing large temperature gradients are derived from the present simulations as well.

The discrepancy between used peak fluence and achieved crater diameter between a-Si:H and tandem processing could be explained by a larger temperature gradient along the thickness

for the tandem absorber. For the same amount of incident pulse energy a larger temperature gradient is achieved for tandem absorber processing leading to larger mechanical stresses than for a-Si:H processing. Of course, the remaining parameters in Equation 6.25 are maybe changed as well so that no distinct conclusion is possible.

Studies on the laser ablation behavior for film side processing of ZnO and CIGS on Mo were made by Buzás et al. [152]. They found out that the ablation threshold values (called fracture and delamination threshold) increase with decreasing laser beam radius just like it was observed for P2 processing in this work. For certain peak fluence regimes combined modeling of the occurring temperatures and thermal expansion indicate that thermal-stresses could be a driving mechanisms for ablation.

Modeling of the experimental results to a Griffith energy criterion [153] showed that an increasing threshold fluence can be described by the fracture behavior induced by a radial non-uniform Gaussian-shaped stress distribution.

Referred to the present results, although it is not clear if the magnitude of thermal-stresses are relevant for P2 processing of thin-film silicon from the substrate side, their results show that the observed ambiguous mechanical constraints on P2 with decreasing beam radii and increased absorber thicknesses are consistent with a thermal-stress induced ablation model.

A comparison with the literature shows that the magnitude of thermal expansion of the absorber layer can, with high enough temperature gradients, generate maximal stresses capable of layer removal. Furthermore, the ambiguous onset peak fluence dependencies in terms of processing beam radius and absorber layer thickness were previously observed for laser processing of CIGS on Mo. Calculations with a mechanical delamination/fracture model can explain the behavior observed from the experiment.

It is possible to answer the first question stated earlier (cf. Section 6.3). Furthermore, different temperature gradients along the thickness of the absorber could be a possible answer to the second question as well.

Simple modeling of the mechanical forces due to gas pressure by hydrogen diffusion to the TCO/absorber interface indicate that such mechanism could be one important factor driving the ablation process. Furthermore, the experimental results in terms of beam radii and/or layer thickness can be described by comparison of the energies required for layer delamination and fracture.

In conclusion, there are no characteristics found for both stress-inducing mechanisms that would contradict with the experimental results. It is likely that depending on the used peak fluence region and processing setup/geometry either hydrogen gas pressure or thermal expansion dominates. A more sophisticated multiphysics FEA simulation taking transient diffusion and thermal stresses into account could help to increase the understanding of the processes.

6.4 Impact on electrical properties

The function of the P2 scribe is the electrical interconnection of two adjacent cell stripes. The front-contact of one cell is connected with the back-contact of the neighboring cell. During processing, the absorber is selectively removed and the interconnection is realized by the back-contact deposition into the scribe. It is therefore of utter importance to have a good electrical contact between front-contact and back-contact. All experiments were conducted with a combination of sputtered ZnO:Al, Ag, and ZnO:Al as the back-contact material.

Due to redeposition of debris, changes of the front-contact surface, or partial ablation of the front-contact an additional series resistance is formed at the front- and back-contact interface [154, 155]. This parasitic series resistance can be defined by a macroscopic resistance $R_{s,P2}$. Just like for shunting by P1 processing, the model by Gupta can be extended to account for these series resistance losses [45].

Series resistance loss fraction: in accordance to the prior introduced fractional loss mechanisms, series resistance losses are defined as followed,

$$P_{P2} = R_{s,P2} J_{MPP}^2 w_a^2 l^2 \quad \text{and} \quad P_{\max} = V_{MPP} J_{MPP} w_a l \quad (6.26)$$

$$\Rightarrow f_{P2} = w_a R_{s,P2} l \frac{J_{MPP}}{V_{MPP}} = w_a R'_{s,P2} \frac{J_{MPP}}{V_{MPP}} \quad \text{with} \quad R_{s,P2} = \frac{R'_{s,P2}}{l}. \quad (6.27)$$

The parameter l is the length perpendicular to the module interconnection. The series resistance losses f_{P2} in Equation 6.27 increase with increasing active cell stripe width w_a and increasing series resistance $R'_{s,P2}$ as well. Figure 6.19 shows model calculations for interconnection module losses considering series resistance losses by the absorber structuring process P2. The plot shows the overall module losses of a tandem solar cell as a function of the active cell stripe width w_a . The losses are parameterized for different series resistance values of 1 Ωcm , 2 Ωcm , 5 Ωcm , and if no losses were apparent (0 Ωcm). Already a resistance value of 1 Ωcm can cause significant losses and even higher values would have a detrimental impact on the module properties. Due to its high impact on the losses knowledge of the specific values for $R'_{s,P2}$ is very important.

By geometrical considerations of the contact formed by the absorber structuring process P2 it is evident that the actual value of $R_{s,P2}$ (or $R'_{s,P2}$) depends on the contact area. Therefore, it depends on the scribe width w_{P2} ,

$$\rho_c = R_{s,P2} A = R_{s,P2} w_{P2} l = R'_{s,P2} w_{P2}. \quad (6.28)$$

In Equation 6.28 ρ_c represents the specific contact resistance. Unfortunately, $R'_{s,P2}$ increases with decreasing P2 scribe width w_{P2} . For the optimization process it is important to evaluate the contact resistance properties. This is necessary to see whether series resistance increases are only caused by geometrical width minimization or if for minimized scribe widths the specific contact resistance ρ_c is also increased.

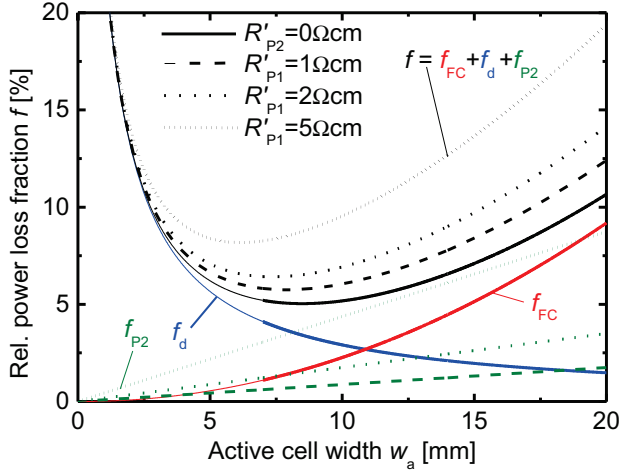


Figure 6.19: Calculated tandem solar module loss fractions due to the integrated series connection plotted against the active cell stripe width w_a and parametrized over different series resistances $R'_{s,P2}$ of: 1 Ωcm , 2 Ωcm , 5 Ωcm , and if no series resistance formation is considered. Tandem solar cell input parameters are: $J_{\text{MPP}}=9.7 \text{ mA/cm}^2$, $V_{\text{MPP}}=1.11 \text{ V}$, $R_{\text{SH}}=8 \Omega$, and $w_d=300 \mu\text{m}$.

Test-structure: a special test procedure is applied for an accurate evaluation since the contact resistance is not directly measurable. Figure 6.20 shows the test-structure for the $I - V$ measurement after P2 absorber processing and back-contact deposition. The total resistance $R_{\text{Total,xy}}=V_{\text{xy}}/I_{\text{xy}}$ from Figure 6.20 can be described as followed,

$$R_{\text{Total}} = R_c + R_{\text{TCO}}(d) + R_c = \frac{R_{\text{SH}}}{W}d + 2R_c. \quad (6.29)$$

Here, W is the width of the contact out-of-plane and R_{SH} is the TCO sheet resistance. The resistance $R_{\text{TCO}}(d)$ is linearly dependent on the distance d between the two contacts. Thus, if the total resistance R_{Total} is measured for different contact distances d a linear behavior is obtained. The extrapolation of R_{Total} with the y -axis intercept will yield two times the contact resistance R_c (distance $d \rightarrow 0$).

In literature this method is known as Transfer Line Method or Transfer Length Method (TLM) introduced by Goetzberger et al. [156]. For the evaluation of the specific contact resistance ρ_c between the front-contact and the back-contact it is not possible to simply multiply R_c with the contact area $A = w_{p2}W$. For the given geometry the TCO thickness d_{TCO} is much smaller than the scribe width w_{p2} . Hence, current crowding beneath the contacts occurs. From transmission line theory [157] the contact resistance R_c (considering current crowding as well) can be evaluated by the following equation,

$$R_c = \frac{\lambda_T R_{\text{SH}}}{W} \coth\left(\frac{w_{p2}}{\lambda_T}\right) = \frac{\sqrt{\rho_c R_{\text{SH}}}}{W} \coth\left(\frac{w_{p2}}{\lambda_T}\right) \quad (6.30)$$

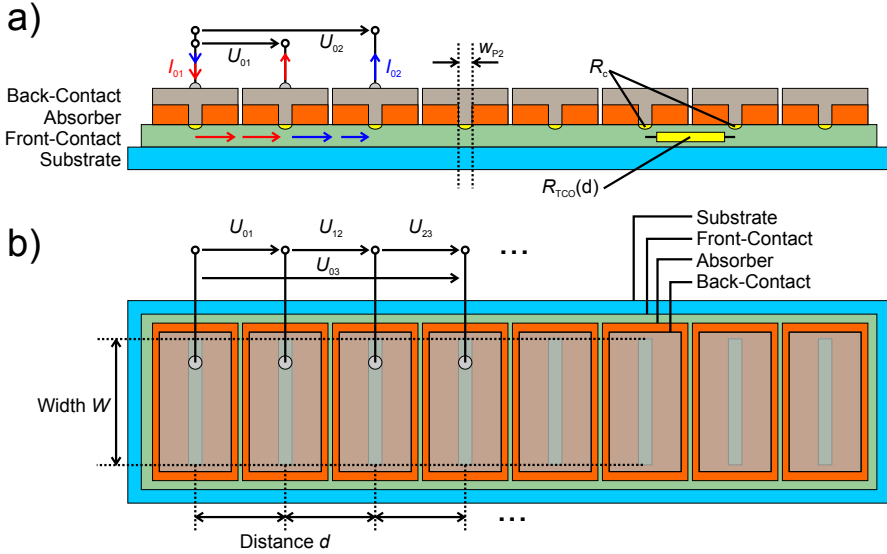


Figure 6.20: Measurement setup for determination of the contact resistance R_c with Transmission Line Method (TLM) with variable distance d between two P2 scribe lines. Here w_{p2} corresponds to the P2 scribing width. Sketches show: a) Front view with the measurement current I defined by two times the contact resistance R_c and TCO resistance for distance d . b) Top view with the eight contact pads used for the measurement with every permutation pair and distances d .

with,

$$\lambda_T = \sqrt{\frac{\rho_c}{R_{SH}}}. \quad (6.31)$$

Here, R_{SH} is, again, the sheet resistance and W the width of the contact in out-of-plane direction. Furthermore, w_{p2} is the contact length and λ_T is the transfer length which is defined by R_{SH} and the specific contact resistance ρ_c . The transfer length can be evaluated from the intersection between the extrapolated total resistance R_{Total} and the x -axis. It is a measure for the transition width beneath the P2 scribe line that is required for the transfer of 63% of the overall current from the TCO to the back-contact above. If λ_T is significantly larger than the physical width of the contact w_{p2} , current crowding occurs. Thus, the contact resistance depends on the contacts dimensions. With Equation 6.30 it is possible to numerically evaluate the specific contact properties ρ_c .

For the measurement a test-structure design with eight contacts and a distance d of 1 cm between each contact was processed. The width W of every contact was 1 cm as well. Mesa definition of the front-contact and absorber at the edges provide uniform current flow in x direction. A Keithley 2400 series SourceMeter was used in 4-Terminal mode sourcing a voltage of -0.5 V to 0.5 V with a step-size of 50 mV. To minimize the influence of non-uniform

sheet resistance values and contact property deviations measurements were conducted with a permutation of every terminal combination. For eight terminals this lead to 28 combinations. Seven with a distance d of 1 cm, six with 2 cm, five with 3 cm, and so on.

Transmission Line Method (TLM): for determination of the parasitic series resistance $R_{s,P2}$ TLM measurements were carried out as a function of the peak fluence F_p . The feed rate v and pulse repetition frequency f_{PRF} was taken from the respective visually optimized scribe (see Figures 6.4, 6.5).

Figure 6.21 shows the results for processing of a-Si:H material with different laser spot radii ω_0 . The trends in the graph look similar for all three spot sizes. Different regions to describe the

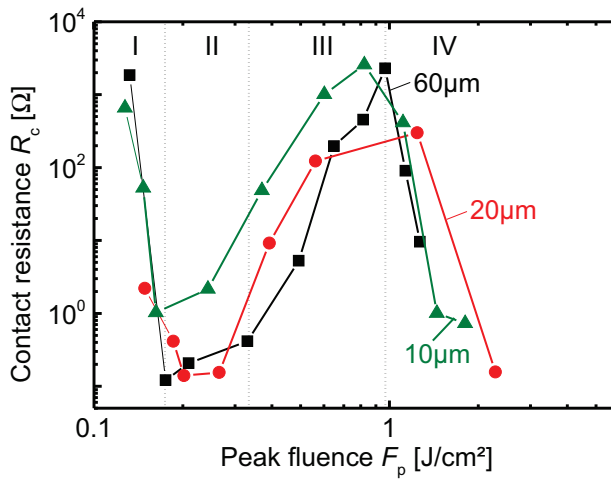


Figure 6.21: Contact resistance R_c after processing of a 300 nm thick a-Si:H absorber layer from TLM measurements vs. peak fluence F_p at fixed feed-rate v and repetition frequency f_{PRF} for different processing laser beam radii ω_0 of 60 μm (squares), 20 μm (circles), and 10 μm (triangles). The distance d between the contacts as well as the contact width W was 1 cm.

curves behavior can be defined and are marked by the dashed lines, exemplary for processing with 60 μm (filled squares).

- Region I: Below 0.2 J/cm⁻² the contact resistance R_c is very high since the scribe line is discontinuous and the contact area $A = w_{p2}W$ is very small.
- Region II: Then R_c rapidly decreases exhibiting a minimum with a comparatively low resistance. The extent of this region defines the stability window for the P2 process.
- Region III: Next, R_c increases significantly with increasing peak fluences. Strong visual changes of the TCO layer beneath are observed in this region.

- Region IV: For very high peak fluences the contact resistance decreases again. In most cases TCO ablation occurs in this regime.

A comparison of the resistance values for the different laser beam radii shows a slightly narrowing process window for higher focusing (extent of region II). Furthermore, in average, an increase of R_c for decreasing ω_0 is observed. This is especially important in region II where the values for ω_0 of 10 μm are strongly increased.

Figure 6.22 shows a plot of the contact resistances R_c for processing of tandem absorber with fixed ν and f_{PRF} chosen according to the visually optimized scribe parameters for the different ω_0 (compare Figure 6.5). The trends show similarities to the plot from Figure 6.21 and the

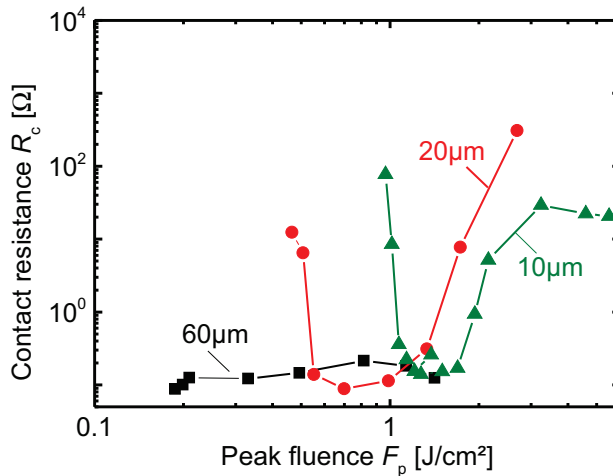


Figure 6.22: Contact resistance R_c after processing of a 1.4 μm thick tandem absorber from TLM measurements vs. peak fluence F_p at fixed feed-rate ν and repetition frequency f_{PRF} for different processing laser beam radii ω_0 of 60 μm (squares), 20 μm (circles), and 10 μm (triangles). The distance d between the contacts as well as the contact width W was 1 cm. For comparison, scales are the same as in Figure 6.21.

different regions can be found accordingly. Only for processing with 60 μm a large region II is obtained and the magnitude of increase in region III is rather low. Furthermore, a shift of region II to higher peak fluences is observed for processing with 20 μm and 10 μm due to the increasing onset peak fluence for these processing radii. With respect to the process stability, the extent of region II is decreasing with decreasing ω_0 .

One explanation for the rise of R_c in the third region is possible deterioration of the TCO layer and increasing debris redeposition within the scribe as it was already shown by Ku et. al [154]. Lauzurica et. al investigated the front-contact surface after P2 scribing with EDX and observed silicon accumulation [155]. Investigations of the front-contact surface morphology

were carried out to see if these effects can explain the observed trend of the contact resistance versus the peak fluence.

6.4.1 Ablation debris redeposition

As indicated earlier, it is widely accepted that the parasitic series resistance for P2 is formed by debris redeposition onto the exposed TCO layer [45, 154, 155]. In the following investigations were carried out to determine whether the series resistance increase for P2 scribes with minimized width can be attributed to an increase/change of debris redeposition.

A large amount of near scribe edge modifications were observed with the optical microscope after back-contact deposition as shown in Figure 6.23 exemplary for the case of a-Si:H processing with 60 μm . The figure shows that with increasing peak fluence the amount of surface changes is also increasing. The shape and distribution is similar to the earlier findings for the surface modifications found for front-contact structuring in the previous Chapter 5. Please note that these changes are visually only observed after back-contact deposition. The increasing pulse energy in Figure 6.23 is in accordance with the used pulse energies from the TLM experiments in Figure 6.21. Figure 6.23(a) and (b) correspond to the region II, (c) to (f) to the region III with increasing contact resistance R_c , and (g) and (h) to the region marked with IV.

In a comparison between the amount of near edge changes and the contact resistance R_c from Figure 6.21 (filled squares) it is concluded that there are only small visual changes for peak fluences within the process window (regime II). However, the amount increases dramatically for higher peak fluences and decreases again for the highest peak fluences. Furthermore, there is a unsymmetrical shift of visual changes that is weighted to the right in the Figures 6.23(d)–(f). For very high peak fluence the shift disappears and visual changes are spread symmetrically around the scribe line.

The increasing brightness of the center of the scribe line is a strong sign for material changes/-damaging of the exposed front-contact material beneath. Furthermore, in Figure 6.23(h) partial ablation of the front-contact is observed as well.

The same behavior was observed, especially, for processing of a-Si:H as well as for tandem absorber processing with decreased laser beam radii of 20 μm , and 10 μm . Surface morphology, before back-contact deposition, was characterized by SEM. This was done to investigate any possible correlations between amount of debris redeposition on the remaining absorber and within the P2 scribe. Figure 6.24 shows a compilation of SEM images of the front-contact surface after P2. For better visualization of the behavior SEM images for processing of a-Si:H material with a laser beam spot radius of 10 μm are shown. The images show that strong debris redeposition is apparent on the front-contact surface (Figure 6.24(a) and (b)) which increases with increasing peak fluence. For high fluence regimes with partial front-contact ablation (Figure 6.24(c) and (d)) the exposed TCO surface is very smooth possibly due to melting, without signs of debris redeposition. This could explain the decrease of the contact resistance R_c in regime IV.

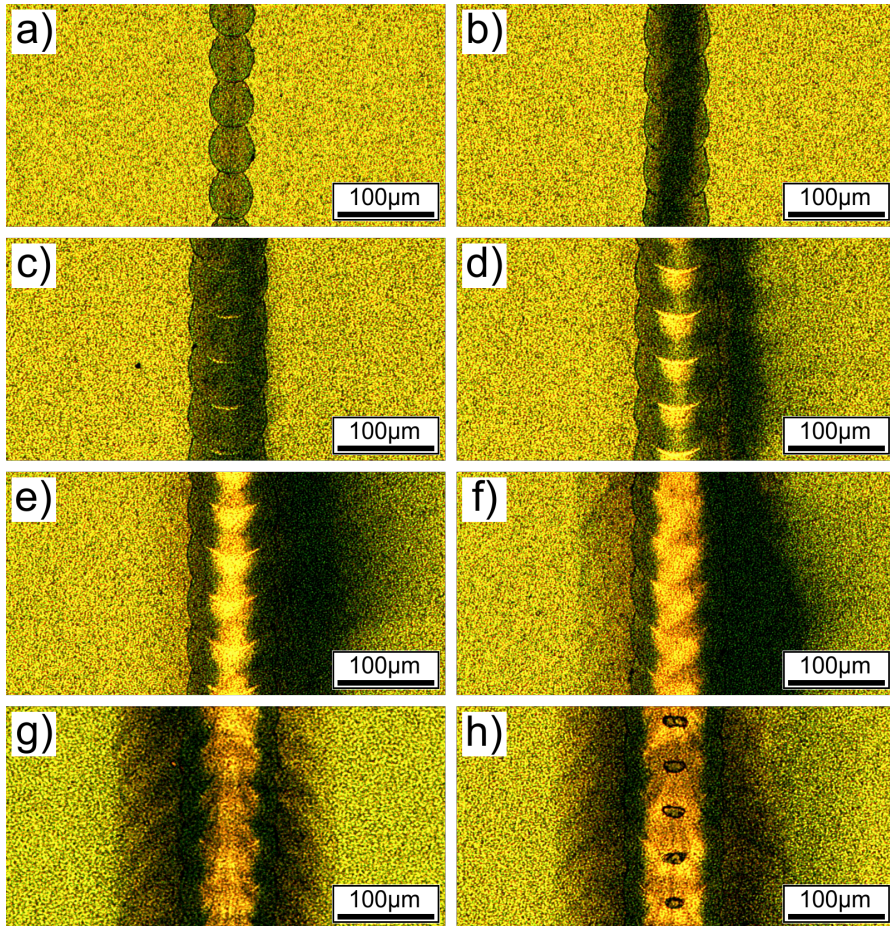


Figure 6.23: Optical microscopy images of P2 scribes on a-Si:H absorber material, with subsequent back-contact deposition, processed with a laser beam spot radius of 60 μm . Images from a) to h) with increasing peak fluence F_p of: 0.21, 0.33, 0.49, 0.65, 0.82, 0.97, 1.13, and 1.27 Jcm^{-2} corresponding to values from Figure 6.21 (filled squares).

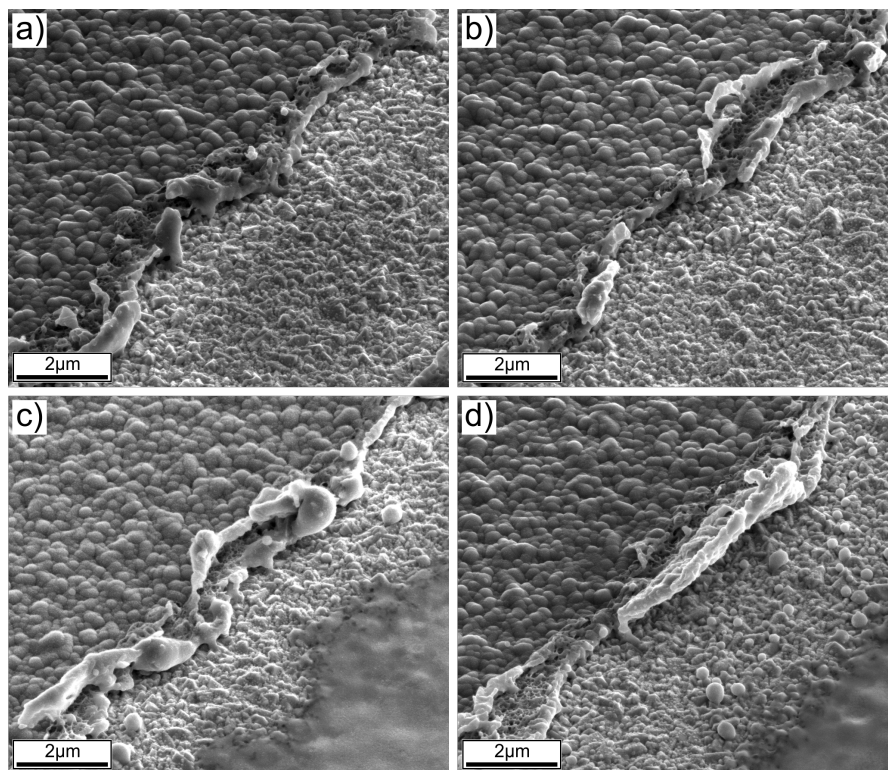


Figure 6.24: SEM images of P2 scribes on a-Si:H absorber material processed with a laser beam spot radius of 10 μm . Images from a) to d) with increasing peak fluence F_p : 0.37, 0.6, 1.45, and 4.59 Jcm^{-2} .

Additionally, the scribe edge morphology shows signs of rupture alongside with melting. Thus, ablation behavior is not purely determined by brittle fracture at the scribe edge, at least for increased peak fluences. Changes of mechanical properties by material melting can have an impact on the resulting scribe width, at least for processing of a-Si:H with 10 μm .

In contrast to this behavior, processing of tandem absorber material exhibits a very steep scribe edge over a large region of peak fluences and beam radii. A comparison between the surface distribution of debris redeposition for processing of a-Si:H and tandem showed differences that could explain the differences in minimal achievable contact resistances (cf. Figure 6.21 and 6.22).

Figure 6.25 shows a comparison between both processing setups. The direct comparison shows that surface residuals for processing of tandem absorbers mainly consist of resolidified silicon filaments (Figure 6.25(b)). In contrast, for a-Si:H processing the front-contact surface is covered by small redeposited spherical particles with a higher surface coverage (Figure 6.25(a)). It is possible that the filaments and fiber-like residuals do not affect the contact resistance as strongly as the layer of spherical particles (Figure 6.25(c)) which was seen by the lower minimal resistances observed for tandem processing.

The amount of surface residuals seen in the SEM is in perfect agreement with the visible modifications seen from the optical microscopy images. They tend to increase with decreasing processing beam radii which was also observed for front-contact structuring before. Correspondingly, it is possible that the residuals have an impact on the active material in adjacency to the P2 scribe. This would be detrimental since no cleaning or post-treatment is intended after P2 structuring.

For the optimization approach it would be helpful to reduce the amount of debris redeposition to increase the processing window as well as achieve lower minimal values of the contact resistance R_c . To investigate this, further experiments under vacuum conditions were carried out.

6.4.2 Atmospheric conditions

It is well-known from literature that the pressure has a significant impact on the laser plasma particle distribution/velocities and therefore on the ablation debris [158, 159, 160]. Experiments of P2 processing on tandem absorbers were conducted with similar laser parameters and a beam spot radius of 20 μm according to the peak fluences from Figure 6.22 (circle symbols). The difference to the previous experiment is that processing was also done at vacuum conditions at a pressure of $1.5 \cdot 10^{-5}$ mbar. Figure 6.26 shows the TLM measurement comparing both processing conditions. Both samples exhibit the same behavior for fluences up to the third region (III). Here, the sample processed under vacuum conditions shows only a slight increase of R_c whereas the sample processed in air exhibits a large increase. Figure 6.27 shows optical microscope images for the two processing parameters marked with stars in Figure 6.26. Visual inspection with optical microscopy reveals a greatly reduced debris redeposition along the

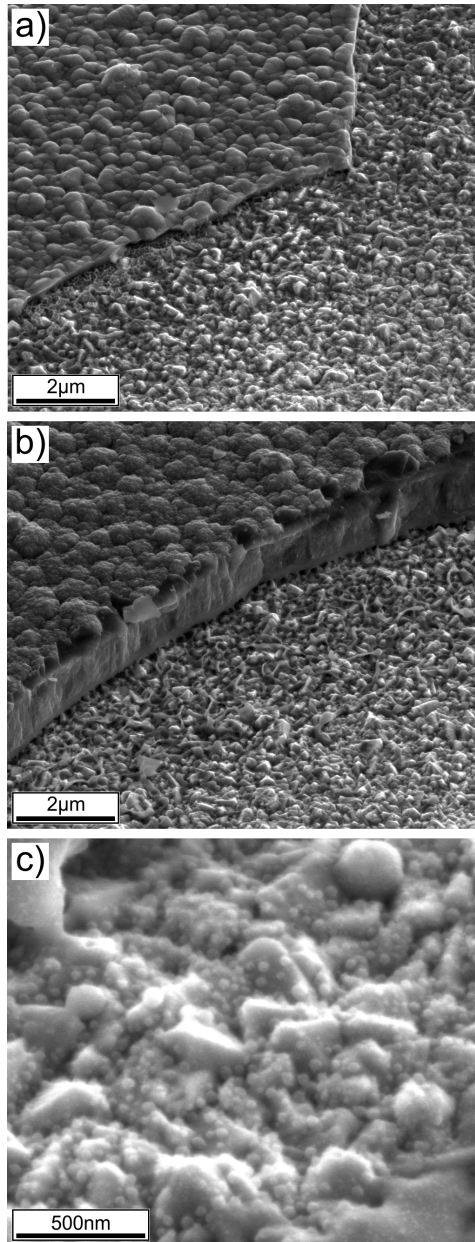


Figure 6.25: SEM images for comparison of P2 scribes processed with a laser beam spot radius of 60 μm. Image show: a) Processed a-Si:H with a peak fluence F_p of 0.49 Jcm^{-2} . b) Tandem absorber processing with 0.21 Jcm^{-2} . c) Magnified view of the surface redeposition for a-Si:H processed with a radius of 10 μm.

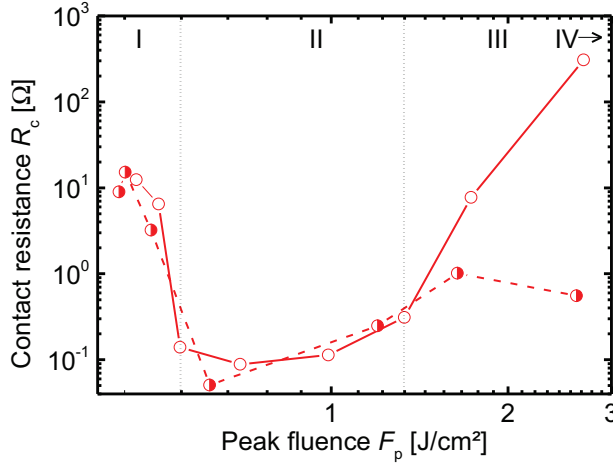


Figure 6.26: Contact resistance R_c after processing of a 1.4 μm thick tandem absorber layer from TLM measurements vs. peak fluence F_p and fixed feed-rate v for a processing laser beam radius of 20 μm in air (filled circles) and at a pressure of $1.5 \cdot 10^{-5}$ mbar (empty circles). Distance d between the contacts as well as the contact width W was 1 cm. Region IV is outside the processing parameter spectrum. Stars mark the parameter where optical microscopy was evaluated after back-contact deposition.

scribe edge for the sample processed in vacuum (Figure 6.27(b)). In contrast, a high amount of residuals are observed for processing in ambient atmosphere (Figure 6.27(a)). Therefore, the high increase in region III for samples processed in air can be owed to the increase of debris redeposition. A slight increase is observed for vacuum processed samples as well which could be explained by TCO layer damage ablation, and minor debris redeposition.

6.4.3 Series resistance solar module losses

Coming back to the electrical properties, for better comparison, all minimal values of R_c from TLM measurements are listed in Table 6.3 for processing of both absorber materials from Figure 6.21 and Figure 6.22. In most cases the value of F_p that belongs to the minimal resistance $R_{c,\text{min}}$ differs from the visually optimized values (see Figure 6.4 and 6.5). This shows that visual evaluation of the scribe lines alone is not sufficient to achieve optimized electrical properties and needs to be considered.

It is interesting to note that values of $R_{c,\text{min}}$ for processing of tandem absorber are all in the same value range while for the a-Si:H absorber $R_{c,\text{min}}$ is strongly increased for processing with 10 μm . This cannot be described just by the contact area reduction due to the very low scribe width w_{p2} . Thus, a change of the specific contact behavior ρ_c is possible.

To see if the processing geometry has an impact on ρ_c or changes are only due to the contact geometry Equation 6.30 was numerically evaluated to determine ρ_c . Table 6.4 shows the

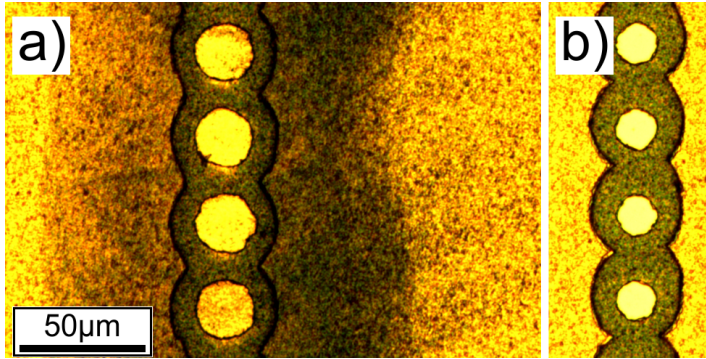


Figure 6.27: Optical images of P2 scribes of 1.4 μm thick tandem solar cell material on $\text{SnO}_2\text{:F}$ TCO after back-contact deposition. Parameters: a) According to filled-stars. b) Matching with empty stars from Figure 6.26. Differences in scribe width are due to slight differences in peak fluences.

Table 6.3: Minimal contact resistance values $R_{c,\text{min}}$ for P2 processing of a-Si:H and tandem absorber layers on $\text{SnO}_2\text{:F}$ TCO with different beam spot radii ω_0 . *No continuous line, single spots.

Absorber type (thickness)	Spot radius ω_0	Peak fluence F_p	Scribe width w_{p2}	Contact resistance $R_{c,\text{min}}$
a-Si:H (300nm)	60 μm	0.17 Jcm^{-2}	*30 μm	121 \pm 2 m Ω
a-Si:H (300nm)	20 μm	0.20 Jcm^{-2}	16 μm	140 \pm 21 m Ω
a-Si:H (300nm)	10 μm	0.16 Jcm^{-2}	6 μm	1024 \pm 6 m Ω
tandem (1.4 μm)	60 μm	0.19 Jcm^{-2}	40 μm	88 \pm 5 m Ω
tandem (1.4 μm)	20 μm	0.70 Jcm^{-2}	36 μm	90 \pm 4 m Ω
tandem (1.4 μm)	10 μm	1.50 Jcm^{-2}	24 μm	152 \pm 3 m Ω

results of this numerical evaluation. The TCO sheet resistance R_{SH} was extracted from the slope of the TLM measurements according to Equation 6.29. A comparison of the first three values of ρ_c from Table 6.4 for a-Si:H absorber processing show quite substantial differences which indicates that there are changes of the contact properties. For very narrow scribe lines a strong increase not only for the R_c but also for ρ_c is observed. For processing of tandem absorber layers (last three rows) ρ_c is almost constant (0.028 Ωmm^2 –0.034 Ωmm^2) indicating contact properties independent from the processing geometry. The number of data points within the region II is quite sparse. Further investigations in this region could be helpful to substantiate the observed deterioration of specific contact properties for P2 processing with smaller beam spot sizes.

Trade-off: it is now possible to obtain the optimal relation between increase of Ohmic losses from increasing values of $R_{c,\text{min}}$ vs. gain of active area w_a . From the reduction of w_{p2} the extended model from Gupta accounting for P2 series resistance losses is used (cf. Equation 6.27).

6.4. Impact on electrical properties

Table 6.4: Calculation of the specific contact resistance ρ_c from Equation 6.30 for P2 processing of a-Si:H and tandem absorber layers on SnO₂:F TCO with the electrically optimal processing parameters from Table 6.3. Parameters are: a-Si:H layers (row 1–3) and tandem layers (row 4–6).

Sheet resistance R_{SH}	Contact resistance $R_{c,min}$	Specific contact resistance ρ_c
$7.68 \pm 0.02 \Omega$	$12 \pm 2 \text{ m}\Omega$	$0.034 \Omega\text{mm}^2$
$7.6 \pm 0.02 \Omega$	$140 \pm 21 \text{ m}\Omega$	$0.021 \Omega\text{mm}^2$
$7.57 \pm 0.01 \Omega$	$1024 \pm 6 \text{ m}\Omega$	$0.061 \Omega\text{mm}^2$
$8.57 \pm 0.01 \Omega$	$88 \pm 5 \text{ m}\Omega$	$0.031 \Omega\text{mm}^2$
$8.67 \pm 0.01 \Omega$	$90 \pm 4 \text{ m}\Omega$	$0.028 \Omega\text{mm}^2$
$8.57 \pm 0.01 \Omega$	$152 \pm 3 \text{ m}\Omega$	$0.034 \Omega\text{mm}^2$

The value $R'_{s,P2} = R_{c,min} W$ is equivalent with the P2 processing series resistance normalized by the cell stripe length (Equation 6.28). Figure 6.28 shows calculations for a tandem module with different P2 scribe widths w_{P2} and the corresponding $R_{c,min}$ to estimate their influence on the overall module loss fraction f . As reference, a calculation with processing parameters commonly used in industry is plotted for comparison assuming an P2 scribe width w_{P2} of $90 \mu\text{m}$ [64] and an series resistance $R_{s,P2}$ of $100 \text{ m}\Omega\text{cm}$. There is only a slight difference

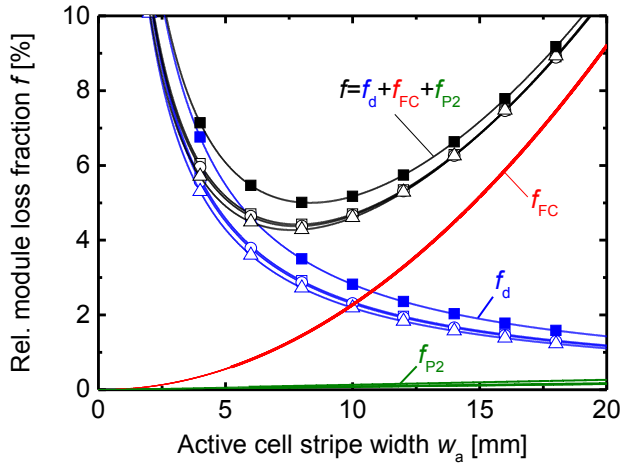


Figure 6.28: Module loss fraction calculation for a tandem solar module with different P2 scribe widths w_{P2} and corresponding $R'_{s,P2}$ values from measurement. Processing parameters are $(w_{P2}/R'_{s,P2})$: $40 \mu\text{m}/88 \text{ m}\Omega\text{cm}$ (empty squares), $36 \mu\text{m}/90 \text{ m}\Omega\text{cm}$ (empty circles), $24 \mu\text{m}/152 \text{ m}\Omega\text{cm}$ (empty triangles), and typical reference values assuming $90 \mu\text{m}/100 \text{ m}\Omega\text{cm}$ (filled squares). The remaining part of the interconnection width w_d was kept at $200 \mu\text{m}$. Solar cell parameters are: $J_{MPP}=9.7 \text{ mA}/\text{cm}^2$, $V_{MPP}=1.1 \text{ V}$, and $R_{SH}=8 \Omega$.

between the electrically optimized P2 processing parameters for w_0 of $60 \mu\text{m}$, $20 \mu\text{m}$, and $10 \mu\text{m}$ (empty squares, empty circles, and triangles). The highest difference is predicted between the reference parameter (filled squares) and the optimized ones. A relative reduction

of module losses by 1% is predicted at the optimal cell stripe width with minimal overall losses f .

A similar calculation was also made for the scribe width reduction of a-Si:H absorber scribing with the electrical parameter for the optimized processes from Table 6.1. Figure 6.29 shows a plot with these calculations. The general behavior is quite similar to the calculations from Fig-

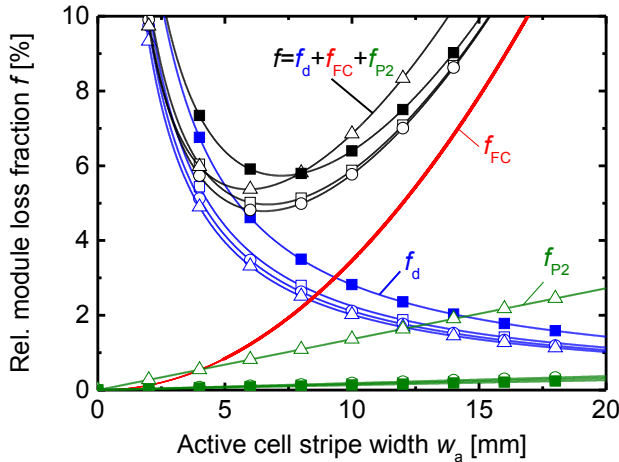


Figure 6.29: Module loss fraction calculation for an a-Si:H solar module with different P2 scribe widths w_{P2} and corresponding $R'_{s,P2}$ values from measurement. Processing parameters are $(w_{P2}/R'_{s,P2})$: $30\ \mu\text{m}/121\ \text{m}\Omega\text{cm}$ (empty squares), $16\ \mu\text{m}/140\ \text{m}\Omega\text{cm}$ (empty circles), $6\ \mu\text{m}/1024\ \text{m}\Omega\text{cm}$ (empty triangles), and typical reference values assuming $90\ \mu\text{m}/100\ \text{m}\Omega\text{cm}$ (filled squares). The remaining part of the interconnection width w_d was kept at $200\ \mu\text{m}$. Solar cell parameters are: $J_{MPP}=10.17\ \text{mA}/\text{cm}^2$, $V_{MPP}=0.765\ \text{V}$, and $R_{SH}=8\ \Omega$.

ure 6.28 except for the parameters from processing with $\omega_0=10\ \mu\text{m}$. Here, the P2 loss fraction f_{P2} is significantly increased. For this case, the width reduction is actually counterproductive when considering the overall losses. Overall losses f tend to decrease from the reference parameters (filled squares) to scribing with the optimized values of $60\ \mu\text{m}$ (empty squares). They reach a minimum for $20\ \mu\text{m}$ (empty circles) but then increase again for processing with $10\ \mu\text{m}$ (empty triangles). Bearing this in mind, a reduction of the overall losses is still possible and is in the range of approx. 1%. The reason for the increase of overall losses for $10\ \mu\text{m}$ processing can be attributed to the strong increase of the f_{P2} loss fraction which is significant in this case.

6.5 Process implementation in mini solar modules

As it was already shown for the scribe width optimization for P1, successful implementation of the optimized processes was tested with tandem mini modules on $\text{SnO}_2:\text{F}$. For the absorber structuring process P2 modules were prepared with optimized P1 and P2 scribes whereas the

standard processing parameters were used for back-contact structuring P3. All scribes were generated using a laser wavelength of 532 nm with laser beam radii of 10 μm for P1, 20 μm for P2, and 60 μm for P3. Figure 6.30 shows optical microscopy images of the interconnection region with the optimized scribes. The three laser scribing parameters for each line are:

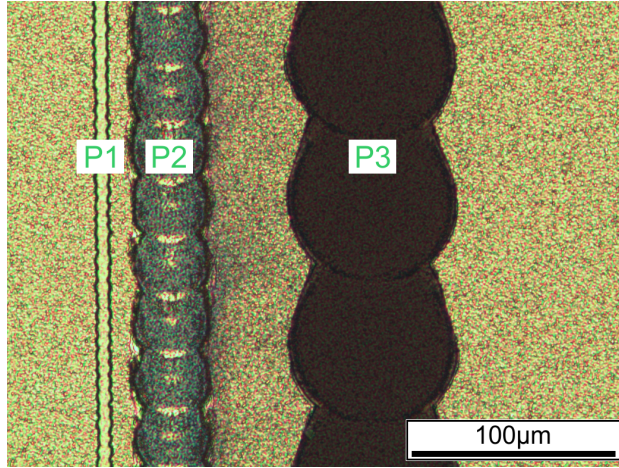


Figure 6.30: Optical microscopy image of the interconnection region of tandem mini modules prepared on $\text{SnO}_2:\text{F}$ TCO material with optimized P1 ($\omega_0=10 \mu\text{m}$, $F_p=3 \text{ Jcm}^{-2}$) and P2 scribes ($\omega_0=20 \mu\text{m}$, $F_p=0.82 \text{ Jcm}^{-2}$). For the back-contact insulation process P3 standard processing parameters were used ($\omega_0=60 \mu\text{m}$, $F_p=0.52 \text{ Jcm}^{-2}$).

$\omega_0=10 \mu\text{m}$, $F_p=3 \text{ Jcm}^{-2}$ for P1, $\omega_0=20 \mu\text{m}$, $F_p=0.82 \text{ Jcm}^{-2}$ for P2, and $\omega_0=60 \mu\text{m}$, $F_p=0.52 \text{ Jcm}^{-2}$ for P3.

Figure 6.30 shows that there are some slight irregularities at the P2 scribe edge observed when this line is compared with the scribe obtained from the scribe line optimization in Figure 6.5(b). Furthermore, the used laser peak fluence is higher as well (0.82 Jcm^{-2} vs. $0.6\text{--}0.7 \text{ Jcm}^{-2}$ in Figure 6.26). This is owed to the fact that all modules were prepared with a higher absorber thickness of approx. $2.2\text{--}2.4 \mu\text{m}$. It was significantly higher compared to the thickness of $1.4 \mu\text{m}$ for the tandem absorbers that were under investigation. Thus, the width of the P2 scribe line is slightly increased as well.

Mini modules with four different active cell stripe widths w_a of 2 mm, 3 mm, 5 mm, and 10 mm were prepared. The cell length l of 30 mm was fixed. The number of interconnected cells was in correspondence with the individual cell stripe width: 40, 25, 16, and 8. Furthermore, single solar cells were prepared as well on the same substrates for comparison. Table 6.5 shows the module parameters extracted from the $I - V$ characteristics. Similar to the optimization of P1, modules with optimized P1 and P2 scribes exhibit no negative impact on the electrical properties. No shunting or increased series resistances are observed for the optimized laser processes. A high fill-factor is achieved for all modules with no large differences to single solar

Table 6.5: AM1.5 $I - V$ characteristics of a-Si:H/ μ c-Si:H tandem solar modules on SnO₂:F with optimized P1, and P2 scribe lines and standard P3 scribes. Laser processing was done with 532 nm. For P1 a beam spot radius of 10 μ m and a peak fluence of $F_p=3 \text{ Jcm}^{-2}$ were used. For P2 processing 20 μ m, and $F_p=0.82 \text{ Jcm}^{-2}$ were used, whereas 60 μ m, and $F_p=0.52 \text{ Jcm}^{-2}$ were used for standard P3 processing. All cell stripe length W are 30 mm. On each substrate three solar cells with an area of 1 cm^2 were prepared for comparison and median values are given.

Substrate number	Active cell stripe width (# cells)	Module efficiency η	Fill-Factor FF	Open-circuit voltage V_{OC}	Short-circuit current I_{SC}
1	2 mm (40)	9.7%	73.2%	50.12 V	6.2 mA
1	3 mm (25)	10.9%	74.4%	33.75 V	9.4 mA
2	5 mm (16)	10.4%	74.4%	21.35 V	15.7 mA
2	10 mm (8)	10.3%	73.1%	10.69 V	31.6 mA
1	10 mm (1)	11.4%	74.6%	1.34 V	11.4 mA
2	10 mm (1)	10.9%	74.6%	1.33 V	10.9 mA

cells. Furthermore, the open-circuit voltage V_{OC} of each module corresponds to the theoretical value except for the module with 2 mm cell stripe with. Here it seems that some cell stripes are short-circuited.

As a conclusion for P2 absorber processing it can be said that for laser-induced substrate side ablation of thin-film silicon layers on TCO the ablation behavior strongly depends on the laser beam spot size and/or layer thickness. Evaluation of the Liu-Plots for the different processing setups showed that the threshold fluence is not sufficient for the characterization. The onset peak fluence, where proper ablation occurs, provides important information and showed that there are limits to width reduction due to increase of said value with decreasing laser spot sizes.

Debris collected during processing indicates that the ablation process is highly assisted by mechanical stresses. Temperature distributions from transient thermal modeling lead to conclude that ablation full phase transitions can be ruled out.

Hydrogen-assisted vapor-stress as well as stress by thermal expansion can explain the observed experimental results. Both in terms of magnitude of occurring forces as well as ablation property changes for different layer geometries and beam spot radii.

For the scribe width reduction it can be concluded that for laser processing from the substrate side thin scribes are only possible with thin absorber layers. The reason is to be found in the delamination and fracture behavior of the layer-stack materials.

The minimal achievable contact resistances $R_{c,min}$ for processing of a-Si:H measured by TLM were somewhat higher than for tandem absorber. This can be accounted to changes of the specific contact resistance ρ_c for a-Si:H processing with a spot radius of 10 μ m. For tandem absorber processing a regime with low resistance values could be found for all three processing laser beam spot radii. But, the scribing parameters for electrically optimal scribe lines differ

6.5. Process implementation in mini solar modules

from the visually evaluated optimal lines. It is therefore necessary to conduct an electrical evaluation of the contact properties to obtain the optimal processing parameters.

An extension of the model by Gupta to account for series resistance losses showed that a reduction of the relative module losses are predicted to be in the range of at least 1%. For the overall tandem module losses the fractional losses due to f_{p2} are almost negligible compared to gain of active area which gives motivation for a further width reduction. However, for processing of a-Si:H solar cell material an improvement of the specific contact resistance ρ_c is necessary to reduce the series resistance losses.

The next chapter is dedicated to the back-contact insulation process P3. However, the laser process is similar to P2. Even higher constraints on the minimal achievable scribe widths due to a higher overall layer-stack thickness (back-contact thickness about 360 nm) can be expected.

7 Back-contact insulation process P3

In this chapter the results for the last interconnection processing step, the back-contact insulation P3, are presented. The laser process for the back-contact ablation is similar to the absorber structuring process P2. In both cases a laser with a wavelength of 532 nm is used for the ablation of the absorber. The back-contact is removed indirectly by removal of the underlying silicon absorber (cf. Figure 2.9). Unfortunately, the same (or even higher) geometrical constraints on the scribe width minimization found for P2 apply to the P3 process as well.

In the first part, basic ablation behavior was investigated by single spot crater ablation of a-Si:H and tandem solar cells (both with ZnO:Al/Ag/ZnO:Al back-contact) for laser processing with 532 nm and beam radii of 60 μm , 20 μm , and 10 μm .

Subsequently, visually optimized scribe lines were created. Before the impact on the solar module due to P3 scribing was characterized theoretical calculations were conducted to estimate the behavior of sub-threshold energy intake as a function of laser peak fluence and beam radius. Afterwards, a special test procedure for P3 processing was used on single solar cells and the impact on the electrical properties was evaluated.

In the last part changes of the active materials microstructure at the direct P3 scribe edge were investigated by Raman microscopy. A possible crystallization of the absorber material can be detected by Raman spectroscopy. A change of crystallinity is known to be linked to an increase of the electrical conductivity at the direct scribe edge leading to parasitic shunting of the cell [161, 45, 118].

7.1 Material ablation behavior

Investigations on the ablation properties as function of the layers and laser beam radii were carried out on a-Si:H and tandem solar cells on SnO₂:F TCO material. For all experiments the same back-contact topology of sputtered ZnO:Al/Ag/ZnO:Al layers was used. The nominal thickness of the individual layers was 80 nm (ZnO:Al), 200 nm (Ag), and again 80 nm (ZnO:Al).

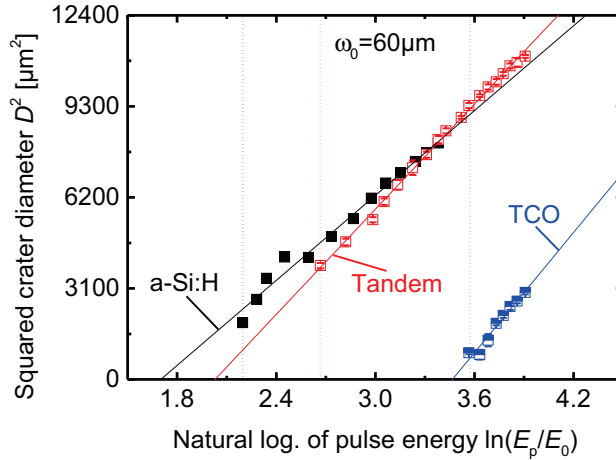


Figure 7.1: Liu-Plot of a-Si:H p-i-n solar cell absorber (filled squares) and tandem material (empty squares) with ZnO:Al/Ag/ZnO:Al back-contact for a laser beam spot radius of $60 \mu\text{m}$. Half-filled squares correspond to TCO damage ablation values (for tandem absorber). Dashed lines mark the onset pulse energies where ablation occurs.

The absorber layer thicknesses were the same as in the previous Chapter 6 with 300 nm for the a-Si:H absorber and $1.4 \mu\text{m}$ for the tandem absorber. The thickness of the $\text{SnO}_2\text{:F}$ front-contact material was approx. 800 nm .

Liu-Plots: both material systems were processed with 532 nm and different laser beam spot radii of $60 \mu\text{m}$, $20 \mu\text{m}$, and $10 \mu\text{m}$. The corresponding Liu-Plots are shown in Figure 7.1, 7.2, and 7.3. The undesired TCO single crater ablation measured from tandem solar cell processing is shown as well for estimation of the processing window. Furthermore, for better comparison, all extracted values from the Liu-Plots are listed in Table 7.1 as well.

First, a comparison of the extracted radii $\omega_{0,\text{Liu}}$ with the measured values ω_0 reveals good agreement between both values. However, there are exceptions for a-Si:H as well as undesired TCO ablation with $10 \mu\text{m}$. These possibly arise from changes of ablation mechanisms between low and high pulse energy regimes (observed also for P2 in Liu-Plot from Figure 6.3).

The same optical machine parameters were used as for processing of P2. The extracted radii exhibit good agreement to the values extracted from the Liu-Plots for P2 investigations as observed from the comparison between Table 6.1 and Table 7.1.

However, certain differences to P2 processing are observed. These can be seen when the difference in squared crater diameter D^2 (shift in the y -axis) is compared between processing of a-Si:H and tandem solar cells. For processing with $60 \mu\text{m}$ and $20 \mu\text{m}$ there is almost no difference observed in contrast to the results for the absorber removal P2 where the diameter for tandem absorber processing was always higher than for a-Si:H ablation.

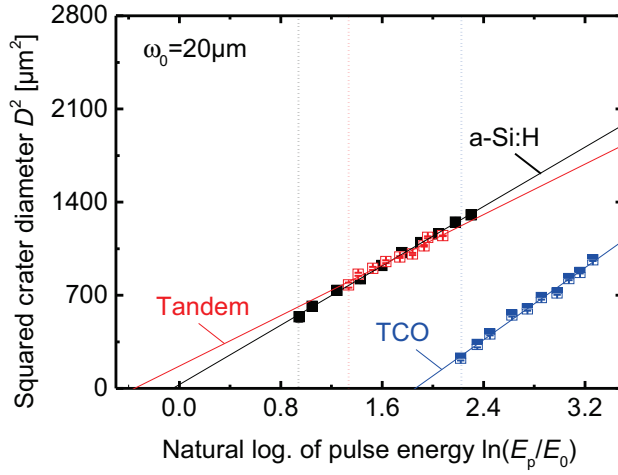


Figure 7.2: Liu-Plot of a-Si:H p-i-n solar cell absorber (filled squares) and tandem material (empty squares) with ZnO:Al/Ag/ZnO:Al back-contact for a laser beam spot radius of $20 \mu\text{m}$. Half-filled squares correspond to TCO damage ablation values (for tandem absorber). Dashed lines mark the onset pulse energies where ablation occurs.

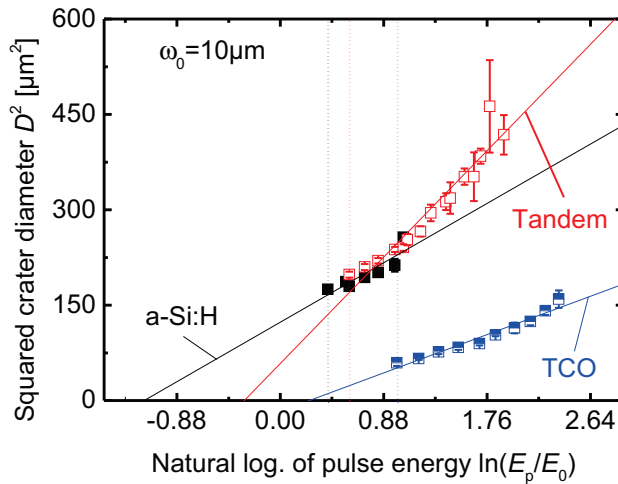


Figure 7.3: Liu-Plot of a-Si:H p-i-n solar cell absorber (filled squares) and tandem material (empty squares) with ZnO:Al/Ag/ZnO:Al back-contact for a laser beam spot radius of $10 \mu\text{m}$. Half-filled squares correspond to TCO damage ablation values (for tandem absorber). Dashed lines mark the onset pulse energies where ablation occurs.

Table 7.1: Extracted values from Liu-Plots of P3 processing for 300 nm thick a-Si:H solar cells and 1.4 μm thick tandem solar cells with 360 nm ZnO:Al/Ag/ZnO:Al back-contact. All samples were deposited on SnO₂:F TCO material (parasitic ablation measured on tandem solar cells). *Linear regression evaluated in the low pulse energy regime. Standard deviation calculated by maximum error estimation by 1st degree Taylor approximation.

Material	Radius from profiler ω_0	Radius from slope $\omega_{0,\text{Liu}}$	Threshold fluence F_{th}	Onset peak fluence $F_{\text{p,on}}$
a-Si:H	60 μm	49.1 \pm 0.9 μm	0.14 \pm 0.21 Jcm ⁻²	0.16 Jcm ⁻²
a-Si:H	20 μm	16.7 \pm 0.1 μm	0.22 \pm 0.04 Jcm ⁻²	0.41 Jcm ⁻²
a-Si:H	10 μm	7.3 \pm 0.8 μm	0.38 \pm 0.21 Jcm ⁻²	0.95 Jcm ⁻²
tandem	60 μm	54.6 \pm 0.3 μm	0.16 \pm 0.08 Jcm ⁻²	0.25 Jcm ⁻²
tandem	20 μm	15.4 \pm 0.5 μm	0.19 \pm 0.16 Jcm ⁻²	0.60 Jcm ⁻²
tandem	10 μm	9.7 \pm 0.4 μm	0.49 \pm 0.16 Jcm ⁻²	1.15 Jcm ⁻²
SnO ₂ :F	60 μm	58.4 \pm 2.4 μm	0.60 \pm 0.69 Jcm ⁻²	0.62 Jcm ⁻²
SnO ₂ :F	20 μm	18.4 \pm 0.3 μm	1.21 \pm 0.17 Jcm ⁻²	1.46 Jcm ⁻²
SnO ₂ :F	10 μm	*5.9 \pm 0.2 μm	*2.38 \pm 0.24 Jcm ⁻²	1.72 Jcm ⁻²

It is possible that the transition point between interface delamination and layer-stack fracture at the perimeter of the crater is dominated by the back-contact system. The thickness of the back-contact is the same for processing of a-Si:H and tandem solar cells.

For processing with 10 μm a conclusive comparison of the crater diameter for both absorber materials is not possible due to large deviations of the crater diameter. However, it seems that in this case the diameter for tandem ablation is slightly higher.

The threshold fluence F_{th} reflects the merging differences between both solar cell topologies as it is seen in Table 7.1. Moreover, the threshold fluence F_{th} increases when the radius is decreased now for both layer-stack configurations. Nevertheless, in terms of characterization of the processing behavior the onset peak fluence is the appropriate parameter.

The comparison of the onset peak fluence $F_{\text{p,on}}$ between the different laser beam radii shows a significant increase with decreasing radii. This is in correspondence with what was already seen for P2 processing. Furthermore, between processing of a-Si:H and tandem for a given beam radius the onset for tandem ablation is always higher than the corresponding onset of a-Si:H ablation. The same trends of $F_{\text{p,on}}$ are observed for parasitic TCO ablation as well.

Most results are not very surprising and are as expected. The lower crater diameter limit is slightly increased compared to P2 due to the higher onset fluences (cf. Table 7.1 with Table 6.1).

Crater morphology: differences of the edge morphology were observed for tandem solar cell processing which can be seen exemplary in Figure 7.4. Similar to the results from P2 processing, the crater edge morphology shows differences between the three different laser beam radii. A clean edge definition is only found for processing with 60 μm (Figure 7.4(a)). For ablation with 20 μm and 10 μm high bulging and delamination of the absorber and back-contact at the crater edge is observed. Furthermore, a change of texture at the bulged region around the crater indicates that melting of the back-contact material occurred.

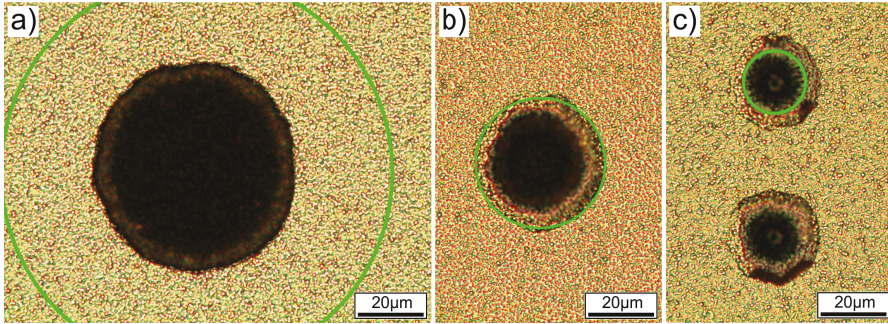


Figure 7.4: Optical microscope images of single crater ablation from tandem layer processing for the back-contact insulation process P3. Laser ablation was done with different beam radii of: a) $60\ \mu\text{m}$ and $0.25\ \text{Jcm}^{-2}$. b) $20\ \mu\text{m}$ and $0.6\ \text{Jcm}^{-2}$. c) $10\ \mu\text{m}$ and $1.15\ \text{Jcm}^{-2}$. The green inset circles represent the processing beam spot size.

In contrast to this, for P3 processing of a-Si:H solar cells a clean crater edge morphology was observed for all beam radii (not shown).

Melting and bulging of the crater edge occurs possibly due to the lower melting temperature of silver than a-Si:H and/or $\mu\text{c-Si:H}$ which is approx. 1234 K compared to 1422–1683 K. Furthermore, it is known that certain metals, like silver, exhibit a ductile fracture behavior [162]. These two thermal and mechanical material properties could be reasons for the distorted edge definition observed for the decreased beam spot sizes in Figure 7.4(b)–(c).

For a-Si:H solar cells the absorber layer thickness is significantly lower than for tandem solar cells. Therefore stronger heating of the back-contact system by heat conduction from the absorber could explain the differences in ablation morphology at the crater edge compared to tandem solar cell ablation.

7.1.1 Geometrical scribe width minimization

The onset fluences that were determined from the Liu-Plots were used to obtain processing parameters that will lead to visually optimized P3 scribe lines with a minimized scribe width. Optical microscopy images of these scribe lines are shown in Figure 7.5. For a-Si:H solar cell processing in Figure 7.5(a)–(c) a scribe width reduction in accordance with the laser beam radii reduction of $60\ \mu\text{m}$, $20\ \mu\text{m}$, and $10\ \mu\text{m}$ is possible. A clean scribe edge definition and minimal damaging of the underlying front-contact is achieved. Furthermore, no flake formation of the back-contact is observed even for the smallest beam spot radius.

Flake formation introduces an additional constraint for the P3 insulation process and is known to have a significant impact on the solar module properties [163].

In contrast to this, processing of tandem solar cells yields very different results as seen in the lower row of Figure 7.5(d)–(f). A similar ablation behavior at the direct scribe edge was already

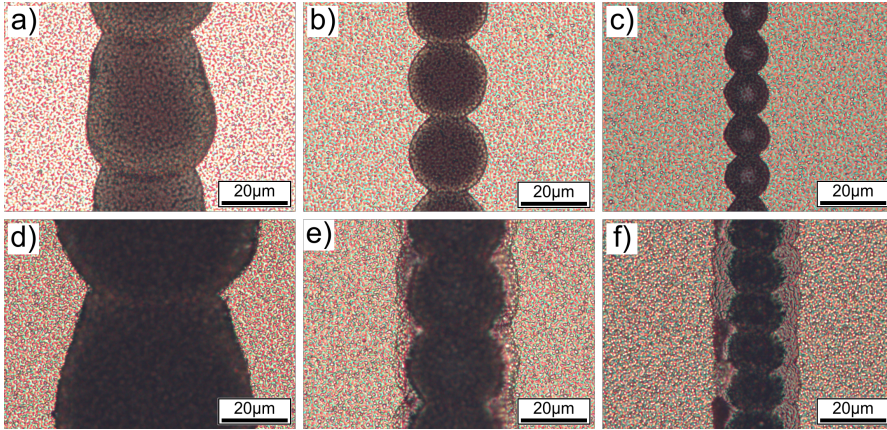


Figure 7.5: Optical microscope images of scribes with minimized widths for the back-contact insulation process P3. Upper row: a-Si:H processing. Lower row: tandem absorber ablation. Processing radii ω_0 and laser peak fluences F_p are: a) 60 μm and 0.16 Jcm^{-2} . b) 20 μm and 0.41 Jcm^{-2} . c) 10 μm and 0.95 Jcm^{-2} . d) 60 μm and 0.25 Jcm^{-2} . e) 20 μm and 0.65 Jcm^{-2} . f) 10 μm and 1.15 Jcm^{-2} .

observed for P2 absorber structuring of tandem absorber in Section 6.1.1. For processing with 20 μm and 10 μm no significant scribe width reduction is achieved and slight flake formation is observed in Figure 7.5(f). It is possible that for increased focusing no clean fracture of the layer-stack occurs. A rather plastic/ductile rip-off due to significant heating of the back-contact metal is likely. Especially when the layer thickness is increased and a higher onset peak fluence is required.

Furthermore, high front-contact damaging and partial ablation was observed for processing with 20 μm and 10 μm (not shown).

For these visually optimized P3 scribe lines in terms of scribe width and back-contact insulation the impact of P3 processing on the electrical properties of the solar cells was determined.

7.2 Impact on electrical properties

Just like it was already introduced for P1 and P2 processing, the back-contact insulation step P3 can have an impact on the electrical properties as well. An extension of the Gupta model is needed to account for these losses.

The main purpose of the P3 step is the final solar cell stripe definition (cf. Figure 2.9). For substrate side processing, the back-contact is removed indirectly by removal of the underlying absorber layer. This is favorable since the processing wavelength of 532 nm is highly absorbed by the silicon absorber avoiding, usually, significant heating of the back-contact.

Furthermore, this procedure is known to have an advantageous energy efficiency compared to direct illumination. For processing with a wavelength of 532 nm the silver metal layer is highly reflective. But, it is also known that shunting between front- and back-contact at the scribe edge can occur [163].

In literature, Haas et al. showed with electrical measurements and SPICE modeling that P3 processing can have a negative impact on the solar cell properties depending on the used processing wavelength [163]. Especially for semi-transparent modules with a high amount of P3 processing within the cell stripe a high influence on the module efficiency is observed [164]. Colina et al. showed with Raman microscopy at the scribe edge after P2 processing that changes of the a-Si:H absorber crystallinity can occur [118]. However, provision of the back-contact topology and thickness is important for the process since heat flux from the absorber to the back-contact occurs during P3 processing [161].

Shunting loss fraction: to account for power losses introduced by P3 the extension of the model by Gupta introduced earlier for P1 (loss fraction f_{p1}) can be extended to account for shunting by P3 (cf. Section 5.5).

A loss fraction describing shunting losses by a parasitic parallel resistance was introduced as an effect originating after absorber deposition into the P1 scribe. Now with P3 processing this parasitic shunt resistance can be redefined as the resulting resistance of the parallel connection of the two shunts $R_{p,P1}$ and a new value $R_{p,P3}$. A redefinition of the loss fraction $f_{p,P1}$ to $f_{p,P1,P3}$ can simply be made as followed,

$$f_{p1,P3} = \frac{V_{MPP}}{J_{MPP}} \frac{1}{R'_{p1,P3} w_a} \quad \text{with,} \quad R'_{p1,P3} = \frac{R_{p,P1} R_{p,P3}}{R_{p,P1} + R_{p,P3}} l. \quad (7.1)$$

The redefinition in Equation 7.1 shows that the shunting losses are represented by the shunt value of the parallel connection of the resistances $R_{p,P1}$ and $R_{p,P3}$ formed by both processes P1 and P3.

The origin of shunting from P3 processing is found at the direct scribe line edge where the resistance between front- and back-contact within one cell stripe is heavily reduced.

For better visualization of the process of shunting a schematic sketch of the possible reason is shown in Figure 7.6. The sketch shows that heat-affected zones (HAZ) are formed at the direct P3 scribe edges. These zones can exhibit changed electrical properties leading to a parasitic conductivity if changes occur throughout the whole thickness of the solar cell. It is reasonable to assume that structural material changes are initiated thermally by the incident spatial pulse fluence that is below the threshold and/or onset. This sub-threshold energy needs to dissipate thermally.

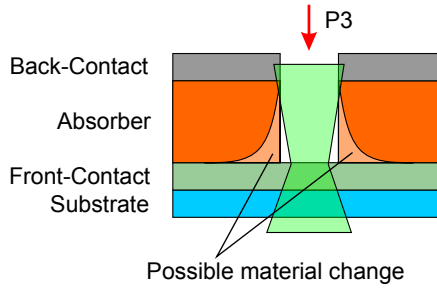


Figure 7.6: Schematic sketch of the P3 back-contact insulation process for laser illumination from the substrate side. Possible material changes at the direct scribe edge leading to a formation of parasitic conductivity between front- and back-contact when the heat-affected zone (HAZ) reaches throughout the whole layer-stack.

7.2.1 Sub-threshold energy intake for Gaussian laser beams

In the following, simple geometrical calculations were made to estimate the amount of energy that dissipates into the absorber thermally. Furthermore, it is estimated how the behavior changes in terms of used beam spot sizes and peak fluences. Different scenarios of processing setups were chosen to show possible impact by sub-threshold energy intake into the active solar cell material.

Peak fluence: in the first example the influence of the peak fluence was evaluated with experimental data from the Liu-Plot for processing of tandem solar cell with $60\ \mu\text{m}$. Figure 7.7 shows the fluence distribution for three different peak fluence with the assumption of a constant threshold fluence F_{th} . As expected, the crater radius increases with increasing peak fluences. The shaded areas represent the sub-threshold energy absorbed in the active material in direct vicinity of the crater edge. This energy needs to dissipate thermally into the solar cell. A recall to Equation 3.5 is required for derivation,

$$F(r, z = 0) = F_p \exp\left(\frac{-2r^2}{\omega_0^2}\right). \quad (7.2)$$

Here, the experimental values are inserted. The overall pulse energy is defined in accordance with Equation 3.9. Hence, the sub-threshold energy is calculated as followed,

$$E_{p,\text{sub}} = \int_0^{2\pi} \int_{r_{\text{crater}}}^{\infty} F(r) d\phi r dr. \quad (7.3)$$

The crater radius r_{crater} is a function of the threshold fluence F_{th} and the peak fluence F_p . Hence, Equation 7.2 can be rewritten to,

$$r_{\text{crater}} = \frac{\omega_0}{\sqrt{2}} \sqrt{\ln\left(\frac{F_p}{F_{\text{th}}}\right)} \quad (7.4)$$

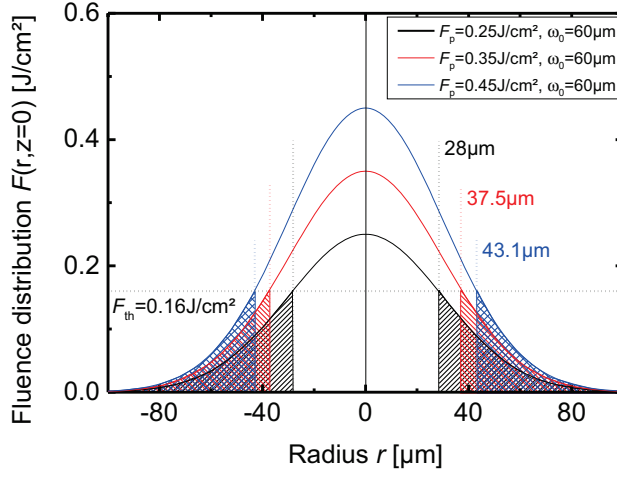


Figure 7.7: Visualization of the P3 ablation process with experimental parameters extracted from Liu-Plot for tandem solar cell processing with $60 \mu\text{m}$. For calculations the peak fluence F_p was increased. The shaded area represents the sub-threshold energy intake into the active solar cell at the scribe edge.

Furthermore, Equation 7.4 and Equation 7.3 can be combined and solved leading to,

$$E_{p,\text{sub}} = \frac{\pi\omega_0^2}{2} F_{\text{th}}. \quad (7.5)$$

This simple equation shows that the absolute sub-threshold energy is not depending on the used peak fluence and constant under the assumption of a constant threshold fluence.

Equation 7.5 can also be generalized to determine the pulse energy enclosed with an arbitrary radial interval with a fluence decay from F_1 to F_2 ,

$$E_{p,\Delta F} = \frac{\pi\omega_0^2}{2} [F_1 - F_2] \quad (7.6)$$

$$= \frac{\pi\omega_0^2}{2} [\Delta F]. \quad (7.7)$$

The area of a ring between fluence F_1 and fluence F_2 can be calculated by using Equation 7.4,

$$A_{1-2} = \pi(r_2^2 - r_1^2) \quad (7.8)$$

$$= \frac{\pi\omega_0^2}{2} \ln \left[\frac{F_1}{F_2} \right] \quad (7.9)$$

Equation 7.9 shows that the area illuminated with a fluence between F_1 and F_2 is independent from the used laser peak fluence F_p . Since the energy $E_{p,\Delta F}$ deposited in the region (ΔF) is also independent from F_p sub-ablation threshold material modifications within an arbitrary

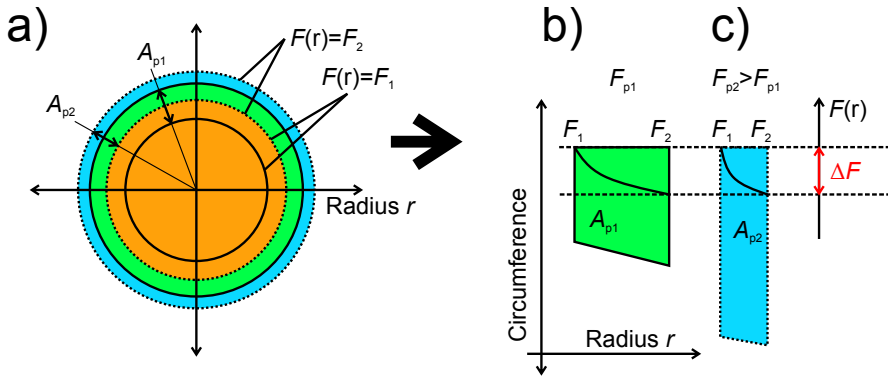


Figure 7.8: Schematic sketch of the area for an arbitrary fluence interval F_1 and F_2 with $F_1 > F_2$ for two different used laser peak fluences F_p . The area A_{p1} enclosed by the solid rings is equal to A_{p2} enclosed by the dotted rings. Different views are: a) Fluence distribution in $r\phi$ -plane with both thresholds and interval areas A_{p1} and A_{p2} derived from the fluence interval for processing with two peak fluence F_{p1} and $F_{p2} > F_{p1}$. b) Area A_{p1} plotted along its circumference and radius with the shape of the fluence distribution $F(r)$ in the interval $F_1 - F_2 = \Delta F$. c) Similar plot for A_{p2} . The higher peak fluence F_{p2} is equivalent with a larger circumference of the interval area. However, this is compensated by the lower radial extent originating from the steeper trend of $F(r)$. Thus, leading to a constant area A with regards to F_p .

fluence interval (F_1 to fluence F_2) are not affected by the peak fluence that is used for processing. Such behavior is possible since the steepness of the fluence distribution increases with increasing peak fluences. Therefore, impact on the material remains constant.

The following sketch in Figure 7.8 illustrates the derived behavior. The sketches show how the interval area is independent from F_p . Plot in Figure 7.8(a) shows the fluence distribution $F(r)$ in the $r\phi$ -plane with both thresholds F_1, F_2 (with $F_1 > F_2$), and interval areas A_{p1} and A_{p2} derived from the fluence interval for processing with two peak fluence F_{p1} and $F_{p2} > F_{p1}$ (areas enclosed by solid and dotted rings).

For better visualization the areas enclosed by the solid and dotted rings are plotted along their circumference length and radius in Figure 7.8(a) and (c). Processing with F_{p1} will yield a certain extent in radial direction where the $F(r)$ decays from F_1 to F_2 . The higher peak fluence F_{p2} is equivalent with a larger circumference of the interval area (cf. Figure 7.8(c)). However, the steeper trend of $F(r)$ leads to a stronger decay from F_1 to F_2 . This is the reason for the lower radial extent of A_{p2} leading to constant areas with regards to F_p .

Beam radius: in a second example the influence of the laser beam radius was evaluated with experimental data from the Liu-Plot for processing of tandem solar cells with a constant peak fluence F_p . Figure 7.9 shows a visualization of the impact on the sub-threshold fluence for changes of the beam radius. As expected, due to the steeper slope, the overall sub-threshold energy decreases significantly for reduced beam radii. Analytically, this can also be seen

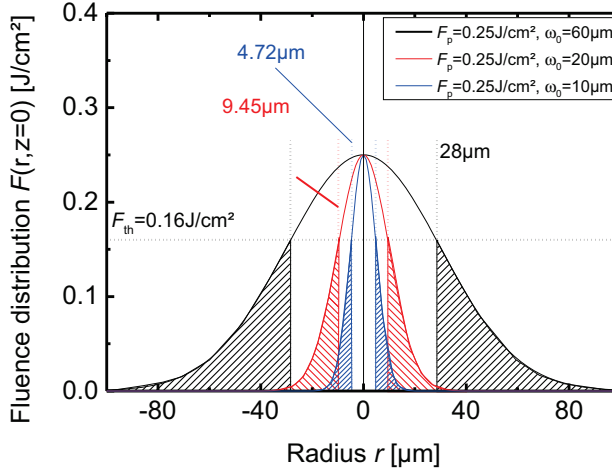


Figure 7.9: Visualization of the P3 ablation process with experimental parameters extracted from Liu-Plot for tandem solar cell processing with 60 μm . For calculations of decreased beam radii the used peak fluence was fixed and a constant threshold fluence was assumed. The shaded area represents the sub-threshold energy intake into the active solar cell at the scribe edge.

directly from the previously derived Equation 7.5. For a constant threshold fluence F_{th} the amount of sub-threshold energy scales with ω_0^2 .

Furthermore, together with Equation 7.9 it also follows that for every sub-threshold fluence interval the area A scales with ω_0^2 as well. Even though the area decreases when a smaller processing beam radius is used the sub-threshold energy decreases as well. Thus, a reduction of the heat-affected zone is expected.

Comparison with experiments: for a realistic evaluation of the geometrical and processing dependencies experimental values were used which were determined from the Liu-Plots for tandem solar cell processing. Figure 7.10 shows a visualization of the pulse fluence distribution of the laser beam for the three different beam radii and peak fluences corresponding to the experimental values at the ablation onset fluences. The threshold fluence is not constant among the different beam spot radii, as it was already seen from the ablation behavior investigations. Furthermore, due to the increase of the onset peak fluence the required peak fluences are adjusted accordingly ($F_p = F_{p,\text{on}}$ in Figure 7.10).

However, this behavior also means that a comparison between the processes is not possible like it was done for the ideal calculations with a constant beam radius or constant peak fluence in Figure 7.7 and Figure 7.9. Due to the change of F_{th} as a function of ω_0 , the fluence intervals with a similar decrease from $F = F_{\text{th}}$ to an arbitrary but constant second threshold are not the same. In terms of potential degree of damaging it is not clear how the deterioration process is correlated to the maximal fluence magnitude which is apparent at the direct crater edge and

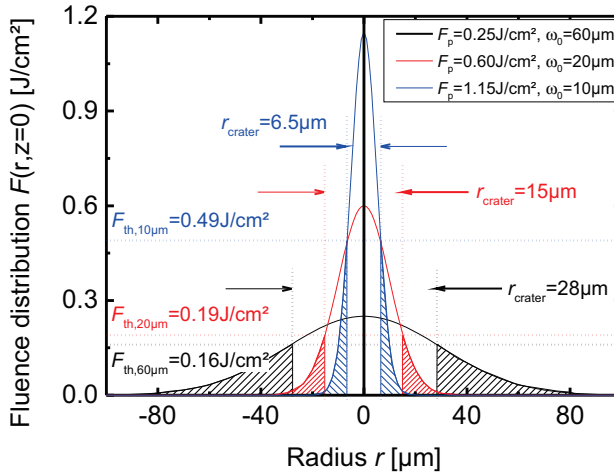


Figure 7.10: Visualization of the P3 ablation process with experimental parameters extracted from Liu-Plots for tandem solar cell processing. Peak fluence parameters correspond to the onset peak fluences from Table 7.1. The shaded area represents the sub-threshold energy intake into the active solar cell at the scribe edge.

not constant among the different processing setups. A similar behavior would be observed for a-Si:H processing as well (not shown, compare trends for a-Si:H from Table 7.1).

Evaluation of the experimental values to an ideal Gaussian fluence distribution shows that material and ablation behavior is strongly depending on the geometry. A conclusive statement in terms of trends for an increase or reduction of cell deterioration when the processing beam radius is decreased is not possible.

In conclusion, the example calculations showed that when the threshold fluence and onset peak fluence are constant and not depending on the beam radius no change of heat-affected zone formation is expected when the peak fluence is increased. Furthermore, a reduction of HAZ formation is assumed when the processing radius is reduced.

However, experimental results show that in fact both F_{th} and $F_{p,on}$ are not constant with regards to the used laser beam radius. Therefore, no distinct statement about the process behavior in terms of HAZ formation is possible.

7.2.2 Shunting behavior of P3 processed solar cells

For the quantitative evaluation of the shunting resistance a special test-structure was used for direct measurement on the solar cell level [163]. The setup and the test-procedure is described in Figure 7.11 schematically. A single solar cell is used for processing with P3 structuring scribe line blocks leading to various overall P3 scribe line lengths d . The $I - V$ characteristics are measured before and after each block of P3 processing into the active cell. This procedure

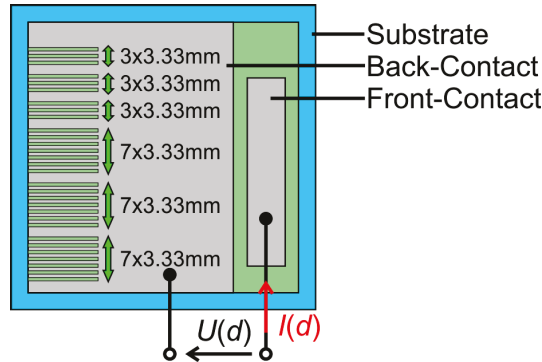


Figure 7.11: Sketch of test-structure used for evaluation of solar cell shunting behavior after P3 processing with various overall processing length d . For a single solar cell $I - V$ characteristics are measured before P3 processing and subsequently after each P3 processing block of three 3.33 mm scribes into the cell. By this procedure $I - V$ measurements are obtained with an effective P3 processing length d of: 0 mm, 10 mm, 20 mm, 30 mm, 53 mm, 76 mm, and 100 mm.

leads to the overall effective lengths d of: 0 mm, 10 mm, 20 mm, 30 mm, 53 mm, 76 mm, and 100 mm. The actual solar cell area is 1 cm^2 .

The impact of shunting of the solar cell by the P3 can be seen in the AM1.5 $I - V$ curve by a decreased fill-factor and/or losses in the open-circuit voltage V_{OC} for strong shunting. When the changes are only subtle they are best observed from the $I - V$ measured under dark conditions. The dark $I - V$ characteristics are very meaningful because even slight changes of parasitic current flow are detected.

Please note that with this structure it is not possible to detect any residual conductivity between two scribe edges of one P3 line, i.e. proper back-contact insulation.

The parameter sets defined for the experiments were defined as followed: for each absorber material (a-Si:H and tandem) solar cells were processed with the three individual laser beam spot radii of $60 \mu\text{m}$, $20 \mu\text{m}$, and $10 \mu\text{m}$. The visually optimized processing parameters from Figure 7.5 were taken as the reference process. The laser peak fluence was varied around this value to determine a processing window where shunting is minimized.

Figure 7.12 shows exemplary the dark $I - V$ characteristics that were measured from the test cycle procedure for two laser parameters. One solar cell P3 processed with low peak fluence close to the onset peak fluence and one processed with a significantly higher peak fluence. The overall differences in current flow are best observed for voltages between -1 V and $+0.5 \text{ V}$. In this voltage range Ohmic behavior of the solar cell prevails. As a reference the dark current flowing at an negative voltage bias of -1 V is taken. A comparison between both processing parameters shows that the final increase in current flow for the low peak fluence parameter is smaller than one order of magnitude (Figure 7.12(a)). A stronger increase, of about three orders of magnitude, is observed for the higher peak fluence in Figure 7.12(b).

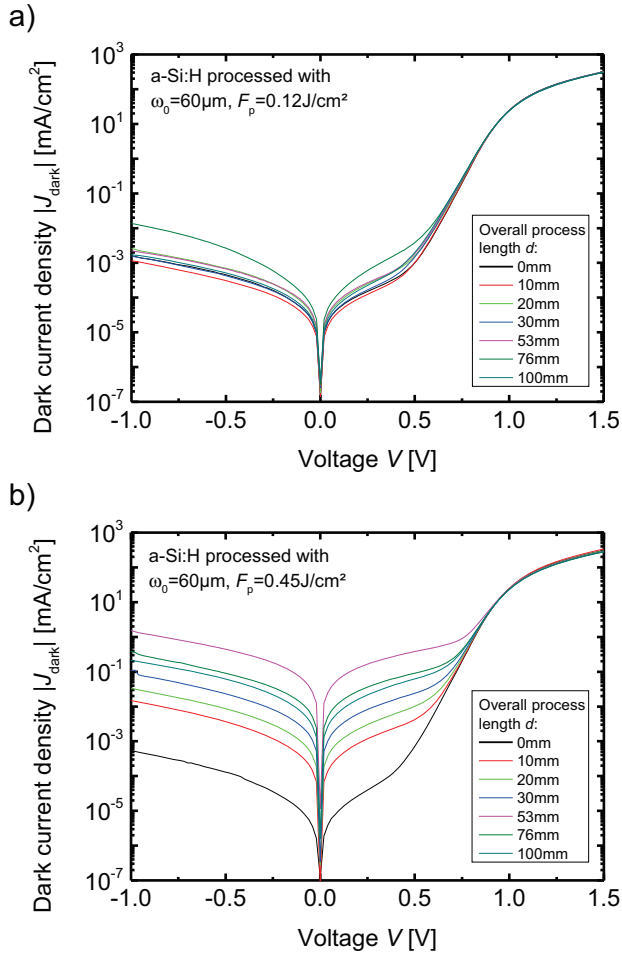


Figure 7.12: Dark $I - V$ characteristics of two a-Si:H solar cells on $\text{SnO}_2:\text{F}$ processed with P3 scribe lines of various lengths d . A laser beam radius of $60\mu\text{m}$ was used. A low current increase is observed with a laser peak fluence of: a) $F_p=0.12\text{J}/\text{cm}^2$. A significant increase is present for a processing laser peak fluence of: b) $F_p=0.45\text{J}/\text{cm}^2$.

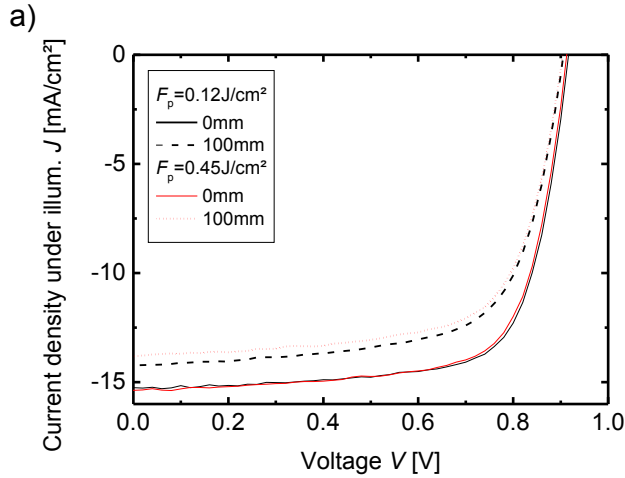


Figure 7.13: AM1.5 $I-V$ characteristics of the two a-Si:H solar cells from Figure 7.12. Solid lines show the graphs before P3 processing with 0.12 Jcm^{-2} (black lines) and 0.45 Jcm^{-2} (red lines), respectively. Graphs plotted with dashed and solid lines were measured after P3 processing.

These large differences are not as easily seen from the $I-V$ measurements under illumination as it is shown in Figure 7.13. The main difference that is observed in Figure 7.13 is the reduction of the short-circuit current density after processing. However, this is mainly attributed to the reduction of active area of the solar cell by the P3 scribe lines (cf. Figure 7.11). The width of each scribe line is also increased for processing with a peak fluence of 0.45 Jcm^{-2} which leads to a higher overall active area loss. Beside these differences there is no strong deterioration observed qualitatively.

The extracted solar cell parameters from the illuminated $I-V$ characteristics, as a function of the P3 processing length, are plotted in Figure 7.14. The cell parameters are extracted and plotted against the processing length. Both, fill-factor and open-circuit voltage decrease with increasing scribing length. However, large differences between both processing parameters are not easily seen here as well. In contrast, from the dark $I-V$ characteristics even very small changes of the current flow are detected. Due to this higher sensitivity for small changes of the cells parasitic currents this measurement is the method of choice.

The dark $I-V$ curves in Figure 7.12 show that the current increase is not exactly monotonously rising. Jumps and strong deviations are clearly visible for processing with the higher peak fluence in Figure 7.12(b). A homogeneous shunting of the material at the scribe edge would yield a linear relation between dark current increase and overall processing length.

A strong current increase/decrease within the processing cycle is possibly owed to localized effects like shunting from flakes, insufficient pulse-to-pulse stability, and intrinsic shunts from inhomogeneity that are activated by the laser process or measurement. Practically, mechanical contacting problems from the experimental setup are possible reasons as well.

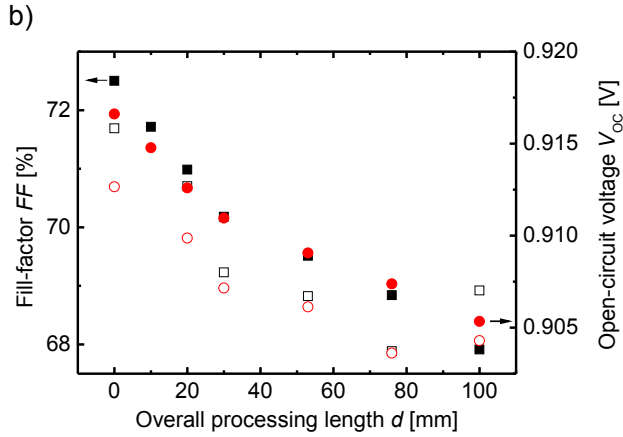


Figure 7.14: Extracted parameters of two a-Si:H solar cells on SnO₂:F processed P3 scribe lines of various lengths d . Extracted fill-factor (squares) and open-circuit voltage (circles) as function of processing length. Filled symbols are processed with the lower peak fluence while empty symbols are scribed with the higher peak fluence.

To extract reasonable values from the experiments only negative impact on the solar cell was assumed. A uniform intake of excess heat into the solar cell at the direct P3 scribe edge would most likely result in a homogeneous deterioration of the electrical properties. Thus, the linear rising part of the current increase vs. process length relation was mainly accounted for. Jumps (strong increase or decrease) in the current increase vs. processing length function are most likely related to localized effects that are (de-)activated by the processing steps and/or measurement.

Figure 7.15 illustrates this approach and shows the differential dark current density increase at a reverse bias voltage of -1 V as a function of the process length for both solar cells from Figure 7.12 and 7.14. Especially, for processing with 0.45 Jcm⁻² a spike of the current flow increase is observed for a length of 53 mm. This jump is accounted for as a deviation from the expected trends.

The slope of the $I - V$ characteristics is defined by the median of the value derived from the current increase divided by the processing length. Furthermore, the minimum and maximum values are extracted as well as a measure of the linearity of the experimental results. The slope of the linear function is taken as a figure-of-merit for the evaluation of the process quality. Ideally, the quotient of the current increase and processing length d would be constant for a purely linear relation. The choice of -1 V reverse bias is partly arbitrary and serves only as a reference where clear differences are easily detected by the setup.

Slope coefficient: for a-Si:H solar cell scribing a compilation of the differential slope coefficient (compare Figure 7.15) vs. the peak fluence F_p for the three beam radii used is plotted in Figure 7.16. A smaller slope value that is extracted from the dark current increase vs. processing

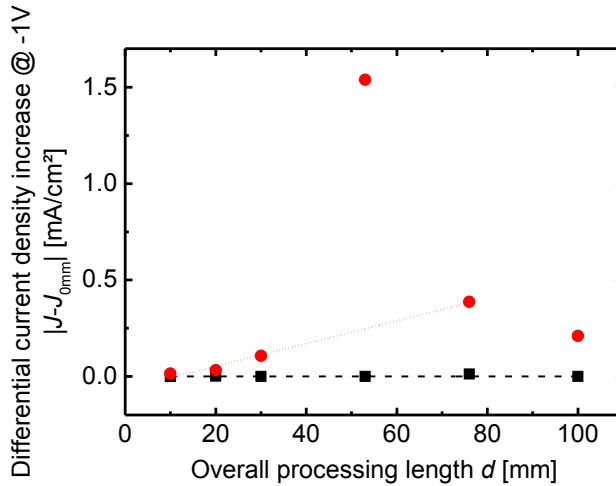


Figure 7.15: Differential dark current density increase at a reverse bias voltage of -1 V as a function of the process length. Black squares: processing with a peak fluence of 0.12 Jcm^{-2} and red circles: processing with 0.45 Jcm^{-2} . The dashed and dotted lines represent linear regressions that were made taking a homogeneous linear increase of the current flow into account.

length curves is equivalent with a lower degree of shunting. When the same P3 processing parameters are used for the interconnection in solar modules the required processing lengths are 5–10 mm depending on the cell-stripe width. However, higher process lengths per cm^2 active cell-stripe can be relevant for special processes like semi-transparency. Here, cell material is removed by a P3 process in order to achieve a certain percentage of optical transparency [164]. Please note that in Figure 7.16 negative minimum values of the slope coefficient are not accounted for. A negative slope would be equivalent with an improvement of the electrical properties which seems not reasonable to assume. Such behavior can be explained by existing shunts that are removed either by the laser scribes or during the measurement of the cell after processing.

The slope value from Figure 7.16 exhibits a change by many orders of magnitude depending on the used laser peak fluence and beam radius. A quite constant behavior is found for processing with $60 \mu\text{m}$. Except for two spikes to significantly lower values all remaining slope values are between 10^{-4} – $10^{-3} (\text{mA}/\text{cm}^2)/\text{mm}$. An increase is only observed for the highest laser peak fluence value above 0.4 Jcm^{-2} .

Interestingly, comparable values are achieved for processing with $20 \mu\text{m}$ over a large range of fluences. However, for a peak fluence below 0.45 Jcm^{-2} there is a strong increase of the slope coefficient. No proper ablation is observed for these parameters. The complete laser pulse energy is absorbed for heating but without ablation the material. Thus, a strong shunting throughout the solar cell within the whole illuminated area is possible.

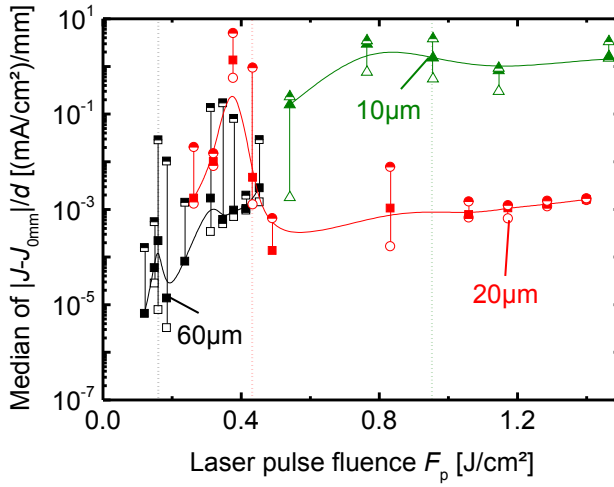


Figure 7.16: Slope coefficient of the differential dark current density increase vs. process length relation at a reverse bias voltage of -1 V for P3 processing of a-Si:H solar cells with different laser beam radii and laser pulse fluences. The coefficient is derived by the median of current increase divided by the process length (filled symbols). Furthermore, minimum (empty symbols) and maximum (half-filled symbols) of the coefficients are plotted as well. Black squares: processing radius of 60 μm , red circles: 20 μm , and green triangles: 10 μm . The dotted lines mark the onset peak fluence parameter were continuous lines are obtained. Solid lines serve as guide to the eye.

For processing with 10 μm no regime is found with a slope comparably low as for the other two processing radii. Furthermore, the value is not significantly depending on the peak fluence. All slope values are at least two orders of magnitude higher than the corresponding optimal values from processing with 60 μm and 20 μm .

The dotted lines in Figure 7.16 mark the onset peak fluence parameters that are required to achieve continuous lines. Below this value only layer bulging and flake formation is observed. A proper electrical insulation of the back-contact is not ensured with laser fluences below these values.

It is surprising to see that although very clean scribe edges without any flake formation are obtained for processing of optimized lines with 10 μm (cf. Figure 7.5(c)) electrical evaluation shows that cell deterioration by shunting is detrimental for this setup. One possible explanation is found by the fact that an increased onset peak fluence is required for proper ablation with higher focusing. For P3 scribing of a-Si:H solar cells significant shunting defines additional constraints on the minimal reasonable scribe width.

A similar study was carried out for processing of tandem solar cells on $\text{SnO}_2\text{:F}$ as well and the results are shown in Figure 7.17. Please note that the overall efficiency of the investigated tandem solar cell were quite bad with average efficiencies of approx. 6% and fill-factors of 60-65%. However, they were still used for processing since they exhibited a low dark current flow at -1 V prior to P3 scribing. Only cells with a current flow below 10^{-4} mA/cm^2 were chosen. The behavior of the slope coefficient is fairly similar to the findings for a-Si:H solar cell processing. Processing windows of a fluence regime with constant minimized slopes are found for at least processing with 60 μm and 20 μm .

A major difference to processing of a-Si:H solar cells is the overall lower slope value for all processing parameters. In general, no slope values above 10^{-1} (mA/cm^2)/mm are observed. This could be contributed to the fact that the tandem absorber thickness is higher and that shunting is not as pronounced.

Another difference to Figure 7.16 is the fact that the minimal slope values for each laser beam radius is in the same range below 10^{-6} (mA/cm^2)/mm. Just like in Figure 7.17 the dotted lines in Figure 7.16 mark the onset peak fluence parameters that are required to achieve continuous lines.

It is somehow surprising that in terms of scribe edge morphology and electrical properties no correlations can be found when comparing a-Si:H and tandem processing from Figure 7.5 with the $I - V$ characteristics.

All evaluations were done with values from the dark current increase that was evaluated at -1 V reverse bias voltage so that Ohmic behavior of the solar cell is dominating. For a quantitative statement of shunting an evaluation of the current increase at the voltage in the maximum power point under illumination is required. This is possible with the simplification that

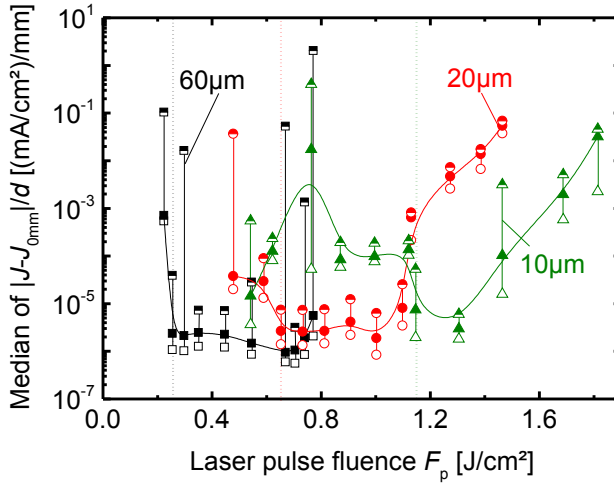


Figure 7.17: Slope coefficient of the differential dark current density increase vs. process length relation at a reverse bias voltage of -1 V for P3 processing of tandem solar cells with different laser beam radii and laser pulse fluences. The coefficient is derived by the median of current increase divided by the process length (filled symbols). Furthermore, minimum (empty symbols) and maximum (half-filled symbols) of the coefficients are plotted as well. Black squares: processing radius of 60 μm, red circles: 20 μm, and green triangles: 10 μm. The dotted lines mark the onset peak fluence parameter were continuous lines are obtained. Solid lines serve as guide to the eye.

7.2. Impact on electrical properties

Table 7.2: Evaluation of shunt resistance formation by P3 scribing of a-Si:H and tandem solar cells with different laser beam radii and laser peak fluences. Process parameters with optimized median and max slope coefficient from dark $I - V$ curves (at -1 V reverse bias voltage) from Figure 7.16 and 7.17 were selected. The shunt resistance R_{P3} is calculated for a process length $d=10$ mm and area $A=1$ cm². *Values extracted directly from illuminated $I - V$ curves.

Material (radius ω_0)	Laser peak fluence F_p	Shunt resistance R_{P3} (median)	Shunt resistance R_{P3} (max)	*Reduction of FF and V_{OC}
a-Si:H, 60 μm	0.16 Jcm ⁻²	456 k Ω	3.5 k Ω	-0.4%, -1.36 mV
a-Si:H, 20 μm	0.50 Jcm ⁻²	726 k Ω	154 k Ω	-0.1%, -1.38 mV
a-Si:H, 10 μm	0.95 Jcm ⁻²	66 Ω	26 Ω	-44.0%, -424.5 mV
tandem, 60 μm	0.25 Jcm ⁻²	42 M Ω	2.5 M Ω	-4.0%, -157.5 mV
tandem, 20 μm	0.65 Jcm ⁻²	37 M Ω	13 M Ω	-4.5%, -160.8 mV
tandem, 10 μm	1.14 Jcm ⁻²	13 M Ω	1.9 M Ω	-3.7%, -104.7 mV

electrical parameters under illumination are only adjusted by the additional photo current (refer to Figure 2.3).

Table 7.2 shows the calculated shunting resistance for the solar cells that were processed with the visually and electrically optimized scribing parameters. The values are calculated from the slope coefficient multiplied with a processing length of 10 mm. Together with the active cell area of 1 cm² this corresponds to a 10 mm cell stripe width in the solar module. The calculated resistance values from the slope coefficient (median and max) at -1 V reverse bias voltage for a-Si:H solar cells are in good correspondence with the direct impact evaluated from the solar cell parameters. The impact on the cell properties can be seen from the reduction of the fill-factor and open-circuit voltage between 0 mm and 10 mm processing length of the test-structure solar cells. Furthermore, for processing with a laser beam radius of 10 μm severe shunting is calculated and confirmed by the massive reduction of the fill-factor.

For tandem solar cell processing all calculated resistances are greater than 1 M Ω which should lead to only a negligible impact on the cell properties. However, the measured cell parameters of the direct impact show that there is a quite strong impact which cannot be described by the calculated shunting values.

It is possible that such differences between dark and illuminated $I - V$ characteristics are caused by a stronger illumination dependence of the parallel resistance of the $\mu\text{c-Si:H}$ bottom-cell than for the a-Si:H top-cell. When the conductivity of the damaged a-Si:H top-cell is strongly increased a discrepancy between dark and illuminated conditions between the tandem cell with and without P3 processing. Furthermore, please remember that the initial $I - V$ characteristics of the tandem cells were not very good so it is possible that the degradation of the performance is somehow enhanced for these cells.

In conclusion, generally the process evaluation with the test-procedure for P3 is suitable for the qualitative characterization of the process window. For a quantitative measurement of the

shunting resistance $R_{p,P3}$ a combined evaluation of the $I - V$ characteristics under dark and under illumination is necessary. A more sophisticated model of the deteriorated cell stripe could be more meaningful [163]. Especially for tandem solar cells the separated damaging of the sub-cell needs to be accounted for.

In terms of shunting behavior, as it was already indicated from the comparison between theoretical and experimental calculations in Section 7.2.1, no decrease of HAZ formation with regards to beam radius reduction was observed. Furthermore, for tandem solar cell processing with 10 μm and 20 μm shunting is increased in the high peak fluence regime.

A simple statement that sub-threshold energy intake alone is responsible for material deterioration is not sufficient for a definite assumption about P3 scribing behavior. The increase of the threshold and onset peak fluence could explain the severe shunting for reduced beam spot sizes. For increasing peak fluences the increasing source of excess energy above the threshold fluence (cf. Figure 7.10) could be responsible for increased shunting on tandem solar cells.

7.3 Near scribe edge material modifications

From the characterization of the electrical properties it was found out that solar cell deterioration as a function of the laser processing beam radius is more severe for decreasing beam radii. This is in contradiction with the assumption that due to a steeper slope (smaller area cf. Equation 7.9) of the Gaussian intensity distribution the sub-threshold deterioration of the scribe edge material decreases with a decreasing beam radius. Hence, leading to a reduced amount of heat-affected material near the P3 scribe edge.

To see whether the increased threshold peak fluence F_{th} is the reason for this behavior the near scribe edge region was characterized.

For a detailed understanding of this behavior Raman microscopy was carried out in the near-edge active region of the P3 scribe lines. Raman microscopy gives insight on the microstructure of the investigated material. A detailed description of Raman scattering and its application for characterization of silicon can be found elsewhere [165, 166].

The Raman crystallinity for a mixture of amorphous and crystalline silicon can be estimated by the following relation,

$$I_c^{RS} = \frac{I_c}{I_c + I_a}. \quad (7.10)$$

In Equation 7.10 I_c and I_a are the integrated intensities of the Raman scattering peaks shifted by 520 cm^{-1} and 480 cm^{-1} . The peak shifted by 520 cm^{-1} can be associated to the crystalline phase of the material. The amorphous phase is associated to the peak shifted by 480 cm^{-1} . The peak leading to I_c is derived by the subtraction of the measurement signal with an amorphous reference signal at 480 cm^{-1} that is scaled to reproduce the amorphous phase of the sample.

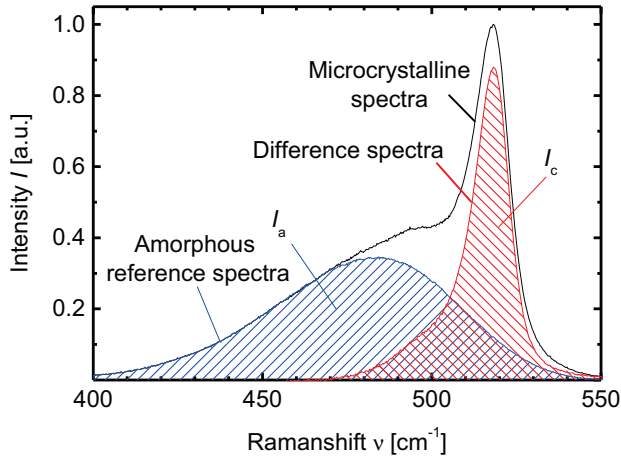


Figure 7.18: Typical Raman spectra of microcrystalline silicon ($\mu\text{c-Si:H}$) in black. Furthermore, scaled reference spectra of an amorphous silicon (a-Si:H) sample and the associated peak area I_a at 480 cm^{-1} given in blue. The spectra associated to the crystalline phase with the peak area I_c at 520 cm^{-1} given in red is obtained by the difference of the measurement spectra and the amorphous reference. Additional shoulder at 495 cm^{-1} is associated with the crystalline phase.

From the subtraction both I_c and I_a can be calculated. Finally, with Equation 7.10, the Raman crystallinity is obtained.

Figure 7.18 shows a typical spectrum measured by Raman spectroscopy with the individual peak I_{520} and I_{480} that are associated with the crystalline and amorphous phase, respectively. It should be noted that after derivation of the difference spectra an additional shoulder can be seen shifted by approx. 495 cm^{-1} that is accounted to dislocations or stacking faults and is therefore associated to the crystalline phase [167].

For P3 processing it is believed that a large increase of the crystallinity can be an important factor determining the parasitic conductivity between front- and back-contact at the P3 scribe edge [161, 163, 164, 168]. Further possible mechanisms of shunting are alloying of the contact materials with the absorber, thermal dopant diffusion, debris redeposition at the scribe edge, and short-circuiting by flake formation.

For all measurements an excitation wavelength of 532 nm was used and illumination was done through the substrate side. Thus, with an absorption coefficient of $\alpha=1\cdot 10^5\text{ cm}^{-1}$ a collection depth of the Raman signal of $\delta=50\text{ nm}$ was estimated ($\delta=1/2\alpha$). Please note that depending on the crystallinity of the investigated silicon layer material is the effective absorption coefficient (and penetration depth) can vary by approx. one order of magnitude. For illumination through the substrate side a low penetration depth ensured selectivity of the measurement on the amorphous (top-)cell where crystallization of the layers was expected to be dominant.

The beam radius of the measurement laser was estimated with $1\ \mu\text{m}$ but was most likely slightly increased due to scattering at the front-contact texture. The incident laser power was adjusted to minimize any significant heating of the sample.

Microstructure: Raman microscopy was carried out at the P3 scribe line edges of samples that were processed for the $I - V$ characteristics in the previous section. A crystallinity map was measured for each absorber type (a-Si:H and tandem absorber) and all three laser beam radii of $60\ \mu\text{m}$, $20\ \mu\text{m}$, and $10\ \mu\text{m}$ ($532\ \text{nm}$ processing wavelength). For a comparison of the impact of the peak fluence for each type/radius set two different laser peak fluences were chosen. One with a low peak fluence close to the onset, and one processed with a increased laser peak fluence.

First, the results of the measurements on a-Si:H solar cells are presented in Figure 7.19. Each map scan was carried out at the scribe edge of two consecutive overlapping laser pulses. The cumulative incident laser fluence is the highest in this region.

There are only slight changes observed for the degree of crystallization (maximal value of I_C^{RS}) and spatial extent perpendicular to the scribe edge into the solar cell found for a constant beam radius between low and high peak fluences.

Furthermore, no correlation is found between the results for the different beam radii. The region extent with increased crystallinity and degree of crystallization is the lowest for processing with $20\ \mu\text{m}$ in Figure 7.19(c)–(d).

A comparison of these results with the theoretical calculations from Section 7.2.1 indicates good agreement with the derived assumptions. For a constant beam radius it was calculated that the impact of sub-threshold energy on the active material at the direct scribe edge would not increase when the used peak fluence for processing is increased.

Furthermore, it was also stated that due to the differences in the threshold fluence and onset peak fluence no reasonable comparison in terms of degree of hazardous material modifications as a function of the laser beam radius is possible. This explains why no distinct trends between the Raman crystallinity maps among the different laser beam radii are found.

A correlation of the Raman measurements to the electrical properties in Figure 7.16 can be found as well. For processing with $20\ \mu\text{m}$ and $10\ \mu\text{m}$ there are no large differences observed of the electrical properties between processing with low and high peak fluences. If the whole minimum and maximum range of the slope coefficient for the $60\ \mu\text{m}$ low peak fluence parameter in Figure 7.16 is taken into account the electrical values are more or less constant as well. Good agreement is also found for the overall magnitude of shunting (cf. Table 7.2) and degree/extent of crystallization for the different beam radii (left column in Figure 7.16).

A similar study was carried out for P3 tandem solar cell processing in the same scheme as for a-Si:H solar cells. For each processing beam radius the two scribe line parameters (low and high peak fluences) were measured by Raman microscopy. The results for these measurements are shown in Figure 7.20.

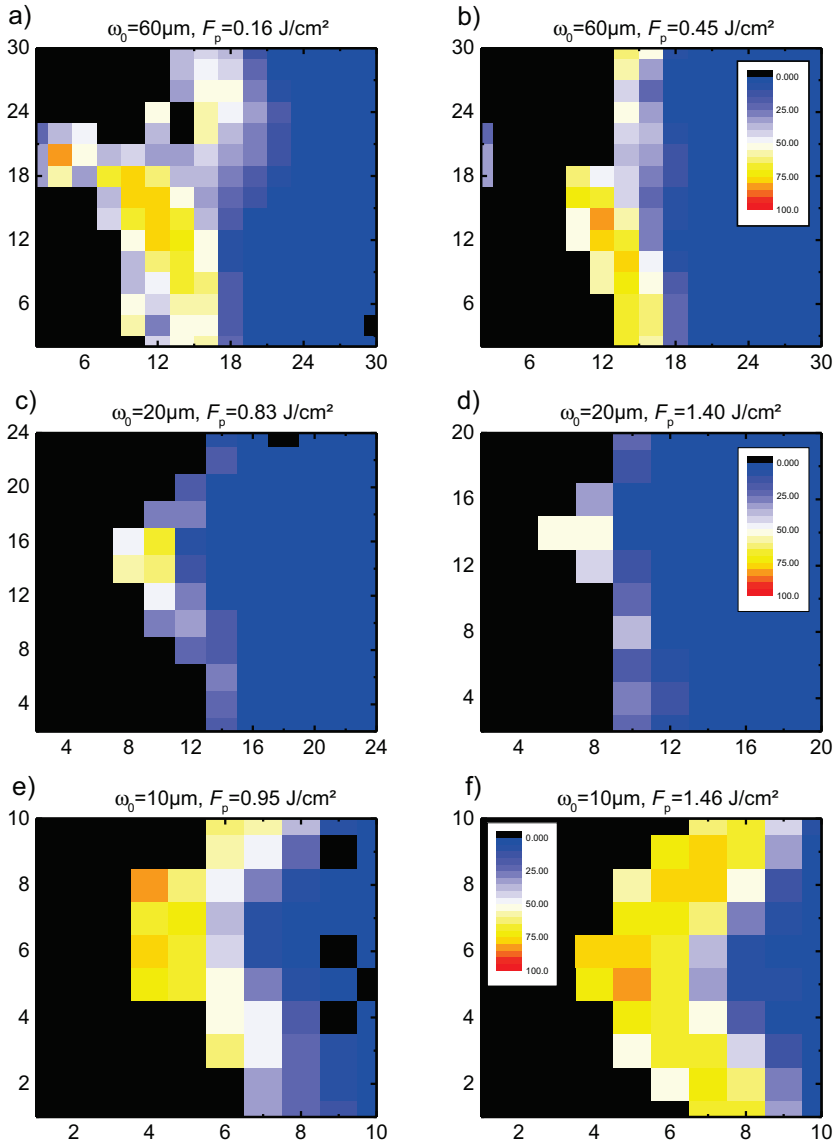


Figure 7.19: Raman microscopy of P3 laser scribe edges on a-Si:H solar cells prepared on $\text{SnO}_2:\text{F}$ TCO. Scribe lines correspond to processing peak fluences from the $I-V$ characteristics in Figure 7.16. All dimensions are in μm and the tile color corresponds to the Raman crystallinity I_C^{RS} . A step-size of $2 \mu\text{m}$ was chosen for row 1–2 while $1 \mu\text{m}$ for row 3.

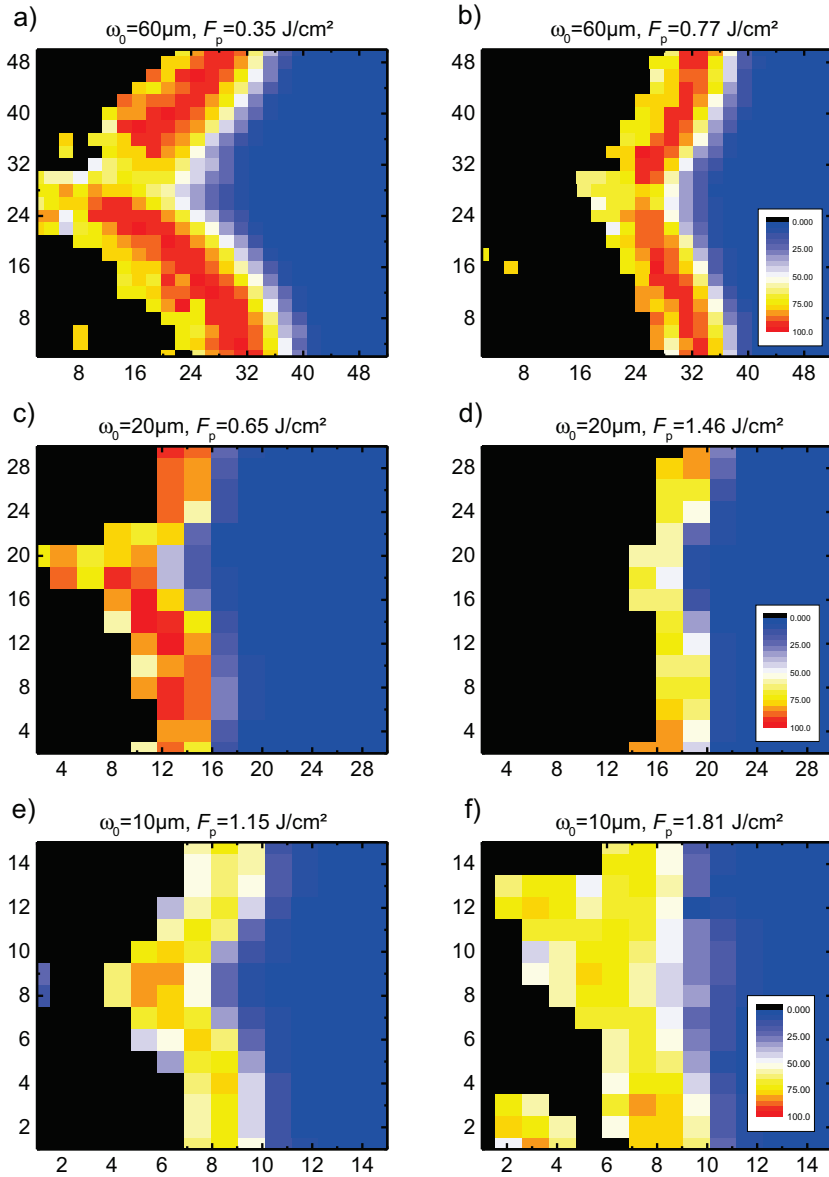


Figure 7.20: Raman microscopy of P3 laser scribe edges on tandem solar cells prepared on $\text{SnO}_2\text{:F}$ TCO. Scribe lines correspond to peak fluences from Figure 7.17. Dimensions are in μm and the tile color equal to Raman crystallinity I_C^{RS} . Step-size of $2\mu\text{m}$ and $1\mu\text{m}$ was chosen for row 1–2 and row 3, respectively.

For the P3 scribe lines processed on tandem solar cells the Raman microscopy maps exhibit distinct differences to a-Si:H solar cell measurements. The overall degree of crystallization and spatial extent from the edge into the solar cell is significantly higher than for processing of a-Si:H solar cells.

However, most of the observations made for a-Si:H solar cells can be found in Figure 7.20 as well. No dramatic differences of the degree/extent of crystallization are found between low and high peak fluences for a constant beam radius. Yet, a detailed look indicates a slight decrease of the spatial extent for processing with 60 μm and 20 μm (degree as well) while for 10 μm the extent is slightly increased.

Furthermore, no correlation between the three processing beam spot radii is observed just like for a-Si:H processing.

The reasons for the lack of correlation between the processing laser beam radii can be accounted to the strongly changed threshold and onset fluences (cf. Section 7.2.1). The constant results between low and high peak fluences are as predicted by the simplified calculations. However, the slight reduction in Figure 7.20(b) and (d) can be accounted the ablation morphology at the scribe edge that was quite different between a-Si:H and tandem solar cells (refer to Figure 7.5). For P3 scribe lines on tandem solar cells a delaminated region remains on the material at the direct edge. It is possible that part of the scribe edge exhibits an increased crystallinity due to the bad thermal contact to the substrate leading to an increased temperature during processing. For higher peak fluences the extent of the delaminated material is decreased. It is probable that such behavior is the reason why the crystallization extent decreases for higher peak fluences rather than reduction of heat-affected zone formation. Yet it remains unclear why such effect is not observed in Figure 7.20(f).

A comparison to the electrical properties from Figure 7.17 with the Raman measurements only show good agreement for processing with 60 μm in Figure 7.20(a)–(b). The strong increase of the current increase slope for high peak fluence processing with 20 μm and 10 μm is not reflected by any strong change of the crystallinity. It is possible that for the case of tandem solar cell processing the depth information of the Raman spectroscopy is not sufficient. Potential damaging of the $\mu\text{c-Si:H}$ bottom-cell is not detected.

The overall higher degree of crystallinity for the measurements on tandem solar cells compared to a-Si:H is not in agreement with the significantly lower slope values in Figure 7.17 and shunt resistances in Table 7.2. As indicated earlier the higher absorber thickness for tandem solar cells and the fact that the laser pulse energy is mainly absorbed in the top-cell could be causing a rather localized damaging of the a-Si:H sub-cell while the bottom-cell remains unaffected. Thus, overall shunting between front- and back-contact is less pronounced.

In conclusion, good agreement was found between theoretical calculations for the sub-threshold energy intake as a function of laser beam radius and peak fluence, and Raman microscopy at the direct P3 scribe edge. Furthermore, for a-Si:H processing correlations were found be-

tween degree and extent of crystallization and shunting behavior extracted from the $I - V$ characteristics in Figure 7.16.

However, the interpretation of the Raman measurements for tandem solar cells turned out to be not definite due to the measurement of delaminated material where it is not clear whether it is in electrical contact with the underlying TCO or not.

Furthermore, due to the limited depth information for the tandem absorber it is not clear to state whether the crystallinity is changed throughout the whole layer-stack. If possible, removal of the back-contact after P3 processing and Raman microscopy from the film side could help to quantify the extent of the heat-affected zone that reaches through to back-contact.

For the electrical measurements possible reasons for the highly non-uniform processing behavior need to be accounted for: rip-off behavior at the scribe edge, layer delamination (and thermal/electrical contact to the substrate). Just as well are flake formation, activation (as well as busting) of pre-existing shunts, material inhomogeneity, mechanical damaging by the measurement contacts, and pulse-to-pulse instabilities all possible reasons for large deviations and non-definite electrical evaluation of the P3 process.

Nonetheless, processing with a beam spot radius of 20 μm showed a comprehensive trend in the measured slope coefficient (for a-Si:H as well as for tandem). This gave motivation for the implementation of optimized P3 scribe lines into mini solar modules.

7.4 Process implementation in mini solar modules

An implementation of optimized P3 back-contact insulation scribe lines into solar modules was done to determine if a reduced scribe width can be used without severe shunting of the solar module.

For this, a-Si:H/ $\mu\text{c-Si:H}$ mini modules on $\text{SnO}_2\text{:F}$ with the standard back-contact were prepared. The interconnection was realized with optimized laser processes for P1, P2, and P3. All processing was done with a wavelength of 532 nm and laser beam radii w_0 of 10 μm (P1), 20 μm (P2), and 20 μm (P3). Figure 7.21 shows an optical microscopy image of the interconnection region of the solar module. Compared to the previously prepared modules at the end of Chapter 5 and Chapter 6 a significant overall width reduction is achieved. Although, the scribe width of P3 is higher than what was found for the geometrical scribe width reduction shown in Figure 7.5(e) and partial TCO ablation is observed as well. This is owed to the fact that the overall absorber thickness is somewhat higher (2.2–2.4 μm vs. 1.4 μm). This is also the reason why a higher peak fluence was required for proper ablation (1.13 Jcm^{-2} vs. 0.65 Jcm^{-2}). The behavior is consistent with the findings from P2 and P3 and shows how sensitive the processes are with regards to laser beam radius and absorber thickness.

Just as for the implementation of optimized P2 scribes (cf. Section 6.5) mini modules with varying cell stripes widths w_a of 2 mm, 3 mm, 5 mm, and 10 mm were prepared. The cell

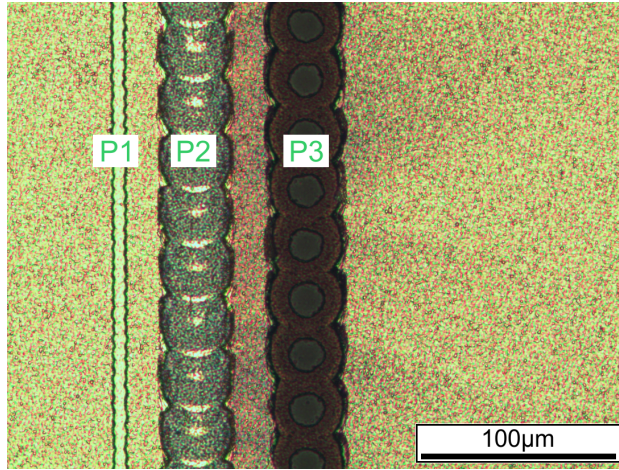


Figure 7.21: Optical microscopy image of the interconnection region of tandem mini modules prepared on $\text{SnO}_2:\text{F}$ TCO material with optimized laser scribes. Process parameters P1–P3: $\omega_0=10\ \mu\text{m}$ and $F_p=3\ \text{Jcm}^{-2}$ (for P1). $\omega_0=20\ \mu\text{m}$ and $F_p=0.82\ \text{Jcm}^{-2}$ (for P2). $\omega_0=20\ \mu\text{m}$ and $F_p=1.13\ \text{Jcm}^{-2}$ (for P3).

length l of 30 mm was fixed. The number of interconnected cells were in correspondence with the individual cell stripe width: 40, 25, 16, and 8. Table 7.3 shows the module parameters extracted from the $I - V$ characteristics. No impact on the electrical properties by shunting

Table 7.3: AM1.5 $I - V$ characteristics of a-Si:H/ μc -Si:H tandem solar modules on $\text{SnO}_2:\text{F}$ with optimized P1, P2, and P3 scribe lines. Processing parameters: P1 $\omega_0=10\ \mu\text{m}$ and $F_p=3\ \text{Jcm}^{-2}$, P2 $\omega_0=20\ \mu\text{m}$, $F_p=0.82\ \text{Jcm}^{-2}$, and P3 $\omega_0=20\ \mu\text{m}$, $F_p=1.13\ \text{Jcm}^{-2}$. On each substrate additional single solar cells with a size of $1\ \text{cm}^2$ were prepared for comparison and median values are given as well.

Substrate number	Active cell stripe width (# cells)	Module efficiency η	Fill-Factor FF	Open-circuit voltage V_{OC}	Short-circuit current I_{SC}
1	2 mm (40)	10.8%	74.6%	53.7 V	6.3 mA
1	3 mm (25)	11.3%	73.9%	33.6 V	9.8 mA
2	5 mm (16)	10.2%	72.2%	21.3 V	15.9 mA
2	10 mm (8)	10.4%	73.6%	10.7 V	31.6 mA
1	10 mm (1)	11.2%	74.2%	1.34 V	11.30 mA
2	10 mm (1)	10.8%	74.8%	1.34 V	11.04 mA

or series resistances created by the optimized laser processes is observed leading to believe that the implementation was successful. A high fill-factor is achieved for all modules with no large differences to single solar cells. Furthermore, the open-circuit voltage V_{OC} of each module corresponds to the theoretical value. As expected from the high shunt resistances obtained for tandem solar cell P3 processing with $20\ \mu\text{m}$ in Table 7.2 the degradation of the

$I - V$ characteristics under illumination (approx. 4% loss in FF) can be accounted to the weak initial performance of the prior used tandem solar cells.

For tandem solar modules with an absorber thickness of 2.2–2.4 μm the overall interconnection width could be reduced from a standard of 300–350 μm down to 100–120 μm . From the implementation it can also be seen that the processes are highly influenced by the layer thicknesses and that proper adjustment of the laser processes is important.

8 Conclusion

The requirement for the integrated series connection is without any doubt. The importance will increase in the future since novel technologies tend towards higher current densities leading to increased Ohmic losses in the contact materials [1].

The area on the solar module that is required for the realization of the interconnection of two neighboring cells is lost. No current is generated in this region. Depending on the technology this lost area can make up 5–10% of the overall module area. Even though reduction of this lost area gives rise to an attractive potential efficiency increase not much research is being found on this topic.

The integrated series connection is commonly done by selective laser ablation in the form of scribe lines across the substrate. Individual layers are removed locally in-between the deposition steps. In the first of three steps the front-contact material is removed from the substrate (P1). In the next step, the absorber is removed exposing the front-contact beneath. Finally, after back-contact deposition the interconnection is formed when the back-contact is removed defining the individual cell stripes (P3).

In the scope of this thesis the scribe width reduction for each individual processing step P1–P3 was investigated for thin-film silicon solar cells. All processing was done through the substrate side with nanosecond laser sources of the wavelengths 355 nm, 532 nm, and 1064 nm. Two different types of front-contact TCO materials were used for processing (ZnO:Al and SnO₂:F). Furthermore, amorphous silicon (a-Si:H) as well as a-Si:H/ μ c-Si:H tandem absorber materials were processed. Lastly, a combination of ZnO:Al/Ag/ZnO:Al was used as the back-contact system.

P1: for the front-contact removal process P1 significant differences in ablation behavior are found depending on the used wavelengths. Investigations on the ablation mechanisms indicate a transition from a highly mechanically-induced ablation process (355 nm) to a more classic ablation by phase changes (532 nm and 1064 nm). The scribe edge morphology indicates that with regards to the minimization of the scribe width the latter seems to be favorable since smoother scribe edges are obtained.

Chapter 8. Conclusion

An increase of debris redeposition onto the remaining front-contact material in direct vicinity of the scribe line is observed when the beam spot radius is reduced below 10 μm . The increased appearance can possibly be accounted to a change of the laser plume distribution. The plume exhibits a spherical evolution for small beam spot sizes. A characterization of the local TCO and solar cell properties reveals a severe impact on the active material with an spatial extent of up to 80 μm into the active solar cell region. Of course, this would foil the width reduction pursue.

Fortunately, the TCO material beneath shows no severe deterioration and impact on the active cell near the scribe edge can be minimized with a proper wet-chemical cleaning of the TCO surface prior to absorber deposition.

The main purpose of P1 is the electrical insulation of two neighboring cell stripes. However, after absorber deposition a parasitic parallel resistance between the neighboring TCO stripes is formed. Furthermore, when considering a linear behavior of the parasitic conductivity as a function of the scribe width, shunting increases with decreasing scribe width. Determination of the value range for this shunt shows an negligible impact on the solar modules performance for typical cell topologies, even for scribe widths $<10 \mu\text{m}$.

As a result a typical P1 scribe width of 40–50 μm could be reduced down to 7–10 μm with proper electrical insulation. The P1 scribe width is primarily limited by the maximal reasonable loss in depth-of-focus from the used optical systems and machine accuracy.

P2: the width reduction optimization was extended for the absorber removal process P2. Since minimal damaging of the exposed front-contact material is required all processing was done with 532 nm and beam spot radii of 60 μm , 20 μm , and 10 μm .

Surprisingly, the minimal achievable scribe width or lower limit is not directly correlated to the used beam radius. This limit is further increased when the thickness of the absorber is increased. The onset peak fluence specifies the minimal laser energy density that is required for proper ablation. Below this value only bulging of the layer occurs. For a-Si:H processing only a slight increase of this value is observed (4x) when the beam spot radius is decreased. In contrast, for processing of tandem absorber the values increase significantly (10x). This behavior sets natural limits for the lower scribe width. It can be concluded that thin scribe lines are only possible for thin absorber layers.

Numerical simulations were carried out to attain insight on the observed ablation behavior from the experiments. For 532 nm a dominantly mechanically-assisted ablation is apparent. Ablation is driven either by mechanical stresses in and between the individual layers due to thermal expansion or formation of blisters by gas pressure, or both. Simulations indicate that vaporization of silicon is unlikely. However, it is possible that hydrogen bound in the absorber diffuses to the TCO/absorber upon heating forming a gas blister.

Both mechanisms of ablation can possibly explain the experimental behavior. The relation between delaminated area at the TCO/absorber interface and the area formed by the absorbers

thickness and craters circumference is a determining factor for the ablation. Such behavior results directly from linear fracture mechanics. This behavior seems to be fundamental for many laser scribing processes that are done through the substrate side (or more general, laser-induced processes).

The electrical purpose of P2 is to create the interconnection of the back-contact from one cell with the front-contact of the next cell. Hence, a low series resistance is required. However, it is known that during P2 processing a contact resistance can form due to debris redeposition onto the exposed front-contact. For processing of a-Si:H a ten-fold increase of the minimal series resistance is observed when the beam spot radius is lowered from 60 μm to 10 μm . Evaluation shows that in the case of a-Si:H processing such increase is partly owed to an increase of the specific contact resistance while the value is more or less constant for tandem absorber processing with decreasing radii. Similar to the findings from P1 an increase of debris redeposition is observed which could be a reason for a change of the specific contact properties. However, for processing of tandem absorber no significant increase of the specific contact resistance is found and low series resistances are achieved for all focusing geometries.

Due to the strong influence of the mechanical ablation behavior, for tandem processing, the commonly used P2 scribe width of 90 μm could only be reduced to approx. 30 μm . For a-Si:H processing a scribe width down to 10 μm is achievable. However, deterioration of the electrical properties gives rise to constraints that limit the reasonable scribe width to higher values.

P3: since the back-contact insulation process P3 is very similar to P2 no significant differences in ablation behavior and morphology are expected. Actually, the constraints are even higher since the overall thickness is increased further by the back-contact (thickness approx. 280 nm). That is exactly what is found for the geometrical scribe width reduction which is limited to even higher minimal widths than for P2. Furthermore, while for a-Si:H a clean scribe edge definition is possible for all three used beam radii strong irregularities are found for processing of tandem solar cells when the radius is decreased.

In terms of impact on the electrical properties of the module P3 is a critical laser scribing process. A shunt is easily formed between front- and back-contact at the direct vicinity of the scribe edge. Due to heating of the active material by excess energy from the shoulders of the Gaussian intensity distribution crystallization of the absorber can occur leading to shunting of the cell stripe in this region.

Calculations with experimental results from the ablation behavior indicate that due to the increased threshold fluences and onset peak fluences (cf. results P2) for reduced laser beam radii, no distinct statement on increase or decrease of sub-threshold energy intake is possible.

Electrical measurements reveal severe impact on a-Si:H solar cells when a beam spot radius of 10 μm is used. However, deterioration is significantly lower for processing of tandem solar cells. It is possible that shunt formation is suppressed due to the higher thickness of the absorber and the more localized heating of the a-Si:H top-cell (532 nm processing wavelength).

Chapter 8. Conclusion

In general, a comparison of dark $I - V$ behavior, solar cell parameters (FF , V_{OC}), and investigation by Raman microscopy all show good agreement for processing of a-Si:H solar cells. For tandem solar cell processing the interpretation is not as distinct. Strong delamination at the direct scribe edge occurs which can be measured by Raman but it remains unclear whether this delaminated region is in electrical contact with the underlying TCO or not.

For a-Si:H solar cell processing with a beam spot radius of $10\ \mu\text{m}$ the severe shunting of the cell defines an additional electrical constraint that limits the reasonable minimal scribe width. Tandem solar cells seem to be more resistant to shunting, even for processing with a radius of $10\ \mu\text{m}$. However, good electrical properties are only achieved in a narrow process windows in terms of peak fluences. For both, scribing with $20\ \mu\text{m}$ as well as $10\ \mu\text{m}$ a strong increase of the current flow slope by many orders of magnitude (factor 10^3 – 10^4) occurs when the peak fluence is increased. Although calculations indicate no change of heat-affected zone formation additional effects that cannot be described simply by sub-threshold energy intake at the scribe edge occur.

Maybe measurements by low current c-AFM from the film side could give insight about the actual electrical properties at the direct scribe edge when the back-contact is removed.

In conclusion, fundamental limitations on the reduction of the interconnection width are found for laser scribing through the substrate side. Exemplary process implementation shows that a reduction from 300 – $350\ \mu\text{m}$ down to 100 – $120\ \mu\text{m}$ is possible for tandem solar modules with an absorber thickness of approx. $2\ \mu\text{m}$.

The interconnection processes need to be optimized for each specific solar cell configuration. A reduction of the dead area by width-reduced scribe lines is possible when narrowing process windows in terms of peak fluences, depth-of-focus losses, dependence of the laser beam radius and layer thickness on the electrical properties of the solar module are all taken into account.

As an outlook better understanding of the mechanical processes behind ablation of P2 and P3, for instance gas pressure by hydrogen diffusion or stresses by thermal expansion is important to further confirm the observed geometrical constraints. For this, it is necessary to carry out transient ablation imaging to obtain insight into the relevant timescales of material removal. It is also feasible to use special beam shapes like Top-Hat profiles, cylindrical lenses or so-called doughnut beams. With these beams it is possible to differentiate between different ablation mechanisms where layer delamination or layer fracture is enhanced.

To overcome the geometrical constraints of the scribes minimal width I strongly believe that one promising approach is film side processing. Here, mechanical effects are most likely not as dominant as for ablation from the substrate side. Of course this is only valid for processes that are only weakly assisted by thermal stresses.

It would be necessary to use ultra short pulsed lasers (USP) for processing from the film side since undesired thermal impact on the material is known to be reduced for shorter pulse durations. Especially, P2 and P3 are difficult to realize with nanosecond lasers without negative

impact on the electrical properties [154, 169]. Technologies like CIS and CIGS do not have an interconnection approach by nanosecond laser ablation because of this reason [42, 54, 170].

Furthermore, it is also true that rel. interconnection losses are comparably lower for thin-film silicon modules than for instance for CIGS, CdTe, and OPV [1, 171]. For these technologies closing the cell to module efficiency gap remains an important challenge. A significantly reduced interconnection width could help to reduce this efficiency gap.

Nonetheless, even if film side processing is combined with USP lasers leading to only optical constraints due to DOF losses, I believe a lower limit for the overall standard interconnection width is between 50–100 μm . This assumption originates from the optimized P1 scribe width processes (approx. 10 μm). The margin in-between the scribes is limited by the scribing tool accuracy. Although modern tools use image processing for proper alignment between the scribes, it is reasonable to assume that the lower limit of the margin will be around 10 μm .

Novel interconnection schemes are required to overcome these inherent dead area limitations. In a first proof-of-concept a new type of interconnection scheme was developed where the interconnection processes P2 and P3 are placed on the back-side of the module. For this, the front-contact is transferred locally to the back of the module. With both contacts on the back it is possible to create the series connection (P2 and P3) without adding to the dead area losses. Only P1 and the local contacts remain on the front side.

Bibliography

- [1] M. A. Green, K. Emery, Y. Hishikawa, W. Warta, and E. D. Dunlop, "Solar cell efficiency tables (version 44)," *Prog. Photovoltaics Res. Appl.*, vol. 22, pp. 701–710, July 2014.
- [2] O. Gabriel, S. Kirner, C. Leendertz, M. Gerhardt, A. Heidelberg, H. Bloefß, R. Schlatmann, and B. Rech, "Large area PECVD of a-Si:H/a-Si:H tandem solar cells," *Phys. status solidi*, vol. 8, pp. 2982–2985, Oct. 2011.
- [3] T. Brammer, W. Reetz, N. Senoussaoui, O. Vetterl, O. Kluth, B. Rech, H. Stiebig, and H. Wagner, "Optical properties of silicon-based thin-film solar cells in substrate and superstrate configuration," *Sol. Energy Mater. Sol. Cells*, vol. 74, pp. 469–478, Oct. 2002.
- [4] B. Yan, J. Yang, and S. Guha, "Amorphous and nanocrystalline silicon thin film photovoltaic technology on flexible substrates," *J. Vac. Sci. Technol. A Vacuum, Surfaces, Film.*, vol. 30, no. 4, p. 04D108, 2012.
- [5] B. Rech, S. Wieder, C. Beneking, A. Loffi, O. Kluth, W. Reetz, and H. Wagner, "Texture etched ZnO:Al films as front contact and back reflector in amorphous silicon p-i-n and n-i-p solar cells," in *Conf. Rec. Twenty Sixth IEEE Photovolt. Spec. Conf.*, (Anaheim, USA), pp. 619–622, IEEE, 1997.
- [6] R. G. Gordon, "Criteria for Choosing Transparent Conductors," *MRS Bull.*, vol. 25, pp. 52–57, Jan. 2011.
- [7] J. Müller, B. Rech, J. Springer, and M. Vanecek, "TCO and light trapping in silicon thin film solar cells," *Sol. Energy*, vol. 77, pp. 917–930, Dec. 2004.
- [8] M. Mizuhashi, Y. Gotoh, and K. Adachi, "Texture Morphology of SnO₂:F Films and Cell Reflectance," *Jpn. J. Appl. Phys.*, vol. 27, pp. 2053–2061, Nov. 1988.
- [9] S. Fay, J. Steinhauser, S. Nicolay, and C. Ballif, "Polycrystalline ZnO:B grown by LPCVD as TCO for thin film silicon solar cells," *Thin Solid Films*, vol. 518, pp. 2961–2966, Mar. 2010.
- [10] H. Zhu, J. Hüpkens, E. Bunte, J. Owen, and S. Huang, "Novel etching method on high rate ZnO:Al thin films reactively sputtered from dual tube metallic targets for silicon-based solar cells," *Sol. Energy Mater. Sol. Cells*, vol. 95, pp. 964–968, Mar. 2011.

Bibliography

- [11] H. Keppner, J. Meier, P. Torres, D. Fischer, and A. Shah, "Microcrystalline silicon and micromorph tandem solar cells," *Appl. Phys. A Mater. Sci. Process.*, vol. 69, pp. 169–177, Aug. 1999.
- [12] R. Das, T. Jana, and S. Ray, "Degradation studies of transparent conducting oxide: a substrate for microcrystalline silicon thin film solar cells," *Sol. Energy Mater. Sol. Cells*, vol. 86, pp. 207–216, Mar. 2005.
- [13] J. Meier, S. Dubail, R. Fluckiger, D. Fischer, H. Keppner, and A. Shah, "Intrinsic microcrystalline silicon ($\mu\text{-Si:H}$)-a promising new thin film solar cell material," in *Conf. Rec. Twenty Fourth IEEE Photovolt. Spec. Conf.*, vol. 1, (Waikoloa, USA), pp. 409–412, IEEE, 1994.
- [14] D. Fischer, S. Dubail, J. Selvan, N. Vaucher, R. Platz, C. Hof, U. Kroll, J. Meier, P. Torres, H. Keppner, N. Wyrsh, M. Goetz, A. Shah, and K.-D. Ufert, "The "micromorph" solar cell: extending a-Si:H technology towards thin film crystalline silicon," in *Conf. Rec. Twenty Fifth IEEE Photovolt. Spec. Conf.*, (Washington, USA), pp. 1053–1056, IEEE, 1996.
- [15] D. E. Carlson and C. R. Wronski, "Amorphous silicon solar cell," *Appl. Phys. Lett.*, vol. 28, no. 11, pp. 671–673, 1976.
- [16] O. Vetterl, F. Finger, R. Carius, P. Hapke, L. Houben, O. Kluth, A. Lambertz, A. Mück, B. Rech, and H. Wagner, "Intrinsic microcrystalline silicon: A new material for photovoltaics," *Sol. Energy Mater. Sol. Cells*, vol. 62, pp. 97–108, Apr. 2000.
- [17] T. Repmann, J. Kirchoff, W. Reetz, F. Birmans, J. Muller, and B. Rech, "Investigations on the current matching of highly efficient tandem solar cells based on amorphous and microcrystalline silicon," in *Proc. 3rd World Conf. Photovolt. Energy Convers.*, vol. 2, (Osaka, Japan), pp. 1843–1846, IEEE, 2003.
- [18] J. Yang, A. Banerjee, and S. Guha, "Triple-junction amorphous silicon alloy solar cell with 14.6% initial and 13.0% stable conversion efficiencies," *Appl. Phys. Lett.*, vol. 70, no. 22, pp. 2975–2977, 1997.
- [19] R. Street, D. Biegelsen, and J. Knights, "Defect states in doped and compensated a-Si:H," *Phys. Rev. B*, vol. 24, pp. 969–984, July 1981.
- [20] H. Okamoto, Y. Nitta, T. Adachi, and Y. Hamakawa, "Glow discharge produced amorphous silicon solar cells," *Surf. Sci.*, vol. 86, pp. 486–491, July 1979.
- [21] D. L. Staebler and C. R. Wronski, "Reversible conductivity changes in discharge-produced amorphous Si," *Appl. Phys. Lett.*, vol. 31, no. 4, pp. 292–294, 1977.
- [22] M. Zeman, R. A. C. M. M. van Swaaij, J. W. Metselaar, and R. E. I. Schropp, "Optical modeling of a-Si:H solar cells with rough interfaces: Effect of back contact and interface roughness," *J. Appl. Phys.*, vol. 88, no. 11, pp. 6436–6443, 2000.
- [23] J. Springer, "Absorption loss at nanorough silver back reflector of thin-film silicon solar cells," *J. Appl. Phys.*, vol. 95, no. 3, pp. 1427–1429, 2004.

- [24] E. Moulin, U. Paetzold, K. Bittkau, M. Ermes, L. Ding, L. Fanni, S. Nicolay, J. Kirchhoff, D. Weigand, A. Bauer, A. Lambertz, C. Ballif, and R. Carius, "Thin-film silicon solar cells applying optically decoupled back reflectors," *Mater. Sci. Eng. B*, vol. 178, pp. 645–650, May 2013.
- [25] O. Berger, D. Inns, and A. G. Aberle, "Commercial white paint as back surface reflector for thin-film solar cells," *Sol. Energy Mater. Sol. Cells*, vol. 91, pp. 1215–1221, Aug. 2007.
- [26] A. V. Shah, H. Schade, M. Vanecek, J. Meier, E. Vallat-Sauvain, N. Wyrsh, U. Kroll, C. Droz, and J. Bailat, "Thin-film silicon solar cell technology," *Prog. Photovoltaics Res. Appl.*, vol. 12, pp. 113–142, Mar. 2004.
- [27] S. M. Sze and K. K. Ng, *Physics of semiconductor devices*. John Wiley & Sons, 2006.
- [28] R. E. I. Schropp and M. Zeman, *Amorphous and Microcrystalline Silicon Solar Cells: Modeling, Materials and Device Technology*. Kluwer Academic, 1998.
- [29] M. A. Green, *Solar Cells: Operating Principles, Technology, and System Applications*. Prentice Hall, 1981.
- [30] U. Stutenbaeumer and B. Mesfin, "Equivalent model of monocrystalline, polycrystalline and amorphous silicon solar cells," *Renew. Energy*, vol. 18, pp. 501–512, Dec. 1999.
- [31] R. S. Crandall, "Modeling of thin film solar cells: Uniform field approximation," *J. Appl. Phys.*, vol. 54, no. 12, pp. 7176–7186, 1983.
- [32] S. S. Hegedus and W. N. Shafarman, "Thin-film solar cells: device measurements and analysis," *Prog. Photovoltaics Res. Appl.*, vol. 12, pp. 155–176, Mar. 2004.
- [33] S. Eidelloth, F. Haase, and R. Brendel, "Simulation Tool for Equivalent Circuit Modeling of Photovoltaic Devices," *IEEE J. Photovoltaics*, vol. 2, pp. 572–579, Oct. 2012.
- [34] J. Merten, J. Asensi, C. Voz, A. Shah, R. Platz, and J. Andreu, "Improved equivalent circuit and analytical model for amorphous silicon solar cells and modules," *IEEE Trans. Electron Devices*, vol. 45, no. 2, pp. 423–429, 1998.
- [35] A. Shah, F. Sculati-Meillaud, Z. Berényi, O. Ghahfarokhi, and R. Kumar, "Diagnostics of thin-film silicon solar cells and solar panels/modules with variable intensity measurements (VIM)," *Sol. Energy Mater. Sol. Cells*, vol. 95, pp. 398–403, Jan. 2011.
- [36] V. Badescu, "Simple optimization procedure for silicon-based solar cell interconnection in a series-parallel PV module," *Energy Convers. Manag.*, vol. 47, pp. 1146–1158, June 2006.
- [37] S. Nakano, T. Matsuoka, S. Kiyama, H. Kawata, N. Nakamura, Y. Nakashima, S. Tsuda, H. Nishiwaki, M. Ohnishi, I. Nagaoka, and Y. Kuwano, "Laser Patterning Method for Integrated Type a-Si Solar Cell Submodules," *Jpn. J. Appl. Phys.*, vol. 25, pp. 1936–1943, Dec. 1986.

Bibliography

- [38] S. Praschek, W. Riedl, H. Hoermann, and H. Goslowsky, "Laser patterning of a-Si solar modules with transparent conducting zinc oxide back electrodes," in *Conf. Rec. Twenty Second IEEE Photovolt. Spec. Conf.*, (Las Vegas, USA), pp. 1285–1289, IEEE, 1991.
- [39] B. Dimmler and H. W. Schock, "Scaling-up of CIS technology for thin-film solar modules," *Prog. Photovoltaics Res. Appl.*, vol. 4, pp. 425–433, Nov. 1996.
- [40] J. Perrenoud, B. Schaffner, S. Buecheler, and A. Tiwari, "Fabrication of flexible CdTe solar modules with monolithic cell interconnection," *Sol. Energy Mater. Sol. Cells*, vol. 95, pp. S8–S12, May 2011.
- [41] A. Burn, M. Murali, S. Pilz, V. Romano, R. Witte, B. Frei, S. Buecheler, S. Nishiwaki, and L. Krainer, "All Fiber Laser Scribing of Cu(In,Ga)Se₂ Thin-Film Solar Modules," *Phys. Procedia*, vol. 41, pp. 713–722, Jan. 2013.
- [42] P.-O. Westin, U. Zimmermann, M. Ruth, and M. Edoff, "Next generation interconnective laser patterning of CIGS thin film modules," *Sol. Energy Mater. Sol. Cells*, vol. 95, pp. 1062–1068, Apr. 2011.
- [43] Y. Gupta, H. Liers, S. Woods, S. Young, R. DeBlasio, and L. Mrig, "Optimization of a-Si solar cell current collection," in *16th Photovolt. Spec. Conf.*, vol. 1, (San Diego, USA), pp. 1092–1101, 1982.
- [44] H. Booth, "Laser Processing in Industrial Solar Module Manufacturing," *J. Laser Micro/Nanoengineering*, vol. 5, pp. 183–191, Dec. 2010.
- [45] S. Haas, *Untersuchung und Optimierung der Serienverschaltung von Silizium-Dünnschicht-Solarmodulen*. PhD thesis, RWTH Aachen, Jülich, 2010.
- [46] S. Haas, A. Gordijn, G. Schöpe, B. E. Pieters, and H. Stiebig, "Influence of the laser parameters on the patterning quality of thin-film silicon modules," in *Proc. SPIE* (B. von Roedern and A. E. Delahoy, eds.), (San Diego, USA), pp. 66510H–66510H–10, Sept. 2007.
- [47] F. Korte, S. Nolte, B. Chichkov, T. Bauer, G. Kamlage, T. Wagner, C. Fallnich, and H. Welling, "Far-field and near-field material processing with femtosecond laser pulses," *Appl. Phys. A Mater. Sci. Process.*, vol. 69, pp. S7–S11, Dec. 1999.
- [48] F. Brunner, G. J. Spühler, J. Au, L. Krainer, F. Morier-Genoud, R. Paschotta, N. Lichtenstein, S. Weiss, C. Harder, A. A. Lagatsky, A. Abdolvand, N. V. Kuleshov, and U. Keller, "Diode-pumped femtosecond Yb:KGd(WO₄)₂ laser with 1.1-W average power," *Opt. Lett.*, vol. 25, pp. 1119–1121, Aug. 2000.
- [49] W. Kautek, J. Krüger, M. Lenzner, S. Sartania, C. Spielmann, and F. Krausz, "Laser ablation of dielectrics with pulse durations between 20 fs and 3 ps," *Appl. Phys. Lett.*, vol. 69, no. 21, pp. 3146–3148, 1996.
- [50] R. Le Harzic, D. Breitling, M. Weikert, S. Sommer, C. Föhl, S. Valette, C. Donnet, E. Audouard, and F. Dausinger, "Pulse width and energy influence on laser micromachining of metals in a range of 100fs to 5ps," *Appl. Surf. Sci.*, vol. 249, pp. 322–331, Aug. 2005.

-
- [51] B. N. Chichkov, C. Momma, S. Nolte, F. Alvensleben, and A. Tünnermann, "Femtosecond, picosecond and nanosecond laser ablation of solids," *Appl. Phys. A Mater. Sci. Process.*, vol. 63, pp. 109–115, Aug. 1996.
- [52] M. Grishin, "Cavity dumping versus stationary output coupling in repetitively Q-switched solid-state lasers," *J. Opt. Soc. Am. B*, vol. 28, pp. 433–444, Feb. 2011.
- [53] J. Dong and P. Deng, "Laser performance of monolithic Cr, Nd:YAG self-Q-switched laser," *Opt. Commun.*, vol. 220, pp. 425–431, May 2003.
- [54] J. Hermann, M. Benfarah, G. Coustillier, S. Bruneau, E. Axente, J.-F. Guillemoles, M. Sentis, P. Alloncle, and T. Itina, "Selective ablation of thin films with short and ultrashort laser pulses," *Appl. Surf. Sci.*, vol. 252, pp. 4814–4818, Apr. 2006.
- [55] T. F. Johnston, "Beam Propagation (M^2) Measurement Made as Easy as It Gets: The Four-Cuts Method," *Appl. Opt.*, vol. 37, pp. 4840–4850, July 1998.
- [56] E. Hecht, *Optik*. Oldenbourg, 2005.
- [57] J. Durnin, "Exact solutions for nondiffracting beams. I. The scalar theory," *J. Opt. Soc. Am. A*, vol. 4, pp. 651–654, Apr. 1987.
- [58] A. Michalowski, C. Freitag, R. Weber, and T. Graf, "Laser surface structuring with long depth of focus," in *Proc. SPIE* (B. Gu, G. Hennig, X. Xu, and H. Niino, eds.), vol. 7920, (San Francisco, USA), pp. 79200W–79200W–7, Feb. 2011.
- [59] F. Courvoisier, J. Zhang, M. K. Bhuyan, M. Jacquot, and J. M. Dudley, "Applications of femtosecond Bessel beams to laser ablation," *Appl. Phys. A*, vol. 112, pp. 29–34, Sept. 2012.
- [60] Y. Matsuoka, Y. Kizuka, and T. Inoue, "The characteristics of laser micro drilling using a Bessel beam," *Appl. Phys. A*, vol. 84, pp. 423–430, June 2006.
- [61] A. Laskin and V. Laskin, " π Shaper – Refractive Beam Shaping Optics for Advanced Laser Technologies," *J. Phys. Conf. Ser.*, vol. 276, p. 012171, Feb. 2011.
- [62] G. Račiukaitis, E. Stankevičius, P. Gečys, M. Gedvilas, C. Bischoff, E. Jäger, U. Umhofer, and F. Völklein, "Laser Processing by Using Diffractive Optical Laser Beam Shaping Technique," *J. Laser Micro/Nanoengineering*, vol. 6, pp. 37–43, Mar. 2011.
- [63] A. Parent, M. Morin, and P. Lavigne, "Propagation of super-Gaussian field distributions," *Opt. Quantum Electron.*, vol. 24, pp. S1071–S1079, Sept. 1992.
- [64] B. Frei, S. Schneeberger, and R. Witte, "Innovative laser based solar cell scribing," in *Proc. SPIE* (B. Gu, G. Hennig, X. Xu, and H. Niino, eds.), vol. 7920, (San Francisco, USA), pp. 792011–792011–13, Feb. 2011.
- [65] W. J. Wang, K. D. Wang, G. D. Jiang, X. S. Mei, and C. J. Yang, "Comparison of femtosecond laser-induced front- and rear-side ablation of films," *Proc. Inst. Mech. Eng. Part B J. Eng. Manuf.*, vol. 225, pp. 520–527, Apr. 2011.

Bibliography

- [66] Z. Chen, D. Bleiner, and A. Bogaerts, "Effect of ambient pressure on laser ablation and plume expansion dynamics: A numerical simulation," *J. Appl. Phys.*, vol. 99, no. 6, p. 063304, 2006.
- [67] N. A. Vasantgadkar, U. V. Bhandarkar, and S. S. Joshi, "A finite element model to predict the ablation depth in pulsed laser ablation," *Thin Solid Films*, vol. 519, pp. 1421–1430, Dec. 2010.
- [68] G. Račiukaitis, M. Brikas, G. Darčianovas, D. Ruthe, and K. Zimmer, "Laser structuring of conducting films on transparent substrates," in *Proc. SPIE* (V. Y. Panchenko, O. A. Louchev, and S. Malyshev, eds.), (Minsk, Belarus), pp. 67320C–67320C–10, June 2007.
- [69] J. M. Liu, "Simple technique for measurements of pulsed Gaussian-beam spot sizes," *Opt. Lett.*, vol. 7, pp. 196–198, May 1982.
- [70] S. Martin, A. Hertwig, M. Lenzner, J. Krüger, and W. Kautek, "Spot-size dependence of the ablation threshold in dielectrics for femtosecond laser pulses," *Appl. Phys. A Mater. Sci. Process.*, vol. 77, pp. 883–884, Dec. 2003.
- [71] A. D. Compaan, I. Matulionis, and S. Nakade, "Laser scribing of polycrystalline thin films," *Opt. Lasers Eng.*, vol. 34, pp. 15–45, July 2000.
- [72] D. Canteli, I. Torres, J. J. García-Ballesteros, J. Cárabe, C. Molpeceres, and J. J. Gandía, "Characterization of direct- and back-scribing laser patterning of SnO₂:F for a-Si:H PV module fabrication," *Appl. Surf. Sci.*, vol. 271, pp. 223–227, Apr. 2013.
- [73] W. K. Yung, J. Liu, H. Man, and T. Yue, "355nm Nd:YAG laser ablation of polyimide and its thermal effect," *J. Mater. Process. Technol.*, vol. 101, pp. 306–311, Apr. 2000.
- [74] J. Cheng, W. Perrie, M. Sharp, S. P. Edwardson, N. G. Semaltianos, G. Dearden, and K. G. Watkins, "Single-pulse drilling study on Au, Al and Ti alloy by using a picosecond laser," *Appl. Phys. A*, vol. 95, pp. 739–746, Dec. 2008.
- [75] J. Bonse, J. Wrobel, J. Krüger, and W. Kautek, "Ultrashort-pulse laser ablation of indium phosphide in air," *Appl. Phys. A Mater. Sci. Process.*, vol. 72, pp. 89–94, Jan. 2001.
- [76] M. D. Abràmoff, P. J. Magalhães, and S. J. Ram, "Image processing with ImageJ," *Biophotonics Int.*, vol. 11, no. 7, pp. 36–43, 2004.
- [77] G. Binnig and C. F. Quate, "Atomic Force Microscope," *Phys. Rev. Lett.*, vol. 56, pp. 930–933, Mar. 1986.
- [78] R. A. Oliver, "Advances in AFM for the electrical characterization of semiconductors," *Reports Prog. Phys.*, vol. 71, p. 076501, July 2008.
- [79] F. Houze, R. Meyer, O. Schneegans, and L. Boyer, "Imaging the local electrical properties of metal surfaces by atomic force microscopy with conducting probes," *Appl. Phys. Lett.*, vol. 69, no. 13, pp. 1975–1977, 1996.

- [80] J. Oh and R. J. Nemanich, "Current-voltage and imaging of TiSi_2 islands on Si(001) surfaces using conductive-tip atomic force microscopy," *J. Appl. Phys.*, vol. 92, no. 6, pp. 3326–3331, 2002.
- [81] A. Vetushka, A. Fejfar, M. Ledinský, B. Rezek, J. Stuchlík, and J. Kočka, "Role of the tip induced local anodic oxidation in the conductive atomic force microscopy of mixed phase silicon thin films," *Phys. status solidi*, vol. 7, pp. 728–731, Feb. 2010.
- [82] R. E. Thomson, "Development of highly conductive cantilevers for atomic force microscopy point contact measurements," *J. Vac. Sci. Technol. B Microelectron. Nanom. Struct.*, vol. 13, pp. 1123–1125, May 1995.
- [83] T. Trenkler, T. Hantschel, R. Stephenson, P. De Wolf, W. Vandervorst, L. Hellemans, A. Malavé, D. Büchel, E. Oesterschulze, W. Kulisch, P. Niedermann, T. Sulzbach, and O. Ohlsson, "Evaluating probes for "electrical" atomic force microscopy," *J. Vac. Sci. Technol. B Microelectron. Nanom. Struct.*, vol. 18, no. 1, pp. 418–427, 2000.
- [84] B. Rezek, J. Stuchlík, A. Fejfar, and J. Kočka, "Microcrystalline silicon thin films studied by atomic force microscopy with electrical current detection," *J. Appl. Phys.*, vol. 92, no. 1, pp. 587–593, 2002.
- [85] R. S. Timsit, "Constriction Resistance of Thin-Film Contacts," in *Proc. 54th IEEE Holm Conf. Electr. Contacts*, (Orlando, USA), pp. 332–336, IEEE, Oct. 2008.
- [86] E. Tevaarwerk, D. G. Keppel, P. Rugheimer, M. G. Lagally, and M. A. Eriksson, "Quantitative analysis of electric force microscopy: The role of sample geometry," *Rev. Sci. Instrum.*, vol. 76, no. 5, p. 053707, 2005.
- [87] A. Efimov and S. R. Cohen, "Simulation and correction of geometric distortions in scanning Kelvin probe microscopy," *J. Vac. Sci. Technol. A Vacuum, Surfaces, Film.*, vol. 18, no. 4, pp. 1051–1055, 2000.
- [88] O. Schneegans, F. Houzé, R. Meyer, and L. Boyer, "Study of the local electrical properties of metal surfaces using an AFM with a conducting probe," *IEEE Trans. Components, Packag. Manuf. Technol. Part A*, vol. 21, pp. 76–81, Mar. 1998.
- [89] J. Carstensen, G. Popkurov, J. Bahr, and H. Föll, "CELLO: an advanced LBIC measurement technique for solar cell local characterization," *Sol. Energy Mater. Sol. Cells*, vol. 76, pp. 599–611, Apr. 2003.
- [90] E. Fortunato, P. Nunes, A. Marques, D. Costa, H. Águas, I. Ferreira, M. Costa, M. Godinho, P. Almeida, J. Borges, and R. Martins, "Influence of the Strain on the Electrical Resistance of Zinc Oxide Doped Thin Film Deposited on Polymer Substrates," *Adv. Eng. Mater.*, vol. 4, pp. 610–612, Aug. 2002.
- [91] A. Schoonderbeek, "Laser Processing of Thin Films for Photovoltaic Applications," *J. Laser Micro/Nanoengineering*, vol. 5, pp. 248–255, Dec. 2010.

Bibliography

- [92] C. Molpeceres, S. Lauzurica, J. García-Ballesteros, M. Morales, G. Guadaño, J. Ocaña, S. Fernández, J. Gandía, F. Villar, O. Nos, and J. Bertomeu, "Selective ablation of photovoltaic materials with UV laser sources for monolithic interconnection of devices based on a-Si:H," *Mater. Sci. Eng. B*, vol. 159-160, pp. 18–22, Mar. 2009.
- [93] D. Bäuerle, *Laser Processing and Chemistry*. Berlin, Heidelberg: Springer Berlin Heidelberg, 2011.
- [94] G. Heise, M. Domke, J. Konrad, S. Sarrach, J. Sotrop, and H. P. Huber, "Laser lift-off initiated by direct induced ablation of different metal thin films with ultra-short laser pulses," *J. Phys. D: Appl. Phys.*, vol. 45, p. 315303, Aug. 2012.
- [95] R. Fardel, M. Nagel, F. Nuesch, T. Lippert, and A. Wokaun, "Fabrication of organic light-emitting diode pixels by laser-assisted forward transfer," *Appl. Phys. Lett.*, vol. 91, no. 6, p. 061103, 2007.
- [96] B. Hopp, T. Smausz, N. Kresz, N. Barna, Z. Bor, L. Kolozsvári, D. B. Chrisey, A. Szabó, and A. Nógrádi, "Survival and proliferative ability of various living cell types after laser-induced forward transfer," *Tissue Eng.*, vol. 11, no. 11-12, pp. 1817–23, 2006.
- [97] N. T. Kattamis, M. S. Brown, and C. B. Arnold, "Finite element analysis of blister formation in laser-induced forward transfer," *J. Mater. Res.*, vol. 26, pp. 2438–2449, Aug. 2011.
- [98] H. Wang, S.-T. Hsu, H. Tan, Y. L. Yao, H. Chen, and M. N. Azer, "Predictive Modeling for Glass-Side Laser Scribing of Thin Film Photovoltaic Cells," *J. Manuf. Sci. Eng.*, vol. 135, p. 051004, Sept. 2013.
- [99] J. Bovatsek, A. Tamhankar, R. S. Patel, N. M. Bulgakova, and J. Bonse, "Thin film removal mechanisms in ns-laser processing of photovoltaic materials," *Thin Solid Films*, vol. 518, pp. 2897–2904, Mar. 2010.
- [100] S. G. Koulikov and D. D. Dlott, "Ultrafast microscopy of laser ablation of refractory materials: ultra low threshold stress-induced ablation," *J. Photochem. Photobiol. A Chem.*, vol. 145, pp. 183–194, Dec. 2001.
- [101] G. Heise, M. Englmaier, C. Hellwig, T. Kuznicki, S. Sarrach, and H. P. Huber, "Laser ablation of thin molybdenum films on transparent substrates at low fluences," *Appl. Phys. A*, vol. 102, pp. 173–178, Aug. 2010.
- [102] W. Zhang, Y. Yao, and K. Chen, "Modelling and Analysis of UV Laser Micromachining of Copper," *Int. J. Adv. Manuf. Technol.*, vol. 18, pp. 323–331, Sept. 2001.
- [103] S. Amoruso, "Modeling of UV pulsed-laser ablation of metallic targets," *Appl. Phys. A Mater. Sci. Process.*, vol. 69, pp. 323–332, Sept. 1999.
- [104] R. Swanepoel, "Determination of the thickness and optical constants of amorphous silicon," *J. Phys. E.*, vol. 16, pp. 1214–1222, Dec. 1983.

- [105] S. Adachi, *Optical Properties of Crystalline and Amorphous Semiconductors*. Boston, MA: Springer US, 1999.
- [106] G. J. Exarhos and X.-D. Zhou, "Discovery-based design of transparent conducting oxide films," *Thin Solid Films*, vol. 515, pp. 7025–7052, June 2007.
- [107] Q. Xu, R. Hong, H. Huang, Z. Zhang, M. Zhang, X. Chen, and Z. Wu, "Laser annealing effect on optical and electrical properties of Al doped ZnO films," *Opt. Laser Technol.*, vol. 45, pp. 513–517, Feb. 2013.
- [108] Y.-Y. Chen, P. W. Wang, J.-C. Hsu, and C.-Y. Lee, "Post-annealing properties of aluminum-doped zinc oxide films fabricated by ion beam co-sputtering," *Vacuum*, vol. 87, pp. 227–231, Jan. 2013.
- [109] I. Kobiakov, "Elastic, piezoelectric and dielectric properties of ZnO and CdS single crystals in a wide range of temperatures," *Solid State Commun.*, vol. 35, pp. 305–310, July 1980.
- [110] I. Barin, *Thermochemical Data of Pure Substances*. Weinheim, Germany: Wiley-VCH Verlag GmbH, Oct. 1995.
- [111] R. H. Lamoreaux, D. L. Hildenbrand, and L. Brewer, "High-Temperature Vaporization Behavior of Oxides II. Oxides of Be, Mg, Ca, Sr, Ba, B, Al, Ga, In, Tl, Si, Ge, Sn, Pb, Zn, Cd, and Hg," *J. Phys. Chem. Ref. Data*, vol. 16, no. 3, pp. 419–443, 1987.
- [112] D. W. Rankin, "CRC Handbook of Chemistry and Physics," *Crystallogr. Rev.*, vol. 15, pp. 223–224, July 2009.
- [113] H. Gr̃unewald, "Taschenbuch f̃ur Chemiker und Physiker Band 1: Makroskopische physikalisch-chemische Eigenschaften," *Angew. Chemie*, vol. 81, pp. 89–89, Jan. 1969.
- [114] G. Hvedstrup Jensen and T. Skettrup, "Absorption edge and urbach's rule in ZnO," *Phys. Status Solidi*, vol. 60, pp. 169–173, Nov. 1973.
- [115] B. Andress, "Über die Lumineszenz und Absorption von ZnO-Kristallen," *Zeitschrift f̃ur Phys.*, vol. 170, pp. 1–21, Feb. 1962.
- [116] K. K. Nagaraja, S. Pramodini, P. Poornesh, and H. S. Nagaraja, "Effect of annealing on the structural and nonlinear optical properties of ZnO thin films under cw regime," *J. Phys. D. Appl. Phys.*, vol. 46, p. 055106, Feb. 2013.
- [117] D. Bartl, A. Michalowski, M. Hafner, A. Letsch, S. Nolte, and A. T̃unnermann, "Time-resolved study of back side ablated molybdenum thin films by ultrashort laser pulses," *Appl. Phys. A*, vol. 110, pp. 227–233, Aug. 2012.
- [118] M. Colina, C. Molpeceres, M. Holgado, J. Gandia, O. Nos, and J. L. Ocaña, "Study of the refractive index change in a-Si:H thin films patterned by 532nm laser radiation for photovoltaic applications," *Thin Solid Films*, vol. 518, pp. 5331–5339, July 2010.

Bibliography

- [119] D. Canteli, S. Fernandez, C. Molpeceres, I. Torres, and J. J. Gandía, "Nanosecond laser ablation processes in aluminum-doped zinc-oxide for photovoltaic devices," *Appl. Surf. Sci.*, vol. 258, pp. 9447–9451, Sept. 2012.
- [120] S. S. Harilal, "Influence of spot size on propagation dynamics of laser-produced tin plasma," *J. Appl. Phys.*, vol. 102, no. 12, p. 123306, 2007.
- [121] I. Weaver and C. L. S. Lewis, "Polar distribution of ablated atomic material during the pulsed laser deposition of Cu in vacuum: Dependence on focused laser spot size and power density," *J. Appl. Phys.*, vol. 79, no. 9, pp. 7216–7222, 1996.
- [122] S. I. Anisimov, B. S. Luk'yanchuk, and A. Luches, "An analytical model for three-dimensional laser plume expansion into vacuum in hydrodynamic regime," *Appl. Surf. Sci.*, vol. 96-98, pp. 24–32, Apr. 1996.
- [123] M. Kubon, E. Boehmer, M. Gastel, F. Siebke, W. Beyer, C. Beneking, and H. Wagner, "Solution of the ZnO/p contact problem in a-Si:H solar cells," in *Conf. Rec. Twenty Fourth IEEE Photovolt. Spec. Conf.*, vol. 1, (Waikoloa, USA), pp. 500–503, IEEE, 1994.
- [124] S. Ku, S. Haas, G. Schoepe, B. E. Pieters, Q. Ye, and U. Rau, "Direct ablation of ZnO with UV and IR laser for thin film solar modules," *J. Optoelectron. Adv. Mater.*, vol. 12, no. 3, pp. 616–620, 2010.
- [125] K. Brecl and M. Topič, "Simulation of losses in thin-film silicon modules for different configurations and front contacts," *Prog. Photovoltaics Res. Appl.*, vol. 16, pp. 479–488, Sept. 2008.
- [126] K. Brecl, M. Topič, and F. Smole, "A detailed study of monolithic contacts and electrical losses in a large-area thin-film module," *Prog. Photovoltaics Res. Appl.*, vol. 13, pp. 297–310, June 2005.
- [127] D. Toet, P. M. Smith, T. W. Sigmon, and M. O. Thompson, "Experimental and numerical investigations of a hydrogen-assisted laser-induced materials transfer procedure," *J. Appl. Phys.*, vol. 87, no. 7, pp. 3537–3546, 2000.
- [128] R. Paschotta, *Field Guide to Laser Pulse Generation*. Bellingham, USA: SPIE Publications, 2008.
- [129] S. Inaba, S. Oda, and K. Morinaga, "Heat capacity of oxide glasses measured by AC calorimetry," *J. Non. Cryst. Solids*, vol. 306, pp. 42–49, July 2002.
- [130] A. Nadarajah, M. E. Carnes, M. G. Kast, D. W. Johnson, and S. W. Boettcher, "Aqueous Solution Processing of F-Doped SnO₂ Transparent Conducting Oxide Films Using a Reactive Tin(II) Hydroxide Nitrate Nanoscale Cluster," *Chem. Mater.*, vol. 25, pp. 4080–4087, Oct. 2013.
- [131] S. Fayette, D. S. Smith, A. Smith, and C. Martin, "Influence of grain size on the thermal conductivity of tin oxide ceramics," *J. Eur. Ceram. Soc.*, vol. 20, pp. 297–302, Mar. 2000.

- [132] V. Gurevich, K. Gavrichev, V. Polyakov, R. Clayton, S. Mineev, G. Hu, V. Gorbunov, and L. Golushina, "Low-temperature heat capacity of tin dioxide: new standard data on thermodynamic functions," *Thermochim. Acta*, vol. 421, pp. 179–184, Nov. 2004.
- [133] Z. Remeš, M. Vaněček, A. Mahan, and R. Crandall, "Silicon network relaxation in amorphous hydrogenated silicon," *Phys. Rev. B*, vol. 56, pp. R12710–R12713, Nov. 1997.
- [134] C. K. Ong, E. H. Sin, and H. S. Tan, "Heat-flow calculation of pulsed excimer ultraviolet laser's melting of amorphous and crystalline silicon surfaces," *J. Opt. Soc. Am. B*, vol. 3, pp. 812–814, May 1986.
- [135] C. Ong, H. Tan, and E. Sin, "Calculations of melting threshold energies of crystalline and amorphous materials due to pulsed-laser irradiation," *Mater. Sci. Eng.*, vol. 79, pp. 79–85, Apr. 1986.
- [136] S. de Unamuno and E. Fogarassy, "A thermal description of the melting of c- and a-silicon under pulsed excimer lasers," *Appl. Surf. Sci.*, vol. 36, pp. 1–11, Jan. 1989.
- [137] H. Kobatake, H. Fukuyama, I. Minato, T. Tsukada, and S. Awaji, "Noncontact measurement of thermal conductivity of liquid silicon in a static magnetic field," *Appl. Phys. Lett.*, vol. 90, no. 9, p. 094102, 2007.
- [138] E. P. Donovan, "Heat of crystallization and melting point of amorphous silicon," *Appl. Phys. Lett.*, vol. 42, no. 8, pp. 698–700, 1983.
- [139] J. M. L. Martin and P. R. Taylor, "A Definitive Heat of Vaporization of Silicon through Benchmark ab Initio Calculations on SiF₄," *J. Phys. Chem. A*, vol. 103, pp. 4427–4431, June 1999.
- [140] I. Henins, "Precision density measurement of silicon," *J. Res. Natl. Bur. Stand. Sect. A Phys. Chem.*, vol. 68A, pp. 529–533, Sept. 1964.
- [141] S. R. Idelsohn, M. A. Storti, and L. A. Crivelli, "Numerical methods in phase-change problems," *Arch. Comput. Methods Eng.*, vol. 1, pp. 49–74, Mar. 1994.
- [142] S. Li, Y. Jiang, Z. Wu, J. Wu, Z. Ying, Z. Wang, W. Li, and G. J. Salamo, "Effect of structure variation on thermal conductivity of hydrogenated silicon film," *Appl. Surf. Sci.*, vol. 257, pp. 8326–8329, Aug. 2011.
- [143] S. Li, Y. Jiang, Z. Wu, J. Wu, Z. Ying, Z. Wang, W. Li, and G. J. Salamo, "Enhancement of thermal conductivity of hydrogenated silicon film by microcrystalline structure growth," *J. Mater. Sci. Mater. Electron.*, vol. 23, pp. 224–228, May 2011.
- [144] Y. Mai, S. Klein, R. Carius, J. Wolff, A. Lambertz, F. Finger, and X. Geng, "Microcrystalline silicon solar cells deposited at high rates," *J. Appl. Phys.*, vol. 97, no. 11, p. 114913, 2005.
- [145] J. C. Conde, E. Martín, S. Stefanov, P. Alpuim, and S. Chiussi, "FEM numerical analysis of excimer laser induced modification in alternating multi-layers of amorphous and nano-crystalline silicon films," *Appl. Surf. Sci.*, vol. 258, pp. 9342–9346, Sept. 2012.

Bibliography

- [146] J.-W. Hong and S. Cheong, "A crack model for the onset of blisters using finite surface thicknesses," *J. Appl. Phys.*, vol. 100, no. 9, p. 094322, 2006.
- [147] X.-Q. Feng and Y. Huang, "Mechanics of Smart-Cut® technology," *Int. J. Solids Struct.*, vol. 41, pp. 4299–4320, Aug. 2004.
- [148] B. Terreault, "Hydrogen blistering of silicon: Progress in fundamental understanding," *Phys. status solidi*, vol. 204, pp. 2129–2184, July 2007.
- [149] S. Timoshenko and S. Woinowsky-Krieger, *Theory of plates and shells*, vol. 2. McGraw-Hill New York, 1959.
- [150] F. Yang, "Hydrogen-induced silicon wafer splitting," *J. Appl. Phys.*, vol. 94, no. 3, pp. 1454–1457, 2003.
- [151] J. Gaspar, A. Gualdino, B. Lemke, O. Paul, V. Chu, and J. P. Conde, "Mechanical and piezoresistive properties of thin silicon films deposited by plasma-enhanced chemical vapor deposition and hot-wire chemical vapor deposition at low substrate temperatures," *J. Appl. Phys.*, vol. 112, no. 2, p. 024906, 2012.
- [152] A. Buzás and Z. Geretovszky, "Nanosecond laser-induced selective removal of the active layer of CuInGaSe₂ solar cells by stress-assisted ablation," *Phys. Rev. B*, vol. 85, p. 245304, June 2012.
- [153] A. A. Griffith, "The Phenomena of Rupture and Flow in Solids," *Philos. Trans. R. Soc. A Math. Phys. Eng. Sci.*, vol. 221, pp. 163–198, Jan. 1921.
- [154] S. Ku, S. Haas, B. E. Pieters, U. Zastrow, A. Besmehn, Q. Ye, and U. Rau, "Investigation of laser scribing of a-Si:H from the film side for solar modules using a UV laser with ns pulses," *Appl. Phys. A*, vol. 105, pp. 355–362, Sept. 2011.
- [155] S. Lauzurica and C. Molpeceres, "Assessment of laser direct-scribing of a-Si:H solar cells with UV nanosecond and picosecond sources," *Phys. Procedia*, vol. 5, pp. 277–284, Jan. 2010.
- [156] A. Goetzberger and R. M. Scarlett, "Research and investigation of inverse epitaxial UHF power transistors," tech. rep., Shockley Research Laboratory, Palo Alto, USA, 1964.
- [157] G. Reeves and H. Harrison, "Obtaining the specific contact resistance from transmission line model measurements," *IEEE Electron Device Lett.*, vol. 3, pp. 111–113, May 1982.
- [158] S. Abdelli-Messaci, T. Kerdja, S. Lafane, and S. Malek, "Fast Imaging of Laser-induced Plasma Emission from a ZnO Target," *Spectrochim. Acta Part B At. Spectrosc.*, vol. 64, pp. 968–973, Oct. 2009.
- [159] S. Amoruso, R. Bruzzese, X. Wang, and J. Xia, "Propagation of a femtosecond pulsed laser ablation plume into a background atmosphere," *Appl. Phys. Lett.*, vol. 92, no. 4, p. 041503, 2008.

- [160] J. Freeman, S. Harilal, P. Diwakar, B. Verhoff, and A. Hassanein, "Comparison of optical emission from nanosecond and femtosecond laser produced plasma in atmosphere and vacuum conditions," *Spectrochim. Acta Part B At. Spectrosc.*, vol. 87, pp. 43–50, Sept. 2013.
- [161] W. Shinohara, M. Shima, S. Taira, K. Uchihashi, and A. Terakawa, "Applications of laser patterning to fabricate innovative thin-film silicon solar cells," in *Proc. SPIE* (F. G. Bachmann, W. Hoving, Y. Lu, and K. Washio, eds.), vol. 6107, (San Jose, USA), pp. 61070J–61070J–18, Feb. 2006.
- [162] M. Kassner, T. Kennedy, and K. Schrems, "The mechanism of ductile fracture in constrained thin silver films," *Acta Mater.*, vol. 46, pp. 6445–6457, Nov. 1998.
- [163] S. Haas, A. Gordijn, and H. Stiebig, "High speed laser processing for monolithical series connection of silicon thin-film modules," *Prog. Photovoltaics Res. Appl.*, vol. 16, pp. 195–203, May 2008.
- [164] J. Wang, H. Wang, J. Du, R. Sun, C. Xu, Y. Zhang, D. Wang, T. Liu, Y. Huang, H. Jia, and Y. Mai, "Performance improvement of amorphous silicon see-through solar modules with high transparency by the multi-line ns-laser scribing technique," *Opt. Lasers Eng.*, vol. 51, pp. 1206–1212, Nov. 2013.
- [165] F. Köhler, *On the microstructure of silicon-based thin films for photovoltaics*. PhD thesis, RWTH Aachen, 2012.
- [166] C. Smit, R. A. C. M. M. van Swaaij, H. Donker, A. M. H. N. Petit, W. M. M. Kessels, and M. C. M. van de Sanden, "Determining the material structure of microcrystalline silicon from Raman spectra," *J. Appl. Phys.*, vol. 94, no. 5, pp. 3582–3588, 2003.
- [167] R. Carius, T. Merdzhanova, S. Klein, O. Vetterl, *et al.*, "A comparison of microcrystalline silicon prepared by plasma-enhanced chemical vapor deposition and hot-wire chemical vapor deposition: electronic and device properties," *Journal of Materials Science: Materials in Electronics*, vol. 14, no. 10-12, pp. 625–628, 2003.
- [168] C. L. Molpeceres, M. Colina, M. Holgado, M. Morales, I. Sanchez-Aniorte, S. Lauzurica, J. J. Garcia-Ballesteros, and J. L. Ocaña, "Optical characterization of the heat-affected zone in laser patterning of thin film a-Si:H," in *Proc. SPIE* (W. Pfleging, Y. Lu, K. Washio, W. Hoving, and J. Amako, eds.), vol. 7202, (San Jose, USA), pp. 72020R–72020R–10, Feb. 2009.
- [169] S. Ku, B. Pieters, S. Haas, A. Bauer, Q. Ye, and U. Rau, "Electrical characterization of P3 isolation lines patterned with a UV laser incident from the film side on thin-film silicon solar cells," *Sol. Energy Mater. Sol. Cells*, vol. 108, pp. 87–92, Jan. 2013.
- [170] X. Wang, M. Ehrhardt, P. Lorenz, C. Scheit, S. Ragnow, X. Ni, and K. Zimmer, "The influence of the laser parameter on the electrical shunt resistance of scribed Cu(InGa)Se₂ solar cells by nested circular laser scribing technique," *Appl. Surf. Sci.*, vol. 302, pp. 194–197, May 2014.

Bibliography

- [171] S. Dongaonkar, S. Loser, E. J. Sheets, K. Zaunbrecher, R. Agrawal, T. J. Marks, and M. A. Alam, "Universal statistics of parasitic shunt formation in solar cells, and its implications for cell to module efficiency gap," *Energy Environ. Sci.*, vol. 6, no. 3, p. 782, 2013.



Publications

- Turan, B., Köhler, F., and Haas, S. (2015),
Impact of scribe width reduction on the back-contact insulation process for the series connection of thin-film silicon solar cells,
Applied Physics A. DOI: 10.1007/s00339-015-9453-0.
- Turan, B., Ding, K., and Haas, S. (2015),
A concept for Lithography-free patterning of silicon heterojunction back-contacted solar cells by laser processing,
Retrieved from <http://arxiv.org/abs/1506.02879>.
- Turan, B., Bauer, A., Lambertz, A., Merdzhanova, T., and Haas, S. (2015),
Novel interconnection scheme for thin-film silicon solar modules with conductive intermediate reflector,
Physica Status Solidi (RRL) - Rapid Research Letters, 9(2), 103–107. DOI: 10.1002/pssr.201409497.
- Turan, B., Haas, S., and Steger, M. (2014), Optimization of front-contact laser scribing for thin-film silicon solar modules,
Solar Energy Materials and Solar Cells, 125, 78–86. DOI: 10.1016/j.solmat.2014.02.029.
- Turan, B., and Haas, S. (2013),
Scribe Width Optimization of Absorber Laser Ablation for Thin-film Silicon Solar Modules,
Journal of Laser Micro/Nanoengineering, 8(3), 234–243. DOI: 10.2961/jlmn.2013.03.0009.
- Kim, S.-H., Jiang, W., Turan, B., Shim, I.-B., and Kingon, A. I. (2011),
Low Electrical Resistivity of Ni-Doped La-Cobaltite Thin Films Using a Novel Chemical Solution Route for Thermoelectric Applications,
Japanese Journal of Applied Physics, 50, 115801. DOI: 10.1143/JJAP.50.115801.



Acknowledgements

First of all I want to thank everybody that supported and encouraged me throughout the past three years that I was working on my PhD thesis.

I want to thank Prof. Dr. Uwe Rau for giving me the opportunity to conduct my thesis at the IEK-5. His supervision and interest in the topic gave me confidence to pursue many of my ideas.

I also want to thank Prof. Dr. Reinhart Poprawe for showing interest in my work and agreeing on being the second referee of this thesis.

I am especially grateful for the supervision of Dr. Stefan Haas. He introduced me to the topic of thin-film silicon solar cells/modules and in particular the broad field of laser material processing. His door was always open for fruitful discussions and constructive criticism. The never ending support and encouragement for the work helped steering my research into the right directions.

Furthermore, I also want to thank Drs. Jürgen Hüpkes, Matthias Meier, and Friedhelm Finger for their expertise and keen insight. Along with this I want to thank especially Dr. Tsvetelina Merdzhanova for the experimental planning and help of the many solar cell/module depositions throughout the years.

I want to thank Tobias Dyck, Erik Schumann, and all colleagues from the laser group for discussions on the topic of laser material processing and optics.

Special thanks go out to all the colleagues at the IEK-5 that helped by processing, depositions, and characterizations of all the solar cell materials, layers, and modules. Most importantly to mention is Andreas Bauer for helping me with every type of laser ablation/processing specific problem. He was always available for trying out new ideas and processes. Equally I want to thank Gunnar Schöpe for his support on all modifications and changes on the scribing machines.

In addition to many more I want to mention and thank furthermore, Sandra Tillmanns, Hilde Siekmann, and Ulrike Gerhards for substrate cleaning and contact depositions, Joachim Kirchoff, Daniel Weigand, and Peter Henning for solar cell depositions, Christoph Zahren and Sabine Kasper for the characterizations of the solar cells and modules. For the Raman

Chapter 8. Acknowledgements

microscopy on the laser processed cells I want to thank Markus Hülsbeck for the many and time-consuming measurements.

For the help on all topics and works related to the organization and administration at the IEK-5 I want to thank Andrea Mülheims, Petra Lorbach, and Susanne Schneider.

Besides thanking all my fellow colleagues I want to thank especially Dr. Stephan Michard, Dr. Ulrich W. Paetzold, Nicolas Sommer, Dr. Florian Köhler, and Björn Grootoink for the many helpful suggestions on practical science problems on a daily basis.

Furthermore, I want to thank Michael Steger for his time and endurance making the many measurements with the conductivity Atomic Force Microscopy in Aachen and Hans-Peter Bochem as well as Dr. Elmer Neumann for the Scanning Electron Microscopy measurements.

Lastly, I want to thank particularly my family, parents, sister and friends for their endless support bearing and enduring my bad mood and absence in the last phase of my thesis.

Jülich, Januar 18th 2016

B. T.

Band / Volume 293

Atrazine in the environment 20 years after its ban: long-term monitoring of a shallow aquifer (in western Germany) and soil residue analysis

D. S. Vonberg (2015), 149 pp

ISBN: 978-3-95806-099-9

Band / Volume 294

Yttria-Stabilized Zirconia / Gadolinium Zirconate Double-Layer Plasma-Sprayed Thermal Barrier Coating Systems (TBCs)

E. Bakan (2015), vi, 132 pp

ISBN: 978-3-95806-100-2

Band / Volume 295

Hydration and dehydration at the tropical tropopause

C. Schiller (2015), 72 pp

ISBN: 978-3-95806-101-9

Band / Volume 296

Influence of Impurities on the Fuel Retention in Fusion Reactors

M. Reinhart (2015), 140 pp

ISBN: 978-3-95806-105-7

Band / Volume 297

The role of abiotic processes in the formation and degradation of gaseous nitrogen compounds in the soil

J. Heil (2015), XIV, 106 pp

ISBN: 978-3-95806-106-4

Band / Volume 298

12th Carolus Magnus Summer School on Plasma and Fusion Energy Physics

edited by Kristel Crombé (2015), 468 pp

ISBN: 978-3-95806-107-1

Band / Volume 299

Optical near-field investigations of photonic structures for application in silicon-based thin-film solar cells

A. M. Ermes (2015), vi, 157 pp

ISBN: 978-3-95806-108-8

Band / Volume 300

Strom- und Gasmärktedesign zur Versorgung des deutschen Straßenverkehrs mit Wasserstoff

M. Robinius (2015), VI, 255 pp

ISBN: 978-3-95806-110-1

Band / Volume 301

**Alterung von Vakuum-plasmagespritzten MCrAlY-Schutzschichten
und ihre Wechselwirkung mit Nickel- und Cobalt-basierten
 γ/γ' -Superlegierungen**

P. J. Terberger (2015), IX, 149 pp
ISBN: 978-3-95806-113-2

Band / Volume 302

Verbundvorhaben ELFA Effiziente Luftfahrzeuge

Brennstoffzellensysteme zur Energieerzeugung BREZEN –
Teilprojekt: Kerosinaufbereitung

R. Peters, J. Meißner, J. Pasel, R. C. Samsun, D. Stolten
(2016), viii, 84 pp
ISBN: 978-3-95806-114-9

Band / Volume 303

**Cavity-Ringdown-Spektroskopie zur Untersuchung der Rolle
höherer Stickoxide für den nächtlichen Schadstoffabbau in der
unteren Atmosphäre**

S. Schrade (2016), II, 118 pp
ISBN: 978-3-95806-116-3

Band / Volume 304

**Thermo-mechanical Properties of Mixed Ionic-Electronic
Conducting Membranes for Gas Separation**

V. K. Stournari (2016), 167 pp
ISBN: 978-3-95806-117-0

Band / Volume 305

**Untersuchungen zu suspensionsplasmagespritzten
Wärmedämmschichtsystemen**

N. Schlegel (2016), X, 136 pp
ISBN: 978-3-95806-118-7

Band / Volume 306

**Laser processing for the integrated series connection of thin-film
silicon solar cells**

B. Turan (2016), xii, 188 pp
ISBN: 978-3-95806-119-4

Weitere **Schriften des Verlags im Forschungszentrum Jülich** unter
<http://www.zb1.fz-juelich.de/verlagextern1/index.asp>

**Energie & Umwelt /
Energy & Environment
Band / Volume 306
ISBN 978-3-95806-119-4**

